

Spring 5-15-2015

Kinematic Modeling of the Determinants of Diastolic Function

Leonid Shmuylovich
Washington University in St. Louis

Follow this and additional works at: https://openscholarship.wustl.edu/art_sci_etds



Part of the [Physics Commons](#)

Recommended Citation

Shmuylovich, Leonid, "Kinematic Modeling of the Determinants of Diastolic Function" (2015). *Arts & Sciences Electronic Theses and Dissertations*. 445.

https://openscholarship.wustl.edu/art_sci_etds/445

This Dissertation is brought to you for free and open access by the Arts & Sciences at Washington University Open Scholarship. It has been accepted for inclusion in Arts & Sciences Electronic Theses and Dissertations by an authorized administrator of Washington University Open Scholarship. For more information, please contact digital@wumail.wustl.edu.

WASHINGTON UNIVERSITY IN ST. LOUIS

Department of Physics

Dissertation Examination Committee:

Sándor J. Kovács, Chair

Anders E. Carlsson

Guy M. Genin

Mark R. Holland

James G. Miller

Samuel A. Wickline

Kinematic Modeling of the Determinants of Diastolic Function

by

Leonid Shmuylovich

A dissertation presented to the
Graduate School of Arts and Sciences
of Washington University in
partial fulfillment of the
requirements for the degree
of Doctor of Philosophy

May 2015

St. Louis, Missouri

© 2015, Leonid Shmuylovich

Table of Contents

List of Figures	v
List of Tables	x
Acknowledgements	xii
Abstract	xv
CHAPTER 1. BACKGROUND	1
1.1 Introduction	2
1.2 Basic Cardiovascular Organ Level Physiology	3
1.3 Techniques for Assessing Function	16
1.4 Conventional Left Ventricular Function Indexes	22
1.5 Kinematic Modeling of Diastolic Filling	31
1.6 Thesis Chapter Summaries	38
1.7 References	42
CHAPTER 2. METHODS SECTION	54
2.1 Introduction to Methodology	55
2.2 Simultaneous Catheterization and Echocardiography	56
2.3 Semi-Automated Post Processing of Simultaneous Data	61
2.4 Model Based Image Processing	67
2.5 Mathematical Insights and Methods	75
2.6 Conclusion	92
2.7 References	93
CHAPTER 3. LEFT VENTRICULAR SUCTION AND EQUILIBRIUM VOLUME: VIEWPOINT AND CONTROVERSY	95
3.1 Introduction	96
3.2 Alternate View of Diastolic Suction	96
3.3 Resolution of Current Inconsistencies	99
3.4 Physiological Implications of Diastasis as the Equilibrium Volume	101
3.5 Common Criticisms of Equilibrium Volume at Diastasis	104
3.6 Conclusions	110
3.7 References	112
CHAPTER 4. MEANINGFUL DIASTOLIC FUNCTION ASSESSMENT AND COMPARISON IS FACILITATED BY INCORPORATION OF CHAMBER PROPERTIES AT DIASTASIS, RATHER THAN AT END-DIASTOLE	119
4.1 Introduction	120
4.2 Methods	121
4.3 Results	126
4.4 Discussion	128
4.5 Limitations	133
4.6 Conclusions	135
4.7 References	137

CHAPTER 5. STIFFNESS AND RELAXATION/VISCOELASTICITY JOINTLY DETERMINE DECELERATION TIME	140
5.1 Introduction	141
5.2 Methods	144
5.3 Results	154
5.4 Discussion	155
5.5 Limitations	163
5.6 Conclusions	167
5.7 References	169
CHAPTER 6. THE E-WAVE DELAYED RELAXATION PATTERN TO LV PRESSURE CONTOUR RELATION: MODEL BASED PREDICTION WITH <i>IN-VIVO</i> VALIDATION	174
6.1 Introduction	175
6.2 Methods	177
6.3 Results	190
6.4 Discussion	195
6.5 Limitations	203
6.6 Conclusions	207
6.7 References	209
CHAPTER 7. APPLICATION OF <i>PRR</i>: IN SILICO ECHOCARDIOGRAPHY	215
7.1 Introduction	216
7.2 In Silico Echocardiography Theoretical Derivation	219
7.3 In Silico Echocardiography Proof of Principle	227
7.4 References	233
CHAPTER 8. LOAD INDEPENDENT INDEX OF DIASTOLIC FUNCTION DERIVATION AND IN VIVO VALIDATION	235
8.1 Introduction	236
8.2 Methods	238
8.3 Results	245
8.4 Discussion	250
8.5 Limitations	259
8.6 Additional Results	260
8.7 Conclusion	265
8.8 References	267
CHAPTER 9. LOAD INDEPENDENT INDEX OF DIASTOLIC FUNCTION: VALIDATION IN THE FACE OF EXTENDED LOAD VARIATION	271
9.1 Introduction	272
9.2 Methods	273
9.3 Results	277
9.4 Discussion	279
9.5 Limitations	284
9.6 Conclusion	286
9.7 References	287
CHAPTER 10. LOAD INDEPENDENT INDEX AND END DIASTOLIC	

PRESSURE RELATION: THEORETICAL DERIVATION AND EXPERIMENTAL VALIDATION	291
10.1 Introduction	292
10.2 Methods	293
10.3 Results	298
10.4 Discussion	299
10.5 Limitations	303
10.6 Conclusion	307
10.7 References	309
CHAPTER 11. LOAD INDEPENDENT INDEX OF ISOVOLUMIC PRESSURE DECAY: MODEL BASED DERIVATION WITH EXPERIMENTAL VALIDATION	312
11.1 Introduction	313
11.2 Methods	314
11.3 Results	328
11.4 Discussion	333
11.5 Limitations	342
11.6 Conclusion	345
11.7 Thematically Related Abstract	346
11.8 References	348
CHAPTER 12. A CLINICALLY IMPLEMENTED GEOMETRIC APPROACH TO PDF MODEL ANALYSIS OF TRANSMITRAL CONTOURS	352
12.1 Introduction	353
12.2 Methods	355
12.3 Results	370
12.4 Discussion	377
12.5 Limitations	384
12.6 Conclusion	385
APPENDIX	387
CURRICULUM VITAE	391

List of Figures

Figure 1.1: A schematic of the cardiovascular system, demonstrating the primary roles of the left and right heart, and the critical sites of gas exchange.	4
Figure 1.2: Schematic showing right and left heart inflow and outflow tracts.	5
Figure 1.3: A multi-scale view of heart anatomy and histology.	8
Figure 1.4: Electrical activation in the heart	11
Figure 1.5: Schematic representation of left ventricular pressure and volume during the cardiac cycle.	13
Figure 1.6: Multiple imaging modalities superimposed.	19
Figure 1.7: Pressure-Volume loop analysis.	23
Figure 1.8: The pressure phase plane.	27
Figure 1.9: Conventional analysis of transmitral contours.	30
Figure 1.10: PDF-model based analysis of transmitral contours	33
Figure 2.1: General overview of data acquisition and analysis. See text for details.	55
Figure 2.2: A schematic of the catheterization lab setup for simultaneous catheterization and echocardiography.	59
Figure 2.3: A pressure vs time plot during a Valsalva maneuver, showing left ventricular (black) and aortic (blue) pressure, with ECG signal in red.	60
Figure 2.4: A screenshot of a custom MATLAB interface for efficient conventional clinical analysis of Doppler echocardiography transmitral velocity contours.	66
Figure 2.5: A screenshot of a LabView interface for PDF model based image processing.	68
Figure 2.6: A closer look at the upslope and downslope of the E-wave, showing limitations inherent in the PDF model of the E-wave velocity contour.	70
Figure 2.7: E-wave from different subjects, demonstrating the merging of E- and A-waves with increased heart rate.	73
Figure 2.8: Visualization of the trigonometric identities in Equation 2.24 and Equation 2.12.	81

Figure 2.9: 3 Underdamped E-waves with increasing damping, showing both exact deceleration time (DT), and inflection point determined deceleration time (DT')..	82
Figure 2.10: A plot of Equation 2.31 (red) and Equation 2.15 (blue) defined deceleration time (DT) vs y .	83
Figure 2.11: 3 overdamped E-waves with increasing y values, showing the inflection point defined deceleration time (DT').	87
Figure 3.1: PV-loop and the kinematics/energetics of filling.	104
Figure 3.2: Simultaneous left ventricular pressure, aortic pressure, and ECG for one cardiac cycle in a subject with first degree AV block	105
Figure 4.1: Comparing simultaneous pressure-volume and echocardiographic data between normal sinus rhythm (left) and chronic atrial fibrillation (right) subjects.	123
Figure 4.2: An example of diastatic pressure-volume relationship (D-PVR) in NSR (panel A) and AF (panel B).	125
Figure 5.1: E-waves of two subjects having indistinguishable DTs, but significantly different values for E-wave derived stiffness k and catheterization-derived stiffness $\Delta P_{AVG}/\Delta V_{AVG}$.	143
Figure 5.2: The PDF model reveals how E-wave deceleration time (DT) is determined jointly by stiffness and relaxation.	150
Figure 5.3: Data for 64 beats from $n=20$ subjects.	153
Figure 5.4: Comparison of measured vs predicted values for DT by the 'stiffness only, DT_k ' and 'stiffness and viscoelasticity, $DT_{k,c}$ ' models in 79 subjects.	154
Figure 6.1: Simultaneous transmitral flow (Doppler echo) superimposed with LV pressure from two subjects with different E-wave shapes and pressure contours	176
Figure 6.2: Theoretical plot of pressure gradient	180
Figure 6.3: Results of numerical experiments	182
Figure 6.4: Pressure tracing showing 12 different choices of fiducial pressures.	188
Figure 6.5: PRR compared to clinical parameters across groups	191
Figure 6.6: PRR vs c for all subjects.	193

Figure 6.7: Schematic summary of the connection between the pressure contour (lower plot) defined pressure recovery ratio and noninvasively measured transmitral contour (upper plot) shape.	196
Figure 6.8: Plot of PRR vs c for 40 subjects.	198
Figure 6.9: Plot of E/A and VTI_E/VT_A to PRR .	203
Figure 7.1: Summary of noninvasive Doppler echocardiography transmitral flow contours.	217
Figure 7.2: A typical real time left ventricular pressure (LVP) and simultaneous ECG signal seen in the catheterization lab during a procedure.	218
Figure 7.3: A plot of Equation 1 vs. time for arbitrarily chosen k , c , and x_0 values in the underdamped regime.	220
Figure 7.4: A flowchart for generation of a simultaneous E-wave velocity contour given synchronized LVP and ECG data.	221
Figure 7.5: Schematic left ventricular pressure, left atrial pressure, Doppler E- and A-wave, and ECG data for one beat.	223
Figure 7.6: In this figure the iterative approach for determining the start of the LVP contour is presented.	226
Figure 7.7: The actual transmitral Doppler velocity contour measured simultaneously during catheterization for the beat presented in Figure 7.2 is shown here.	230
Figure 7.8: An independent assessment of the close agreement between the In Silico Echocardiography determined E-wave and measured Doppler E-wave.	231
Figure 8.1: Theoretical analysis of the peak driving force (kx_0) to peak resistive force (cE_{peak}) plane	241
Figure 8.2: The determination of the load independent index of diastolic function (LIIDF), requires multiple E-waves with different shapes.	245
Figure 8.3: A) E- and A-waves acquired from healthy subject at 3 different tilt-table positions (HU=head up, HD= head down).	247
Figure 8.4: kx_0 vs cE_{peak} plane for one subject and for the group.	248
Figure 8.5: Comparison between groups	249
Figure 8.6: Comparison of normal and diastolic dysfunction subject in the kx_0 vs cE_{peak} plane.	254

Figure 8.7: Analysis of randomness in the kx_o vs cE_{peak} plane.	256
Figure 8.8: Theoretical kx_o vs cE_{peak} relations for subjects with normal and abnormal diastolic function.	258
Figure 8.9: The forces of filling plane for a subject with diastolic dysfunction (left) and for a subject with normal diastolic function (right).	261
Figure 8.10: Comparison of diastolic reserve between diastolic dysfunction and normal subjects	262
Figure 8.11: Comparison of KFEI between E-wave with low damping (left) and high damping (right).	263
Figure 8.12: Theoretical plot of kx_o/cE_{peak} vs the kinematic filling efficiency index (KFEI).	264
Figure 8.13: Plot of diabetic (red) and nondiabetic (blue) subjects in the kx_o vs cE_{peak} plane	265
Figure 9.1: Typical data showing six consecutive beats from one subject.	275
Figure 9.2: Representative beats from one subject.	278
Figure 9.3: kx_o vs cE_{peak} plot for 4 subjects.	280
Figure 9.4: kx_o vs. cE_{peak} for subject 7.	283
Figure 10.1: Pressure volume schematic.	294
Figure 10.2: Correlation of E/E' and B to EDP .	299
Figure 10.3: Correlation of E/E' and B to P_{min} and ΔP	305
Figure 11.1: Comparison of 'clean' (left) and 'noisy' (right) data.	320
Figure 11.2: Plot of the Chung model predicted tautology (Eq. 5.12) for all beats from all subjects in the current study.	322
Figure 11.3: Model-predicted pressure contour between P_{MAX}^* and $P(t_{dP/dt\text{MIN}})$.	323
Figure 11.4: Data from all subjects and all beats in current study.	324
Figure 11.5: Summary of the method for IVPD load independent index analysis.	325
Figure 11.6: The automated process by which hemodynamic data analysis is performed is shown.	326
Figure 11.7: The $E_k \cdot (P_{\text{MAX}}^* - P_{\infty})$ vs. $\tau_c \cdot (dP/dt_{\text{MIN}})$ plot for 74 beats in subject 5.	330
Figure 11.8: Correlation of M_{LIIIVPD} with physiologic parameters.	332
Figure 11.9: Theoretical load independent index of isovolumic pressure decay plot.	335

Figure 11.10: RMSE cutoff results	340
Figure 11.11: Visualizing isovolumic pressure decay in the τ_c vs E_k plane.	346
Figure 12.1: Plots of c , k and x_0 vs AT and AT/(AT+DT).	358
Figure 12.2: Plot of (AT/DT) vs y in overdamped regime.	361
Figure 12.3: Plot of AT/DT vs y extended to underdamped regime.	362
Figure 12.4: DT and DT' for E-wave with increasing y .	363
Figure 12.5: Summary of triangle based methodology for PDF fitting.	366
Figure 12.6: Comparison of inverse solution and geometric method.	371
Figure 12.7: Comparison of inverse solution and geometric method when AT agrees.	372
Figure 12.8: Multiple fitting approaches applied to the same E-wave	374
Figure 12.9: Correlation for PDF parameters between alternative fitting methods	376
Figure 12.10: Interobserver variability for multiple methods.	378
Figure 12.11: Correlation for lumped indexes between alternative fitting methods	379

List of Tables

Table 4.1: Clinical descriptors for NSR and AF groups.	122
Table 4.2: Invasive hemodynamic and noninvasive echocardiographic measurements in NSR and AF groups.	127
Table 5.1: Comparison of hemodynamic stiffness and DT between two subjects	143
Table 5.2: Subject Demographics	151
Table 6.1: Simultaneous catheterization echo data from 2 subjects	176
Table 6.2: Summary of Results	186
Table 6.3: R^2 values of the linear correlations between alternately defined PRR values and c across 363 NSR beats.	194
Table 8.1: Demographics of simultaneous catheterization-echocardiography subjects analyzed retrospectively	244
Table 8.2: Average values of Doppler indexes and PDF parameters in one typical tilt table subject at three different preload states	246
Table 8.3: Averaged, normalized percent increase or decrease relative to baseline (horizontal tilt table position) for all tilt table subjects	246
Table 8.4: Comparison of the slope (M), intercept (B), and LVEDP for all (n=27) subjects comprised of the tilt table group (n=16) and the catheterization-echocardiography group (n=11)	249
Table 9.1: Subject Demographics.	273
Table 9.2: Summary of results	277
Table 10.1: Subject demographics.	297
Table 11.1: Subject Demographic	327
Table 11.2: Hemodynamic Values	328
Table 11.3: LIIIVPD Analysis	331
Table 12.1: Correlation coefficient (r^2) between inverse solution determined and geometric method determined PDF and triangle parameters.	373
Table 12.2: Mean Square Error To Input Velocity Contour For Each Investigator	375
Table 12.3: Interobserver variability for PDF model parameters and conventional triangle parameters measured by multiple approaches	375

Table 12.4: Correlation coefficient (r^2) between inverse solution determined and geometric method determined PDF lumped indexes	377
Table 12.5: Interobserver variability for PDF model lumped indexes.	377

Acknowledgements

I would like to begin by thanking my family for giving me the opportunity to pursue my passion. My parents' bravery many years ago to immigrate to this country has granted me immense freedoms and a persistent drive to put maximum effort in all of my endeavors. My mother, father, and sister have always been my biggest fans, and it's much easier to stay focused when you have a cheering section.

Next I would like to thank my mentors. I have been blessed with phenomenal mentorship throughout my academic career. David Newburg was my science team coach in High School and became a trusted friend and advisor. Without his influence I would likely not have pursued research in the life sciences, and I am forever grateful for his continued influence in my life. My thesis advisor, Sándor J Kovács, has had a tremendous impact on me both professionally and personally. His enthusiasm for science, and big picture thinking in particular, is thrilling and contagious. He can't help but be original, and his creativity and forward thinking spirit are traits that I hope to emulate as I move forward in my career. He is also a mentor on a personal level, as he is one of the few researchers I know who successfully balances being fully engaged in family life while being absolutely committed to his work. He's also the only cardiologist at the American College of Cardiology Conference that shows up in a Hawaiian shirt, and I hope one day to join him in that distinction. He is someone that I have always looked up to, and it is an honor to be one of his mentees.

I must also thank those who provided materials and assistance in completing this thesis. The American Heart Association and its reviewers believed in my research plan and provided 3 years of predoctoral fellowship support, which I am very grateful for. Beth Engeszer and others at the Washington University School of Medicine have helped me immensely through numerous

bureaucratic hurdles that could have been far worse headaches were it not for their assistance. I must also thank Jeff Gordon MD, Claude Bernard PhD, Sophia Hayes PhD, and James G Miller PhD for their letters of reference in support of my fellowship. I am thankful to the Department of Physics for welcoming me from the medical school and challenging me to think hard about deep problems. I have been honored to take classes with brilliant faculty and I thank Carl Bender and Zohar Nussinov in particular for stretching my mind in ways that only a great physics problem set can.

I would like to thank the staff of the Cardiac Procedure Center at Barnes Jewish Hospital. The CPC staff, in particular Maddie, have provided invaluable assistance in obtaining hemodynamic data and helping troubleshoot when necessary. I would also like to thank Peggy Brown, our expert sonographer, for being always positive and kind, especially to me, and for being so skilled in her practice.

I thank my Dissertation Committee: Anders Carlsson, Sam Wickline, Jim Miller, Guy Genin, and Mark Holland, for reviewing this work. In addition, this work could not have been completed without the support of the members of the Cardiovascular Biophysics Laboratory. Charles Chung taught me everything I know about the Cardiovascular Biophysics Laboratory and was a blast to collaborate with. Former members of our lab who have helped me develop ideas and thoughts include: Wei Zhang, Matt Riordan, and Yue (Ryan) Wu, and I thank them for their contribution to my academic growth. Current members that I would like to thank for their collaborative efforts include Erina Ghosh and Sina Mossahebi. I am also thankful to collaborators that I have worked with, who have given me opportunities to extend my work into new experimental and physiological realms. I would like to thank Troy Wildes and Michael Avidan in particular, for teaching me how to intubate and giving me access to absolutely

beautiful physiological data. In addition I would like to thank Chris Lloyd for being dedicated and showing up to cath lab without fail for many years, even when the data didn't look so good.

Finally, I must thank my wife, my kids, and my friends for keeping my spirits up and reminding me that there is more to life than science and math.

Leonid Shmuylovich

Washington University in St. Louis

May 2015

ABSTRACT OF THE DISSERTATION

Kinematic Modeling of The Determinants of Diastolic Function

by

Leonid Shmuylovich

Doctor of Philosophy in Physics

Washington University in St. Louis, 2015

Professor Sándor J. Kovács, Chair

Multiple modalities are routinely used in clinical cardiology to determine cardiovascular function, and many of the indexes derived from these modalities are causally interconnected. A correlative approach to cardiovascular function however, where indexes are correlated to disease presence and progression, fails to fully capitalize on the information content of the indexes.

Causal quantitative modeling of cardiovascular physiology on the other hand offers a predictive rather than accommodative approach to cardiovascular function determination. In this work we apply a kinematic modeling approach to understanding diastolic function. We discuss novel insights related to the physiological determinants of diastolic function, and define novel causal indexes of diastolic function that go beyond the limitations of current established clinical indexes. Diastolic function is typically characterized by physiologists and cardiologists as being determined by the interplay between chamber stiffness, chamber relaxation/viscoelasticity, and chamber filling volume or load. In this work we provide kinematic modeling based analysis of each of these clinical diastolic function determinants.

Considering the kinematic elastic (stiffness) components of filling, we argue for the universality of diastolic suction and define a novel in-vivo equilibrium volume. Application of this novel equilibrium volume in the clinical setting results in a novel approach to determination of global chamber stiffness.

Considering the viscoelastic components of filling, we demonstrate the limitations associated with ignoring viscoelastic effects, an assumption often made in the clinical setting. We extend the viscoelastic component of filling into the invasive hemodynamic domain, and demonstrate the causal link between invasively recorded LV pressure and noninvasively recorded transmitral flow by describing a method for extracting flow contours from pressure signals alone.

Finally, in considering load, we solve the problem of load dependence in diastolic function analysis. Indeed all traditional clinical indexes of diastolic function are load dependent, and therefore are imperfect indexes of intrinsic diastolic function. Applying kinematic modeling, we derive a load independent index of diastolic function. Validation involves showing that the index is indeed load-independent and can differentiate between control and diastolic dysfunction states. We apply this novel analysis to derive surrogates for filling pressure, and generalize the kinematic modeling approach to the analysis of isovolumic relaxation.

To aid widespread adoption of the load independent index, we derive and validate simplified expressions for model-based physiological parameters of diastolic function.

Our goal is to provide a causal approach to cardiovascular function analysis based on how things move, to explain prior phenomenological observations of others under a single causal paradigm, to discover ‘new physiology’, facilitate the discovery of more robust indexes of cardiovascular function, and provide a means for widespread adoption of the kinematic modeling approach suitable for the general clinical setting.

CHAPTER 1
BACKGROUND

1.1 Introduction

Theoretical physics-based modeling of cardiovascular function is not the primary approach taken by the general cardiovascular research community. Instead, basic cardiovascular research is driven by sophisticated molecular biology or tissue/muscle characterization experiments (83), and clinical cardiology is driven by carefully controlled clinical experiments and trials (93). These well established approaches have resulted in numerous novel insights into the molecular components of cardiovascular function and disease, and have led to successful therapeutic approaches that improve patient outcomes.

In clinical cardiology in particular, however, there seems to be an endless supply of clinical indexes that clinicians must measure and follow in order to diagnose and treat cardiovascular disease (52). These extend beyond the clinic, because they are often used by basic science researchers to validate the impact of a particular knockout gene or other molecular intervention. As new imaging modalities or measurement techniques are developed, new indexes are suggested and validated against clinical parameters of interest, and the already large list of possible clinical indexes grows further.

While there is no limit in principle to the number of useful clinical indexes related to cardiovascular function, the large number that currently exists in the clinical and research setting is a clear symptom of the correlative nature of the majority of current cardiovascular research. The complexity of the cardiovascular system and of clinical medicine leads one to a correlative approach because a causal approach seems impossible given the number of seemingly independent variables that one must consider. However, because of the large number of variables, a correlative approach is likely to be extremely sensitive to interdependence of variables. Indeed, without a causal framework, it is impossible to understand how various

clinical indexes relate to each other or to the underlying physiological determinants of cardiovascular function. A correlative approach also makes prediction of physiological responses difficult, and gives little confidence in the general applicability of particular clinical indexes to novel physiologic or pathophysiologic settings.

Thus, while it is not a widespread approach in the field, theoretical modeling through causality is critical in the cardiovascular research community. A causal framework has the potential to unify seemingly unrelated cardiovascular function indexes and naturally provides mechanistic insight into the physiological determinants of clinical indexes. In our lab over past 3 decades we have taken a causal approach to cardiovascular physiology in general, and diastolic function in particular. In this thesis we discuss several examples that demonstrate the power of a quantitative causal approach to cardiovascular physiology. Before we can discuss these examples, however, it is prudent to review cardiovascular physiology at both the cellular and organ level, and to discuss general approaches to quantitatively modeling cardiovascular physiology.

1.2 Basic Cardiovascular Organ Level Physiology

1.2.1 Dual Function of the Cardiovascular System

The purpose of the cardiovascular system is to deliver oxygen to the cells of the body. This is achieved by pumping oxygen rich blood to a branching network of blood vessels that end in small diameter (10 μm) capillaries that are in close proximity to every cell in the body. Across the capillary membrane cells exchange carbon dioxide, a waste product from internal energy production, for oxygen, a key fuel for new energy production. Thus the blood is depleted of oxygen and rich with carbon dioxide beyond the capillaries. This blood is replenished with

oxygen when it returns to the lungs, where oxygen in the lungs and carbon dioxide in the blood exchange across a capillary membrane. The newly oxygen rich blood is then once again pumped back to the cells of the body. (9, 26)

Thus the cardiovascular system contains two parallel pumps, one that pumps oxygen rich blood from the lungs to the periphery, and one that pumps the resulting oxygen poor blood back to the lungs. Indeed the heart is divided into two large chambers; the left side accepts blood from the lungs and pumps blood to the periphery, while the right side accepts oxygen poor blood from the periphery and pumps blood back to the lungs.

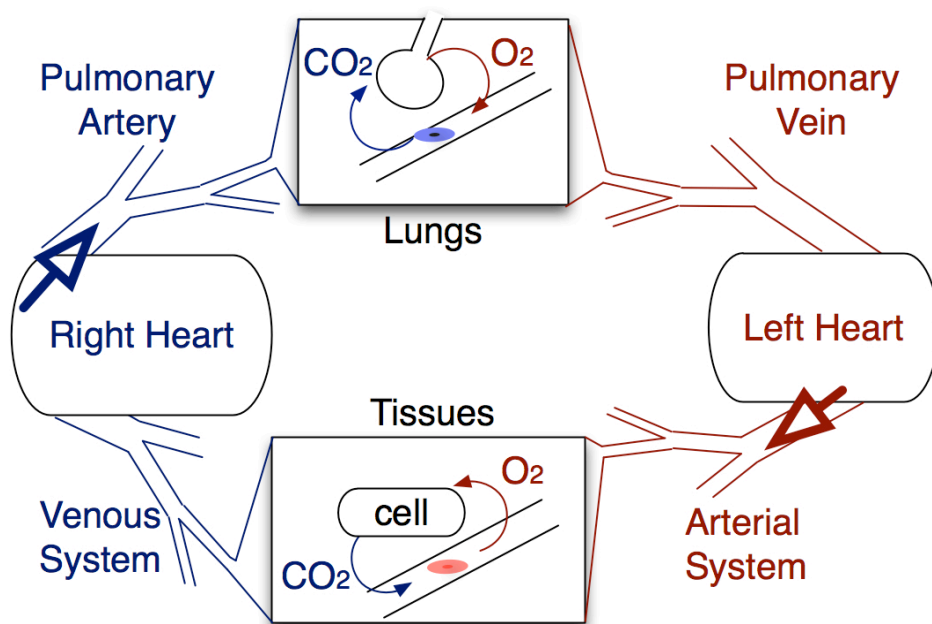


Figure 1.1 A schematic of the cardiovascular system, demonstrating the primary roles of the left and right heart, and the critical sites of gas exchange. Oxygenated blood from the left heart is pumped to the tissues, where it is taken up by the cells in exchange for carbon dioxide. The venous system brings the oxygen poor blood to the right heart, where it is subsequently pumped into the lungs. Here carbon dioxide is exchanged for oxygen, and the resulting oxygen rich blood is sucked back into the left heart to be pumped to the tissues again.

1.2.2 Right and Left Heart Anatomy

The human heart consists multiple chambers surrounded by a thin layer of lubricant and fixed pericardial sac. The right side of the heart consists of two sub-chambers: an atrium that accepts oxygen poor blood from the periphery by way of two large veins (the inferior and superior vena cava), and a ventricle that ejects blood into the lungs by way of the pulmonary valve. The atrium and ventricle are separated by a valve that acts as a rectifier and in the absence of pathology allows only atrial to ventricular flow. The left side of the heart similarly consists of an atrium and a ventricle separated by a one-way valve called the bicuspid valve. The atrium accepts blood from the lungs through 4 pulmonary veins and the ventricle ejects blood to the periphery through the aorta, the largest artery in the body. It is helpful to visualize this general anatomy through a simplified cylindrical model of both chambers (Figure 1.2). This model will

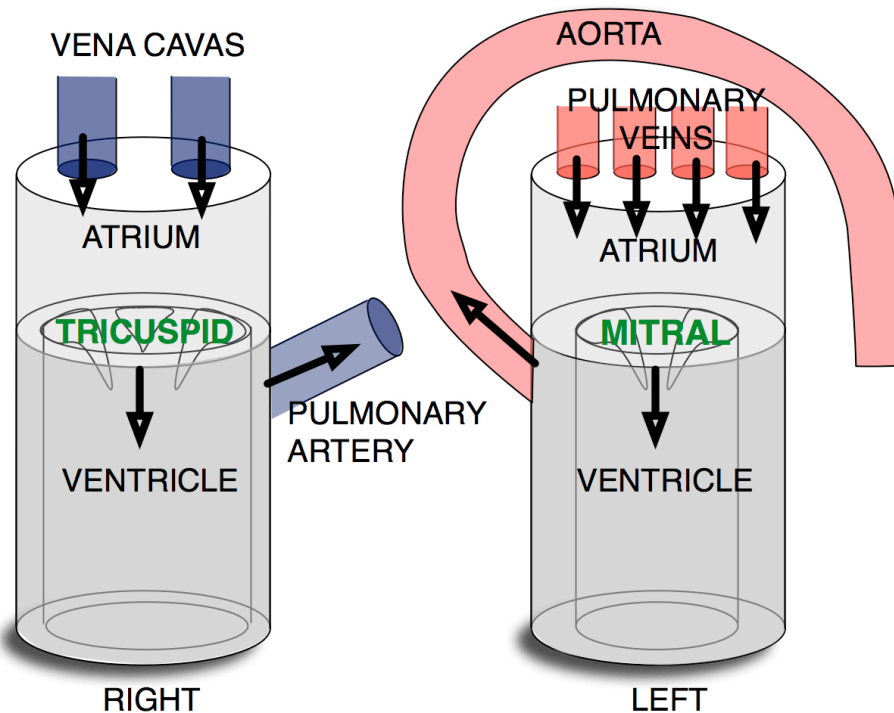


Figure 1.2. Schematic showing right and left heart inflow and outflow tracts. Both sides of the heart have a thin walled chamber called the atrium that accepts blood from outside of the heart. The atrium passively and actively delivers blood to the ventricle across a one-way valve (tricuspid or mitral), and the ventricle ejects blood out of the heart.

be useful in future discussion as well.

Though Figure 1.2 is a schematic representation of the heart, it captures some of the essential anatomical differences between chambers. These anatomical differences are best understood in the context of the physiological role of each chamber. The average human heart beats 60 times per minute, delivering nearly 5 L of blood in that interval. Both the left and right heart have a similar size of approximately 400 mL (7). It is not surprising that the size of both sides of the heart is similar, because in a steady-state sense, both hearts fill with and eject the same blood volume. An imbalance in volume between left and right sides would result in accumulation of fluid volume in either the peripheral or pulmonary vasculature with deleterious effects on health.

While the overall size is similar, the left side and right side eject blood into systems with dramatically different resistance to flow. Indeed the left ventricle ejects blood into a vascular system at a very high pressure in order to overcome the high resistance encountered in the various branches of the arterial system, primarily occurring at the level of the arterioles. For this reason the left ventricle is the chamber with the thickest muscle wall and most vigorous contraction. The right ventricle, on the other hand, ejects blood to the pulmonary vasculature at a pressure nearly an order of magnitude lower than the systemic side, and therefore the wall of the right ventricle is significantly thinner than the left ventricular wall. In contrast to the ventricles, both atria are thin walled because they are primarily conduits for fluid volume (8).

1.2.3 Cardiac Cell Structure and Function

Large Scale Cellular Organization

Ventricular tissue consists of ventricular cells embedded in a sponge-like meshwork of

extracellular matrix, composed primarily of collagen and elastin fibers (67). Cells that make up the heart also include fibroblasts, which are primarily supportive cells that create and maintain the extracellular matrix, pacemaker and specialized conduction cells, which are responsible for setting and distributing the electrical rhythm of the heart (76), and contractile cells, which are the muscle cells responsible for contraction and relaxation of the chamber. Cardiac muscle cells consist of many repeating contractile elements called sarcomeres. The membranes of cardiac muscle cells have repeating invaginations called T-Tubules that aid in the delivery of calcium to the contractile machinery. T-tubules are all interconnected through transverse tubules which are the sarcoplasmic reticulum. The sarcoplasmic reticulum contains specific protein channels that are responsible for release and sequestration of calcium during the cardiac cycle. Every sarcomere has one T-tubule and sarcoplasmic reticulum, and this architecture ensures robust distribution of calcium to the contractile elements (53).

Contractile Machinery

Each sarcomere contains overlapping thin filaments, composed of actin and tropomyosin woven together helically, and thick filaments, composed primarily of the protein myosin. When viewed along their long axis, the filaments are arranged hexagonally, with the thin filaments arranged along the vertices of a hexagon and the thick myosin filaments arranged along the middle of the hexagon. One sarcomere is defined by two Z-disks, and attached to each Z-disk are thin filaments that span nearly half the sarcomere. The thick filament on the other hand is centered between Z-disks, connected to the thin filaments through molecular cross bridges, and anchored to the Z-disk through the giant protein titin (Figure 1.3) (24).

The molecular details of sarcomere contraction are complex (15, 78). The cross-bridge

theory states that when calcium, coming from the T-Tubules and sarcoplasmic reticulum binds a troponin-tropomyosin complex, it induces a conformational change in tropomyosin that exposes a myosin binding site on actin.

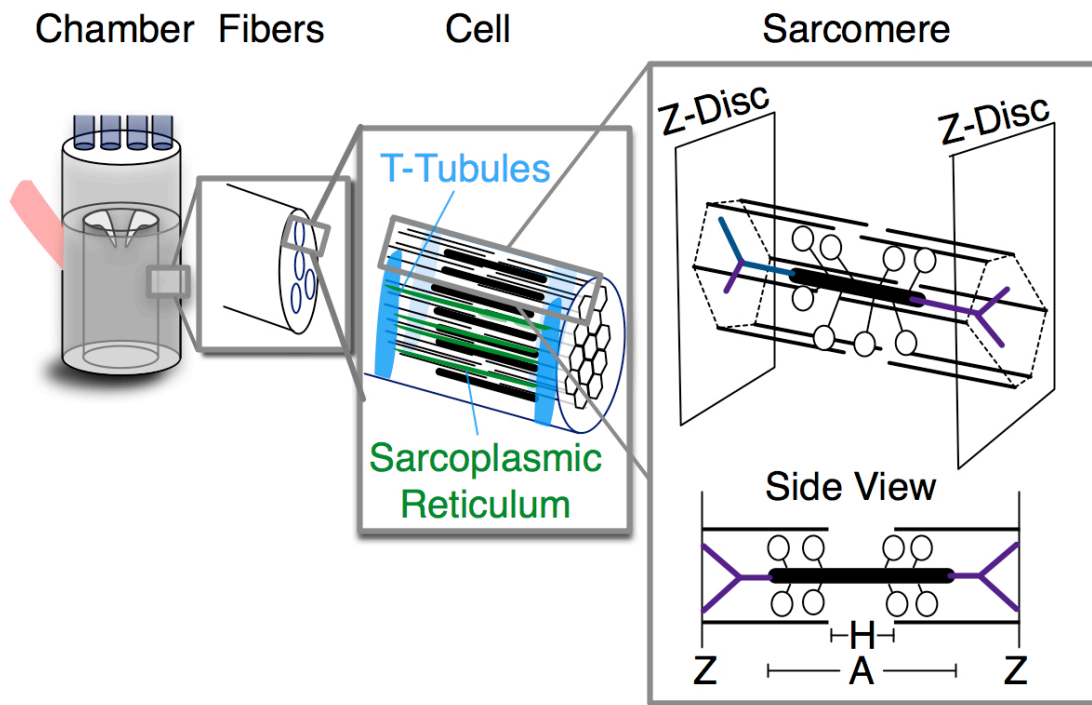


Figure 1.3. A multi-scale view of heart anatomy and histology. Muscle tissue consists of bundles of muscle fibers, and each fiber is a muscle cell. Muscle cells have membrane invaginations called T-tubules (blue) which are interconnected by transverse sarcoplasmic reticulum (green). Each cell contains multiple sarcomeres with contractile machinery composed of thin (actin) and thick (myosin) filaments. The sarcomere is defined by Z-discs, the longitudinal space between thin filaments is the H-band, and the thick filaments define the A-band. See text for details.

This results in a binding of an ATP-bound myosin cross-bridge head (part of the thick filament) to actin (part of the thin filament). When myosin is bound to actin in this fashion, myosin has ATPase activity and therefore hydrolyzes the ATP bound to it. ATP hydrolysis releases energy and causes a conformation change in the myosin head that pulls the thin filament horizontally towards the thick filament, thereby producing contraction. Thus if myosin cross-bridge heads were reversed relative to Z-disks, sarcomeres would be pushed apart upon each ‘contraction’. Release of the myosin head from actin requires both removal of calcium from the troponin-tropomyosin complex, as well as binding of ATP to the ADP-bound myosin cross-

bridge head. Removal of calcium occurs through re-sequestration of calcium into the sarcoplasmic reticulum by the action of ATP dependent calcium pumps. Thus without ATP, thick and thin filaments remain bound and muscle tension can not be released, and this provides a mechanisms for *rigor mortis*. ATP mediated release of actin-myosin binding reduces muscle tension but does not relengthen the sarcomere, and the mechanism for sarcomere relengthening in the absence of external tension or load, and by extension chamber recoil, has been an active area of research for many years.

Cellular Elastic Recoil

Skeletal muscles, such as biceps, have opposing muscles, such as triceps, whose contraction has the mechanical effect of relengthening the opposing muscle. Cardiac muscle, however, does not have an opposing muscle group tasked with expanding the cardiac chamber, and therefore the cyclical recoil of the ventricular chamber following contraction is at first puzzling. Early experimental studies predicted that cellular elastic elements must be responsible for sarcomere relengthening (44) The role of titin as a series elastic element that drives sarcomere relengthening and ventricle recoil was only recently appreciated, however (23-25, 29, 30). In 1996 Helmes demonstrated that titin behaves as a linear bidirectional spring, producing an intracellular restoring force as it is stretched or compressed (30). Sarcomere contraction forces the titin protein into an entropically unfavored orientation and has the effect of loading the titin spring with elastic potential energy that is released in accordance with a linear force vs. length relation upon relaxation of the systolic cramp. The linear bidirectional nature of sarcomere recoil was anticipated decades prior to its discovery and a linear, bi-directional spring is the

mechanistic basis for a kinematic model of diastolic suction generating chamber recoil that we discuss in section 1.5 below.

1.2.4 Electrical Activation of Cardiovascular Chambers

The release of calcium from the sarcoplasmic reticulum and subsequent activation of contractile machinery requires electrical depolarization of the cardiac myocyte. The network of cardiac myocytes in the heart represent an excitable medium, because they are electrically interconnected through protein channels (called gap junctions) and therefore depolarization spreads quickly from cell to cell. All cardiac cells contain leaky ion channels that predispose them to periodic spontaneous depolarization. The cells with the shortest period of spontaneous depolarization, the pacemaker cells are located in the sinoatrial node on the right atrium, set the rhythm for all cardiac cells. Pacemaker cells are predisposed to depolarize at a 2 Hz frequency, though under normal physiologic conditions they are inhibited by parasympathetic innervation and depolarize at a slower 1 Hz frequency. Thus electrical activation of the heart begins at the sinoatrial node on the right atrium and spreads as a wave across the right and left atrium (17). The electrical depolarization travels quickly along a conduction system made up of specialized nerve cells that is designed to ensure efficient contraction of atrial and ventricular tissue (Figure 1.4). Atrial contraction adds volume to the ventricle before ventricular ejection and stretches sarcomeres an additional 5-10% relative to their resting length, and therefore ventricular contraction must ideally occur after atrial contraction. Thus the conduction system that carries the electrical depolarization from the sinoatrial node to the atrioventricular His bundle and right and left septal branches includes a time delay between atrium and ventricle to ensure that atrial mechanical contraction and atrioventricular flow is complete before ventricular contraction

occurs. This built-in time delay is insured by the atrioventricular node, a part of the conduction system that is located on the right atrium toward the atrioventricular junction. Past the atrioventricular node, the depolarization wave splits along the left and right bundles of the conduction system, and then Purkinje fibers come off the bundles and deliver the depolarization wave to the endocardial (inner wall) ventricular tissue. Cell to cell depolarization by gap junctions and differences in action potential duration from endocardium to epicardium (outside wall) result in contraction from endocardium to epicardium followed by repolarization from epicardium to endocardium.

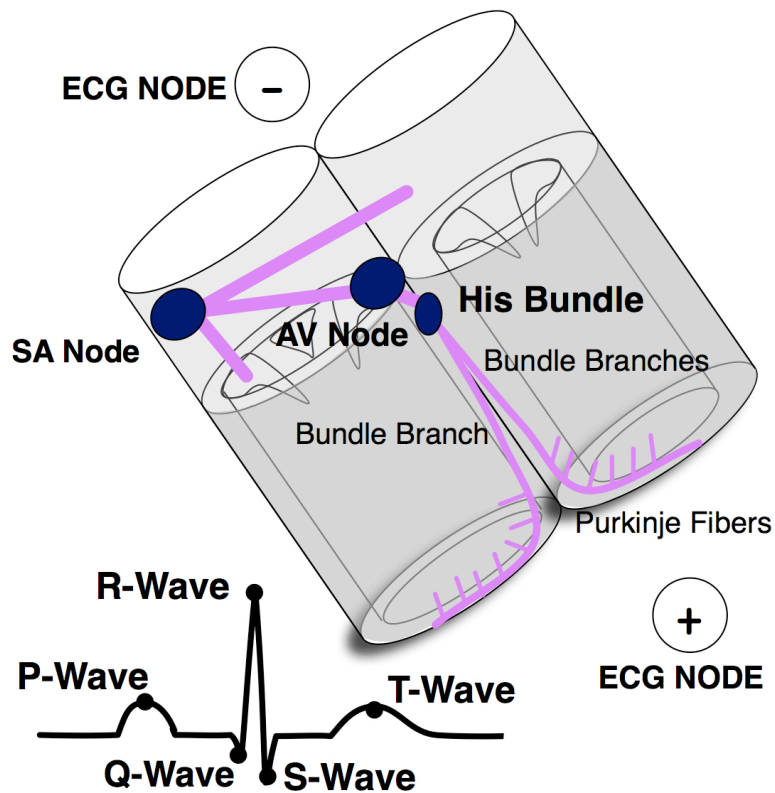


Figure 1.4 Electrical activation in the heart follows a specific pathway and timing, and this results in a reproducible surface electrode signal that is measured by the electrocardiogram (ECG). The PQRST peaks of the ECG represent specific electrical activation and deactivation events. See text for details.

While cardiac cells have a variety of depolarization profiles and properties based on their location in the chamber, the global electrical behavior of the heart can be appreciated through the electrocardiogram (ECG), where electrical leads are connected to the body in an orientation that is roughly along the primary direction of chamber depolarization. Thus as the positive depolarization wave approaches the positive ECG lead, a positive deflection is observed. While a variety of ECG patterns are routinely observed in the clinical setting, the general pattern consistent with normal electrical activation is shown in Figure 1.4. The atrial depolarization is seen on the ECG as the positive P-wave deflection. The QRS complex that follows is the ventricular depolarization and contraction, and the delay between P-wave and QRS complex arises from the atrioventricular delay discussed above. An atrioventricular block results in a prolongation of the P-R interval and the hemodynamic consequences of that delay are described in Chapter 3. Following ventricular depolarization and contraction, which is well approximated on the surface ECG by the QT interval,, the tissue must relax and repolarize so as to accommodate filling of the chamber before the next ejection. This repolarization is the positive T-wave deflection on the ECG signal, and the sign of the T-wave is notable. The only way for a negative repolarization wave to cause a positive deflection on the ECG is for the negative wave to move away from the positive ECG electrode. This suggests that while depolarization occurs from endocardium to epicardium, repolarization occurs from epicardium to endocardium. Thus epicardial and endocardial cardiac cells must have dramatically different action potential durations, and this is a finding that has been validated by direct experimental recordings (68).

1.2.5 Pressure and Volume Variation During Cardiac Cycle

The heart cycle consists of systolic contraction/ejection and diastolic relaxation/filling. We may follow the timeline of electrical activation, beginning with the P-wave, to track pressures and volumes throughout the heart (Figure 1.5) (26). The P-wave indicates atrial depolarization and contraction (atrial systole), and contraction of atrial chambers increases atrial pressure above corresponding ventricular pressures. The resulting pressure gradient accelerates blood flow forward across mitral (bicuspid) and tricuspid valves and increases ventricular volume. Increasing ventricular volume distends the chamber and leads to a rise in ventricular pressure. A reversal of the atrioventricular pressure gradient decelerates ventricular inflow and may result in mitral regurgitation, for example, in the setting of atrioventricular delay (1). Under normal conditions the R-wave ventricular contraction (start of ventricular systole) rapidly

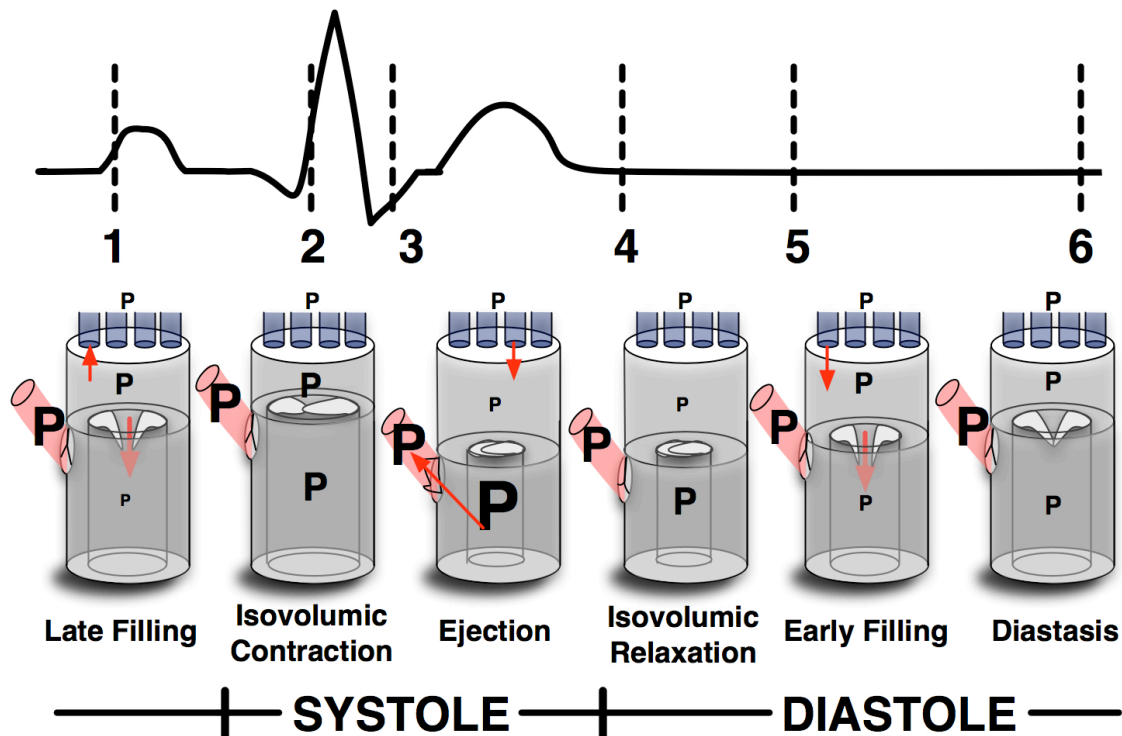


Figure 1.5 Schematic representation of left ventricular pressure and volume during the cardiac cycle. The red outflow tract is the aorta, and the blue inflow tracts are the pulmonary veins, as in Figure 1.2. P stands for pressure, and font size indicates relative magnitude of pressure. For example, during ejection, the highest pressure inside the left ventricle. The lower pressure in the aorta allows for aortic outflow, whereas the lower pressure in the atrium causes mitral valve closure. See text for details.

increases ventricular pressure and closes the mitral (or tricuspid) valves. While ventricular pressure is below outflow (aortic and pulmonary artery) pressures, the contraction and resulting pressure rise is isovolumic. Once ventricular pressure exceeds outflow pressure the aortic (or pulmonary) valve opens and the pressure gradient between ventricle and outflow tract accelerates blood out of the ventricle. Ventricular relaxation reduces chamber tension and results in a drop in ventricular pressure and a reversal in the ventricle to outflow pressure gradient. The reversed pressure gradient decelerates the out-flowing blood, and eventually the dropping ventricular pressure falls below outflow pressure and the outflow valves (aortic or pulmonary) close, marking the start of diastole. The pressure continues to fall as the ventricle relaxes its systolic cramp and recoils under the action of stored elastic energy, but the chamber remains isovolumic until the falling pressure drops below atrial pressure. Once ventricular pressure falls below atrial pressure the mitral (or tricuspid) valve opens and the atrioventricular pressure gradient accelerates blood into the ventricular chamber, marking the start of early diastolic filling.

Unlike the case of late diastolic filling following atrial contraction, the ventricle continues to recoil in early diastole, simultaneously dropping in pressure while increasing in volume ($dP/dV < 0$). Thus the ventricle sucks in blood during early diastole, and we discuss ventricular suction at length in Chapter 3. Eventually ventricular pressure reaches a minimum and begins to rise, and the atrioventricular gradient subsequently reverses. Reversal of the gradient leads to deceleration of atrioventricular flow, and eventually flow stops, marking the end of early diastolic filling. Depending on heart rate, a diastatic interval follows where pressure and volume are constant follows, and the end of diastasis is marked by the next P-wave and atrial systolic contraction.

Constant Volume Attribute of the Heart

Figure 1.5 schematically demonstrates an important principle of cardiac physiology: the nearly constant volume nature of the contents of the pericardial sack during the cardiac cycle (7). Previous work has demonstrated that the pericardial sack ejection fraction is at most 5%, and this finding also applies to both sides of the heart individually. This intriguing finding is the result of the simultaneous reciprocation of volume between atrium and ventricle. When the ventricle ejects the atrioventricular annular plane moves down, like a piston, and sucks in additional volume to the atrium from the pulmonary vasculature or venous system. The ventricular apex and epicardial radius remains fairly constant, and the wall thickness increases while the endocardial radius decreases. As ventricular filling proceeds, the atrioventricular annulus moves away from the apex, the ventricular wall thins, endocardial radius increases, and atrial volume falls. Thus a simplified model of the ventricle, where l is the distance along the long axis from valve annulus to ventricular apex, r is the endocardial radius, and R is the epicardial radius, has the following constraints:

$$\begin{aligned}
 V_m &= \pi l (R^2 - r^2) & V &= \pi l r^2 \\
 \frac{dV_m}{dt} &= 0 & \frac{dR}{dt} &= 0
 \end{aligned}
 \tag{Equation 1.1}$$

, where V_m is the volume of ventricular muscle. This simple model captures the essential connection between longitudinal and radial volume accommodation. Applying it to the case of the left ventricle, transmitral velocity in this model is simply:

$$v = \frac{1}{\pi r^2} \frac{dV}{dt} = \frac{(2lr\dot{r} + \dot{l}r^2)}{r^2} = 2l\frac{\dot{r}}{r} + \dot{l}
 \tag{Equation 1.2}$$

Furthermore, the time derivative of l is simply the annular mitral tissue velocity. Thus the equation above demonstrates that a deep connection exists between transmitral flow, endocardial radial expansion, and longitudinal tissue motion. Because total volume is conserved, we know

that the volume coming across the mitral valve must be balanced by the volume swept out by the epicardial radius:

$$\pi r^2 \cdot v = \pi R^2 \cdot i \Rightarrow \left(\frac{i}{l}\right) = \frac{2\left(\frac{\dot{r}}{r}\right)}{\left(\frac{R}{r}\right)^2 - 1} \quad \text{Equation 1.3}$$

This is identical to the expression that we find if we expand $dV_m/dt=0$ from Equation 1.1. Thus we have an expression that relates longitudinal and radial strain rate through epicardial and endocardial radii. In addition, this expression limits the longitudinal tissue velocity to be identical in sign to the sign of radial velocity. In other words, longitudinal lengthening is predicted to occur only with endocardial expansion and vice versa (64). In practice, however, longitudinal shortening is often seen in the late stages of early filling while radial expansion continues. This finding demonstrates that the dR/dt constraint, while a reasonable first approximation, does not fully apply in practice. The deviation of dR/dt from 0 is part of the 5% deviation from the constant volume property of the heart.

1.3 Techniques for Assessing Function

A variety of clinical techniques exist for assessing cardiovascular function, and the primary methods applied in this thesis are described in detail in Chapter 2. First, however, we provide a brief overview of the typical methods applied in the clinical setting, and recast the cardiac cycle described above in the context of the commonly employed clinical methods for assessing cardiovascular function.

1.3.1 Cardiac Catheterization- Pressure Volume Analysis

Cardiac catheterization has become a routine procedure in the diagnosis and management of heart disease, especially in the treatment of coronary artery disease (36, 89). Typically, fluid filled catheters are inserted into the femoral artery through a valve sheath and guided in a retrograde fashion under fluoroscopic control until the desired location is reached. At the aortic valve the catheter may be positioned near the origin of the coronary arteries, and contrast may be injected in order to assess coronary artery patency. Advancing the catheter across the aortic valve allows for ventricular pressures to be recorded, and injecting contrast into the ventricle and tracking the silhouette of the contrast filled chamber over time (ventriculography) allows one to determine ventricular volumes throughout systole and diastole. In addition to fluid filled catheters, high fidelity Millar catheters with multiple piezoelectric pressure transducers may be used to obtain high quality pressure signals at both aortic and ventricular levels (Figure 1.6). In this thesis invasive pressures are all obtained from Millar catheters, and the data acquisition procedure is detailed in Chapter 2. Conventional analysis and indexes derived from invasive pressures are discussed in section 1.4 below.

1.3.2 Echocardiography

In addition to the bedside physical examination of the heart, echocardiography is the preferred noninvasive method for cardiovascular function assessment (2). Numerous applications of echocardiography exist in clinical practice. All applications rely fundamentally on using an ultrasonic piezoelectric transducer to send an ultrasonic pulse into tissue and receive and process the reflected signal (21). Structures further from the source of the ultrasonic pulse require more time for the scattered signal to return, and therefore a plot of echo amplitude vs time represents a plot of echo amplitude vs depth of ultrasonic penetration. Peaks in the amplitude vs time signal

represent structures that reflect the ultrasonic pulse. Because the ultrasonic signal is expected to attenuate, the amplitude must be corrected by a depth dependent gain before it can be converted to a grayscale. In this fashion cardiac structure may be visualized along the line of the ultrasonic pulse. The earliest clinical application of echocardiographic imaging, M-Mode imaging, consisted of measuring and displaying cardiac structures along one ultrasonic pulse line over time. Technological advances allowed echocardiographers to send and receive multiple ultrasonic pulses in a variety of beam shapes, thereby allowing for live 2D and 3D imaging during the echocardiographic exam. In addition, technological advances allowed for the introduction of Doppler echocardiography, where the frequency shift of the scattered ultrasonic pulse may be analyzed to yield velocity information by the Doppler equation. Typically 2D imaging is used to orient the Doppler pulse location, and subsequently a Doppler pulse is aimed along a line of interest and a sample volume at a specific depth (time interval) is selected for Doppler analysis. Finally the reflected signal is processed, velocities measured at the sample volume are plotted versus time. Blood velocity at the mitral valve, aortic valve, and at the pulmonary veins may be measured using Doppler echo, and with appropriate filtering, tissue velocity at the mitral annular may be also assessed. Velocity data acquired by Doppler echocardiography is routinely used in various Chapters of this thesis, and the specific methodology by which Doppler echocardiography data is acquired is presented in Chapter 2. Additional echocardiographic applications exist (85), including strain and strain rate imaging, tissue characterization by ultrasonic backscatter measurement (49), and color M-mode imaging (90). While these are important clinically relevant techniques they were not applied in the main work of this thesis and therefore are not discussed in detail.

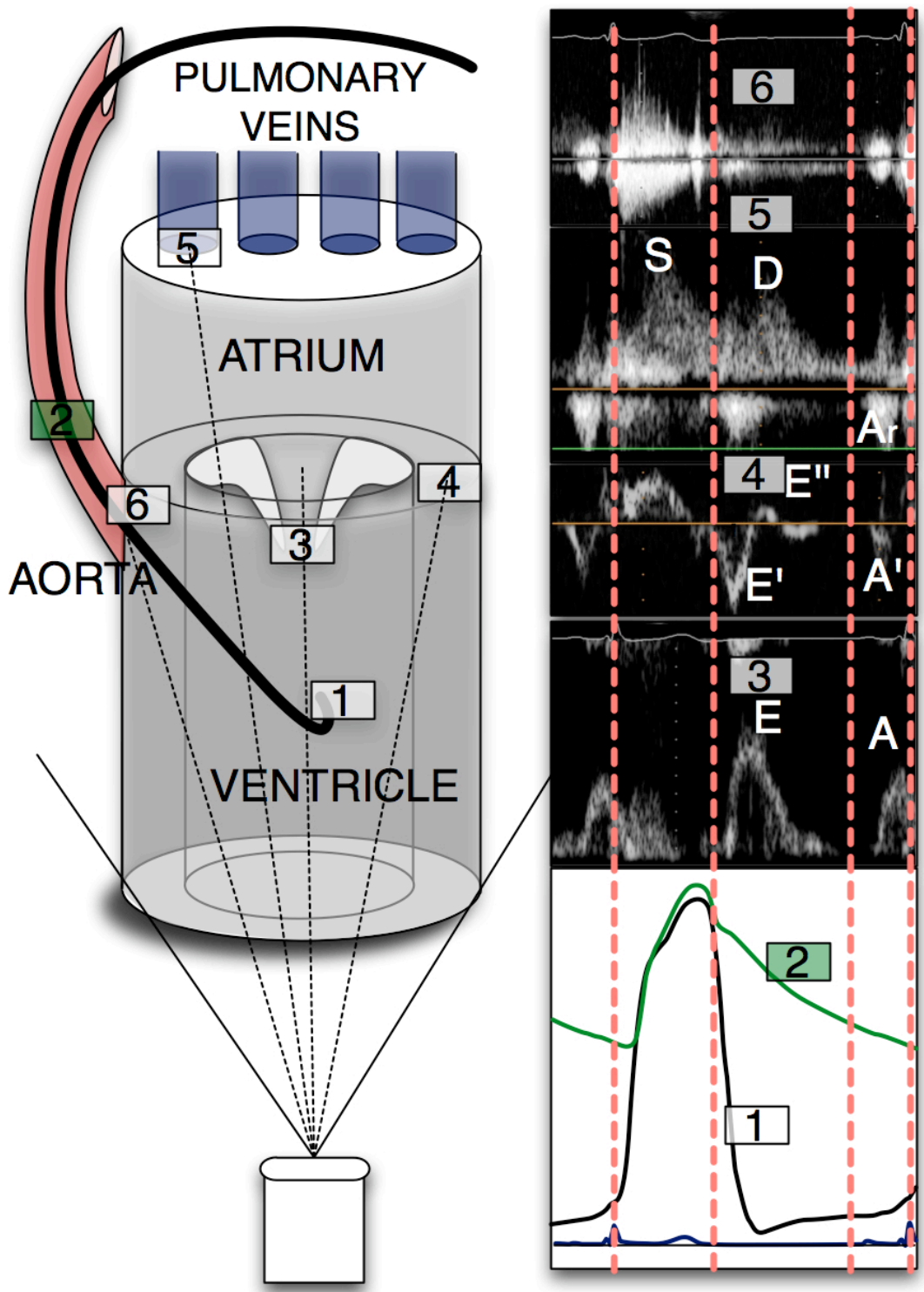


Figure 1.6 A schematic of the left ventricle, showing simultaneous Doppler echocardiography derived velocities (3, 4, 5, 6) and catheter measured pressures (1, 2). In practice only one of the Doppler velocities can be measured at one time. See text for details.

It is instructive to consider all of the pressures and flows that can be assessed through a combination of routine cardiac catheterization and Doppler echocardiography. Figure 1.6 shows representative transmitral flow, aortic flow, pulmonary flow, Doppler tissue velocity, and Millar pressure and ECG data synchronized schematically in the figure. Atrial pressure, though not routinely measured clinically, is shown as well for demonstrative purposes.

Each of the velocity contours has characteristic patterns associated with the various events of the cardiac cycle. The aortic outflow velocity [6] shows a negative velocity contour (flow away from the transducer) following the ventricular contraction and the R-wave peak. Notice that the ventricular pressure exceeds aortic pressure during the acceleration of the aortic velocity contour. This pressure gradient is reversed, however, during the deceleration of the aortic contour. The pulmonary vein velocities [5] have 3 characteristic waves that play an important role in volume flow, and the first one is a positive contour called the S-wave that occurs during ventricular systole, simultaneously with the aortic outflow velocity. This flow represents filling of the atrium as the ventricular volume decreases during ejection, and clearly demonstrates the principle of conservation of volume. Notice that a positive velocity wave is also seen in the tissue Doppler velocity signal [4] during systole, and this represents the systolic motion of the annulus towards the ventricular apex (also toward the ultrasonic transducer). Once ventricular relaxation reduces ventricular pressure below aortic pressure, the aortic valve closes and the ventricle remains in an isovolumic state until the decaying ventricular pressure falls below atrial pressure. As soon as there is an atrioventricular pressure gradient, the transmitral velocity signal [1], which in systole shows no flow, shows the early E-wave velocity contour (14). The time-integral of the E-wave, multiplied by an effective mitral valve leaflet cross sectional area, represents early diastolic filling volume (6). Because ventricular pressure

continues to drop as E-wave related filling volume increases, the mechanism for each filling must be mechanical, ventricular suction, and this point is discussed in greater detail in Chapter 3. Two velocity waves occur simultaneously with the E-wave, the D-wave in the pulmonary vein velocity signal, and the E'-wave in the tissue Doppler velocity signal. The D-wave demonstrates that pulmonary vein flow brings in volume to the atrium as the atrium loses volume to the ventricle. Thus ventricular suction brings in volume from the lungs, and the atrium can be thought of as a conduit during early diastole (8). The negative E'-wave represents longitudinal lengthening during early diastole, which is a necessary consequence of longitudinal volume accommodation and conservation of ventricular tissue and chamber volume. The positive E''-wave contour seen in Figure 1.6 provides a fascinating example of longitudinal oscillation of the chamber and the slight associated deviation from the precise constant volume property of the chamber (65). The E''-wave occurs during E-wave and D-wave filling, thus during volumetric chamber expansion. A positive E''-wave indicates longitudinal shortening, however, and therefore epicardial radial expansion must be occurring during the E''-wave. (this is a quadrupole mode of oscillation for the cylinder)

Recent work has also demonstrated that the D-wave volume in part accounts for epicardial radial expansion and the 5% deviation from the constant volume state of the heart (66). E-wave deceleration is driven in part by the reversal in atrioventricular pressure gradient, and following the end of the E-wave, a diastatic interval with no pressure change and no or low flow commences. Diastasis ends with the P-wave and atrial contraction. Atrial contraction results in a positive atrioventricular pressure gradient that accelerates the late diastolic filling transmitral A-wave. There is no valve between the pulmonary veins and atrium, and therefore atrial contraction also results in retrograde flow that can be seen in the pulmonary vein velocity signal

as the A_r velocity wave. It follows that if the LV chamber presents a high resistance (i.e. increased LV stiffness) to atrial systole and the associated transmitral flow, a greater pulmonary vein peak A_r velocity (87) is observed. In addition the duration of the A_r wave is longer than the duration of the transmitral Doppler A-wave. Because atrial systole ‘pulls up’ on the mitral annulus, most of the A-wave volume is accommodated longitudinally, and therefore one observes the A’-wave simultaneous with the transmitral A-wave. Continued ventricular filling from the A-wave increases ventricular pressure and once the atrioventricular pressure gradient reverses, the A-wave decelerates. The A-wave ends abruptly with R-wave driven ventricular contraction and pressure rapid pressure rise and closure of the mitral valve. Isovolumic contraction follows and the cardiac cycle repeats. Figure 1.6 provides a useful method for understanding normal systolic and diastolic physiology. Many indexes are routinely derived from these velocity and pressure signals in the clinical setting, and these indexes are used to diagnose and manage a variety of cardiovascular diseases.

1.4 Conventional Left Ventricular Function Indexes

A heart that is an ineffective pump is said to exhibit systolic dysfunction. Over time systolic dysfunction may transition to systolic heart failure, where the heart fails to deliver sufficient cardiac output to fully oxygenate the cells of the body. A heart that can not effectively fill, on the other hand, is said to exhibit diastolic dysfunction. Diastolic dysfunction may progress to diastolic heart failure, where residual fluid essentially inflates the pulmonary vasculature, eventually leaking into the alveoli and causing pulmonary edema (94, 95). A variety of tools are used in the clinical and research setting to diagnose and treat systolic and diastolic dysfunction, and we discuss several examples relevant to this thesis below.

1.4.1 Pressure Volume Loop Analysis

Plotting ventricular pressure versus volume over multiple cardiac cycles provides novel insights into cardiovascular function, and many clinical indexes are derived from or based upon pressure volume analysis (36). Volume and pressure may be measured simultaneously with specialized catheters that contain both pressure transducers (as discussed above) and specialized electrodes for measuring conductance. Electrodes along the catheter create an electric field, and the resulting voltage change (and by Ohm's law conductance of the chamber) is measured by receiving electrodes on the catheter. Because conductance and volume to a first approximation have been shown to be linearly related (3), the measurement of conductance changes in the

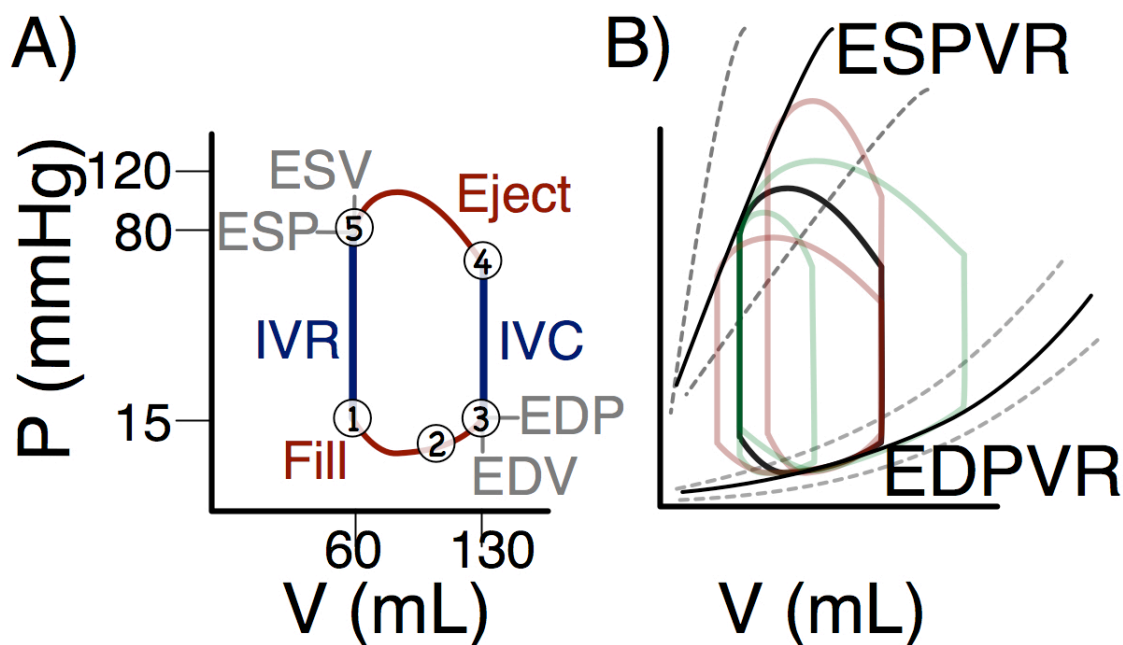


Figure 1.7. A) Normal pressure volume loop. IVC- isovolumic contraction; IVR- isovolumic relaxation; EDP- end diastolic pressure; EDP- end diastolic volume; ESP- end systolic pressure; ESV- end systolic volume. B) Changes in pressure volume loop with isolated changes in preload (green) or afterload (red). Despite changes in afterload or preload, the end-systolic points fall along a linear end-systolic pressure volume relation (ESPVR). The slope of the ESPVR changes with changes in contractility. The end diastolic pressure volume relation is generated by load varying end-diastolic coordinates, and the slope of the EDPVR represents chamber stiffness. See text for details.

chamber may be used to determine volume changes in real time. When pressure and volume are measured simultaneously through conductance catheters or through other methods, one typically observes the plot in Figure 1.7a.

The stages of the cardiac cycle may be mapped onto the pressure volume loop, with [1] corresponding to mitral valve opening and the start of early filling, [2] corresponding to diastasis, [3] corresponding to the end of diastolic filling, closure of the mitral valve, and start of isovolumic contraction, [4] corresponding to the opening of the aortic valve and the start of ventricular ejection, and finally [5] corresponding to the closing of the aortic valve and the start of isovolumic relaxation. The area inside the pressure volume loop defines the external work done by the ventricle. Recently we have demonstrated that the area under the diastolic filling portion alone is related diastolic recoil energy (See Appendix).

The difference between end-diastolic and end-systolic volume [3]-[5] is the ventricular stroke volume and therefore the width of the pressure volume loop may be used to easily assess changes in ejected volume. The ratio of stroke volume to end diastolic volume defines the ventricular ejection fraction:

$$EF = \frac{ESV - EDV}{EDV} = \frac{SV}{EDV} \quad \text{Equation 1.4}$$

Ejection fractions below 50% are typically viewed as indicative of systolic dysfunction, and patients in severe systolic heart failure may have ejection fractions as low as 10%, requiring that their ventricles be dilated (62). Ejection fraction may be determined from conductance catheter volume measurements, but are routinely determined by contrast ventriculography or by 2D or 3D echocardiography.

Preload and Afterload

The concepts of preload and afterload may be appreciated with the pressure volume loop as well. Preload and afterload are terms that apply more directly to muscle mechanics, where the preload is the initial stretch in an isolated muscle before a contraction occurs, and afterload is the load against which the muscle is contracting. Applying these terms to the chamber, we see that the stretch prior to the contraction can be determined from the end-diastolic point [3], and indeed end-diastolic pressure and volume are often used as surrogates for ventricular preload. The ventricle ejects into the aorta, and because aortic pressure is close to end-systolic pressure [5], end-systolic pressure is typically used to estimate ventricular afterload.

Changes in preload and afterload lead to shifts in the shape and location of the pressure volume loop in the pressure volume plane (Figure 1.7B). Preload changes occur with respiratory variation, premature ventricular contractions, body position variation, and more invasive experimental perturbations, such as injection of additional volume during filling or occlusion of venous return and reduction of filling volume. Isolated decreases or increases in preload have the effect of shifting the end-diastolic volume and pressure down and to the left or up and to the right, while the end-systolic point remains constant. Increased preload activates both the length-tension relationship of muscle, which accounts for increased force of contraction at greater sarcomere pre-stretch, and the force velocity curve, which accounts for greater speed of contraction with increased pre-stretch. Taken together, these mechanisms are the basis for the Frank Starling principle, which predicts greater force of ventricular contraction for increases in preload (16, 77). Thus as preload increases the maximum pressure generated by the ventricle and the stroke volume is expected to increase as well.

Isolated changes in afterload have a different impact on the pressure volume loop. Increased muscle afterload has the effect of reducing the velocity of contraction, and because the

time for ejection is fairly conserved for a given heart rate, reduced velocity of contraction has the effect of reducing stroke volume. Decreased afterload has the opposite effect. Thus isolated increases in afterload move the end-systolic point [5] up and to the right while decreases in afterload move the end-systolic point down and to the left.

End Systolic Pressure Volume Relation and Systolic Contractility

Plotting multiple pressure volume loops from the same chamber under a variety of preload and afterload conditions reveals further physiological chamber properties. Suga showed that the end-systolic coordinates from load varying pressure volume loops in the physiologic range fall on a single line (80). This line defines the end-systolic pressure volume relation, and the slope of the line is called the maximum elastance, E_{max} . Maximum elastance at a fixed inotropic state represents a load independent index of cardiac muscle contractility, and increases in contractility (by sympathetic activation, for example), increase the slope of the end-systolic pressure volume relation and therefore alters the general location of load-varying pressure volume loops. Recently investigators have determined methods to estimate maximum elastance from only a single recorded or estimated pressure volume coordinate (69). It is interesting to note that maximum elastance is a load independent index derived by varying load and measuring a quantity that is conserved in the face of load variation. Chapter 8 through 11 in the thesis apply that general principle to diastolic function assessment.

End Diastolic Pressure Volume Relation and Diastolic Chamber Compliance

In principle any point on the pressure volume loop may be tracked across multiple beats, thereby defining normalized isochrones (13, 39). Historically the end-diastolic pressure volume

coordinate has been tracked across multiple beats to define the end diastolic pressure volume relation (36). The ratio of pressure to volume in an elastic chamber is similar to the ratio of force to displacement in a spring, and therefore the slope of the end-diastolic pressure volume relation defines an effective chamber stiffness (inverse of compliance). Both linear and exponential functions are used in practice to fit the end-diastolic pressure volume relation, and details and limitations of the relation are presented in more depth in Chapter 4.

1.4.2 Phase Plane Analysis

An additional tool for cardiovascular function analysis is the pressure phase plane, where the pressure derivative is plotted against pressure (Figure 1.8). Key landmarks of the cardiac

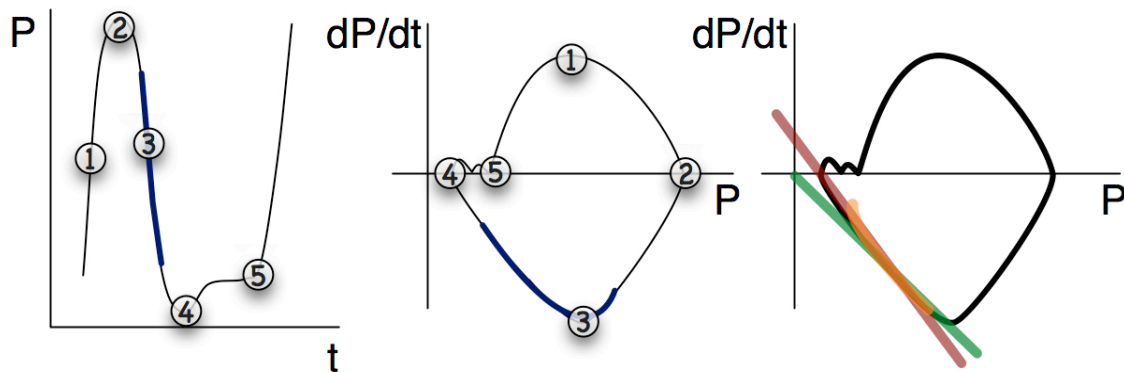


Figure 1.8. The pressure phase plane is a convenient tool for analysis of the pressure contour, and is generated by plotting the time derivative of pressure (dP/dt) vs pressure (P). Peak positive dP/dt (1), peak pressure (2), peak negative dP/dt (3), and minimum pressure (4) define the 4 corners of the phase plane loop. The isovolumic pressure decay contour is highlighted in blue in both the pressure vs time and phase plane plot. Alternative models of isovolumic pressure decay are shown as fits to the isovolumic pressure decay contour in the phase plane. The curved fit (orange) is the logistic model of isovolumic pressure decay, whereas the straight curves (red, green) represent the floating asymptote and zero asymptote monoexponential models of isovolumic pressure decay, respectively.

cycle can be appreciated in the phase plane by mapping points from the pressure vs. time plot onto the phase plane (19). Analysis of the phase plane area has provided insights into the onset of diastole (12), and provides a useful means by which models of isovolumic relaxation can be assessed (see below).

Isovolumic Relaxation Analysis

Multiple approaches have been pursued in the quantitation of isovolumic relaxation. The simplest approach was proposed by Weiss, who noticed that a plot of $\ln(P)$ vs P yielded a linear relationship during the isovolumic relaxation interval (84). Thus Weiss proposed the following equation for isovolumic pressure decay:

$$P(t) = P_o e^{-\frac{1}{\tau_w} t} \quad \text{Equation 1.5}$$

where $-1/\tau_w$ is the slope of the $\ln(P)$ vs P regression. Alternatively, one can derive τ_w as the negative inverse of the slope of the best fit line, with zero intercept, defined by points in the phase plane approximately 5 m/s after minimum dP/dt and 5 m/s before mitral valve opening. An alternative approach with non-zero pressure intercept was put forward by Raff et al [(59)]:

$$P(t) = P_o e^{-\frac{1}{\tau_R} t} + P_\infty \quad \text{Equation 1.6}$$

Once again, the phase plane may be used to determine the time constant for Equation 1.6, but now the intercept need not be set to zero. As is evident in Figure 1.8, the non-zero pressure intercept model predicts higher values for the isovolumic relaxation time constant τ compared to the Weiss model. Both Equation 1.5 and 1.6 define straight line contours in the phase plane, and curved phase plane contours are routinely seen in the clinical setting. To overcome the limitations of Equation 1.5 and 1.6, Matsubara proposed the following nonlinear expression for isovolumic pressure decay based on a logistic equation:

$$P(t) = \frac{2(P_\infty - P_o)}{1 + e^{-\frac{t}{\tau_L}}} + 2P_o - P_\infty \quad \text{Equation 1.7}$$

where τ_L is the logistic time constant. In clinical practice both τ_L and τ_R are used to quantify isovolumic relaxation, though often normal and abnormal τ cutoffs in clinical studies are based on historical work that employed τ_w (50). In Chapter 11 we discuss an additional model of isovolumic pressure decay that was developed in our lab (11), and show how application of that model leads to a novel load independent index of isovolumic relaxation.

1.4.3 Echocardiographic Analysis

Analysis of invasively derived pressures and volumes represents the gold standard for systolic and diastolic function assessment. However, a noninvasive approach to diagnosis and management of cardiovascular disease is preferred, and echocardiography is the primary noninvasive methodology used in practice. While many echocardiography based indexes exist, the primary focus of the thesis is analysis of transmitral flow and therefore we limit the discussion below to conventional indexes derived from E and A-wave contours.

Conventional Analysis of Transmitral Flow

Conventional analysis of E- and A-wave is based solely on E- and A-wave shapes, approximated for simplicity as triangles. Clinicians or sonographers simply select the start, peak, and end of each wave, thereby defining the acceleration time (AT, A_{AT}), deceleration time (DT, A_{DT}) and peak velocity (E_{peak} , A_{peak}), for each wave. Different clinical entities have been found to correlate with differences in triangle shapes, and while there are many clinical nuances, DF via E-waves is categorized into 4 patterns in order of worsening diastolic function: normal, delayed relaxation, pseudonormal, and constrictive-restrictive (2) (Figure 1.9). The hallmark of the delayed relaxation pattern is prolonged DT and E-wave velocity peak to A-wave velocity

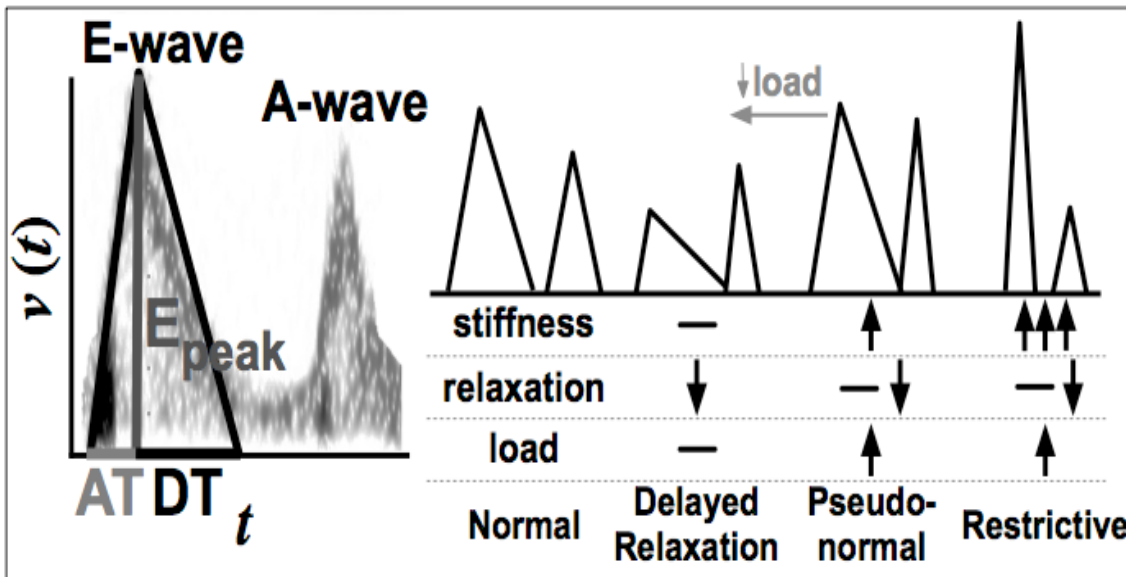


Figure 1.9. Visual inspection of transmitral early rapid filling and late atrial filling (E- and A-waves) via Doppler echocardiography is the preferred method for assessing progressive diastolic dysfunction. Changes in diastolic function determinants leads to changes in E- and A-wave shape. These changes are quantitated by triangle approximations to the velocity contours. See text for details.

peak (E/A ratio) reversal (from $E/A > 1$ to $E/A < 1$). The compensatory response to delayed relaxation is increased filling pressure and LVEDP, and this normalizes the E- and A-wave pattern to the pseudonormal pattern. While the pseudonormal pattern appears similar to the normal pattern, it may be unmasked clinically by load variation. Indeed preload reduction following a Valsalva maneuver turns a pseudonormal pattern into a delayed relaxation pattern. In general E- and A-waves, and all conventional indexes of diastolic function are known to be load dependent, and this poses a significant challenge for diagnosis of intrinsic diastolic dysfunction (10, 33, 34, 57, 58, 86). The effects of load variation on E-wave shape are discussed in greater detail in Chapter 8.

There is agreement that the different patterns reflect changes in diastolic function determinants, such as chamber stiffness, relaxation/viscoelasticity, and load (37). However, clinical decisions are made based primarily on pattern recognition and experience, and the causal connection between determinants of diastolic function and E- and A-wave shape is not

appreciated or utilized in the clinical setting. In our laboratory we have put forward a causal kinematic model of diastolic filling that provides insight into the connections between determinants of diastolic function and, among other things, E- and A-wave shape. We describe the kinematic model below, and in the chapters of the thesis, demonstrate applications of this model to a variety of clinical and physiology problems.

1.5 Kinematic Modeling of Diastolic Filling

1.5.1 PDF Model

In the discussion above we described several physiological principles that govern diastolic filling, and any model of diastolic filling must be consistent with these physiological principles. Systolic contraction stores elastic strain energy both intracellularly and extracellularly, and this energy powers mechanical recoil and the ventricular suction process. Thus physiology requires that early filling be modeled as an unforced oscillator recoiling towards equilibrium. This elastic recoil must be opposed by 1) a lumped resistive force coming from not fully relaxed tissue and molecular interactions, and 2) blood and tissue inertia (\ddot{x}). An external driving force would be appropriate for modeling the atrial filling portion of diastole, where an external force, namely atrial contraction, drives filling. Thus, the E-wave is appropriately modeled by:

$$\ddot{x} + c\dot{x} + kx = 0 \quad \text{Equation 1.8}$$

where x is the displacement of an equivalent spring, and c and k are damping and spring constants normalized per unit mass (Figure 1.10) (41). Similarly the A-wave can be modeled by:

$$\ddot{x}_A + c_A\dot{x}_A + k_Ax_A = F_o \sin(\omega_A t) \quad \text{Equation 1.9}$$

, where x_A , c_A , k_A , and ω_A are the A-wave equivalent oscillator displacement, damping constant, spring constant, and forcing frequency, and F_o is the forcing function amplitude. Details

regarding the A-wave model have been previously described (27). and are not the focus of this thesis.

This modeling paradigm is motivated by motion (kinematics) and is referred to as the Parameterized Diastolic Filling (PDF) formalism. It is a lumped parameter, predictive rather than accommodative model (46), that characterizes transmitral flow in analogy to damped simple harmonic oscillator motion in terms of elastic, inertial and damping forces. The three (mathematically) independent model parameters: k (spring constant), c (relaxation/viscosity/damping constant), and x_o (initial spring displacement), fully characterize the velocity of the simple harmonic oscillator (i.e. E-wave velocity contour). Because the equation of motion is linear, the parameters can be determined, for each beat, by solving the “inverse” problem, using the clinical E-wave contour as the beat-by-beat input, and the mathematically unique model parameters (x_o , c and k) as the best-fit determined output (see Chapter 2.4.2) (28).

The initial conditions for the equation of motion are determined by diastolic physiology. First, there is no flow prior to mitral valve opening, therefore the oscillator recoils from rest ($v(0)=0$). Furthermore the spring displacement at $t=0$ must be non-zero $x(0) = x_o$, in analogy to a spring that has been previously displaced beyond its equilibrium length. These initial conditions generate the ‘underdamped’ solution to Equation 1.8:

$$v(t) = \frac{kx_o}{\omega} e^{-\alpha t} \sin(\omega t) \quad 1.10$$

, where $\omega = \sqrt{k - \alpha^2}$, $\alpha = \frac{c}{2}$. The overdamped solution is obtained by applying the

transformation $\omega = i\beta$, where $\beta = \sqrt{\alpha^2 - k}$, to Equation 1.10. The critically damped solution is defined by the $\omega = \beta = 0$ limit of Equation 1.10.

The undamped limit ($c=0$) of Equation 1.8 is notable because it was independently put

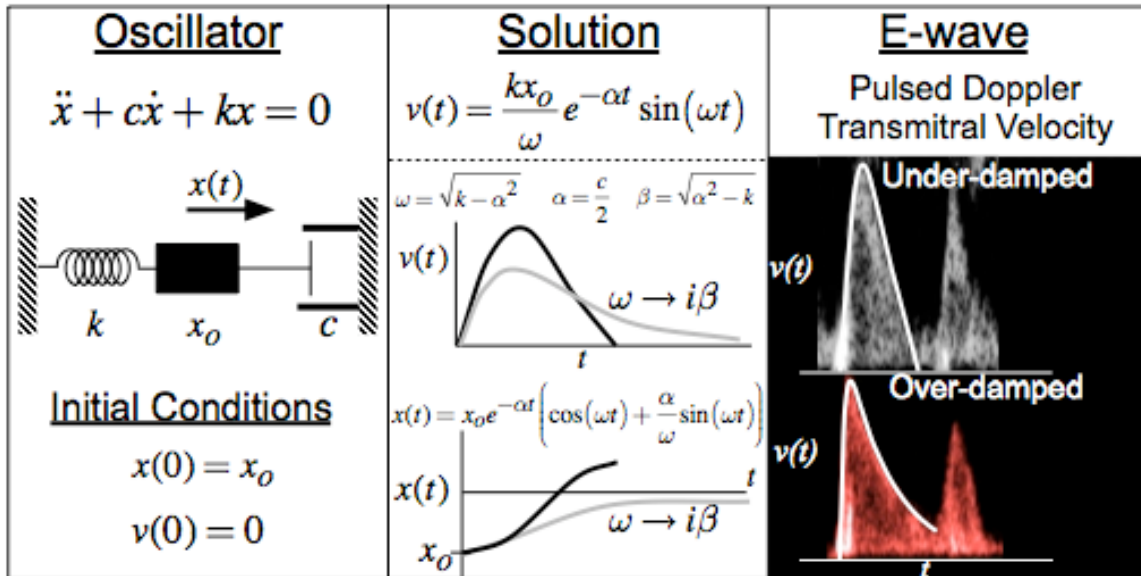


Figure 1.10. The PDF model accurately predicts clinically recorded early rapid filling transmitral flow velocity contours. Both underdamped and overdamped kinematic regimes are observed clinically. See text for details.

forward, in slightly different form and based on a different mathematical derivation several years after the original PDF model was described (48). It models diastolic kinematics in terms of stiffness only:

$$\ddot{x} + kx = 0 \tag{1.11}$$

and predicts a cosine fit to the deceleration portion of the E-wave. While this captures the physiology in some clinical limits, it does not account for the inflection point in the deceleration portion of the E-wave that is nearly always observed in the clinical setting. Further discussion comparing the undamped model with the full PDF model can be found in Chapter 5.

Validation- Physiological Analogues

The PDF model predicted velocity (Eq. 1.10), and its ‘overdamped’ equivalent, provides an

excellent fit to all clinically recorded Doppler E-wave contours (41, 42). The PDF parameters have physiologic analogues that have been experimentally validated in-vivo. For example, based on a large sample ($n = 131$), Lisauskas et al showed that average LV chamber stiffness ($\Delta P/\Delta V_{AVG}$), obtained from simultaneous echocardiographic-hemodynamic invasive measurements of flow, pressure and volume, showed a strong linear correlation with the PDF model-derived elastic stiffness (k), extracted purely from the E-wave contour (47). Additionally, kx_o , the peak-force that drives the oscillator, is the analog of the peak instantaneous atrioventricular pressure gradient generating transmitral flow (4); the slope of the kx_o vs cE_{peak} relation obtained at variable loads, has recently been shown in normal control and diastolic dysfunction subjects to be a load-independent index of diastolic function (LIIDF) (74); $1/2kx_o^2$ is the potential energy (ergs) available prior to valve opening (41); and x_o is linearly related to the volumetric load, i.e. the VTI of the E-wave (41). Further mathematical details related to the PDF parameters and indexes derived from them are discussed in Chapter 2.

The PDF formalism has been tested and validated in control subjects and those with a wide range of cardiac pathologies and loads including, hypertension (43), heart failure (61), diabetes (63), and caloric restriction (51).

1.5.2 The Physiologic Analogs of the PDF Parameters

Spring Constant k

Contraction is muscle's primary role, and therefore the mechanical recoil-based expansion of the chamber during diastole can at first be difficult to comprehend. Evidence of suction in isolated turtle hearts(38, 44) led early investigators to argue for the presence of restoring elastic forces driving diastolic recoil, but the source of those forces remained unclear for many years.

Only recently has a part of the answer emerged, though it is clear that our understanding of the source of elastic recoil will continue to expand.

In addition to the extracellular matrix (ECM) composed of primarily elastin and collagen(67), recent work (24) has shown that each myocyte has an intracellular source of recoil generated by the giant protein titin (see above). In remarkable agreement with the 1985 PDF model prediction that a linear, bidirectional spring is responsible for the shape of observed transmittal flow contours, Helmes (30) has demonstrated the bi-directional linear force vs. sarcomere length relationship for titin. Furthermore the existence of titin isoforms (of variable stiffness) (23) underscores the ability of k to vary depending on physiologic circumstance.

In addition to ECM and titin, recent work by Jobsis (35) has demonstrated the striking elastic properties of the visceral pericardium, thus adding a further chapter to the still developing story of the sources of ventricular elastic recoil.

Damping Constant c

Indeed viscoelasticity has been observed and measured in diastole through both organ level and molecular-based studies. For example, Templeton *et al.* (81) applied a sinusoidal volume variation to an isolated LV chamber and measured its viscoelastic response via the phase-delay of the resulting pressure response. Additionally, Rankin *et al.* found that in order to fit the diastatic stress-strain relationship, a viscoelastic, rather than purely elastic model is needed (60). Similar results have been reported by Hess *et al.* in humans (31), and other investigators have observed viscoelastic chamber properties in a variety of experimental settings (20, 40, 54, 79, 96).

Viscous effects may be understood at the cellular level by considering the mechanisms of resistance to myocyte recoil. Delayed calcium reuptake or myofilament deactivation may be a major factor in acting kinematically as a viscosity like term (18, 32, 79), especially during isovolumic relaxation (but possibly less so during filling). In addition, intrinsic viscous components of actin-myosin sliding affect chamber relaxation. For example, a binding between the proline-valine-glutamic acid-lysine (PEVK) rich region of titin and actin has been shown to function as a viscous component in-vitro (45, 88). Evidence suggests that cardiac myosin binding C (cMyB-C) also retards the motion of actin (70) and in pathological conditions, intermediate filaments such as microtubules potentially contributes to viscosity (55). Thus, multiple physical restraints, and molecular/physiological constraints are present to oppose and modulate recoil during the isovolumic phase. Although other mechanisms remain to be elucidated in the isovolumic relaxation process, formulating the kinematics using a lumped parameter and linear formulation will likely accommodate these yet to be discovered components. While there are likely multiple additional mechanisms contributing to myocyte and myocardial viscoelasticity, such as 3-d fiber architecture, it is clear that any viable kinematic model of filling must take viscous effects into account.

1.5.3 Is The PDF Model Too Simple?

The use of second order ordinary, linear differential equation to model the complex phenomena that govern ventricular filling dynamics is at first glance hard to justify. Indeed, many well-established models of ventricular filling dynamics often include nearly two dozen or more free parameters that specifically account for all of the variables of the system, including nonlinear tissue and system behavior (82). These models were devised to replicate standard,

physiologically measured parameters and relationships and usually followed an electric circuit analog of the physiology. In contrast, a key motivator for the PDF approach was inclusion of the physiology via a kinematics of filling paradigm, i.e., ventricular mechanical suction based filling, which other models did not consider. A potential concern was that the physiology, as modeled previously by others, is much too complex to be reasonably well approximated by a linear system. This concern has been addressed in detail in previous work, where the PDF model was subject to a crucial test: the predicted E-wave contours from the PDF model was compared to the E-wave contours predicted by nonlinear-noninvertible models. It was determined that the PDF model generated a fit to the clinical E-wave contour that was numerically indistinguishable from the complex and non-linear models (56).

An important advantage of the PDF model, is that it is uniquely invertible by using the clinically measured Doppler E-wave contour as input, whereas the nonlinear models are non-invertible. Apparently, despite the simultaneous nonlinear viscoelastic and complex fluid dynamics elements that govern the components of filling, the summed, lumped kinematic consequence of these individually nonlinear processes is to generate motion that is amenable to linear approximation.

1.5.4 General Clinical Connection to PDF Model

In agreement with the descriptive terms used in clinical practice, the PDF model accounts for the effects of stiffness (kx), relaxation (cv), and load (x_o) on E-waves. Normal E-wave contours are well fit by solutions to Equation 1.8 falling in the underdamped kinematic regime where damping is low relative to stiffness:

$$y = \frac{c}{2\sqrt{k}} < 1 \tag{1.12}$$

As one increases the relative value of the damping constant c while keeping stiffness k unchanged, the wave takes on the ‘delayed relaxation’ pattern seen clinically. Indeed the PDF model predicts a transition from low resistance ‘underdamped’ kinematics to high resistance ‘overdamped’ kinematics once c exceeds $2\sqrt{k}$. This is exactly what one encounters clinically in the ‘delayed relaxation’ pattern. Increasing k will abolish the ‘delayed relaxation’ pattern and eventually lead to a tall narrow E-wave, as encountered in the ‘constrictive-restrictive’ pattern, known to be associated with chambers having significantly elevated stiffness.

1.6 Thesis Chapter Summaries

In the preceding discussion we have provided an introduction to cardiovascular physiology and clinical assessment of cardiovascular function. We have described an approach to modeling diastolic function in particular, and in the chapters that follow we provide examples of the insights that may be gleaned from causally based quantitative analysis of cardiovascular function in general, and diastolic function in particular.

Much of the work presented in this thesis utilizes physiological data from subjects undergoing simultaneous echocardiography and catheterization. In Chapter 2 we describe the experimental methodology for this data acquisition and the semi-automated methods that are employed to process the acquired data. In addition we provide detailed methodology for extracting PDF parameters from clinical data, and provide further mathematical analysis of the PDF model, including many of the mathematical insights that form the basis for much of the theoretical modeling that is presented in several of the Chapters.

In Chapter 3 the physiology of suction is discussed in detail. Chapter 3 combines the work of 2 peer reviewed publications (71, 91) that argue for the universality of diastolic suction

as the driving mechanism for early filling, and by extension propose that diastasis must be the in-vivo equilibrium volume. Both publications generated commentary and interest from the cardiovascular physiology/cardiology community, and some of the responses to that commentary are incorporated into Chapter 3 as well.

Chapter 4 consists of a publication currently under review that is a natural extension of the physiological arguments presented in Chapter 3 and extends the discussion surrounding the end diastolic pressure volume relationship above. Instead of measuring chamber stiffness using end-diastolic pressure volume coordinates, Chapter 4 argues for the use of diastatic pressure volume relation, and provides a specific clinical example where the choice of diastasis vs end-diastole has significant consequences.

Chapters 5 through 7 include 2 peer reviewed publications (73, 92) and a submitted patent focused on the damping parameter c . Chapter 5 discusses the limitations of earlier models of E-wave deceleration time that ignored the impact of filling related viscous damping, and demonstrates clearly that E-wave deceleration time is determined jointly by stiffness and relaxation. In the past invasive clinical measures of relaxation were limited to the isovolumic relaxation time constant discussed above, which has only limited correlation to the damping parameter c and the more conventional E-wave delayed relaxation pattern. In Chapter 6, however, a novel invasive pressure based index, called the pressure recovery ratio (PRR), is derived that is the hemodynamic analogue of c and the associated delayed relaxation pattern observed on the E-wave. Finally in Chapter 7 PRR and other previously validated hemodynamic analogues of E-wave determinants are combined to yield an in-silico echocardiography method where LV pressure and ECG contour may be used to derive a simultaneous E-wave velocity contour.

Chapters 8 and 9 are based on a patent and 2 peer reviewed publications (5, 74) focused on deriving and validating a PDF model based load independent index of diastolic function from load-dependent E-waves. Chapter 8 provides the derivation and describes initial validation studies as well as some theoretical implications of the load independent index of diastolic function, while Chapter 9 extends the range of load variation over which the novel index remains load independent.

Chapter 10 provides an interesting extension of the load independent index analysis by deriving a novel noninvasive surrogate of left ventricular end diastolic pressure. By correlation with invasively determined end-diastolic pressure, this novel index is compared to the clinically established noninvasive surrogate for end diastolic pressure. The work in Chapter 10 has been described partially in abstracts and a manuscript is in preparation

Chapter 11 is based on a published peer reviewed manuscript (75), a published conference proceeding paper (72), and a published conference abstract and details a generalization of the methods described in chapter 8-10 to invasive assessment of isovolumic relaxation. While conventional indexes of isovolumic relaxation also show beat by beat load variation, a load independent index based on a kinematic model of isovolumic pressure decay is shown to remain constant in the face of load variation and reflect intrinsic function.

Finally Chapter 12 provides a unification of conventional clinical analysis and PDF analysis techniques, allowing for a remapping of many of the results in previous chapters and other publications from the lab using the established language and indexes familiar to clinical cardiologists.

Additional Contributions

In addition to the main Chapters of this thesis, several collaborative contributions that have been published or are pending publication, including a hemodynamic surrogate for diastolic recoil energy, a kinematic expression for vortex formation time in early filling (22), and a causal connection between PDF parameters and parameters derived from the cyclic variation of ultrasonic backscatter, are described as abstracts in the Appendix.

1.7 REFERENCES

1. **Appleton CP, Basnight MA, and Gonzalez MS.** Diastolic mitral regurgitation with atrioventricular conduction abnormalities: relation of mitral flow velocity to transmitral pressure gradients in conscious dogs. *Journal of the American College of Cardiology* 18: 843-849, 1991.
2. **Appleton CP, Firstenberg MS, Garcia MJ, and Thomas JD.** The echo-Doppler evaluation of left ventricular diastolic function. A current perspective. *Cardiology clinics* 18: 513-546, ix, 2000.
3. **Baan J, van der Velde ET, de Bruin HG, Smeenk GJ, Koops J, van Dijk AD, Temmerman D, Senden J, and Buis B.** Continuous measurement of left ventricular volume in animals and humans by conductance catheter. *Circulation* 70: 812-823, 1984.
4. **Bauman L, Chung CS, Karamanoglu M, and Kovács SJ.** The peak atrioventricular pressure gradient to transmitral flow relation: kinematic model prediction with in vivo validation. *Journal of the American Society of Echocardiography : official publication of the American Society of Echocardiography* 17: 839-844, 2004.
5. **Boskovski MT, Shmuylovich L, and Kovács SJ.** Transmitral flow velocity-contour variation after premature ventricular contractions: a novel test of the load-independent index of diastolic filling. *Ultrasound in medicine & biology* 34: 1901-1908, 2008.
6. **Bowman AW, Frihauf PA, and Kovács SJ.** Time-varying effective mitral valve area: prediction and validation using cardiac MRI and Doppler echocardiography in normal subjects. *Am J Physiol Heart Circ Physiol* 287: H1650-1657, 2004.
7. **Bowman AW and Kovács SJ.** Assessment and consequences of the constant-volume attribute of the four-chambered heart. *Am J Physiol Heart Circ Physiol* 285: H2027-2033, 2003.

8. **Bowman AW and Kovács SJ.** Left atrial conduit volume is generated by deviation from the constant-volume state of the left heart: a combined MRI-echocardiographic study. *Am J Physiol Heart Circ Physiol* 286: H2416-2424, 2004.
9. **Burton A.** *Physiology and biophysics of the circulation.* Chicago: Year Book Medical Publishers Incorporated, 1972.
10. **Choong C, Herrmann H, Weyman A, and Fifer M.** Preload dependence of Doppler-derived indexes of left ventricular diastolic function in humans. *J Am Coll Cardiol* 10: 800-808, 1987.
11. **Chung CS and Kovács SJ.** Physical determinants of left ventricular isovolumic pressure decline: model prediction with in vivo validation. *Am J Physiol Heart Circ Physiol* 294: H1589-1596, 2008.
12. **Chung CS and Kovács SJ.** Pressure phase-plane based determination of the onset of left ventricular relaxation. *Cardiovascular engineering (Dordrecht, Netherlands)* 7: 162-171, 2007.
13. **Claessens TE, Georgakopoulos D, Afanasyeva M, Vermeersch SJ, Millar HD, Stergiopoulos N, Westerhof N, Verdonck PR, and Segers P.** Nonlinear isochrones in murine left ventricular pressure-volume loops: how well does the time-varying elastance concept hold? *Am J Physiol Heart Circ Physiol* 290: H1474-1483, 2006.
14. **Courtois M, Kovács SJ, and Ludbrook PA.** Transmitral pressure-flow velocity relation. Importance of regional pressure gradients in the left ventricle during diastole. *Circulation* 78: 661-671, 1988.
15. **de Tombe PP.** Cardiac myofilaments: mechanics and regulation. *Journal of biomechanics* 36: 721-730, 2003.

16. **de Tombe PP, Mateja RD, Tachampa K, Mou YA, Farman GP, and Irving TC.** Myofilament length dependent activation. *J Mol Cell Cardiol* 48: 851-858, 2010.
17. **Dubin D.** *Rapid interpretation of EKG's*. Hong Kong: Cover Inc. , 2000.
18. **Esch BT and Warburton DER.** Left ventricular torsion and recoil: implications for exercise performance and cardiovascular disease. *J Appl Physiol* 106: 362-369, 2009.
19. **Eucker S, Lisauskas J, Singh J, and Kovacs S.** Phase plane analysis of left ventricular hemodynamics. *J Appl Physiol* 90: 2238-2244, 2001.
20. **Ewert D, Wheeler B, Doetkott C, Ionan C, Pantalos G, and Koenig SC.** The effect of heart rate, preload, and afterload on the viscoelastic properties of the swine myocardium. *Ann Biomed Eng* 32: 1211-1222, 2004.
21. **Feigenbaum H.** *Echocardiography*. Baltimore: Williams & Wilkins, 1993.
22. **Ghosh E, Shmuylovich L, and Kovacs SJ.** Determination of early diastolic LV vortex formation time (T^*) via the PDF formalism: a kinematic model of filling. *Conf Proc IEEE Eng Med Biol Soc* 2009: 2883-2886, 2009.
23. **Granzier H, Helmes M, Cazorla O, McNabb M, Labeit D, Wu Y, Yamasaki R, Redkar A, Kellermayer M, Labeit S, and Trombitás K.** Mechanical properties of titin isoforms. *Adv Exp Med Biol* 481: 283-300; discussion 300-284, 2000.
24. **Granzier H and Labeit S.** The Giant Protein Titin A Major Player in Myocardial Mechanics, Signaling, and Disease. *Circ Res*, 2004.
25. **Granzier HL and Labeit S.** The giant protein titin: a major player in myocardial mechanics, signaling, and disease. *Circ Res* 94: 284-295, 2004.
26. **Guyton A.** *Textbook of medical physiology*. Philadelphia: W B Saunders Company, 1983.

27. **Hall AF, Aronovitz JA, Nudelman SP, and Kovács SJ.** Automated method for characterization of diastolic transmitral Doppler velocity contours: late atrial filling. *Ultrasound in medicine & biology* 20: 859-869, 1994.
28. **Hall AF and Kovács SJ.** Automated method for characterization of diastolic transmitral Doppler velocity contours: early rapid filling. *Ultrasound in medicine & biology* 20: 107-116, 1994.
29. **Helmes M, Lim CC, Liao R, Bharti A, Cui L, and Sawyer DB.** Titin determines the Frank-Starling relation in early diastole. *J Gen Physiol* 121: 97-110, 2003.
30. **Helmes M, Trombitás K, and Granzier H.** Titin develops restoring force in rat cardiac myocytes. *Circ Res* 79: 619-626, 1996.
31. **Hess OM, Grimm J, and Krayenbuehl HP.** Diastolic simple elastic and viscoelastic properties of the left ventricle in man. *Circulation* 59: 1178-1187, 1979.
32. **Hinken AC and Solaro RJ.** A dominant role of cardiac molecular motors in the intrinsic regulation of ventricular ejection and relaxation. *Physiology (Bethesda, Md)* 22: 73-80, 2007.
33. **Hurrell DG, Nishimura RA, Ilstrup DM, and Appleton CP.** Utility of preload alteration in assessment of left ventricular filling pressure by Doppler echocardiography: a simultaneous catheterization and Doppler echocardiographic study. *J Am Coll Cardiol* 30: 459-467, 1997.
34. **Jacques DC, Pinsky MR, Severyn D, and Gorcsan J.** Influence of alterations in loading on mitral annular velocity by tissue Doppler echocardiography and its associated ability to predict filling pressures. *Chest* 126: 1910-1918, 2004.
35. **Jöbsis PD, Ashikaga H, Wen H, Rothstein EC, Horvath KA, McVeigh ER, and Balaban RS.** The visceral pericardium: macromolecular structure and contribution to passive

mechanical properties of the left ventricle. *Am J Physiol Heart Circ Physiol* 293: H3379-3387, 2007.

36. **Kass DA.** Assessment of diastolic dysfunction. Invasive modalities. *Cardiology clinics* 18: 571-586, 2000.

37. **Kass DA, Bronzwaer JGF, and Paulus WJ.** What mechanisms underlie diastolic dysfunction in heart failure? *Circ Res* 94: 1533-1542, 2004.

38. **Katz L.** The role played by the ventricular relaxation process in filling the ventricle. *American Journal of Physiology*, 1930.

39. **Kind T, Westerhof N, Faes TJC, Lankhaar J-W, Steendijk P, and Vonk-Noordegraaf A.** Cardiac phase-dependent time normalization reduces load dependence of time-varying elastance. *Am J Physiol Heart Circ Physiol* 296: H342-349, 2009.

40. **Koide M, Hamawaki M, Narishige T, Sato H, Nemoto S, DeFreyte G, Zile MR, Cooper G IV, and Carabello BA.** Microtubule depolymerization normalizes in vivo myocardial contractile function in dogs with pressure-overload left ventricular hypertrophy. *Circulation* 102: 1045-1052, 2000.

41. **Kovács SJ, Barzilai B, and Pérez JE.** Evaluation of diastolic function with Doppler echocardiography: the PDF formalism. *Am J Physiol* 252: H178-187, 1987.

42. **Kovács SJ, Meisner JS, and Yellin EL.** Modeling of diastole. *Cardiology clinics* 18: 459-487, 2000.

43. **Kovács SJ, Rosado J, Manson McGuire AL, and Hall AF.** Can transmitral Doppler E-waves differentiate hypertensive hearts from normal? *Hypertension* 30: 788-795, 1997.

44. **KRANER JC and OGDEN E.** Ventricular suction in the turtle. *Circ Res* 4: 724-726, 1956.

45. **Kulke M, Fujita-Becker S, Rostkova E, Neagoe C, Labeit D, Manstein DJ, Gautel M, and Linke WA.** Interaction between PEVK-titin and actin filaments: origin of a viscous force component in cardiac myofibrils. *Circ Res* 89: 874-881, 2001.
46. **Lipton P.** Testing hypotheses: prediction and prejudice. *Science* 307: 219-221, 2005.
47. **Lisauskas JB, Singh J, Bowman AW, and Kovács SJ.** Chamber properties from transmitral flow: prediction of average and passive left ventricular diastolic stiffness. *J Appl Physiol* 91: 154-162, 2001.
48. **Little WC, Ohno M, Kitzman DW, Thomas JD, and Cheng CP.** Determination of left ventricular chamber stiffness from the time for deceleration of early left ventricular filling. *Circulation* 92: 1933-1939, 1995.
49. **Madaras EI, Barzilai B, Perez JE, Sobel BE, and Miller JG.** Changes in myocardial backscatter throughout the cardiac cycle. *Ultrason Imaging* 5: 229-239, 1983.
50. **Matsubara H, Takaki M, Yasuhara S, Araki J, and Suga H.** Logistic time constant of isovolumic relaxation pressure-time curve in the canine left ventricle. Better alternative to exponential time constant. *Circulation* 92: 2318-2326, 1995.
51. **Meyer TE, Kovács SJ, Ehsani AA, Klein S, Holloszy JO, and Fontana L.** Long-term caloric restriction ameliorates the decline in diastolic function in humans. *Journal of the American College of Cardiology* 47: 398-402, 2006.
52. **Nagueh SF, Appleton CP, Gillebert TC, Marino PN, Oh JK, Smiseth OA, Waggoner AD, Flachskampf FA, Pellikka PA, and Evangelista A.** Recommendations for the evaluation of left ventricular diastolic function by echocardiography. *Journal of the American Society of Echocardiography : official publication of the American Society of Echocardiography* 22: 107-133, 2009.

53. **Nikolaev VO, Moshkov A, Lyon AR, Miragoli M, Novak P, Paur H, Lohse MJ, Korchev YE, Harding SE, and Gorelik J.** Beta2-adrenergic receptor redistribution in heart failure changes cAMP compartmentation. *Science* 327: 1653-1657, 2010.
54. **Nikolic SD, Tamura K, Tamura T, Dahm M, Frater RW, and Yellin EL.** Diastolic viscous properties of the intact canine left ventricle. *Circ Res* 67: 352-359, 1990.
55. **Nishimura S, Nagai S, Katoh M, Yamashita H, Saeki Y, Okada J-i, Hisada T, Nagai R, and Sugiura S.** Microtubules modulate the stiffness of cardiomyocytes against shear stress. *Circ Res* 98: 81-87, 2006.
56. **Nudelman S, Manson AL, Hall AF, and Kovács SJ.** Comparison of diastolic filling models and their fit to transmitral Doppler contours. *Ultrasound in medicine & biology* 21: 989-999, 1995.
57. **Oğuzhan A, Arınç H, Abacı A, and Topsakal R.** Preload dependence of Doppler tissue imaging derived indexes of left ventricular diastolic function. ..., 2005.
58. **Paelinck BP, van Eck JWM, De Hert SG, and Gillebert TC.** Effects of postural changes on cardiac function in healthy subjects. *European journal of echocardiography : the journal of the Working Group on Echocardiography of the European Society of Cardiology* 4: 196-201, 2003.
59. **Raff GL and Glantz SA.** Volume loading slows left ventricular isovolumic relaxation rate. Evidence of load-dependent relaxation in the intact dog heart. *Circ Res* 48: 813-824, 1981.
60. **Rankin JS, Arentzen CE, McHale PA, Ling D, and Anderson RW.** Viscoelastic properties of the diastolic left ventricle in the conscious dog. *Circ Res* 41: 37-45, 1977.

61. **Rich MW, Stitzel NO, and Kovács SJ.** Prognostic value of diastolic filling parameters derived using novel image processing technique in patients \geq 70 years of age with congestive heart failure. *American Journal of Cardiology* 84: 82-86, 1999.
62. **Rihal CS, Nishimura RA, Hatle LK, Bailey KR, and Tajik AJ.** Systolic and diastolic dysfunction in patients with clinical diagnosis of dilated cardiomyopathy. Relation to symptoms and prognosis. *Circulation* 90: 2772-2779, 1994.
63. **Riordan MM, Chung CS, and Kovács SJ.** Diabetes and diastolic function: stiffness and relaxation from transmitral flow. *Ultrasound in medicine & biology* 31: 1589-1596, 2005.
64. **Riordan MM and Kovács SJ.** Elucidation of spatially distinct compensatory mechanisms in diastole: radial compensation for impaired longitudinal filling in left ventricular hypertrophy. *J Appl Physiol* 104: 513-520, 2008.
65. **Riordan MM and Kovács SJ.** Quantitation of mitral annular oscillations and longitudinal "ringing" of the left ventricle: a new window into longitudinal diastolic function. *J Appl Physiol* 100: 112-119, 2006.
66. **Riordan MM and Kovács SJ.** Relationship of pulmonary vein flow to left ventricular short-axis epicardial displacement in diastole: model-based prediction with in vivo validation. *Am J Physiol Heart Circ Physiol* 291: H1210-1215, 2006.
67. **Robinson TF, Factor SM, and Sonnenblick EH.** The heart as a suction pump. *Sci Am* 254: 84-91, 1986.
68. **Sengupta PP, Khandheria BK, Korinek J, Wang J, Jahangir A, Seward JB, and Belohlavek M.** Apex-to-base dispersion in regional timing of left ventricular shortening and lengthening. *J Am Coll Cardiol* 47: 163-172, 2006.

69. **Senzaki H, Chen CH, and Kass DA.** Single-beat estimation of end-systolic pressure-volume relation in humans. A new method with the potential for noninvasive application. *Circulation* 94: 2497-2506, 1996.
70. **Shaffer JF, Kensler RW, and Harris SP.** The myosin-binding protein C motif binds to F-actin in a phosphorylation-sensitive manner. *J Biol Chem* 284: 12318-12327, 2009.
71. **Shmuylovich L, Chung CS, Kovács SJ, Yellin EL, and Nikolic SD.** Left ventricular volume during diastasis IS/IS NOT the physiologic in-vivo equilibrium volume and IS/IS NOT related to diastolic suction. *J Appl Physiol*, 2009.
72. **Shmuylovich L and Kovacs SJ.** Automated method for calculation of a load-independent index of isovolumic pressure decay from left ventricular pressure data. *Conf Proc IEEE Eng Med Biol Soc* 2009: 3031-3034, 2009.
73. **Shmuylovich L and Kovács SJ.** E-wave deceleration time may not provide an accurate determination of LV chamber stiffness if LV relaxation/viscoelasticity is unknown. *Am J Physiol Heart Circ Physiol* 292: H2712-2720, 2007.
74. **Shmuylovich L and Kovács SJ.** Load-independent index of diastolic filling: model-based derivation with in vivo validation in control and diastolic dysfunction subjects. *J Appl Physiol* 101: 92-101, 2006.
75. **Shmuylovich L and Kovács SJ.** Stiffness and relaxation components of the exponential and logistic time constants may be used to derive a load-independent index of isovolumic pressure decay. *Am J Physiol Heart Circ Physiol* 295: H2551-2559, 2008.
76. **Snider P, Standley KN, Wang J, Azhar M, Doetschman T, and Conway SJ.** Origin of Cardiac Fibroblasts and the Role of Periostin. *Circ Res* 105: 934-947, 2009.

77. **Solaro RJ.** Mechanisms of the Frank-Starling law of the heart: the beat goes on. *Biophys J* 93: 4095-4096, 2007.
78. **Solaro RJ, Rosevear P, and Kobayashi T.** The unique functions of cardiac troponin I in the control of cardiac muscle contraction and relaxation. *Biochem Biophys Res Commun* 369: 82-87, 2008.
79. **Stehle R, Solzin J, Iorga B, and Poggesi C.** Insights into the kinetics of Ca²⁺-regulated contraction and relaxation from myofibril studies. *Pflugers Arch* 458: 337-357, 2009.
80. **Suga H, Sagawa K, and Shoukas AA.** Load independence of the instantaneous pressure-volume ratio of the canine left ventricle and effects of epinephrine and heart rate on the ratio. *Circ Res* 32: 314-322, 1973.
81. **Templeton GH and Nardizzi LR.** Elastic and viscous stiffness of the canine left ventricle. *Journal of Applied Physiology* 36: 123-127, 1974.
82. **Thomas JD, Newell JB, Choong CY, and Weyman AE.** Physical and physiological determinants of transmitral velocity: numerical analysis. *Am J Physiol* 260: H1718-1731, 1991.
83. **van Heerebeek L, Borbély A, Niessen HWM, Bronzwaer JGF, van der Velden J, Stienen GJM, Linke WA, Laarman GJ, and Paulus WJ.** Myocardial structure and function differ in systolic and diastolic heart failure. *Circulation* 113: 1966-1973, 2006.
84. **Weiss JL, Frederiksen JW, and Weisfeldt ML.** Hemodynamic determinants of the time-course of fall in canine left ventricular pressure. *J Clin Invest* 58: 751-760, 1976.
85. **Weyman AE.** The year in echocardiography. *Journal of the American College of Cardiology* 49: 1212-1219, 2007.

86. **Yalçın F, Kaftan A, Muderrisoğlu H, Korkmaz ME, Flachskampf F, Garcia M, and Thomas JD.** Is Doppler tissue velocity during early left ventricular filling preload independent? *Heart* 87: 336-339, 2002.
87. **Yamamoto K, Nishimura RA, Burnett JC, and Redfield MM.** Assessment of left ventricular end-diastolic pressure by Doppler echocardiography: contribution of duration of pulmonary venous versus mitral flow velocity curves at atrial contraction. *Journal of the American Society of Echocardiography : official publication of the American Society of Echocardiography* 10: 52-59, 1997.
88. **Yamasaki R, Berri M, Wu Y, Trombitás K, McNabb M, Kellermayer MS, Witt C, Labeit D, Labeit S, Greaser M, and Granzier H.** Titin-actin interaction in mouse myocardium: passive tension modulation and its regulation by calcium/S100A1. *Biophys J* 81: 2297-2313, 2001.
89. **Yang LB, H Goldberg.** *From cardiac catheterization to hemodynamic parameters.* Philadelphia: FA David Company, 1988.
90. **Yotti R, Bermejo J, Antoranz JC, Desco MM, Cortina C, Rojo-Alvarez JL, Allué C, Martín L, Moreno M, Serrano JA, Muñoz R, and García-Fernández MA.** A noninvasive method for assessing impaired diastolic suction in patients with dilated cardiomyopathy. *Circulation* 112: 2921-2929, 2005.
91. **Zhang W, Chung C, and Shmuylovich L.** Is left ventricular volume during diastasis the real equilibrium volume, and what is its *Journal of Applied Physiology*, 2008.
92. **Zhang W, Shmuylovich L, and Kovács SJ.** The E-wave delayed relaxation pattern to LV pressure contour relation: model-based prediction with in vivo validation. *Ultrasound in medicine & biology* 36: 497-511, 2010.

93. **Zile MR, Baicu CF, and Gaasch WH.** Diastolic heart failure--abnormalities in active relaxation and passive stiffness of the left ventricle. *N Engl J Med* 350: 1953-1959, 2004.
94. **Zile MR and Brutsaert DL.** New concepts in diastolic dysfunction and diastolic heart failure: Part I: diagnosis, prognosis, and measurements of diastolic function. *Circulation* 105: 1387-1393, 2002.
95. **Zile MR and Brutsaert DL.** New concepts in diastolic dysfunction and diastolic heart failure: Part II: causal mechanisms and treatment. *Circulation* 105: 1503-1508, 2002.
96. **Zile MR, Richardson K, Cowles MK, Buckley JM, Koide M, Cowles BA, Gharapuray V, and Cooper G.** Constitutive properties of adult mammalian cardiac muscle cells. *Circulation* 98: 567-579, 1998.

CHAPTER 2

BACKGROUND EXPERIMENTAL AND THEORETICAL METHODS

2.1 Introduction to Methodology

This Chapter is divided into both experimental and theoretical sections, and the experimental methodology is covered first. Nearly every chapter of the current work utilizes data from the Cardiovascular Biophysics Laboratory simultaneous echocardiography and catheterization database. This database is the largest of its kind in the world and has been enrolling subjects for several decades. In total contains simultaneous echo-cath data from over 400 subjects. Through the years the amount of data and quality of data has evolved, with newer catheters with additional pressure channels, new echocardiographic imagers, and updated semi-automated methodologies for rapid data analysis. However, the basic process for data acquisition and analysis has remained fairly consistent, and this process is described below. The latest version of this approach is summarized in the figure below, which may be used as a reference throughout the current chapter.

In addition to experimental techniques, there is a significant amount of theoretical background, specifically related to mathematical approximations and simplifications to capture the essential features of the in-vivo physiology and properties of the PDF model, that provide the

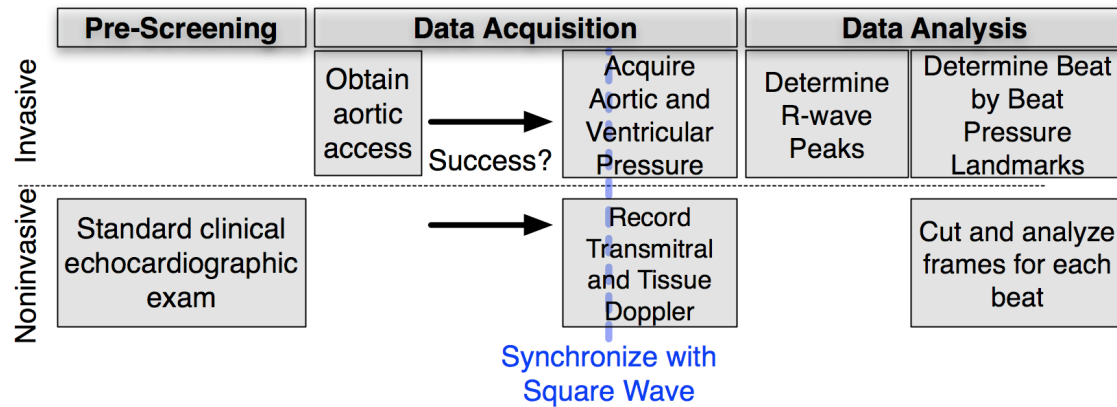


Figure 2.1 General overview of data acquisition and analysis. See text for details.

basis for much of the analysis presented in the various chapters of the current work. The general simplifications and insights are presented below, but specifics are reserved for particular chapters.

2.2 Simultaneous Catheterization and Echocardiography

2.2.1 Subject Selection

Subjects in the Cardiac Catheterization laboratory, referred by their personal physician for elective diagnostic cardiac catheterization to evaluate the possibility of coronary artery disease, are recruited to participate in the simultaneous catheterization and echocardiography study. All enrolled subjects must meet the following inclusionary criteria: (i) scheduled for elective diagnostic left-heart cardiac catheterization, in a fasting, non-sedated state, (ii) judged to be clinically stable, and (iii) willing to participate by giving informed consent in accordance with a study protocol approved by the Washington University Medical Center Human Research Protection Office (HRPO). Subject's inclusion in the study further requires that the subject have no evidence of valvular disease or active ischemia.

2.2.2 Echocardiography Prescreening

Prior to catheterization, subjects have a complete 2D/echo-Doppler screening study using an echocardiographic imaging system (Acuson, HP, or Philips ie33) with 2.5 MHz transducer. With the patient supine, both short-axis and long-axis views are obtained. Short axis views are obtained at the level of the mitral and aortic valves in order to visualize both valves. Additional short axis views are obtained at the mitral leaflet tip and mid-LV in order to estimate LV size. Continuous wave Doppler is used to record aortic outflow and mitral inflow from the apical view

for determination of isovolumic relaxation time using a sweep speed of 10 cm/sec. Pulmonary S- and D- waves and transmitral E- and A- waves are recorded in pulsed Doppler mode with sample volumes gated at the pulmonary veins and mitral leaflet tips respectively. For pulsed Doppler imaging the wall filter is set at 125 Hz or 250 Hz, the baseline is adjusted to take advantage of the full width of the display, and the velocity scale is adjusted to exploit the dynamic range of the output without aliasing. Medial and Lateral E'- and A'-waves are recorded in Tissue Doppler mode with sample volumes at the medial and lateral sides of the mitral annulus, respectively. In addition, Color M-Mode imaging is used to obtain diastolic early and late filling interventricular velocity maps.

If a poor echo window, bicuspid aortic valve or significant calcification or stenosis of the aortic valve is observed by echocardiography, then the routine cardiac catheterization study proceeds, but the subject is not enrolled in the simultaneous high-fidelity catheterization and echocardiography portion of the study. If the subject has an appropriate echocardiographic window and no aortic valve abnormalities then the simultaneous high-fidelity catheterization and echocardiography study proceeds.

2.2.3 Catheterization Procedure

After appropriate sterile skin prep and drape of the patient, local anesthesia (1% xylocaine), is given and percutaneous right and left femoral arterial and venous (if a right heart cath is requested) access is obtained in preparation for the performance of catheterization, using a valved sheath (6-F, Arrow Inc, Reading, PA). If necessary, right heart catheterization is performed via the Seldinger technique using a 7.3 F Swan-Ganz balloon tipped or 6F or smaller diameter Cournand catheter (12). After arterial access and placement of a 64cm sheath (Arrow

Inc, Reading, PA), a 6F micromanometer-tipped pigtail (triple pressure transducer) pressure-volume, conductance catheter (Model 560-1, 560-5, SSD-1034 Millar Instruments, Houston, TX) is directed into the mid-LV in a retrograde fashion across the aortic valve under fluoroscopic control. The three pressure transducers are located such that the distal and middle transducers record LVP, and the proximal pressure transducer records simultaneous aortic root pressure. Prior to insertion, the manometer-tipped catheter is calibrated against "zero" by submersion just below the surface of NS bath, and again after insertion relative to hydrostatic "zero" using the lumen with respect to the mid-thoracic fluid filled transducer (HP). Each pressure channel is balanced using a transducer control unit (Model TC-510, Millar Instruments, Houston, TX). Pressures are fed to the Catheterization Laboratory amplifier (Quinton Diagnostics, Bothell, WA, General Electric, CT) at a sampling frequency of 200Hz or 240Hz. The LV pressure, the LV volume from the conductance catheter and one ECG channel are also simultaneously recorded on disk in digital format using our multichannel physiologic data acquisition system, consisting of a Pentium class computer, with 100 MB hard disk, 64 MB RAM and NB-M10-16H digitizing board. The sampling rates are controlled using Leycom Software (Leycom Sigma-5, CardioDynamics, Rijnsburg, The Netherlands). Distal pressure and one ECG channel are simultaneously input to the physiological ports of the Doppler imaging system for synchronization (HP, Acuson or Philips ie33).

2.2.4 Simultaneous Echocardiography

Figure 2.2 provides a summary of the catheterization lab setup during simultaneous echocardiography-catheterization. After completion of a complete 2D-echo Doppler study at the time of procedure initiation, and after the catheter has been advanced into the LV, with the

subject supine, apical four-chamber views are obtained by the sonographer with the sample volume gated at 1.5 to 2.5 mm and directed between the tips of the mitral valve leaflets orthogonal to the MV plane.

To synchronize the hemodynamic and Doppler data, a fiducial marker in the form of a square wave signal is simultaneously fed from the catheter transducer control unit to both the echocardiographic imager and the PC. Approximately 25 to 50 beats of continuous, simultaneous transmitral Doppler and LV pressure signals are recorded on the imager's internal memory. In addition 10-15 cardiac cycles via DTI are recorded with the sample volume being located at lateral portion of the mitral annulus along with the simultaneous LV pressure signal. Images of individual beats are captured in DICOM format from the disk for offline analysis using custom image processing software. The entire case is also recorded onto VHS tape (Accuson and HP) or burned to DVD (ie33), and processed the resulting continuous data stream is processed offline.

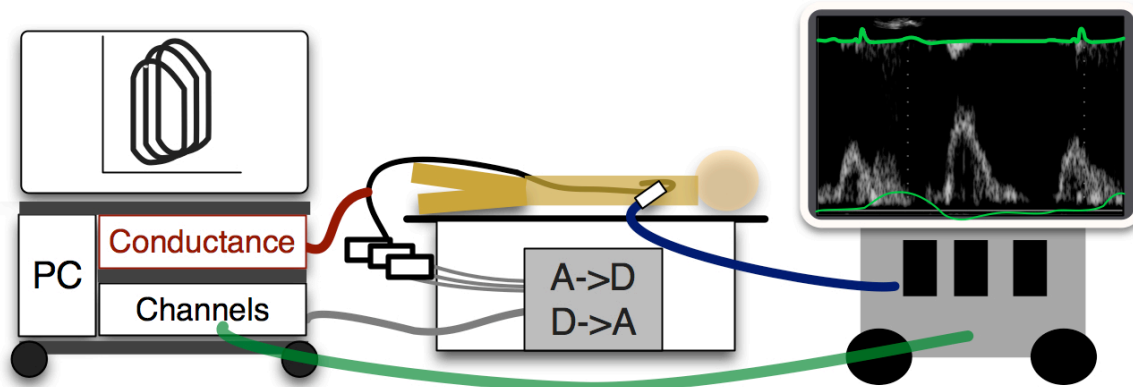


Figure 2.2. A schematic of the catheterization lab setup for simultaneous catheterization and echocardiography. The customized personal computer (PC) on the left accepts, displays, and stores multiple pressure signals and a conductance volume channel from the catheter. One pressure signal and a split ECG signal is fed to the echocardiographic imager (right) from the PC input for simultaneous display of ECG and pressure on the transmitral velocity display. See text for details.

2.2.5 Load Variation During Catheterization

To assess load-dependence, a 10-second Valsalva maneuver is performed with simultaneous transmitral flow-LVP recording(5). Subjects are instructed to perform a breathhold and bear down so as to increase intrathoracic pressure and reduce ventricular preload. This physiological perturbation is easily observed as an increase in left ventricular pressure during the strain-phase followed by a steady decrease in mean left ventricular pressure during the recovery phase. See Figure 2.3a for further details.

Load-dependence is further assessed by analysis of the hemodynamic response following spontaneous or catheter-generated premature ventricular contractions (1). Non-ejecting premature ventricular contractions are often followed by more vigorous filling and contraction, and therefore the filling beats following a premature ventricular contractions represent natural physiological load perturbations. See Figure 2.3b for more detail.

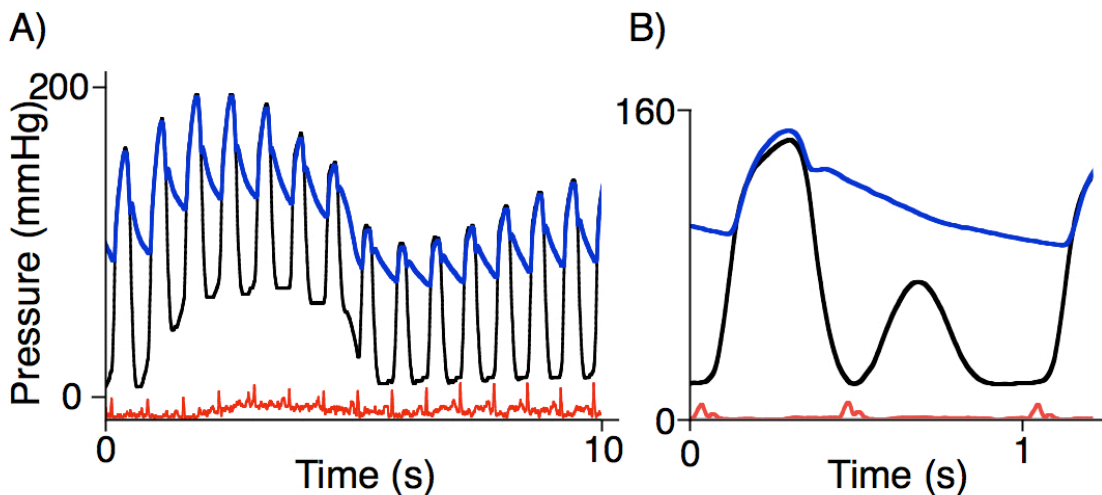


Figure 2.3. A) A pressure vs time plot during a Valsalva maneuver, showing left ventricular (black) and aortic (blue) pressure, with ECG signal in red. Pressure rises dramatically as the subject is instructed to bear down during a breath hold. High intrathoracic pressure leads to reduced venous return and decreased preload. Release of strain leads to decrease in pressures and normalization of venous return. Finally pressures increase in response to the recovery in cardiac output. B) Similar plot to A), but focused on the pressure response to a premature ventricular contraction. Notice that the left ventricular pressure does not exceed the aortic pressure following the premature ventricular contraction. This indicates that no ejection occurs during the premature ventricular contraction. The beats following a premature ventricular contraction have increased preload due to the increased pre-stretch during the premature contraction.

2.2.6 Remainder of Catheterization

Ejection fraction is subsequently determined through ventriculography, performed using a 6F bent, pigtail catheter (Cordis) using 33cc's of contrast injected at 11 cc's/sec. The image is calibrated for volume using a cm grid placed at the mid-axillary level and this subsequent image analysis of end-systolic and end-diastolic frames provides a fairly robust measure of end-systolic and end-diastolic volume. The remainder of the catheterization and coronary angiography proceeds in accordance with established clinical practices (12)..

2.3 Semi-Automated Post Processing of Simultaneous Data

2.3.1 Determining Landmarks in the Pressure, Pressure Derivative, and ECG signals

Determination of Square Waves

Square waves are at least 1 second long step functions with an amplitude of 100 mmHg that are introduced into the pressure signal by the transducer control box for calibration and synchronization purposes. An automated script finds square waves by looking for extended minima in the pressure derivative signal that are flanked by extreme maxima and minima, and manual analysis is employed to confirm the start and stop of the automatically discovered square waves. If the square wave amplitudes or absolute values deviate from 0 mmHg and 100 mmHg then the entire pressure signal is shifted and scaled appropriately.

Initial ECG Analysis

The typical hemodynamic signal captured in the catheterization laboratory consists of simultaneous pressure and ECG signals, and several automated analysis steps are performed to make the data easier to work with. The first step in data analysis involves the determination of all

ECG R-wave peaks. A custom MATLAB code achieves this task by searching for local maxima in the DC filtered ECG signal over successive windows defined by the dominant period (determined by the frequency of the peak in the Fourier power spectrum) in the signal.

Initial Pressure Analysis

The sequence of R-wave peaks defines successive cardiac cycles. For each cycle, multiple analysis steps are performed. To be clear the later R-wave peak defines the beat in question, so the 2nd R-wave beat in the data set defines the 1st measured beat. Furthermore, to avoid errors that arise from respiratory modulation of the pressure signal, maxima and minima in the pressure signal are determined from data that has been appropriately filtered to remove low frequency respiratory signals (0.15 Hz and below). The maximum and minimum pressure between R-wave peaks define the maximum and minimum pressure for that beat, and similarly the maximum and minimum pressure derivatives between R-wave peaks define dP/dt_{MAX} and dP/dt_{MIN} respectively. Similar analysis of the aortic pressure signal between R-wave peaks yields maximum and minimum aortic pressure and pressure derivatives. The maximum pressure between the later R-wave peak and the minimum pressure defines the LVEDP for the beat in question. In most cases this is equal to the pressure at the R-wave peak, but in cases of 1st degree AV block, left ventricular pressure reaches a maximum and then falls back toward diastatic pressure.

Full ECG Analysis

With the basic pressure and pressure derivative landmarks in place, further analysis of the ECG signal is performed. The QRST complex is analyzed by applying linear approximations to the upslope and downslope of the R-wave and determining crossover points with the baseline

zero voltage level of the DC filtered signal. The first minima preceding and following those crossover points define the Q and S waves respectively. The maximum in the absolute value of the ECG signal between the S wave and the time at which minimum pressure occurs defines the T-wave peak. Linear approximation of the T-wave upslope and downslope define the start and end of the T-wave respectively, and the maximum in the absolute value of the ECG signal between the end of the T-wave and the start of the following R-wave defines the P-wave peak. Linear approximation to the upslope and downslope of the P-wave finally defines the approximate start and end of the P-wave. Following automated analysis, manual analysis is performed to adjust any errors due to lack of P-wave or spurious ECG data.

Full Pressure Analysis

The estimated mitral valve opening time t_{MVO} is defined as the time between maximum and minimum pressure where the pressure is closest to LVEDP. The diastasis pressure is defined by the pressure at the P-wave peak, when the P-wave is present, and by the LVEDP otherwise. The start of diastasis is estimated by an iterative process. The midpoint between the time at the P-wave peak and minimum pressure is assumed to be the start of diastasis. A linear regression of the pressures between the assumed start of diastasis and time of minimum pressure, as well as a linear regression of the pressures between the assumed start of diastasis and the time of P-wave peak are constructed. The intersection of these linear regressions defines the next guess of the start of diastasis, and this process is repeated until it converges on a single value or a set of repeated values. If the process converges on a loop of values then the average of those values defines the time at which diastasis starts.

2.3.2 Analysis of the Isovolumic Pressure Decay Contour

Finally the isovolumic portion of the cardiac cycle is analyzed. First the inflection point in the pressure derivative is determined from the local minimum in the second pressure derivative between the time of maximum pressure and minimum pressure derivative. This in turn is used to define the isovolumic pressure decay contour, which is taken to be the pressure signal beginning at the determined inflection point in the pressure derivative and ending 5 msec before t_{MVO} .

Conventional Analysis

Initially conventional analysis is applied to the isovolumic pressure decay contour. First, the original Weiss formulation to define τ_W is applied, by determining the negative reciprocal of the slope of the regression of $\ln(P)$ vs P over the isovolumic pressure decay contour (11). In addition, a more recent non-zero pressure asymptote model (10) of isovolumic relaxation time is applied to define τ_R . The simplest method for determining τ_R is to find the negative reciprocal of the slope of the linear regression defined by the isovolumic pressure decay plotted in the pressure phase plane (Figure 1.8). Finally the logistic time constant, τ_L , is extracted from the isovolumic pressure decay contour by applying a Levenberg Marquardt algorithm to find the τ_L value that minimizes the error in the pressure phase plane between the measured pressure decay contour and phase plane contour predicted by the following equation and its time derivative:

$$P(t) = \frac{2(P_\infty - P_o)}{1 + e^{-\frac{t}{\tau_L}}} + 2P_o - P_\infty \quad \text{Equation 2.1}$$

where P_∞ is the pressure asymptote and P_o is the initial pressure (8).

Kinematic Model Based Analysis

Once conventional analysis is complete, we analyze the isovolumic decay contour through a kinematic approach as well. Following previous work of Chung et al as (3) as well as the methods described in Chapter 11, kinematic parameters of isovolumic relaxation, including τ_c and E_k , are extracted from the isovolumic pressure decay contour by applying a Levenberg-Marquardt algorithm to find the kinematic parameters that minimize the error in the phase plane between the measured pressure decay contour and phase plane contour predicted by the underdamped or overdamped version of the following equation and its time derivative:

$$P(t) = e^{-t \frac{\tau_c}{2}} \left[\frac{\dot{P}_o + \frac{1}{2} \tau_c P_o}{\omega} \sin(\omega t) + P_o \cos(\omega t) \right] + P_\infty \quad \text{Equation 2.2}$$

where P_o is the initial pressure assuming zero pressure asymptote, \dot{P}_o is the initial time derivative of pressure, and $\omega = \sqrt{E_k - \frac{(\tau_c)^2}{4}}$. See Chapter 11 for further details.

All of the preceding isovolumic pressure decay analysis is accomplished through automated MATLAB scripts.

2.3.3 Preprocessing and Conventional Analysis of Simultaneous Echocardiography Data

Continuous transmitral flow data is captured synchronously with the Millar pressure data in the form of a video file. Alignment of the transmitral contours and Millar data is achieved by introducing a time offset in the video file that ensures that the start of the square wave in the pressure signal corresponds to the start of the square wave in the video. With this offset in place, the R-wave peak times are used to determine the corresponding frame number in the video file

(29.97 frames per second on DVD or 14.99 frames per second on VHS) where the R-wave for that beat occurs. Typically the frame that comes several frames beyond the R-wave is extracted to ensure no loss of A-wave signal. These frames are extracted programmatically from the video

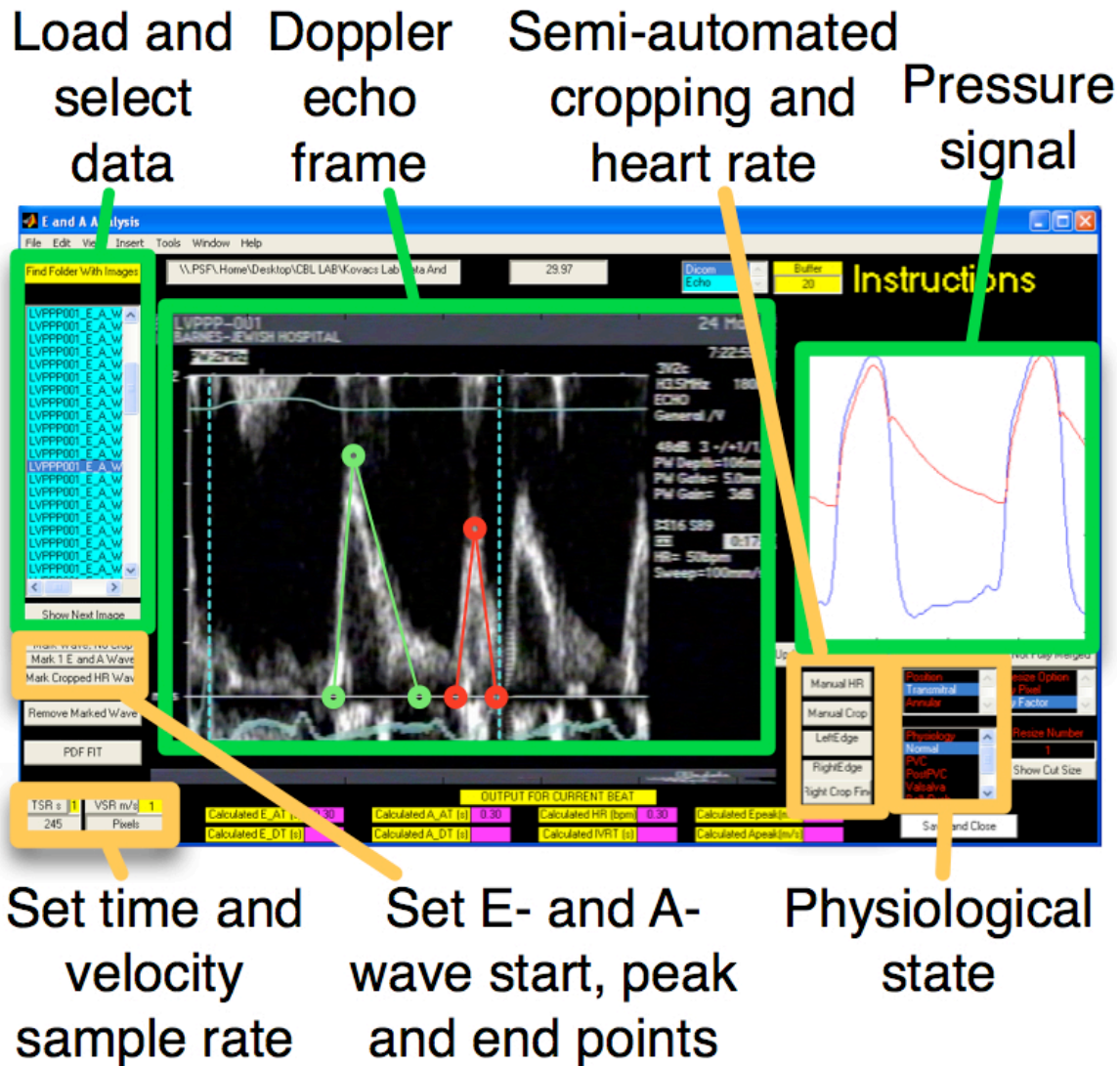


Figure 2.4. A screenshot of a custom MATLAB interface for efficient conventional clinical analysis of Doppler echocardiography transmitral velocity contours. A previously saved frame corresponding to the end of the diastolic interval is read in by the interface, and the user is provided multiple options. If available, the simultaneous pressure contour is displayed. The user must first set the scale of the image by determining the time and velocity sample rates (TSR and VSR). Then the R-R interval must be determined and the E-wave and A-wave start, peak, and end points must be selected. The resulting conventional transmitral contour parameters are saved for future use. If the pressure and simultaneous ECG signal is available and synchronized, then the R-R interval determination may be performed in a semi-automated fashion without full user input. The user determined start and end points are used to define bounds for cropping the image, and the cropped image is exported, with the TSR and VSR values saved in the name of the cropped image. The exported image may be read in by the model based image processing program described below for PDF model based analysis.

file based on the previously determined R-wave peaks. The resulting image stills are fed into a custom MATLAB interface that allows for conventional echocardiographic analysis as well as further post-processing (See Figure 2.4).

The custom MATLAB interface in Figure 2.4 shows synchronized simultaneous pressure and transmitral contour data. The transmitral data is in the form of a freeze frame corresponding to the R-wave peak following the atrial kick associated with that filling interval. This interface allows the user to set the time and velocity sample rates associated with the freeze frame image. Following that step the user may mark the R-wave limits of the image, as well as the peak, start, and end of the E-wave and A-wave, thereby simply implementing conventional triangle shape based analysis of transmitral flow. A similar MATLAB interface exists for processing E'- and A'-wave data, including any extra E'' or E''' annular oscillations. All data is stored and written to a tab-delimited text file, and cropped E- and A-wave images (or E'- and A'- wave images) are exported and renamed in a form that is readily accessible by a custom LabView program designed to extract PDF parameters from E- and A-waves using a nonlinear least-squares Levenberg-Marquardt algorithm. In this manner each measured E-wave is analyzed by conventional clinical techniques and processed for PDF model based analysis.

2.4 Model Based Image Processing

2.4.1 User Selection of Wave Limits and Amplitude

The cropped images output by the conventional analysis MATLAB interface described above, with time and velocity sample rates stored in the image file name, are imported into a custom PDF analysis LabView program (see Figure 2.5). Before the PDF parameters can be

determined, the user must manually set the maximum velocity envelope (MVE) and left and right bounds of the E-wave and A-wave.

These user defined limits set the raw pixel data that is input into the Levenberg-Marquardt algorithm, and different choices for these constraints lead to different algorithmically determined best-fit PDF parameters.

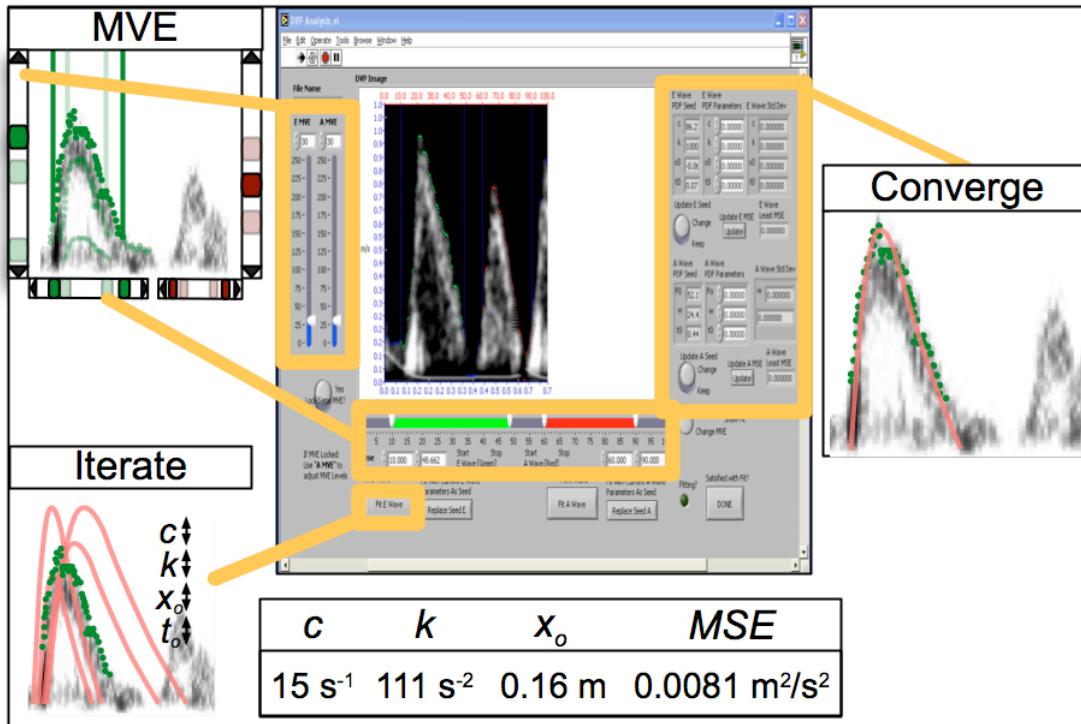


Figure 2.5. A screenshot of a LabView interface for PDF model based image processing. Only E-wave analysis is shown for simplicity. First the user selects the maximum velocity envelope (MVE), and the start and end of the E-wave. A Levenberg-Marquardt algorithm iterates over parameter space until the mean square error (MSE) between model fit and user defined input data is minimized.

Choice of Maximum Velocity Envelope

When blood velocity is homogeneous across the sample volume, the envelope of the Doppler velocity contour is expected to be relatively thin. If on the other hand, blood velocity is heterogeneous across the sample volume, then the envelope will have significant thickness, thereby clearly defining a minimum velocity envelope, mean velocity envelope, and maximum

velocity envelope. Thus as sample volume velocity heterogeneity increases, the envelope thickness increases, with a lower and lower minimum velocity envelope but a fairly constant maximum velocity envelope. For this reason the maximum velocity envelope is deemed to be a more consistent and robust measure of transmitral blood flow velocity, and indeed conventional triangle based analysis draws a triangle relative to the maximum velocity envelope. Thus, in order to ensure that the PDF model provides E-wave parameters consistent with the conventional analysis techniques, the maximum velocity envelope is applied to extract velocity data from the E- and A-wave images. It is important to note that care must be taken for image contrast and brightness to be fairly consistent so that the pixels extracted from the image correctly correspond to the measured maximum velocity envelope.

Choice of E-wave Start And End

Only the data between the user selected start and end of the E-wave is used to generate the best-fit PDF parameters. While theoretically speaking only 3 points are needed to determine all PDF parameters exactly, the realities of noisy clinical data require that a large number of data points be included in the analysis, so as to average out the effects of noise and spurious data. Thus at first glance it would seem that the proper choice of E-wave start and end would be the velocity minima that precede and follow the E-wave peak, respectively. However, there are some theoretical and experimental challenges to that approach, and they begin with the applicability of the PDF model at the start of the E-wave.

The PDF model assumes that the force driving transmitral flow at the start of filling is instantaneously equal to kx_0 , and therefore the velocity is predicted to have a non-zero acceleration equal to kx_0 at $t=0$. Furthermore, this is the PDF model predicted maximum E-wave

acceleration, and there is no predicted inflection point in the E-wave upslope for $t > 0$ according to the PDF model. This is not in precise agreement with the physiology because at mitral valve opening the driving force, or atrioventricular pressure gradient, is initially zero. As filling commences the maximum AV pressure gradient is rapidly attained (in ms) as ventricular pressure falls much faster than the simultaneous atrial pressure can drop. Rapidly the maximum acceleration is reached (E-wave upslope inflection point), and following that the acceleration proceeds to decline until it is zero again at the E-wave peak. This physiological finding has been demonstrated in numerous studies (4). Furthermore, direct inspection of the upslope of transmitral velocity contours recapitulates the established behavior of the atrioventricular pressure gradient. At mitral valve opening, the E-wave begins flat and concave up, goes through an inflection point in a few ms, usually before it reaches 25% of peak velocity, and becomes concave down as it approaches peak velocity. It is important to note that an accurate measure of the early E-wave upslope velocity may be challenging because of baseline velocity filters and artifact due to early filling leaflet motion. Because peak AV gradient develops very rapidly starting from zero, but the PDF model initiates motion with the maximum force (max AV gradient analog) at $t=0$, the PDF model is not physiologically consistent at the start of the E-wave (Figure 2.6). Beyond the

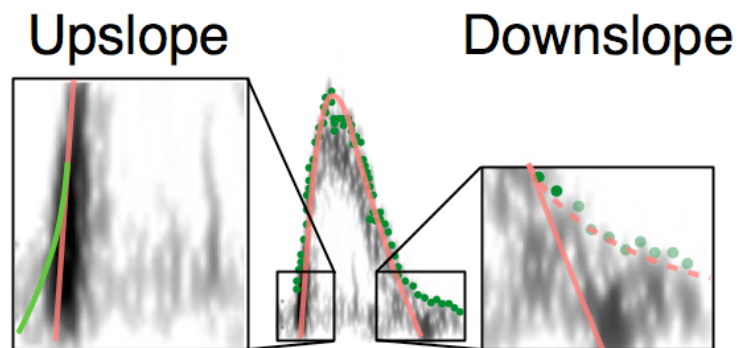


Figure 2.6. A closer look at the upslope and downslope of the E-wave, showing limitations inherent in the PDF model of the E-wave velocity contour. The upslope of the E-wave is a smooth function that begins flat and rapidly increases (green), whereas the upslope of the PDF-model predicted contour begins with a non-zero slope. The downslope of the E-wave contains low velocity data that may not be physiological. Inclusion of this data may extend the E-wave deceleration tail significantly.

inflection point of the acceleration portion, the model accurately predicts the E-wave contour. Thus care must be taken to select E-wave data beyond the start of the E-wave. In general setting the left start at a time at or just beyond the inflection point at which the wave reaches 30-40% of the peak E-wave height ensures that the data is beyond the range of both extraneous valve noise and E-wave acceleration concave-up portion, and maximizes the amount of data included before the E-wave peak.

The choice of E-wave end must also be made with care. If there is absence of diastasis then the choice must be at a time less than or equal to the E-wave and A-wave intersection. When diastasis is present, however, the selection of E-wave end is not trivial. In some cases E-wave deceleration shows a biphasic characteristic, and in those cases only the first phase of deceleration should be included. Most clinically measured E-wave waves are not biphasic, however, and therefore in principle one could select the E-wave minimum as the end of the data to be included in the best-fit algorithms. However, as the E-wave velocity falls to levels near the baseline, the signal and noise become indistinguishable, and any baseline filtering that is present begins to have a dramatic impact on the best-fit determined contour. The inclusion of extraneous data towards the end of the wave generates best-fit contours with long tails, biased towards the critically or overdamped kinematic regimes. This leads to an E-wave contour with a predicted DT that far exceeds the conventionally (triangle shape based) determined DT, and thereby makes the PDF model predicted fit inconsistent with conventional analysis techniques (Figure 2.6). While the PDF model provides mechanistic insight beyond conventional analysis, it is important for traditional E-wave shape-based indexes to be consistent with PDF model derived shape based indexes, and therefore the conventional triangle fit deceleration slope should be considered as one selects the proper E-wave end point to include in the best-fit algorithmic analysis. This is

achieved typically by selecting the E-wave end at a time where the E-wave velocity is 20-30% of the E-wave peak.

Choice of A-wave Start And End

The choice of A-wave start and end follows the same rationale as the E-wave fitting portion. When diastasis is absent the A-wave start is the point at which E-wave and A-wave intersect. When diastasis is present, selecting a start point at the time where A-wave velocity is 30% of the A-wave peak velocity is appropriate. The end point for A-wave fitting may be chosen at the lowest A-wave velocity preceding the ECG R-wave peak, and this is typically at an A-wave velocity that is 20% of the A-wave peak velocity.

Heart Rate Limitations

An important limitation arises in relation to setting the end of the E-wave and start of the A-wave when heart rate is elevated, diastasis is abolished, and E- and A-waves are partially merged. When heart rate is only modestly elevated (~ 80 BPM) the degree of E- and A-wave merging is not significant, and the end of the E-wave may be at a time when the velocity is 20% of the E-wave peak velocity. However, as heart rate increases the degree of merging increases as well, and at heart rates around 95 BPM, the E- and A-wave peaks become indistinguishable. As this transition occurs, less and less of the E-wave deceleration portion is visible before the E-wave A-wave intersection, and therefore the amount of E-wave data that may be used as input to the fitting algorithm decreases with increased heart rate (Figure 2.7). In general an E-wave with $\frac{1}{2}$ - $\frac{2}{3}$ rds of its deceleration portion visible can be accurately fit, even if the remaining $\frac{1}{3}$ of the wave is merged with the A-wave. If on the other hand less than half of the deceleration portion is

unmerged, then the number of data points that can be input into the fitting algorithm is insufficient to generate a robust fit, and therefore subjects with significantly increased heart rate are not amenable to current PDF model analysis techniques. The heart rate at which diastasis is lost, and the E-wave start to A-wave end duration may be predicted and understood in kinematic terms, however (2).

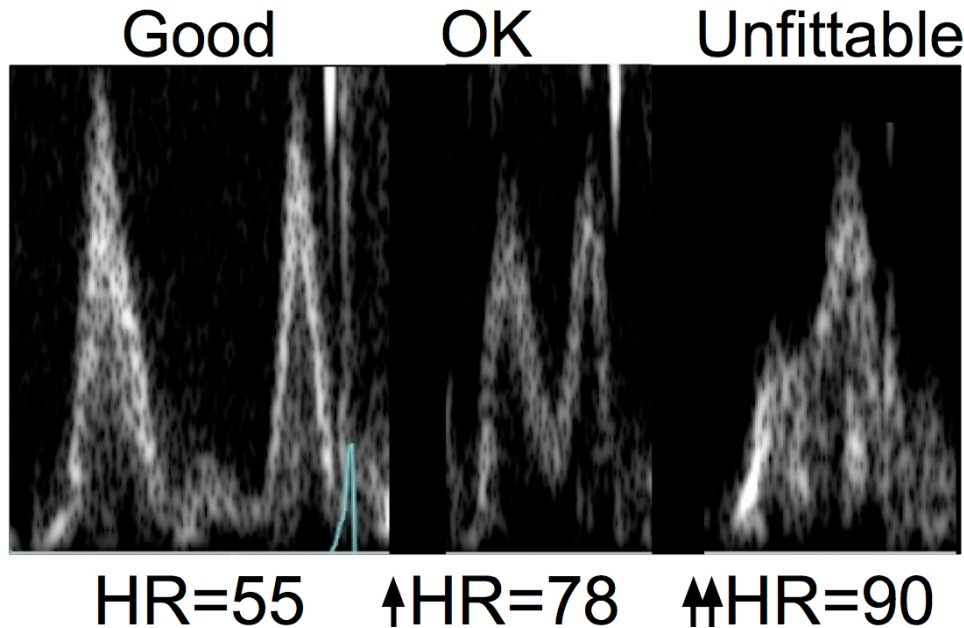


Figure 2.7. E-wave from different subjects, demonstrating the merging of E- and A-waves with increased heart rate. PDF fitting is possible when waves are partially merged, but not possible when merging is significant, as shown in the rightmost panel.

2.4.2. Levenberg Marquardt Fitting of Data

Solving the Inverse Problem

The user selected portions of the E-wave and A-wave contours are input into a Levenberg-Marquardt algorithm that iterates over E-wave (c, k, x_o, t_o) and A-wave (F_o, w, t_o) parameter space until a minimum in the square error between model predicted E-wave and A-wave velocities and input data is found. Velocity contour data outside of the user selected range does not impact the fitting algorithm or the determined mean square error between model fit and

input data. Because the PDF model is linear and invertible, in principle there is only one point in parameter space that uniquely fits the input data. However, because the data always contains noise or error, in practice there may be a locus of points in parameter space that accurately fit the input data. Nevertheless, because the model is linear and invertible, we can be confident that the algorithm determined best-fit parameters are close to (in parameter space) the ideal noise-free unique solution. Thus the Levenberg Marquardt algorithm allows for the solution of the ‘inverse problem of diastolic function’ (6, 7) , whereby mechanistic physiological diastolic function parameters that determine the velocity contours are extracted from clinically measured E- and A-waves.

The algorithm is adapted from FORTRAN code outlined in Numerical Recipes [(9), and runs in both LabView and MATLAB. The general mathematical approach of the Levenberg Marquardt algorithm, which has been previously described (6, 7), combines steepest-descent and gradient based methods to efficiently iterate over parameter space and converge to a solution.

Algorithm Determined Standard Deviations

The Levenberg Marquardt algorithm provides best-fit PDF parameters, as well as the standard deviation for the best-fit parameters. A noisy input data set that is not well fit by the PDF model, for example, may have significant standard deviations in c , k , and x_0 determined values. However, care must be taken to interpret the algorithm determined parameter standard deviations, because a critical aspect of the parameter standard deviation is the standard deviation of the input data. If the input data standard deviation is not known, then the algorithm determined parameter standard deviation values will not be accurate. This is an important limitation to consider when working with digitized image data as the input. The image data does not have any

clear indication of the velocity standard deviations, and therefore when working from digitized image data, one must assume a standard deviation value for input velocity. Using an average percentage value based on machine settings or parameters is a reasonable approach. In the ideal case, one would use the raw Doppler ultrasound velocity signal and standard deviation as input to the Levenberg Marquardt algorithm so as to ensure accurate determination of the best-fit parameter standard deviations.

Manual Correction and Final Output Data

The best-fit determined parameters for both E-waves and A-waves may be applied to evaluate the PDF velocity contour expressions in order to generate and superimpose the model-predicted velocity contours. This allows for a visual inspection of the model predicted contour relative to the input data, and if a significant deviation is observed then a manual correction may be applied. This may occur if the start and end points of the waves were incorrectly set, or if spurious pixels were included in the raw input data. Manual adjustment must be accompanied by a recalculation of the mean square error between model predicted contour and input data.

Once the final best-fit parameters are set, the best-fit determined parameters and any mathematically related indexes are stored and saved in a tab-delimited text file. This process is repeated for each measured wave and results in a set of PDF parameter values and indexes for any given subject.

2.5 Mathematical Insights and Methods

As described in Chapter 1, the PDF model provides an accurate fit to a wide variety of clinically encountered E- and A-wave velocity contours, and the PDF model parameters have

physiological analogues that have been validated in numerous studies. In addition to providing an accurate fit to the E- and A-wave velocity contours, however, the PDF model parameters and indexes derived from algebraic manipulation of the PDF model parameters provide mechanistic insight into the physiology of diastole and by extension diastolic function. These mechanistic insights require a deeper understanding of the mathematical implications and properties of the PDF kinematic model, which we describe below. As described in Chapter 1, the governing differential equations for E-waves and A-waves respectively are:

$$\ddot{x} + c\dot{x} + kx = 0 \quad \text{Equation 2.3}$$

$$\ddot{x}_A + c_A\dot{x}_A + k_A x_A = F_o \sin(\omega_A t) \quad \text{Equation 2.4}$$

2.5.1 Conventional Indexes of Underdamped Waves

Underdamped kinematics are encountered when stiffness effects dominate damping effects, and mathematically $4k > c^2$. It is useful to define a dimensionless parameter, $y = \frac{c}{2\sqrt{k}}$, whose relative magnitude determines the underdamped vs overdamped kinematic behavior. Thus underdamped kinematics correspond to $0 \leq y < 1$, and the velocity and displacement equations may be rewritten in terms of the velocity and displacement equations (Equation. 1.10 and its integral) may be rewritten in terms of y , k , ω and x_o :

$$v(t) = \frac{kx_o}{\omega} e^{-(y\sqrt{k})t} \sin(\omega t) \quad \text{Equation 2.5}$$

$$x(t) = -x_o e^{-(y\sqrt{k})t} \left[\cos(\omega t) + \frac{y}{\sqrt{1-y^2}} \sin(\omega t) \right] \quad \text{Equation 2.6}$$

where $\omega = \frac{\sqrt{4k - c^2}}{2} = \sqrt{k} \sqrt{1 - y^2}$.

E-wave Duration

The underdamped velocity contour is predicted to oscillate and therefore cross the x-axis. The time at which this occurs is given by the first non-zero root of $\sin(\omega t)$, and therefore the duration of the E-wave, called E_{dur} , is:

$$t = E_{dur} = \frac{\pi}{\omega} = \frac{\pi}{\sqrt{k}}(1 - y^2)^{-\frac{1}{2}} \quad \text{Equation 2.7}$$

It is clear that the E-wave duration is expected to increase without bound as the critically damped ($y=1$) kinematic regime is approached. While the velocity vanishes at the end of the E-wave, the oscillator displacement is nonzero, except in critically damped ($y=1$) limit:

$$x(E_{dur}) = x_0 e^{-\frac{\pi y}{\sqrt{1-y^2}}} \quad \text{Equation 2.8}$$

E-wave Acceleration Time

The E-wave acceleration time (AT) is the time from the start of the wave to the peak of the wave. This may be determined by finding the time at which the derivative of the velocity is zero. Alternatively, one can set the second derivative of displacement to zero in the governing differential equation, and solve for time:

$$0 + c\dot{x}(AT) + kx(AT) = 0 \quad \text{Equation 2.9}$$

Canceling out like terms and rearranging we find:

$$\frac{c}{\omega} \sin(\omega AT) = \cos(\omega AT) + \frac{c}{2\omega} \sin(\omega AT) \quad \text{Equation 2.10}$$

$$\frac{y}{\sqrt{1-y^2}} = \cot(\omega AT) \quad \text{Equation 2.11}$$

Solving for AT we find:

$$AT = \frac{1}{\omega} \tan^{-1} \left(\frac{\sqrt{1-y^2}}{y} \right) = \frac{1}{\omega} \cos^{-1}(y) = \frac{1}{\sqrt{k}} \frac{\cos^{-1}(y)}{\sqrt{1-y^2}} \quad \text{Equation 2.12}$$

It is interesting to consider the $y=0$ and $y=1$ limits of the second term in the equation above:

$$\frac{\cos^{-1}(0)}{\sqrt{1-0^2}} = \frac{\pi}{2} \quad \lim_{y \rightarrow 1} \frac{\cos^{-1}(y)}{\sqrt{1-y^2}} = 1 \quad \text{Equation 2.13}$$

Thus as the E-wave goes from undamped ($y=0$) to critically damped ($y \sim 1$), AT varies as:

$$\frac{\pi}{2\sqrt{k}} \geq AT > \frac{1}{\sqrt{k}} \quad \text{Equation 2.14}$$

E-wave Deceleration Time

Deceleration time (DT) is the time between E-wave peak and E-wave end, and therefore can be determined from:

$$DT = E_{dur} - AT = \frac{1}{\omega} \left(\pi - \cos^{-1}(y) \right) = \frac{1}{\sqrt{k}} \left(\frac{\pi - \cos^{-1}(y)}{\sqrt{1-y^2}} \right) \quad \text{Equation 2.15}$$

See Chapter 5 for further discussion related to E-wave deceleration time and its determinants.

E-wave Peak

Evaluating Eq 2.5 at the peak time AT yields an expression for E-wave peak velocity (E_{peak}):

$$E_{peak} = \frac{kx_o}{\omega} e^{-y\sqrt{k} \frac{1}{\omega} \cos^{-1}(y)} \sin(\cos^{-1}(y)) = x_o \sqrt{k} e^{-\frac{y \cos^{-1}(y)}{\sqrt{1-y^2}}} = x_o \frac{c}{2y} e^{-\frac{y \cos^{-1}(y)}{\sqrt{1-y^2}}} \quad \text{Equation 2.16}$$

Again, considering the limits $y=0$ and $y=1$, we have the following limits for the E-wave peak velocity between the undamped and critically damped regimes:

$$x_o\sqrt{k} > E_{peak} > x_o \frac{\sqrt{k}}{e} = x_o \frac{c}{2e} \quad \text{Equation 2.17}$$

E-wave Area

The E-wave velocity time integral (VTI) is often calculated as the area of the triangle fit to the E-wave, and when multiplied by effective mitral valve area, provides an estimate of the E-wave filling blood volume. The E-wave area is the difference in E-wave displacement between the end and start of the wave, and therefore, from Equation 6 is given as:

$$VTI_E = x(E_{dur}) - x(0) = x_o \left(1 + e^{-\frac{\pi y}{\sqrt{1-y^2}}} \right) \quad \text{Equation 2.18}$$

Again, considering the undamped ($y=0$) and critically damped ($y=1$) limits, one obtains the following limits for E-wave area (VTI_E):

$$2x_o \geq VTI_E > x_o \quad \text{Equation 2.19}$$

These limits have been used in the previous work to define an index of filling efficiency, called the kinematic filling efficiency index (13), and several interesting applications of this efficiency index are described in Chapter 8 and 12.

2.5.2 Additional Indexes of Underdamped E-waves

E-wave Upslope and Downslope

The slope of the E-wave at the start is interesting to consider, because it provides an important distinction between actual physiology and approximations made by the PDF model. At the start and end of filling the velocity vanishes, and Equation 2.3 becomes:

$$\ddot{x} = -kx \quad \text{Equation 2.20}$$

Plugging in $t=0$, we can determine the E-wave upslope:

$$E_{Upslope} = |kx_o| \quad \text{Equation 2.21}$$

and plugging in $t=E_{dur}$ and applying Eq 2.5 we can determine the E-wave downslope:

$$E_{Downslope} = - \left| kx_o e^{-\frac{\pi y}{\sqrt{1-y^2}}} \right| \quad \text{Equation 2.22}$$

Physiologically the E-wave initial upslope should be zero since the fluid accelerates from rest and the Av pressure gradient is zero at MVO., The non-zero upslope predicted by Eq 2.21 demonstrates a limitation of the PDF model at the start of filling, described above.

E-wave Inflection Point

One primary difference between a triangle fit to the E-wave and the PDF model E-wave contour is the E-wave deceleration portion inflection point. The inflection point is routinely observed with clinical E-wave data but is disregarded when one approximates the wave as a triangle. The mathematics of the inflection point are surprisingly simple, and can be appreciated by finding the time at which the second derivative of velocity vanishes:

$$\begin{aligned} \frac{dv(t)}{dt} &= \frac{kx_o}{\omega} e^{-(y\sqrt{k})t} \left(-y\sqrt{k} \sin(\omega t) + \omega \cos(\omega t) \right) \\ \frac{d^2v(t)}{dt^2} = 0 &= \frac{kx_o}{\omega} e^{-(y\sqrt{k})t_{inf}} \left[\left(y^2k - \omega^2 \right) \sin(\omega t_{inf}) - 2y\sqrt{k}\omega \cos(\omega t_{inf}) \right] \end{aligned} \quad \text{Equation 2.23}$$

Applying the fact that $\omega = \sqrt{k}\sqrt{1-y^2}$, we find:

$$\tan(\omega t_{\text{infl}}) = 2 \frac{\sqrt{1-y^2}}{y \left(1 - \frac{1-y^2}{y^2}\right)} \quad \text{Equation 2.24}$$

If we apply Eq 2.11 above, with the preceding equation we may visualize both acceleration time and inflection time graphically (Figure 2.8).

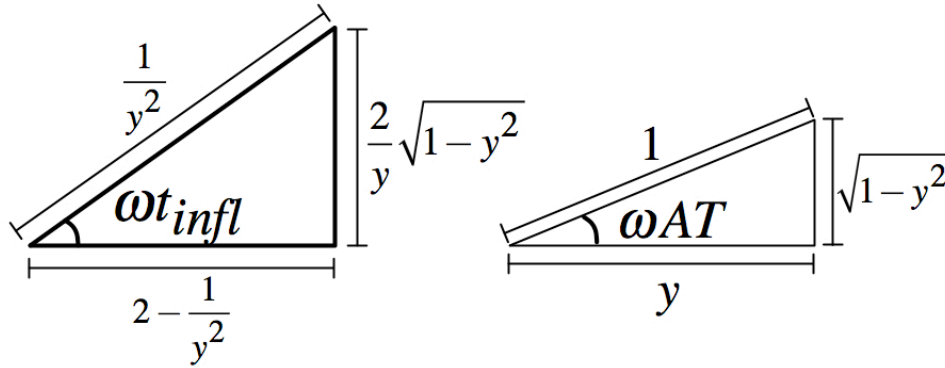


Figure 2.8. Visualization of the trigonometric identities in Equation 2.24 and Equation 2.12. See text for details.

We can use Figure 2.8 to determine the relationship between the inflection time and acceleration time. First, let's determine the sin and cosine of the angles in the figure:

$$\sin(\omega t_{\text{infl}}) = 2y\sqrt{1-y^2}, \quad \sin(\omega AT) = \sqrt{1-y^2}, \quad \cos(\omega AT) = y \quad \text{Equation 2.25}$$

Applying the $\sin(2x)$ trigonometric identity we find:

$$\sin(2\omega AT) = 2 \sin(\omega AT) \cos(\omega AT) = \sin(\omega t_{\text{infl}}) \quad \text{Equation 2.26}$$

And thus we have derived the remarkable result that the E-wave inflection point occurs at twice the acceleration time:

$$t_{\text{infl}} = 2AT \quad \text{Equation 2.27}$$

This result is simple and powerful, and could be predicted by considering the $c=y=0$ un-damped case, where the inflection point occurs at first non-zero root of the symmetric E-wave. Further insight may be gained by determining the velocity at the inflection point:

$$v(2AT) = 2y\sqrt{k}x_0 e^{-\frac{2y\cos^{-1}(y)}{\sqrt{1-y^2}}} = 2y\frac{v^2(AT)}{\sqrt{k}x_0} \quad \text{Equation 2.28}$$

In addition, there is a fascinating connection to the acceleration at the inflection point, which can be easily determined by differentiating Eq 2.3 and setting the velocity second derivative to zero:

$$\dot{v}(2AT) = -\frac{k}{c}v(2AT) = -\frac{\sqrt{k}}{2y}v(2AT) = -\frac{1}{x_0}v^2(AT) \quad \text{Equation 2.29}$$

Thus there is a deep connection between the peak E-wave velocity and the downslope at the E-wave inflection point.

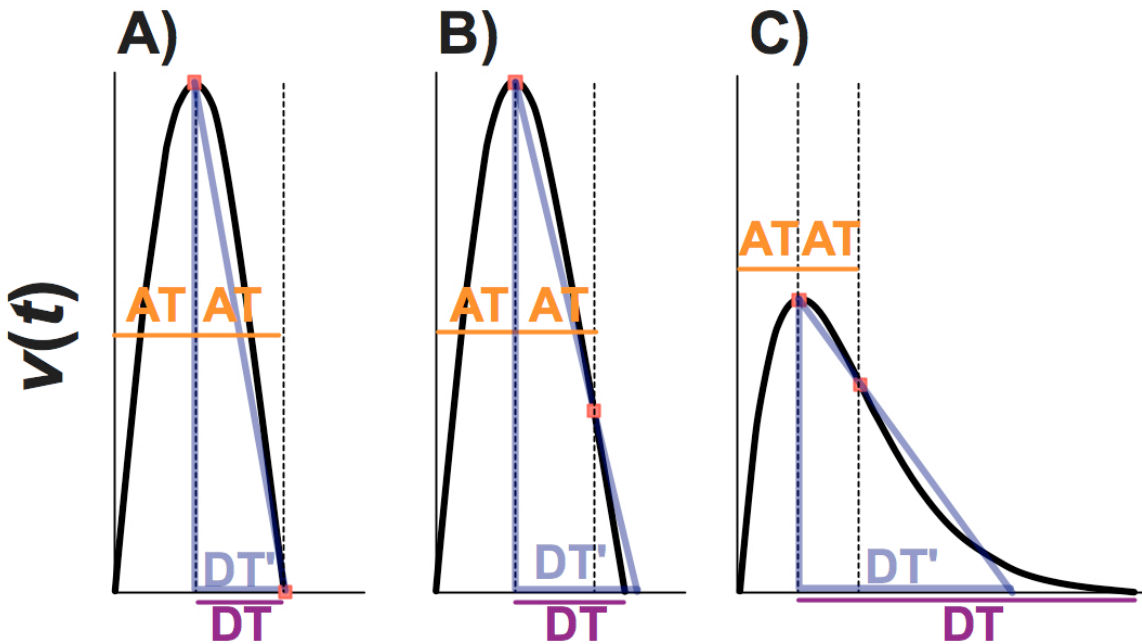


Figure 2.9. 3 Underdamped E-waves with increasing damping, showing both exact deceleration time (DT), and inflection point determined deceleration time (DT'). In each case the inflection point is found by doubling the acceleration time (AT). A) An undamped ($c=0$) E-wave, where AT is equal to DT. In this case DT' and DT are equal, because the inflection point occurs at the E-wave end. B) A slightly damped E-wave, with $DT > AT$, showing the close agreement between DT' and DT. C) A nearly critically damped E-wave $DT \gg AT$, showing the difference between DT' and DT.

E-wave Inflection and Deceleration Time

As described above, the inflection time is identical to the E-wave duration in the $c=y=0$

case. This brings up an interesting connection between inflection point and deceleration time, because in the $c=y=0$ case, the base of the right triangle with hypotenuse defined between E-wave peak and E-wave inflection point defines the deceleration time exactly (Figure 2.9). It is interesting to analyze the effectiveness of approximating the E-wave deceleration time with a triangle defined by the peak and inflection point.

Using similar triangles it is easy to show that:

$$\frac{v(AT) - v(2AT)}{AT} = \frac{v(AT)}{DT'} \quad \text{Equation 2.30}$$

where DT' is the inflection point defined triangle deceleration time.

Solving for DT' we find:

$$DT' = \frac{AT}{1 - \frac{v(2AT)}{v(AT)}} = \frac{1}{\sqrt{k}} \frac{\frac{\cos^{-1}(y)}{\sqrt{1-y^2}}}{1 - 2ye \frac{y \cos^{-1}(y)}{\sqrt{1-y^2}}} \quad \text{Equation 2.31}$$

Plotting this and the exact expression for DT against y , (Eq 2.15) with a fixed k we find that DT' is a suitable approximation for DT (Figure 2.10).

2.5.3 Conventional Indexes of Overdamped E-waves

We can transform underdamped results to overdamped results with the substitution $\omega \rightarrow i\beta$, where

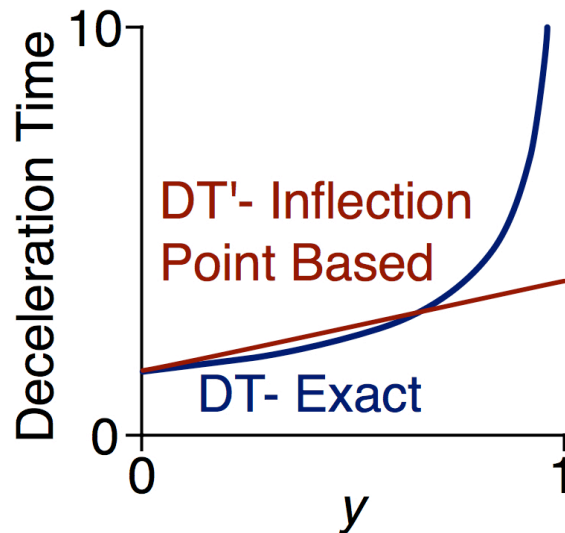


Figure 2.10 A plot of Equation 2.31 (red) and Equation 2.15 (blue) defined deceleration time (DT) vs y . Notice that the exact and approximate values for DT are in close agreement for $y \ll 1$. See text for details.

$\beta = \sqrt{(c/2)^2 - k} = \frac{c}{2}\sqrt{1 - y^{-2}}$. Thus, the E-wave overdamped velocity expression is:

$$v(t) = \frac{kx_o}{i\beta} e^{-(y\sqrt{k})t} \sin(i\beta t) =$$

$$v(t) = \frac{kx_o}{\beta} e^{-(y\sqrt{k})t} \sinh(\beta t) = \frac{kx_o}{\beta} e^{-\alpha t} \sinh(\beta t)$$

Equation 2.32

where $\alpha = \frac{c}{2}$. Similarly the expression for overdamped displacement is:

$$x(t) = -x_o e^{-\alpha t} \left[\cos(i\beta t) + \frac{\alpha}{i\beta} \sin(i\beta t) \right]$$

$$x(t) = -x_o e^{-\alpha t} \left[\cosh(\beta t) + \frac{\alpha}{\beta} \sinh(\beta t) \right]$$

Equation 2.33

E-wave Acceleration Time

Making a similar substitution in the acceleration time expression above, we find the acceleration time for the over damped E-wave:

$$AT = \frac{1}{i\beta} \tan^{-1} \left(\frac{i\beta}{\alpha} \right) = \frac{1}{\beta} \tanh^{-1} \left(\frac{\beta}{\alpha} \right)$$

$$AT = \frac{\alpha}{\sqrt{1 - y^{-2}}} \tanh^{-1} \left(\sqrt{1 - y^{-2}} \right)$$

Equation 2.34

We may find an alternative expression for AT by taking the hyperbolic tangent of both sides of the equation above:

$$\frac{\beta}{\alpha} = \tanh(\beta AT) = \frac{e^{\beta AT} - e^{-\beta AT}}{e^{\beta AT} + e^{-\beta AT}}$$

Equation 2.35

$$AT = \frac{1}{2\beta} \ln \left(\frac{\alpha + \beta}{\alpha - \beta} \right)$$

Equation 2.36

E-wave Peak

Plugging in equation 2.36 into equation 2.32 we find the overdamped E-wave peak velocity:

$$E_{peak} = \frac{kx_o}{\beta} e^{-\frac{\alpha}{2\beta} \ln\left(\frac{\alpha+\beta}{\alpha-\beta}\right)} \sinh\left(\ln\sqrt{\frac{\alpha+\beta}{\alpha-\beta}}\right) = \sqrt{k}x_o \left(\frac{\alpha+\beta}{\alpha-\beta}\right)^{-\frac{\alpha}{2\beta}} \quad \text{Equation 2.37}$$

E-wave Area and Upslope

The E-wave area in the overdamped case is simple because the oscillator displacement and velocity reach zero only at infinite time. Thus, the total area is equal to the initial displacement, which is x_o . In addition, the E-wave upslope is identical in the underdamped and overdamped cases.

E-wave Inflection Point

The overdamped E-wave contour has an inflection point which may be determined using the methods outlined above. Because switching from underdamped to overdamped requires a substitution of frequency only, we expect the relationship between inflection time and acceleration time to hold. To derive the inflection time, we take the 2nd derivative of Eq 2.32 and solve for the time where it vanishes:

$$\frac{d^2v(t)}{dt^2} = 0 = \frac{kx_o}{\beta} e^{-\alpha t_{inf}} \left[(\alpha^2 + \beta^2) \sinh(\beta t_{inf}) - 2\alpha\beta \cosh(\beta t_{inf}) \right]$$
$$\tanh(\beta t_{inf}) = \frac{2\alpha\beta}{(\alpha^2 + \beta^2)} = 2 \frac{\frac{\beta}{\alpha}}{1 + \left(\frac{\beta}{\alpha}\right)^2} \quad \text{Equation 2.38}$$

It is useful to derive an identity related to $\tanh(x)$ here:

$$z = e^{\tanh^{-1}(x)} \Rightarrow \tanh(\ln(z)) = \frac{z - \frac{1}{z}}{z + \frac{1}{z}} = \frac{z^2 - 1}{z^2 + 1} = x$$

$$\Rightarrow z = \frac{x+1}{\sqrt{1-x^2}}$$

$$\therefore e^{2 \tanh^{-1}(x)} = \frac{(x+1)^2}{1-x^2}$$

Equation 2.39

Thus:

$$\tanh\left(2 \tanh^{-1}(x)\right) = \frac{e^{2 \tanh^{-1}(x)} - e^{-2 \tanh^{-1}(x)}}{e^{2 \tanh^{-1}(x)} + e^{-2 \tanh^{-1}(x)}}$$

$$\tanh\left(2 \tanh^{-1}(x)\right) = \frac{(x+1)^2 - (1-x)^2}{(x+1)^2 + (1-x)^2} = \frac{2x}{1+x^2}$$

Equation 2.40

Finally, this identity may be applied to equation 2.38 to yield:

$$\tanh(\beta t_{\text{inf}}) = \frac{2 \frac{\beta}{\alpha}}{1 + \left(\frac{\beta}{\alpha}\right)^2} = \tanh\left(2 \tan^{-1}\left(\frac{\beta}{\alpha}\right)\right) = \tanh(2\beta AT)$$

$$\therefore t_{\text{inf}} = 2AT$$

Equation 2.41

Thus, as expected, the time of the inflection point in the deceleration portion of the E-wave is twice the acceleration time for both the underdamped and overdamped E-wave. Finally we can determine the velocity at the inflection point by plugging in Eq 2.41 into the overdamped expression for velocity:

$$v(2AT) = 2\alpha x_o \left(\frac{\alpha + \beta}{\alpha - \beta}\right)^{-\frac{\alpha}{\beta}} = \frac{2y}{\sqrt{kx_o}} v^2(AT)$$

Equation 2.42

Therefore the connection between inflection point velocity and peak velocity is consistent across different kinematic regimes.

E-wave Deceleration Time

The overdamped limit of the PDF model at first glance suggests that DT would be infinite, because the E-wave never vanishes beyond the peak. When one applies a triangular fit to the E-wave, however, one draws a best fit line from the peak through the deceleration portion, even if the deceleration tail is prolonged. We can mathematically mimic this purely visual approach to fitting by connecting the peak and inflection point in the deceleration portion of the E-wave with a line, and determining the intersection of this line with the time axis. The time from the E-wave peak to the found intersection point is therefore the inflection-defined DT . It is interesting to note that this approximate approach is exact when $c=0$, as we show above, because the inflection point occurs when velocity vanishes. To ensure that this mathematical approximation is appropriate in the overdamped setting, Figure 2.11 provides results from numerical experiments with overdamped E-waves showing that the essential aspect ratio of the wave is well approximated by the line constructed from E-wave peak and inflection point.

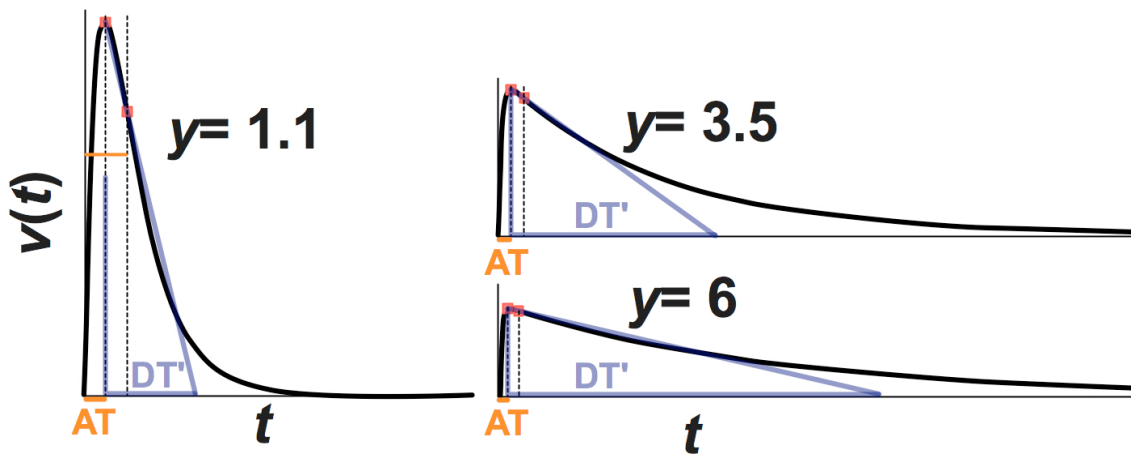


Figure 2.11. 3 overdamped E-waves with increasing y values, showing the inflection point defined deceleration time (DT'). Notice that the inflection point occurs at a time $t=2AT$, where AT is the acceleration time of the wave. Deceleration time is routinely determined in the clinical setting by a linear best fit approximation to the deceleration portion of the wave, but mathematical determination is challenging because the PDF model derived exact deceleration time for overdamped E-waves is infinite. The inflection point approximation serves as a reasonable method for mathematical determination of clinically defined E-wave deceleration time. See text for details.

Thus, following the approach outlined above with underdamped waves, the overdamped E-wave deceleration time may be determined from similar triangles:

$$\frac{v_{over}(AT) - v_{over}(2AT)}{AT_{over}} = \frac{v(AT_{over})}{DT_{over}} \quad \text{Equation 2.43}$$

where the ‘over’ subscript is intended to clarify that this expression is specific to overdamped E-waves. Solving for overdamped DT we find:

$$DT_{over} = AT_{over} \frac{1}{1 - \frac{v_{over}(2AT)}{v_{over}(AT)}} = AT_{over} \frac{1}{1 - \frac{2yE_{peak}}{\sqrt{k}x_0}} \quad \text{Equation 2.44}$$

This may be expanded with the help of Eq. 2.37 and 2.42 to obtain an expression for DT independent of x_0 :

$$DT_{over} = -\frac{1}{\alpha} \frac{\ln\left(\frac{\alpha + \beta}{\alpha - \beta}\right)^{-\frac{\alpha}{2\beta}}}{1 - 2y\left(\frac{\alpha + \beta}{\alpha - \beta}\right)^{-\frac{\alpha}{2\beta}}} = \left(\frac{1}{\sqrt{k}}\right) \frac{\Upsilon}{2y^2 e^{\Upsilon} - y} \quad \text{Equation 2.45}$$

$$\Upsilon = \ln\left(\frac{\alpha + \beta}{\alpha - \beta}\right)^{-\frac{\alpha}{2\beta}}$$

And this may be expressed in terms of y by manipulating Υ :

$$\Upsilon = \ln\left(\frac{1 + \sqrt{1 - y^{-2}}}{1 - \sqrt{1 - y^{-2}}}\right)^{-\frac{1}{2\sqrt{1 - y^{-2}}}} \quad \text{Equation 2.46}$$

Alternatively one can write the overdamped velocity approximation as:

$$DT_{over} = \frac{1}{\sqrt{k}} f(\varphi) \quad \text{Equation 2.47}$$

, where $\varphi = 1 - y^{-2}$,

$$f(\varphi) = \frac{(1-\varphi)\Phi(\varphi)}{2 \cdot e^{\Phi(\varphi)} - \sqrt{1-\varphi}}, \text{ and } \Phi(\varphi) = -\frac{\ln(1+\sqrt{\varphi}) - \ln(1-\sqrt{\varphi})}{2\sqrt{\varphi}}. \quad \text{Equation 2.48}$$

E-wave Duration

The E-wave duration is the sum of acceleration time and deceleration time, and is therefore simply:

$$E_{dur} = AT_{over} + DT_{over} = \left(\frac{\Upsilon}{y\sqrt{k}} \right) \left(\frac{2ye^{\Upsilon} - 2}{2ye^{\Upsilon} - 1} \right) \quad \text{Equation 2.49}$$

2.5.4 A-wave Indexes

In previous work it was shown that the critically damped resonant forcing regime ($4k_A = c_A^2$, $k_A = \omega^2$) of Equation 2.4 provided an accurate fit to a wide variety of clinical A-wave contours (6). The mathematical expression for this solution to Equation 2.4 is:

$$v(t) = \frac{F_o}{2} \left(\frac{\sin(\omega_A t)}{\omega_A} - te^{-\omega_A t} \right) \quad \text{Equation 2.50}$$

where F_o is the amplitude of the forcing function and ω_A is the resonant critical damping frequency.

A-wave Duration

We may solve for the time at which A-wave velocity is zero by setting Eq 2.50 to 0:

$$\sin(\omega_A A_{dur}) = \omega_A A_{dur} e^{-\omega_A A_{dur}} \quad \text{Equation 2.51}$$

Numerical solution shows that the first non-zero solution is:

$$\omega_A A_{dur} = 2.9907 \quad \text{Equation 2.52}$$

Thus, we have determined an expression for the A-wave duration in terms of the resonant critical damping frequency:

$$A_{dur} = \frac{2.9907}{\omega_A} \quad \text{Equation 2.53}$$

A-wave Acceleration Time

To find the A-wave acceleration time, we must find the root of the derivative of Eq 2.50:

$$\frac{dv(t)}{dt} = 0 = \frac{F_o}{2} \left(\cos(\omega_A A_{AT}) - e^{-\omega_A A_{AT}} + A_{AT} \omega_A e^{-\omega_A A_{AT}} \right) \quad \text{Equation 2.54}$$

This yields:

$$\cos(\omega_A A_{AT}) = e^{-\omega_A A_{AT}} (1 + \omega_A A_{AT}) \quad \text{Equation 2.55}$$

Once again, numerical estimation must be applied to determine the first nonzero solution, and the A-wave acceleration time can therefore be written as:

$$A_{AT} = \frac{1.69897}{\omega_A} \quad \text{Equation 2.56}$$

It is curious to note that according to the model, the ratio of A-wave acceleration and deceleration time is therefore independent of resonant damping frequency and constant for all A-waves:

$$\frac{A_{AT}}{A_{dur}} = 0.568 \quad \text{Equation 2.57}$$

Furthermore, because the ratio in Eq 2.57 is above 0.5, we see that the PDF model predicts that A-wave contours are asymmetric, with greater acceleration time than deceleration time. This is what is observed clinically. E-waves on the other hand, as discussed above, have acceleration times that are less than or equal to E-wave deceleration time.

A-wave Deceleration Time

With the expressions for acceleration time and A-wave duration in place, determination of A-wave deceleration time becomes:

$$A_{DT} = A_{dur} - A_{AT} = \frac{2.99074}{\omega_A} - \frac{1.69897}{\omega_A} = \frac{1.29177}{\omega_A} \quad \text{Equation 2.58}$$

As with the acceleration time, the ratio of deceleration time to A-wave duration or A-wave acceleration time is therefore independent of resonant damping frequency:

$$\frac{A_{DT}}{A_{dur}} = 0.432 \quad \frac{A_{DT}}{A_{AT}} = 0.760 \quad \text{Equation 2.59}$$

A-wave Peak

Plugging the expression for A-wave acceleration time we find the expression for A-wave peak velocity in terms of forcing amplitude and frequency:

$$A_{peak} = 0.20045 F_o \cdot A_{AT} \quad \text{Equation 2.60}$$

A-wave Area

Finally we can determine the A-wave area by integrating Equation 2.50 between $t=0$ and A_{dur} :

$$\begin{aligned} VTI_A &= \frac{F_o}{2\omega_A} \int_0^{A_{dur}} \left(\sin(\omega_A t) - \omega_A t e^{-\omega_A t} \right) dt = \\ VTI_A &= \frac{F_o}{2\omega_A^2} \left[e^{-\omega_A t} (\omega_A t + 1) - \cos(\omega_A t) \right] \Big|_0^{A_{dur}} \quad \text{Equation 2.61} \\ VTI_A &= 0.59459 \frac{F_o}{\omega_A^2} \end{aligned}$$

2.6 CONCLUSION

The preceding analysis demonstrates the power of mathematical modeling and provides multiple insights into the determinants of diastolic function and E- and A-wave contour shape. These insights are applied throughout the following chapters to a number of important clinical problems.

2.7 REFERENCES

1. **Boskovski MT, Shmuylovich L, and Kovács SJ.** Transmitral flow velocity-contour variation after premature ventricular contractions: a novel test of the load-independent index of diastolic filling. *Ultrasound in medicine & biology* 34: 1901-1908, 2008.
2. **Chung CS, Karamanoglu M, and Kovács SJ.** Duration of diastole and its phases as a function of heart rate during supine bicycle exercise. *Am J Physiol Heart Circ Physiol* 287: H2003-2008, 2004.
3. **Chung CS and Kovács SJ.** Physical determinants of left ventricular isovolumic pressure decline: model prediction with in vivo validation. *Am J Physiol Heart Circ Physiol* 294: H1589-1596, 2008.
4. **Courtois M, Kovács SJ, and Ludbrook PA.** Transmitral pressure-flow velocity relation. Importance of regional pressure gradients in the left ventricle during diastole. *Circulation* 78: 661-671, 1988.
5. **Gottdiener JS, Bednarz J, Devereux R, Gardin J, Klein A, Manning WJ, Morehead A, Kitzman D, Oh J, Quinones M, Schiller NB, Stein JH, Weissman NJ, and Echocardiography ASo.** American Society of Echocardiography recommendations for use of echocardiography in clinical trials. *Journal of the American Society of Echocardiography : official publication of the American Society of Echocardiography* 17: 1086-1119, 2004.
6. **Hall AF, Aronovitz JA, Nudelman SP, and Kovács SJ.** Automated method for characterization of diastolic transmitral Doppler velocity contours: late atrial filling. *Ultrasound in medicine & biology* 20: 859-869, 1994.

7. **Hall AF and Kovács SJ.** Automated method for characterization of diastolic transmitral Doppler velocity contours: early rapid filling. *Ultrasound in medicine & biology* 20: 107-116, 1994.
8. **Matsubara H, Takaki M, Yasuhara S, Araki J, and Suga H.** Logistic time constant of isovolumic relaxation pressure-time curve in the canine left ventricle. Better alternative to exponential time constant. *Circulation* 92: 2318-2326, 1995.
9. **Press ST, WT Vetterling.** *Numerical Recipes: the art of scientific computing.* New York: Cambridge University Press, 1986.
10. **Raff GL and Glantz SA.** Volume loading slows left ventricular isovolumic relaxation rate. Evidence of load-dependent relaxation in the intact dog heart. *Circ Res* 48: 813-824, 1981.
11. **Weiss JL, Frederiksen JW, and Weisfeldt ML.** Hemodynamic determinants of the time-course of fall in canine left ventricular pressure. *J Clin Invest* 58: 751-760, 1976.
12. **Yang LB, H Goldberg.** *From cardiac catheterization to hemodynamic parameters.* Philadelphia: FA David Company, 1988.
13. **Zhang W, Chung CS, Riordan MM, Wu Y, Shmuylovich L, and Kovács SJ.** The kinematic filling efficiency index of the left ventricle: contrasting normal vs. diabetic physiology. *Ultrasound in medicine & biology* 33: 842-850, 2007.

CHAPTER 3

LEFT VENTRICULAR SUCTION AND EQUILIBRIUM VOLUME: VIEWPOINT AND CONTROVERSY

“Whatever role cardiac suction of venous blood may play in determining circulatory dynamics, no one can deny that mention of this term (diastolic suction) has proven a most effective method of raising blood pressure in several generations of cardiovascular physiologists”

–GA Brecher 1958

3.1 INTRODUCTION

Recent articles (49, 51) illustrate the challenge in providing a self consistent definition of ventricular suction. Conceptually different definitions are treated equivalently despite the fact that they lead to disparate conclusions. We discuss various definitions of suction, their physiological implications, and propose a unifying concept based on an in-vivo definition that requires a new perspective on the meaning of diastolic equilibrium volume.

3.2 ALTERNATE VIEW OF DIASTOLIC SUCTION

3.2.1 Diastolic Suction From the Ventricular Perspective

The experimental observation of diastolic suction or “*vis a fronte*” (a force acting from in front) dates back nearly 2 millennia to Galen, who concluded that the heart can fill itself (42). However, controversy regarding diastolic suction has persisted. Brecher noted (6) experimental evidence of diastolic suction by showing that excised beating animal hearts submerged in fluid draw fluid back into the ventricle after systole. Numerous investigators have described similar events (4, 11, 46-48, 51), but quantification of diastolic suction had to wait until the pioneering work of Louis Katz in 1930 (24).

Katz observed that in early diastole, turtle ventricular pressure (P_{LV}) decreases simultaneously with increasing ventricular volume (V_{LV}). This observation provided a conceptually simple and elegant quantitative definition of ventricular diastolic suction, namely, that diastolic suction is present when:

$$dP_{LV}/dV_{LV} < 0 \qquad \text{Equation 3.1}$$

This definition is a ‘relative’ index, as it depends only on intraventricular pressure and volume *changes*, and therefore is independent of ‘absolute’ ventricular pressures or volumes. That $dP_{LV}/dV_{LV} < 0$ after mitral valve opening is well established (11, 47) and depends on the endocardium mechanically recoiling faster than blood can fill the chamber. The observation of $dP_{LV}/dV_{LV} < 0$ in early filling has even been demonstrated in zebrafish heart development (14).

3.2.2 Diastolic Suction From the Atrio-Ventricular Perspective

The $dP_{LV}/dV_{LV} < 0$ definition depends only on ventricular measures and therefore represents a “ventricular perspective”. When going beyond the ‘ventricular perspective’, the source of filling must be handled with care, because the atrium rather than the atmosphere represents the source for filling, and flow requires generation of a pressure gradient. During early-rapid ventricular filling the atrium is a passive conduit and atrial pressure always decreases immediately after mitral valve opening. Thus LV pressure decreases below atrial pressure and inscribes the atrioventricular pressure gradient that accelerates flow into the chamber. Thus a consistent definition of diastolic suction that incorporates the atrium must recognize the role of atrioventricular gradients (2, 17, 25, 51). Since all ventricles generate atrioventricular gradients in early diastole it follows that all ventricles must operate as suction pumps in early diastole. An

atrioventricular pressure gradient is also observed during late atrial filling following atrial contraction, but the cause of that gradient is atrial activity, and the hemodynamic consequences differ from those observed in early filling. See section 3.5.1 for further discussion regarding the role of the atrium.

3.2.3. Diastolic Suction From the Equilibrium Volume Perspective

Early investigators speculated that elastic components must be responsible for ventricular chamber recoil in early diastole, and that these components, when relaxed or balanced by other forces defined an equilibrium chamber volume. Before the contributors to ventricular elastic properties, such as titin, collagen, and visceral pericardium (16, 19, 22, 37) were appreciated, Brecher defined ventricular elastic equilibrium volume intuitively as the volume where the ventricle's "transmural pressure is zero [$\Delta P=0$] and no stress is applied on its structural elements." (8). Based on this definition, Nikolic, Yellin and others used pioneering experimental techniques to measure equilibrium volume (30). They occluded the mitral valve at various filling volumes and determined the minimum pressure reached by canine ventricles in an open chest, open pericardial setting. The post-occlusion asymptotic pressures were the fully relaxed chamber pressures for the particular volume at which occlusion occurred. The lower the volume when the mitral valve is occluded, the stronger the suction force is, as shown by the more negative fully relaxed pressure. The asymptotic P-V points generated a nonlinear relationship that was fit logarithmically, and the x-intercept defined the volume at which ventricular pressure and atmospheric pressure was equal. The development of subatmospheric pressures was defined to be evidence of suction. Therefore by these criteria suction exists only when:

$$P_{LV} < P_{\text{atmospheric}}$$

Equation 3.2

The critical volume at which the ventricle generates atmospheric filling pressures experimentally defined V_0 (21, 30, 43), and ventricles with the end systolic volume (ESV) below V_0 would be expected to generate subatmospheric pressures (30). This value was taken to be the Brecher defined $[\Delta P=0]$ equilibrium volume and supported the traditional view that suction only occurs when ventricular $ESV < V_0$.

The experimental definition proposed by Nikolic is widely accepted (15, 35, 46), and other investigators have also measured equilibrium volume (27, 30, 43). In particular, the $P_{\text{atmospheric}}$ definition has been applied in the closed-chest, in-vivo setting, generating controversy regarding diastolic suction. Levine et al (27), defined diastolic suction by Equation 3.2 and concluded that intact closed-chest ventricles did not generate suction after bed-rest associated atrophy because their end-systolic volumes were higher than the equilibrium volume. Rankin et al (35), and others using closed-chest measurements (15, 46), concluded that *in-vivo* hearts, in general, do not exhibit diastolic suction. These conclusions are inconsistent with the work of Katz. Thus, while it is appropriate to consider the volume at which relaxed ventricular pressure is atmospheric in the open-chest setting, in the *in-vivo* closed-chest setting this choice may be less applicable.

3.3 RESOLUTION OF CURRENT INCONSISTENCIES

3.3.1 Difficulties with Suction Relative to the Atmosphere

There are some difficulties with the application of the $P_{\text{atmospheric}}$ definition (Equation 3.2) to diastolic suction. To put these in context, we note that the absolute pressure ($P_{LV} < P_{\text{atmospheric}}$) condition is based on a presumed zero wall-stress, where transmural forces are balanced because

the transmural pressure gradient vanishes (4, 6, 30, 46). However, in the closed-chest setting, $P_{LV} \equiv P_{\text{atmospheric}}$ does not imply zero transmural pressure gradient, since pericardial pressure is usually not atmospheric (18). Furthermore, recent work by Omens and Fung, and Jöbsis (22, 31) shows that even when fully relaxed, the LV wall has residual stress. This presence of residual stresses negates Brecher's implied connection between $\Delta P=0$ and a state where 'no stress is applied' on ventricular elastic elements. Thus, the requirement that transmural pressures vanish ($\Delta P=0$) need not be invoked in order to achieve equilibrium.

It should be noted that suction requires only that the receiving chamber drop its pressure below the source pressure, and does not require negative transmural pressures. Brecher recognized this, saying plainly that "it was thought that only the occurrence of negative intraventricular transmural pressure could be taken as evidence for the existence of ventricular diastolic vis a fronte. A brief consideration of the physical forces will show that this conclusion is fallacious"(7). Indeed, consider a compressed turkey baster submerged in any depth of water; the baster always returns to its equilibrium position even though the pressure never falls below atmospheric. The elastic recoil of the baster is analogous to the kinematics of the heart at low or high pressure environments, and the motion observed in excised hearts (3).

3.3.2 Defining Equilibrium Volume Kinematically

It is appropriate to define diastolic suction as Nikolic and others have, relative to an equilibrium volume, but this volume must reflect a mechanical equilibrium. Mechanical and kinematic equilibrium is achieved when all residual forces and stresses (including pressure in the

atrium, residual stress in the wall, etc.) are balanced, rather than only when the transmural forces or transmural pressure gradients are zero. This distinction is physiologically realistic, it is unambiguous, and its consequences (static vs. moving) are easily discernable. Thus we propose a physiologically intuitive, functional equilibrium: diastasis.

$$V_{eq} \equiv V_{diastasis} \qquad \text{Equation 3.3}$$

When ventricular filling commences, the chamber expands (recoils) faster than it can fill, and aspirates blood from the atrium by rapidly decreasing chamber pressure with simultaneous volume expansion $dP/dV < 0$ (14, 24). Wall recoil requires a net restoring force generated by the integrated action of loaded elastic elements seeking to return to their equilibrium dimension (3, 12, 16, 19, 22). As ventricular filling (Doppler E-wave) continues, the elastic elements approach their equilibrium dimension and elastic forces decrease. Once diastasis is reached, there is no wall motion, no atrioventricular pressure gradient, no flow, and no change in volume or pressure. Thus at diastasis, all forces and strains must be balanced (they are not zero), and there is no net force or wall-motion. Hence, diastasis must be the in-vivo equilibrium volume, and every ventricle approaches diastasis by suction initiated filling.

3.4 Physiological Implication of Diastasis as the Equilibrium Volume

3.4.1 Revised View of $V_{eq} < ESV$

In analogy to the Nikolic et al determinations of equilibrium volume and suction, Equation 3.3 implies the presence of diastolic suction only if the end-systolic volume (ESV) is below the diastasis volume (equilibrium volume). In general, ESV is always less than diastatic volume and thus, because $dP/dV < 0$ as the ventricle enters mechanical diastole, our definition of equilibrium

volume being the diastatic volume is consistent with Katz' definition of diastolic suction and is consistent with the conclusion that diastolic suction is present when $ESV < \text{equilibrium volume}$.

In our view Equation 3.3 is the functional *in-vivo* closed-chest equilibrium volume, because it defines an easily discernible mechanical equilibrium, resolves ('relative' vs. 'absolute') inconsistencies between various definitions, and does not require a zero transmural pressure gradient.

3.4.2 Connection to Chamber Elastic Components and Mechanism for Suction

Recent experiments indicate that proteins such as titin, acting as a bi-directional, linear spring, together with extracellular matrix and microtubules, etc. play roles in generating elastic recoil (16, 33). Deactivation (crossbridge uncoupling) unmasks stored elastic strain energy and leads to decreased elastic wall-stress and ventricular chamber pressure (by LaPlace's law). Abnormal crossbridge deactivation has been associated with (clinically defined) delayed relaxation (23), and has been shown to prevent the recoil (release of stored strain) of myofibrils (33).

Accepting diastasis as the equilibrium volume means that for all ventricles these elastic elements are displaced at end-systole, and it is the recoil of these elastic elements towards equilibrium that initiates filling with $dP/dV < 0$ and drives the ventricle towards diastasis. Elastic recoil moves the wall so the chamber expands faster than it can fill (14, 24), powers torsion (12, 39), and generates the negative atrio-ventricular pressure gradient that initiates the Doppler E-wave (11, 13). Thus ventricular suction, including the intraventricular pressure gradient (11) must always be present as a result of the recoil of displaced elastic elements returning toward equilibrium. The degree of recoil can be observed hemodynamically (53) and has been shown to

relate to tissue relaxation properties (see Chapter 6). Furthermore, suction and its link to recoil towards equilibrium as a diastolic mechanism is included in the current American Society of Echocardiography standards (29).

3.4.3 1st Degree A-V Block as a Test Case

If we assume V_0 is equilibrium, a serious kinematic inconsistency arises in the case of $V_0 < ESV$. In this setting tissue elastic elements would remain displaced above their equilibrium position at end-systole, and would be expected to exert force opposing chamber enlargement at the start of filling. However, as the mitral valve opens and filling commences, there is always a net expansive force responsible for recoil of the ventricular tissue. An atrial ‘push’ cannot account for this force, because it would cause LV pressure to increase immediately upon mitral-valve opening. Relaxation of the LV tissue by itself cannot account for this force either, because relaxation only relieves a compressive force, but does not generate motion. When elastic elements are displaced above equilibrium (Figure 3.1), it is not clear what provides the expansive force opposing the early-filling related compressive elastic forces. It is also unclear what mechanism prevents the ventricle from shrinking towards its equilibrium volume when diastasis is reached in the case of $V_0 < ESV$.

This inconsistency is avoided by rejecting V_0 , determined by $\Delta P = 0$ and accepting diastasis as the equilibrium volume. When ventricular volume exceeds diastatic volume, the chamber does oppose this volumetric enlargement with a net compressive force. This force can be appreciated in the presence of 1st degree AV block, for example, where one observes late diastolic mitral regurgitation (1), and a decline in LVP towards equilibrium, despite $\Delta P \neq 0$. (Figure 3.2) By accepting diastasis as the in-vivo equilibrium, late diastolic mitral regurgitation

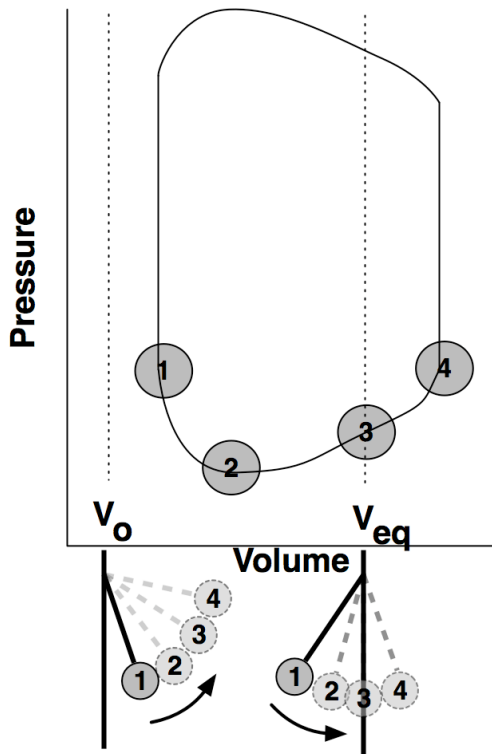


Figure 3.1 PV-loop and the kinematics/energetics of filling. Schematic Pressure-Volume loop indicating (1) end systolic volume at mitral valve opening (2) minimum LV pressure, (3) diastasis, and (4) end-diastolic volume. Vertical dashed lines denote alternative locations of equilibrium volume, (V_o defined by $\Delta P=0$), (V_{eq} defined as volume at diastasis). If V_o is the equilibrium volume and $V_o < ESV$, then elastic elements are displaced further from equilibrium as filling continues. Idealized via an oscillator (pendulum, bottom left), the displacement of the pendulum away from vertical equilibrium represents the displacement of lumped ventricular elastic elements from ventricular equilibrium volume. If diastasis is the equilibrium volume, then ESV is always less than V_{eq} and the displaced elastic elements are unmasked by the relaxation process and passively return toward equilibrium as early filling progresses. (Idealized via a pendulum, bottom right). Atrial filling displaces elastic elements beyond equilibrium, and this stored elastic energy powers late diastolic mitral regurgitation if 1st degree AV block is present. Numeric labels of pendulum position correspond to PV loop labeling.

is the predictable result of displaced elastic elements that recoil toward diastasis and return the ventricle toward its equilibrium volume. Because, we never observe a ventricle recoiling back from diastasis volume towards V_o , but do observe ventricles recoiling toward diastasis in 1st degree AV block, we conclude that the $V_o < ESV$ definition for equilibrium is incompatible with the physiology.

3.5 COMMON CRITICISMS OF EQUILIBRUM VOLUME AT DIASTASIS

3.5.1 The Role of the Atrium

Ventricular pressure falls as the chamber relaxes isovolumically, and this finding, along with the mitral valve occlusion studies by Nikolic (30) and others has been used to support the claim that pressure drops in early filling without substantial recoil or suction. Investigators

supporting this claim reason that atrial pressure is elevated from previous systolic events, and because pressure drops below atrial, it is the atrium that is the primary driver of early filling.

This view is held by many (32) and theoretically is plausible, but it is not consistent with physiological findings.

Is the Atrium Required For Suction?

Experiments have clearly demonstrated that the atrium is not necessary for filling to

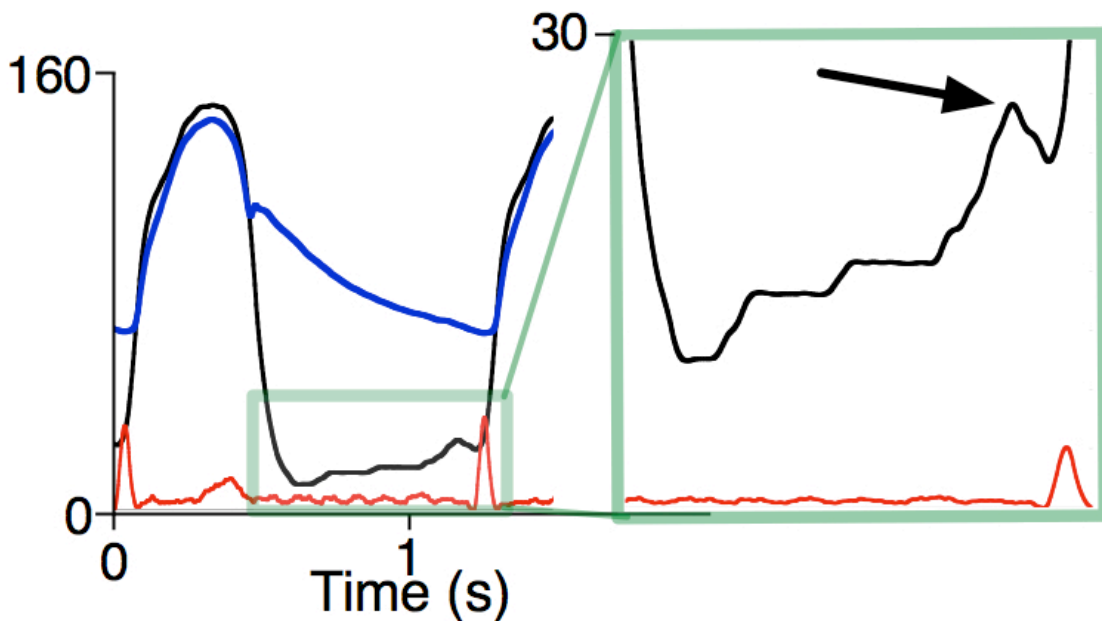


Figure 3.2 Simultaneous left ventricular pressure, aortic pressure, and ECG for one cardiac cycle in a subject with first degree AV block. Notice the decay in pressure following the atrial contraction related pressure rise. Ventricular contraction increases pressure dramatically following the pressure late diastolic pressure decline. A similar pressure decline does not occur at diastasis. See text for details.

occur. Even when the atrium has been removed in its entirety (4) the LV fills by elastic recoil and diastolic suction. Bloom showed this beautifully by placing an excised rat heart in saline and observing it as it swam around, propelling itself during systole and drawing in fluid during diastole(4). Thus the energy source for early filling and diastolic suction can come completely

from ventricular activity without any atrial influence. While these results are not disputed, some investigators claim that in these isolated ventricle experiments the end-systolic volume is much lower than the volume encountered in-vivo, and therefore while the experiments show that the ventricle CAN suck, they claim that in normal steady state physiology, suction plays no role, and instead atrial pressure pushes blood in.

Atrial Push and the Doppler A-wave

To see the difference between an atrial push driving filling and a ventricular suction driving filling, one needs to look no further than the Doppler A-wave. After all, we see an atrioventricular gradient ($LAP > LVP$) generated exclusively from atrial systolic activity during the Doppler A-wave. In other words, atrial contraction is the cause of the pressure gradient that drives transmitral flow during late atrial filling. The ventricle expands slower than it can fill, and therefore BOTH ventricular pressure and volume increases. The rise in atrial pressure also generates transient retrograde flow into the pulmonary veins. These are key properties of an atrial push that must be accounted for in any scenario where the atrium is purported to be the driving force behind filling.

Importantly, restoring forces cannot be ignored during atrial (non-suction) filling. As we discuss above, when the R-wave is delayed, as in 1st degree AV block, late diastolic mitral regurgitation ensues and ventricular pressure falls back towards diastatic pressure. This pressure decline clearly demonstrates that passive chamber elastic elements were displaced above their equilibrium dimension during the A-wave, and because of delayed systole, take the opportunity to return toward equilibrium. This is a critical point, because it emphasizes the fact that in the

absence of suction, an atrial push must work against ventricular elastic elements stretched away from equilibrium.

Can Atrial “Push” drive the Doppler E-wave?

While it is possible for high left atrial pressure to contribute to early filling,, physiological observations rule out an atrial push as the sole E-wave generator. First, the observation that $dP/dV < 0$ at the start of all E-waves demonstrates that the LV expands faster than it can fill, which is not what one sees during the atrial push of the Doppler A-wave. Second, the atrium is a conduit in early filling (5), as the LV aspirates blood from the lungs (Doppler pulmonary vein D-wave) while atrial pressure drops. Thus ventricular suction draws in blood through the atrium, and we do not see retrograde pulmonary vein flow in early filling.

3.5.2 Can Sarcomere Deactivation Alone Drive Suction?

The kinematic approach that we apply assumes that elastic elements are loaded and unloaded through mechanical tissue displacements. From that perspective, it is clear that the filling process must either load or unload ventricular elastic elements. Such a claim would be invalidated if it were possible for the ventricle to, as Yellin and Nikolic, “completely relax without relengthening” (41). However recent studies show strong coupling between cross-bridge deactivation/relaxation and elastic recoil/relengthening. Deactivation independently accounts for only 3-5% of maximal force (i.e pressure) decline after calcium activation, while the majority of force (pressure) decline occurs with sarcomere relengthening (45). This is in precise agreement with chamber mechanics, where, during and after calcium sequestration (20), elastic recoil (motion) is observed, manifesting as torsion during isovolumic relaxation (38). This conceptual

foundation motivated a model that accurately predicts isovolumic pressure decline by unifying recoil and deactivation (10).

Indeed, it is the dynamic balance between stored elastic energy and cross-bridge deactivation that determines wall-stress and resulting decreasing chamber pressure (10, 20, 44). Deactivation alone cannot drop pressures fully. Only motion, i.e. the expansion of the ventricle faster than it can fill can generate the atrioventricular pressure gradient to initiate suction. Chamber expansion would not occur if relaxation (cross-bridge uncoupling) were not coupled with recoil and release of stored elastic energy.

3.5.3 Diastasis Varies With Load, Depends on HR, and Is Not Always a Zero Flow State

Diastatic volume varies in response to load variation, and the diastatic interval is lost in the setting high heart rate(9). Several investigators note this intrinsic variability of diastasis (41) and argue that diastasis volume can therefore not be the equilibrium volume. In contrast, V_0 defined by zero transmural pressure gradient is a constant that shows no beat by beat variability.

Beat By Beat Variation of Diastatic Volume

Variation in diastatic pressure and volume is due to load, atrial properties, and ventricular properties, but that does not negate the functional role of diastasis as the equilibrium volume. Ventricular and atrial tone, contractility, and load balance at diastasis, and are dynamic physiologic variables. Thus, equilibrium volume must also be dynamic. In fact, quantifying diastatic pressure and volume variation provides fundamental chamber properties in the form of passive stiffness(52).

Cases Where Diastasis is Not Observed

The loss of diastatic interval when heart rate is sufficiently elevated makes the determination of diastatic volume difficult, but does not invalidate diastasis as the equilibrium volume. At higher heart rates the ventricle may pass through equilibrium without stopping before atrial filling, but the key point is that elastic elements returning toward equilibrium are driving early filling and suction. After all, an oscillator that is kicked with a driving force during its recoil from maximum displacement to equilibrium is still driven initially toward equilibrium by stored elastic energy.

In some setting ventricles may possess mid-diastolic flow, often seen in the transmitral profile as an L-wave. When L-waves are present, or in other cases where LV volume continuously changes, $V_{\text{diastasis}}$ is not achieved. However, these cases are exceptions to the rule, and most ventricles possess diastasis. Indeed intracavity flow exists during early diastole (34), but by diastasis there is no net volume change and intracavity swirling diminishes to minimal levels(Figure 2E, (40)). As we argue with the case of elevated heart rate, however, a ventricle that passes through diastasis still has filling driven by elastic elements returning toward equilibrium.

3.5.4 Suction and its (Patho)physiologic Importance

Yellin et al have suggested that a definition of diastolic suction based on $dP/dV < 0$ has little “utilitarian value”, because it means that every ventricle initiates early rapid filling by being a suction pump (50). Yellin et al argues that the more traditional V_o approach has value, on the hand, precisely because it differentiates between ventricles that possess suction (those with $ESV < V_o$), and ventricles that don't (those with $ESV > V_o$).

However, the “utilitarian value” of suction is enhanced by the recognition of its general applicability and quantification. Indeed its physiological value is enhanced when one assesses its effectiveness on a continuum. For example, work by Yotti and a related editorial by Little suggests that diagnosing and quantifying suction via pressure gradients is important in understanding pathophysiology (28, 51). Dilated ventricles are poor suction pumps, aspirating a relatively small volume in early filling and compensating with atrial contraction and a resting tachycardia to maintain cardiac output. In this case restoring forces may be weak and early filling (suction) may be modest or poor, but diastasis remains the volume at which forces are balanced and equilibrium is achieved. Healthy ventricles on the other hand store (and release) greater amounts of elastic energy during systole (and diastole) and are therefore more effective suction pumps. Thus the importance of suction is revealed through mechanistic understanding of how it is modulated, how it determines the contour of the E-wave (25, 26) and how a lack of suction affects patients clinically and physiologically.

3.6 CONCLUSIONS

Prior conceptual and experimental results regarding diastolic suction and the equilibrium volume of the LV have been interpreted inconsistently. To resolve the inconsistencies generated by different (‘absolute’ vs. ‘relative’) definitions and different (closed-chest vs. open chest) preparations, we advocate $dP_{LV}/dV_{LV} < 0$ as the necessary and sufficient condition for initiation of diastolic suction. This definition (ventricular recoil) follows not only from physiologic constraints but from kinematic considerations (the release of stored elastic strain). This definition naturally leads to the kinematics-based definition that the LV volume at diastasis must be the

functional, in-vivo equilibrium volume and diastolic suction is the primary mechanism by which the ventricle attains this equilibrium.

This conclusion is just one of several insights gained by a kinematic perspective of diastole. Indeed a kinematic perspective consolidates a range of observations by providing consistency with and between experiments, from the myofiber to the ventricle, and from ventricular development to disease(10, 36, 41, 44, 51, 52).

3.7 REFERENCES

1. Appleton CP, Basnight MA, and Gonzalez MS. Diastolic mitral regurgitation with atrioventricular conduction abnormalities: relation of mitral flow velocity to transmitral pressure gradients in conscious dogs. *Journal of the American College of Cardiology* 18: 843-849, 1991.
2. Bauman L, Chung CS, Karamanoglu M, and Kovács SJ. The peak atrioventricular pressure gradient to transmitral flow relation: kinematic model prediction with in vivo validation. *Journal of the American Society of Echocardiography : official publication of the American Society of Echocardiography* 17: 839-844, 2004.
3. BLOOM WL. Diastolic filling of the beating excised heart. *Am J Physiol* 187: 143-144, 1956.
4. BLOOM WL and FERRIS EB. Negative ventricular diastolic pressure in beating heart studied in vitro and in vivo. *Proc Soc Exp Biol Med* 93: 451-454, 1956.
5. Bowman AW and Kovács SJ. Left atrial conduit volume is generated by deviation from the constant-volume state of the left heart: a combined MRI-echocardiographic study. *Am J Physiol Heart Circ Physiol* 286: H2416-2424, 2004.
6. BRECHER GA. Critical review of recent work on ventricular diastolic suction. *Circ Res* 6: 554-566, 1958.
7. BRECHER GA and KISSEN AT. Ventricular diastolic suction at normal arterial pressures. *Circ Res* 6: 100-106, 1958.
8. BRECHER GA, Kolder H, and Horres AD. Ventricular volume of nonbeating excised dog hearts in the state of elastic equilibrium. *Circ Res* 19: 1080-1085, 1966.

9. Chung CS, Karamanoglu M, and Kovács SJ. Duration of diastole and its phases as a function of heart rate during supine bicycle exercise. *Am J Physiol Heart Circ Physiol* 287: H2003-2008, 2004.
10. Chung CS and Kovács SJ. Physical determinants of left ventricular isovolumic pressure decline: model prediction with in vivo validation. *Am J Physiol Heart Circ Physiol* 294: H1589-1596, 2008.
11. Courtois M, Kovács SJ, and Ludbrook PA. Transmitral pressure-flow velocity relation. Importance of regional pressure gradients in the left ventricle during diastole. *Circulation* 78: 661-671, 1988.
12. Esch BT and Warburton DER. Left ventricular torsion and recoil: implications for exercise performance and cardiovascular disease. *J Appl Physiol* 106: 362-369, 2009.
13. Flewitt JA, Hobson TN, Wang J, Johnston CR, Shrive NG, Belenkie I, Parker KH, and Tyberg JV. Wave intensity analysis of left ventricular filling: application of windkessel theory. *Am J Physiol Heart Circ Physiol* 292: H2817-2823, 2007.
14. Forouhar AS, Liebling M, Hickerson A, Nasiraei-Moghaddam A, Tsai H-J, Hove JR, Fraser SE, Dickinson ME, and Gharib M. The embryonic vertebrate heart tube is a dynamic suction pump. *Science* 312: 751-753, 2006.
15. Gilbert JC and Glantz SA. Determinants of left ventricular filling and of the diastolic pressure-volume relation. *Circ Res* 64: 827-852, 1989.
16. Granzier HL and Irving TC. Passive tension in cardiac muscle: contribution of collagen, titin, microtubules, and intermediate filaments. *Biophys J* 68: 1027-1044, 1995.

17. Greenberg NL, Vandervoort PM, Firstenberg MS, Garcia MJ, and Thomas JD. Estimation of diastolic intraventricular pressure gradients by Doppler M-mode echocardiography. *Am J Physiol Heart Circ Physiol* 280: H2507-2515, 2001.
18. Guyton A. *Textbook of medical physiology*. Philadelphia: W B Saunders Company, 1983.
19. Helmes M, Trombitás K, and Granzier H. Titin develops restoring force in rat cardiac myocytes. *Circ Res* 79: 619-626, 1996.
20. Hinken AC and Solaro RJ. A dominant role of cardiac molecular motors in the intrinsic regulation of ventricular ejection and relaxation. *Physiology (Bethesda, Md)* 22: 73-80, 2007.
21. Ingels NB, Daughters GT, Nikolic SD, DeAnda A, Moon MR, Bolger AF, Komeda M, Derby GC, Yellin EL, and Miller DC. Left atrial pressure-clamp servomechanism demonstrates LV suction in canine hearts with normal mitral valves. *Am J Physiol* 267: H354-362, 1994.
22. Jöbsis PD, Ashikaga H, Wen H, Rothstein EC, Horvath KA, McVeigh ER, and Balaban RS. The visceral pericardium: macromolecular structure and contribution to passive mechanical properties of the left ventricle. *Am J Physiol Heart Circ Physiol* 293: H3379-3387, 2007.
23. Kass DA. Assessment of diastolic dysfunction. Invasive modalities. *Cardiology clinics* 18: 571-586, 2000.
24. Katz L. The role played by the ventricular relaxation process in filling the ventricle. *American Journal of Physiology*, 1930.
25. Kovács SJ, Barzilai B, and Pérez JE. Evaluation of diastolic function with Doppler echocardiography: the PDF formalism. *Am J Physiol* 252: H178-187, 1987.
26. Kovács SJ, Meisner JS, and Yellin EL. Modeling of diastole. *Cardiology clinics* 18: 459-487, 2000.

27. Levine BD, Zuckerman JH, and Pawelczyk JA. Cardiac atrophy after bed-rest deconditioning: a nonneural mechanism for orthostatic intolerance. *Circulation* 96: 517-525, 1997.
28. Little WC. Diastolic dysfunction beyond distensibility: adverse effects of ventricular dilatation. *Circulation* 112: 2888-2890, 2005.
29. Nagueh SF, Appleton CP, Gillebert TC, Marino PN, Oh JK, Smiseth OA, Waggoner AD, Flachskampf FA, Pellikka PA, and Evangelista A. Recommendations for the evaluation of left ventricular diastolic function by echocardiography. *Journal of the American Society of Echocardiography : official publication of the American Society of Echocardiography* 22: 107-133, 2009.
30. Nikolić S, Yellin EL, Tamura K, Vetter H, Tamura T, Meisner JS, and Frater RW. Passive properties of canine left ventricle: diastolic stiffness and restoring forces. *Circ Res* 62: 1210-1222, 1988.
31. Omens JH and Fung YC. Residual strain in rat left ventricle. *Circ Res* 66: 37-45, 1990.
32. Opdahl A, Remme EW, Helle-Valle T, Lyseggen E, Vartdal T, Pettersen E, Edvardsen T, and Smiseth OA. Determinants of left ventricular early-diastolic lengthening velocity: independent contributions from left ventricular relaxation, restoring forces, and lengthening load. *Circulation* 119: 2578-2586, 2009.
33. Opitz CA, Kulke M, Leake MC, Neagoe C, Hinssen H, Hajjar RJ, and Linke WA. Damped elastic recoil of the titin spring in myofibrils of human myocardium. *Proc Natl Acad Sci USA* 100: 12688-12693, 2003.

34. Peskin C and McQueen D. A three-dimensional computational method for blood flow in the heart I. Immersed elastic fibers in a viscous incompressible fluid. *Journal of Computational Physics*, 1989.
35. Rankin JS, Arentzen CE, McHale PA, Ling D, and Anderson RW. Viscoelastic properties of the diastolic left ventricle in the conscious dog. *Circ Res* 41: 37-45, 1977.
36. Rich MW, Stitzel NO, and Kovács SJ. Prognostic value of diastolic filling parameters derived using a novel image processing technique in patients \geq 70 years of age with congestive heart failure. *Am J Cardiol* 84: 82-86, 1999.
37. Robinson TF, Factor SM, and Sonnenblick EH. The heart as a suction pump. *Sci Am* 254: 84-91, 1986.
38. Rosen BD, Gerber BL, Edvardsen T, Castillo E, Amado LC, Nasir K, Kraitichman DL, Osman NF, Bluemke DA, and Lima JAC. Late systolic onset of regional LV relaxation demonstrated in three-dimensional space by MRI tissue tagging. *Am J Physiol Heart Circ Physiol* 287: H1740-1746, 2004.
39. Rothfeld JM, LeWinter MM, and Tischler MD. Left ventricular systolic torsion and early diastolic filling by echocardiography in normal humans. *Am J Cardiol* 81: 1465-1469, 1998.
40. Sengupta PP, Khandheria BK, Korinek J, Jahangir A, Yoshifuku S, Milosevic I, and Belohlavek M. Left ventricular isovolumic flow sequence during sinus and paced rhythms: new insights from use of high-resolution Doppler and ultrasonic digital particle imaging velocimetry. *J Am Coll Cardiol* 49: 899-908, 2007.
41. Shmuylovich L, Chung CS, Kovács SJ, Yellin EL, and Nikolic SD. Left ventricular volume during diastasis IS/IS NOT the physiologic in-vivo equilibrium volume and IS/IS NOT related to diastolic suction. *J Appl Physiol*, 2009.

42. Siegel R. *Galen's System of Physiology and Medicine*. Switzerland: Karger, 1968.
43. Solomon SB, Nikolic SD, Glantz SA, and Yellin EL. Left ventricular diastolic function of remodeled myocardium in dogs with pacing-induced heart failure. *Am J Physiol* 274: H945-954, 1998.
44. Stehle R, Solzin J, Iorga B, and Poggesi C. Insights into the kinetics of Ca²⁺-regulated contraction and relaxation from myofibril studies. *Pflugers Arch* 458: 337-357, 2009.
45. Stoddard MF, Pearson AC, Kern MJ, Ratcliff J, Mrosek DG, and Labovitz AJ. Influence of alteration in preload on the pattern of left ventricular diastolic filling as assessed by Doppler echocardiography in humans. *Circulation* 79: 1226-1236, 1989.
46. Suga H, Goto Y, Igarashi Y, Yamada O, Nozawa T, and Yasumura Y. Ventricular suction under zero source pressure for filling. *Am J Physiol* 251: H47-55, 1986.
47. Thomas J and Weyman A. Echocardiographic Doppler evaluation of left ventricular diastolic function. Physics and physiology. *Circulation* 84: 977-990, 1991.
48. Wang Z, Jalali F, Sun Y-H, Wang J-J, Parker KH, and Tyberg JV. Assessment of left ventricular diastolic suction in dogs using wave-intensity analysis. *Am J Physiol Heart Circ Physiol* 288: H1641-1651, 2005.
49. Weyman AE. The year in echocardiography. *Journal of the American College of Cardiology* 49: 1212-1219, 2007.
50. Yellin EL and Meisner JS. Physiology of diastolic function and transmitral pressure-flow relations. *Cardiology clinics* 18: 411-433, vii, 2000.
51. Yotti R, Bermejo J, Antoranz JC, Desco MM, Cortina C, Rojo-Alvarez JL, Allué C, Martín L, Moreno M, Serrano JA, Muñoz R, and García-Fernández MA. A noninvasive method

for assessing impaired diastolic suction in patients with dilated cardiomyopathy. *Circulation* 112: 2921-2929, 2005.

52. Zhang W and Kovacs S. The diastatic pressure-volume relationship is not the same as the end-diastolic pressure- *AJP-Heart and Circulatory Physiology*, 2008.

53. Zhang W, Shmuylovich L, and Kovács SJ. The E-wave delayed relaxation pattern to LV pressure contour relation: model-based prediction with in vivo validation. *Ultrasound in medicine & biology* 36: 497-511, 2010.

CHAPTER 4.

MEANINGFUL DIASTOLIC FUNCTION ASSESSMENT AND COMPARISON
IS FACILITATED BY INCORPORATION OF CHAMBER PROPERTIES AT
DIASTASIS, RATHER THAN AT END-DIASTOLE.

4.1 INTRODUCTION

The growing ‘epidemic’ of heart failure with normal ejection fraction (2, 15) has cast a spotlight on diastolic function and its determinants. In particular, left ventricular chamber stiffness is one of the parameters by which diastolic function is conventionally assessed. While noninvasive estimates of chamber stiffness exist (11, 13), the gold standard remains analysis of invasively derived pressure-volume data.

One of the most important methods for characterizing passive chamber stiffness has been the end-diastolic pressure volume relation (EDPVR), defined by the locus of points inscribed by end-diastolic pressures and volumes at varying loads. The resulting EDPVR is an exponential, power law, or linear fit to those points over variable regimes (6). The slope, dP/dV , of the EDPVR has been interpreted as passive chamber stiffness. Recently a simplified ‘single-beat’ approach has been described where a single end-diastolic pressure and volume measurement is used to determine a generic, two parameter EDPVR of the form $P=\alpha V^{\beta}$ (7, 8).

Considering the EDPVR in the setting of chronic atrial fibrillation (AF) raises a concern, however. Due to the lack of coordinated atrial contraction, end-diastole in (rate controlled) AF is the hemodynamic equivalent of diastasis, not end-diastole, in normal sinus rhythm (NSR). Thus comparing EDPVR between AF and NSR is equivalent to comparing chamber stiffness at diastasis to chamber stiffness at (post Doppler A-wave) end-diastole, and this may obscure actual stiffness differences.

We hypothesize that measuring chamber stiffness at end-diastole, either through a single beat or multiple beat approach, confounds stiffness comparison between chronic AF and NSR groups. To test this hypothesis we measure and compare both the EDPVR and the diastatic pressure volume relation (D-PVR)(19) in AF and NSR groups, using both the single-beat and the traditional load-varying multiple-beat approach.

4.2 METHODS

4.2.1 Subject Selection and Data Acquisition

Thirty-two subjects were selected from the existing Cardiovascular Biophysics Laboratory database (See Chapter 2). All subjects were referred by their cardiologists for catheterization to rule out the presence of suspected coronary artery disease, and provided informed consent prior to the procedure in accordance with a protocol approved by the Washington University Human Research Protection Office (HRPO).

Twenty-four subjects were in NSR, while 8 subjects had established history of chronic AF and were in AF during data acquisition. Average duration of AF was 6.4 ± 4.4 years. Selection criteria for the NSR group were: no active ischemia, normal valvular function, normal ejection fraction (LVEF $\geq 50\%$), no history of myocardial infarction, peripheral vascular disease, or bundle branch block, and clearly visible diastatic intervals following transmitral Doppler E-waves. Selection criteria for the AF group were similar, with the exception of four AF subjects with LVEF $< 50\%$. No subjects were in heart failure, and all subjects were normotensive at the time of data acquisition. See Table 4.1 for further clinical descriptors. See Chapter 2 for a detailed description of the method by which simultaneous echocardiographic and high-fidelity pressure data is acquired.

Table 4.1. Clinical descriptors for NSR and AF groups.

Clinical Descriptors	NSR Group	AF Group	Significance
<i>n</i>	24	8	N.A.
<i>Age (y)</i>	53 ± 12	62 ± 10	<0.05
<i>Gender (male/female)</i>	14/10	7/1	N.A.
<i>Heart Rate (bpm)</i>	67 ± 7	76 ± 11	<0.02
<i>Ejection Fraction (LVEF) (%) *</i>	71 ± 21	51 ± 18	<0.00003

Data are presented as mean ± standard deviation. LVEF=left ventricular ejection fraction. NSR, normal sinus rhythm. AF, atrial fibrillation. N.S. not significant. * LVEF determined by calibrated ventriculography.

4.2.2 Load Variation

As previously described (19), physiological load variation was achieved in all 32 subjects through respiratory variation. In 14 out of 24 NSR subjects, additional physiologic load variation was achieved during the recovery phase of the Valsalva maneuver. In the remaining 10 NSR subjects, additional load variation was observed in the beats following either catheter generated or isolated spontaneous premature ventricular contractions (PVC).

4.2.3 Data Analysis

After ventriculography-based calibration of volume, LV pressures and volumes at both diastasis (P_D , V_D) and end diastole (P_{ED} , V_{ED}) were measured for 8-12 cardiac cycles with a custom LabView interface (National Instruments, Austin, TX). For AF subjects, only cardiac cycles with R-R intervals generating relatively constant diastatic pressures and volumes following early filling were included. See Figure 4.1 for representative simultaneous catheterization-echocardiography data in NSR and AF subjects. Timing of end-diastole was identified by ECG R-wave peaks. Diastasis was identified by ECG P-wave peaks for NSR subjects, and was measured at end-diastole for AF subjects.

The measured (P_D , V_D) and (P_{ED} , V_{ED}) values were used to construct pressure-volume relations both by single-beat and multiple beat approaches. P_{ED} and V_{ED} defined the EDPVR, while P_D and V_D values defined the diastatic pressure volume relation (D-PVR).

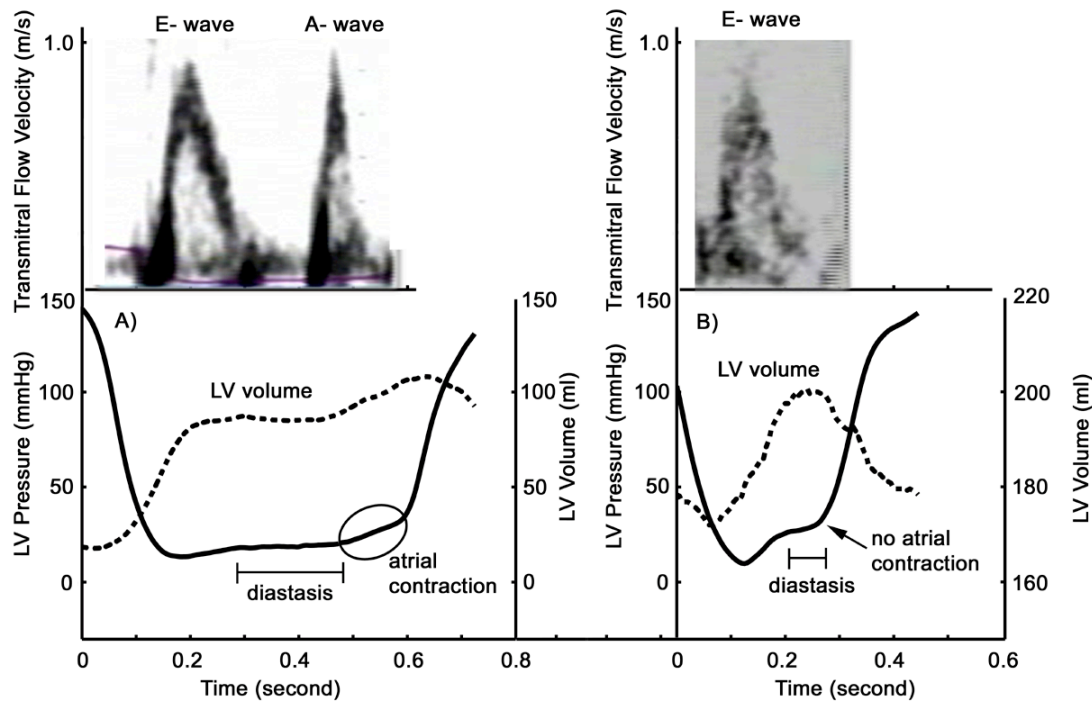


Figure 4.1. Comparing simultaneous pressure-volume and echocardiographic data between normal sinus rhythm (left) and chronic atrial fibrillation (right) subjects. Notice the absence of an A-wave in the atrial fibrillation subject.

Single Beat Estimates of Stiffness

The single-beat method for pressure volume relation estimation has been previously detailed(7, 8). By applying empirical correlations that normalize for heart size, parameters α and β in the pressure volume relation $P=\alpha V^\beta$ may be calculated from a single measured pressure and volume (P_m , V_m). First $V_0=V_m \cdot (0.6-0.0006 \cdot P_m)$ and $P^*=(P_m/27.278)^{(-1/2.76)}$ are calculated. If $P_m < 22\text{mmHg}$, one determines $V_{30}=V_0+P^* \cdot (V_m-V_0)$, and then calculates $\beta=\log(P_m/30)/\log(V_m/V_{30})$ and

$\alpha=30/V_{30}^{\beta}$. If $P_m > 22\text{mmHg}$, one determines $V_{15}=V_0+0.8\cdot P^*\cdot(V_m-V_0)$, and then calculates $\beta=\log(P_m/15)/\log(V_m/V_{15})$ and $\alpha=P_m/V_m^{\beta}$. For AF subjects steady-state average P_D, V_D values (equivalent to P_{ED}, V_{ED}) were used to calculate single-beat estimated D-PVR parameters (α_{AF}, β_{AF}). For NSR subjects both average (P_{ED}, V_{ED}) and (P_D, V_D) values were used to find estimated EDPVR ($\alpha_{NSR-ED}, \beta_{NSR-ED}$) and DPVR ($\alpha_{NSR-D}, \beta_{NSR-D}$) parameters.

Multiple Beat Estimates of Stiffness

The V_{ED}, P_{ED} and V_D, P_D values were measured at physiologically varying load states, and therefore could be used, as was previously described(19), to construct an EDPVR, and D-PVR respectively. Thus for each NSR subject the EDPVR was generated by finding the best fit linear regression defined by the 8-12 measured (V_{ED}, P_{ED}) locus of points in the P-V plane (see Figure 4.2). Previous work (19) showed that linear or exponential fits to the points yielded similar goodness of fit measurements (by mean square error), and therefore a linear function was used for simplicity. The D-PVR was similarly generated using (V_D, P_D), not (V_{ED}, P_{ED}) coordinates. For the AF subjects diastatic and end- diastolic values were identical, and therefore only a D-PVR was generated.

For NSR subjects chamber stiffness was estimated both from the EDPVR and D-PVR slopes ($dP/dV_{NSR-ED}, dP/dV_{NSR-D}$ respectively). Similarly, for AF subjects chamber stiffness was estimated from the DVPR slope (dP/dV_{AF}).

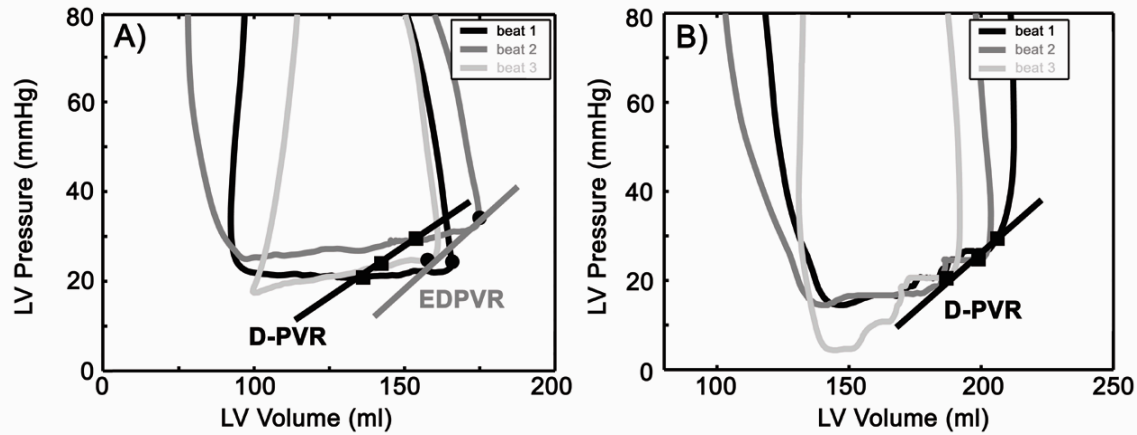


Figure 4.2. An example of diastatic pressure-volume relationship (D-PVR) in NSR (panel A) and AF (panel B). Black line, D-PVR approximated by a straight line. Gray line, end-diastolic pressure-volume relationship (EDPVR) in NSR, approximated by a straight line. Note that the D-PVR and EDPVR in AF is defined by the same data in the P-V plane due to the lack of coordinated atrial contraction. The average diastatic and end-diastolic pressures and volumes define a single point which is used to calculate the single beat estimated chamber stiffness parameters. See text for details.

Echocardiographic Analysis

Approximately 5 (continuous) Doppler transmitral flow contours per subject were selected and analyzed by conventional triangle shape approximations (see Chapter 2), yielding peak E-wave velocity (E_{peak}), E-wave deceleration time (DT), and peak A-wave velocity (A_{peak}).

In addition, E- and A-wave contours were fit via the parameterized diastolic filling formalism (see Chapter 2) to yield PDF c , k , and x_0 parameters. Thus in addition to conventional analysis, all E-waves for the AF and NSR groups were analyzed kinematically to yield noninvasive stiffness estimates (k_{AF} , k_{NSR} respectively).

4.2.4 Statistical Analysis

For each subject parameters were averaged for the measured beats. Within the NSR group P_D , V_D , $dP/dV_{\text{NSR-D}}$ and $b_{\text{NSR-D}}$ were compared to P_{ED} , V_{ED} , $dP/dV_{\text{NSR-ED}}$, and $b_{\text{NSR-ED}}$ by

paired *t*-test. Comparisons of dP/dV , b , DT , k , and other relevant parameters between NSR and AF groups were carried out by Student's *t*-test using MS-Excel (Microsoft, Redmond, WA).

4.3 RESULTS

4.3.1 Volume and Pressure Comparison

As expected, NSR diastatic volumes and pressures were significantly smaller than corresponding NSR end-diastolic pressures and volumes (V_D vs V_{ED} : 122 ± 31 ml vs 160 ± 32 ml $p < 10^{-7}$; P_D : 13 ± 3 mmHg vs 19 ± 5 mmHg $p < 10^{-10}$). While diastatic (and therefore end-diastolic) pressures in the AF group were slightly smaller than end-diastolic pressures and volumes in the NSR group, pressures and volumes measured at diastasis in AF were similar to end-diastolic pressures and volumes in the NSR group (AF V_D vs. NSR V_{ED} : 168 ± 43 ml vs. 160 ± 32 ml, $p=0.54$; AF P_D vs. NSR P_{ED} : 18 ± 6 mmHg vs. 19 ± 5 mmHg, $p=0.75$). See Table 2 for additional hemodynamic details.

4.3.2 Single Beat Parameters Comparison

Four of the NSR subjects and 1 of the AF subjects had average $P_{ED} > 22$ mmHg, and therefore for these subject the V_{15} method was applied in order to calculate single beat estimated EDPVR (for NSR subjects) and DVPR α and β parameters. The V_{30} method was applied for the remaining subjects. In the NSR group β_{ED-NSR} was significantly greater than β_{D-NSR} (7.54 ± 0.69 vs 7.06 ± 0.41 $p < 0.009$). Between AF and NSR groups, β_{ED-NSR} was not significantly different from β_{D-AF} (7.54 ± 0.69 vs 7.82 ± 1.01 $p > 0.38$). However, when hemodynamic states were matched based on physiology, (diastasis in AF vs. diastasis in NSR), a β_{D-AF} was found to be significantly higher than β_{D-NSR} (7.82 ± 1.01 vs 7.06 ± 0.41 $p < 0.005$).

Table 4.2. Invasive hemodynamic and noninvasive echocardiographic measurements in NSR and AF groups.

	NSR Group	AF Group	p	p NSR_{ED} vs NSR_D
<i>Invasive Parameters:</i>				
P_{ED} (mmHg)	19 ± 5	18 ± 6	0.76	$p < 0.0001$
V_{ED} (ml)	160 ± 32	168 ± 43	0.54	$p < 0.0001$
P_D	13 ± 3	18 ± 6	< 0.01	-
V_D (ml)	122 ± 31	168 ± 43	< 0.01	-
dP/dV_{ED} (mmHg/ml)	0.14 ± 0.09	0.14 ± 0.10	0.96	$p < 0.0001$
dP/dV_D (mmHg/ml)	0.09 ± 0.06	0.14 ± 0.10	0.074	-
β_{ED}	7.54 ± 0.69	7.82 ± 1.01	0.38	$p < 0.01$
β_D	7.06 ± 0.41	7.82 ± 1.01	< 0.01	-
<i>Echocardiographic Parameters</i>				
Peak E-wave velocity (E_{peak})	78 ± 20	92 ± 37	0.16	
E-wave deceleration time	203 ± 28	176 ± 20	< 0.05	
E/A	1.1 ± 0.2	N.A.	N.A.	
k ($1/s^2$)	188.7 ± 30.9	245.6 ± 83.3	< 0.01	

Data are presented as mean \pm standard deviation. NSR_{ED} , end diastolic values for NSR group. NSR_D , diastatic values for NSR group. P_{ED} , left ventricular end-diastolic pressure. V_{ED} , left ventricular end-diastolic volume. P_D , left ventricular diastatic pressure. V_D , left ventricular diastatic volume. E_{peak} , peak E-wave velocity. DT, E-wave deceleration time. E/A, ratio of E_{peak} and A_{peak} . k , kinematic model based E-wave derived chamber stiffness. NSR, normal sinus rhythm. AF, atrial fibrillation.

4.3.3. Multiple Beat Comparison

Consistent with previous findings (19), chamber stiffness measured in the NSR group by the slope of the EDPVR (dP/dV_{NSR-ED}) was significantly greater than stiffness measured by the slope of the D-PVR (dP/dV_{NSR-D}) in the same group (0.14 ± 0.09 mmHg/ml vs 0.09 ± 0.06 mmHg/ml $p < 10^{-5}$). Between AF and NSR groups, comparing the hemodynamics based on the same physiology revealed that the slope of the D-PVR in AF subjects (dP/dV_{AF-D}) was higher than dP/dV_{NSR-D} (0.14 ± 0.10 mmHg/ml vs. 0.09 ± 0.06 mmHg/ml, $p < 0.074$). Similar to the

single beat finding, when hemodynamics are not matched the statistical significance between AF and NSR stiffness is lost (dP/dV_{AF-D} vs dP/dV_{NSR-ED} : 0.14 ± 0.10 mmHg/ml vs. 0.14 ± 0.09 mmHg/ml, $p > 0.95$).

4.3.4 Noninvasive Parameters

Heart rate in the AF group was higher than the NSR group (76 ± 11 bpm vs. 67 ± 7 , $p < 0.02$). Echocardiographic E-wave deceleration time (DT) was significantly shorter in the AF group than NSR group (176 ± 20 msec vs. 203 ± 28 msec, $p < 0.05$). E- wave peak velocities (E_{peak}) in the AF and NSR groups were similar (0.92 ± 0.37 m/s vs. 0.78 ± 0.20 m/s, respectively, $p = N.S.$). The E-wave derived PDF stiffness parameter in AF was significantly higher than that in the NSR group (k_{AF} vs. k_{NSR} : $245 \pm 83/s^2$ vs. $188 \pm 31/s^2$, $p < 0.01$).

4.4 DISCUSSION

In this work the value of matching the same phases of diastole for chamber stiffness comparison between NSR and AF groups was assessed. Traditional invasive measures of stiffness rely upon one or more end-diastolic P-V measurements. This is an appropriate choice for comparing chamber stiffness between groups when end-diastole is hemodynamically and physiologically equivalent between groups. In chambers with chronic AF, however, end-diastole and diastasis (when R-R intervals are sufficiently long) are physiologically and hemodynamically the same (same point on the P-V plane). This equivalence does not exist in NSR, and previous work (19) has shown that in the same NSR heart, the D-PVR and EDPVR are physiologically distinct relations, with significantly different slopes and therefore different values for chamber stiffness. The single-beat and multiple-beat analyses included in the current

study are concordant and show that in the same heart, stiffness at diastasis and end-diastole are physiologically distinct and distinguishable in NSR subjects.

Because diastasis and end-diastole is equivalent in (rate controlled) AF, a comparison of EDPVR between AF and NSR is indistinguishable from a comparison between D-PVR in AF and EDPVR in NSR. Diastasis and end-diastole are not hemodynamically equivalent between AF and NSR subjects, however, and a resulting comparison would be expected to systematically overestimate NSR chamber stiffness relative to AF chamber stiffness. Indeed in the current work, AF chamber stiffness is found to be higher than NSR chamber stiffness, and the difference between groups becomes significant only when physiologically matched hemodynamic states (diastasis vs. diastasis) are compared. This finding provides strong evidence for the claim that proper comparison of AF and NSR chamber stiffness requires using diastasis as the fiducial hemodynamic/physiologic state in which analysis must be done.

4.4.1 Equilibrium Volume

The implication that diastasis is the proper hemodynamic/physiologic state on the P-V loop when passive chamber stiffness should be measured is not surprising given a kinematic perspective of diastatic physiology. Elastic elements, displaced from their equilibrium dimension in systole, recoil toward their equilibrium diastatic position and power suction initiated early rapid filling. At diastasis there is no bulk tissue or fluid movements and the chamber is momentarily static; there is no atrioventricular pressure gradient, no net force, and no net flow. As discussed in Chapter 3, diastasis is therefore the in-vivo equilibrium chamber volume, and represents the most relaxed and passive in-vivo state of the ventricle. Displacement to a volume above equilibrium by atrial systole loads elastic elements and couples the contracted atrium in

series with a now stretched, non-equilibrium ventricle. Such a state is expected to be stiffer than the relaxed diastatic state, and indeed the results of this and previous work (19) confirm that prediction. Thus while the conventional standard is to use end-diastole as the fiducial marker for chamber stiffness, measuring chamber stiffness at the equilibrium (diastatic) volume is likely to provide a more accurate measure of actual passive chamber stiffness.

4.4.2 Applying the Single Beat Method

In this work we applied a previously described (7, 8) single-beat approach for the pressure volume relation. Previously this single-beat method utilized end-diastolic pressures and volumes in order to generate the EDPVR. In this work we generalize the single-beat approach and use diastatic pressures and volumes as input values to the single-beat algorithm. This generalization may not seem appropriate, for several reasons. First, the assumptions of the single-beat method are based on a conserved EDPVR across species and disease states, and this assumption may not hold for the D-PVR. Second, the empiric correlations used in the single-beat method are based upon end-diastolic P-V values measured from ex-vivo hearts (3), and therefore the correlations may be different if one were to make the calibration measures at diastasis. There is an argument to be made, however, that P-V relations defined by consistent physiological states have conserved shapes when appropriately normalized. The P-V relation defined by end-systole (ESPVR), for example, has been shown to have a consistent normalized shape, and that has led investigators to suggest single-beat estimation algorithms for the ESPVR (16). In addition, it is important to consider the experimental set-up used by investigators to show that the normalized EDPVR shape was conserved and to determine appropriate empirical correlations. Specifically, the experimental set up consisted of ex-vivo hearts with atria surgically removed. With the

absence of an atrium, diastasis and end-diastole become identical hemodynamic states. Thus the EDPVRs that investigators measured in the ex-vivo setting are likely indistinguishable from D-PVRs. Therefore the empirical correlations and results from the single-beat approach may actually be more applicable to end-diastole in AF or diastasis in NSR, precisely because of the absence of atrial contribution in the original experimental set up.

4.4.3 Noninvasive Indexes

In addition to invasive approaches, the stiffness of the LV chamber can also be estimated noninvasively. The PDF parameter k obtained from echocardiographic E- waves is mathematically (9) and experimentally related to the invasively measured average chamber stiffness during early rapid filling (10). E-wave deceleration time (DT) has also been correlated with stiffness (12), though that approach has limitations, as discussed in Chapter 5.

Both the triangle based (DT) and PDF model based (k) noninvasive estimates of chamber stiffness showed significant difference between the AF and NSR groups, consistent with the invasive chamber stiffness findings between groups at diastasis. The significantly shorter DT in the AF group is not likely to be explained by the higher average HR of the AF group since it is known that in the presence of a diastatic interval, E-wave DT remains essentially unchanged when the HR increases (5). In addition, it is important to appreciate that E- wave DT is determined jointly by stiffness and relaxation (k and c) rather than stiffness alone (17), and therefore it is more accurate to consider the value of k when estimating chamber stiffness from E-wave contours.

4.4.4 Chamber Stiffness in Sinus Rhythm and Atrial Fibrillation

There are a limited number of studies that focus on comparing diastolic function between AF and NSR groups. One study by Pozzoli followed heart failure subjects over a period of 2 years and compared diastolic function parameters between 18 subjects that developed chronic AF, and 34 control subjects that remained in NSR (14). While they found values of DT consistent with the current study, and a decrease in DT between AF and NSR subjects, the difference was not significant. However all of their subjects were in systolic heart failure (average EF=25%), and therefore may have already had significantly increased LV stiffness. In contrast, all NSR subjects in the current study had normal EF, and this may help explain the more significant DT difference observed in the current study. Furthermore, Pozzoli did not have simultaneous, invasively determined measures of chamber stiffness to support their echocardiographic DT based findings.

Invasive parameters were measured by Takagaki et al, in a study that compared myocardial compliance (the inverse of stiffness) in sheep before and after induction of atrial fibrillation (18). To our knowledge, this is the only other invasive study where chamber stiffness was compared between AF and NSR groups. Interestingly, Takagaki et al found no difference in invasively determined EDPVR parameters between AF and NSR sheep. However, as we show in the current work, a comparison of 'end-diastole' in AF with end-diastole in NSR is physiologically and hemodynamically inconsistent. End-diastole in (rate controlled) AF allows the chamber to achieve diastasis, and therefore a comparison of the D-PVR between AF and NSR sheep in the Takagaki et al study would have been more appropriate. By using end-diastole, Takagaki et al likely over-estimated the NSR chamber stiffness relative to AF, and therefore obscured any potential significant difference.

4.5 LIMITATIONS

4.5.1 Measuring Volume

The conductance catheter method of volume determination has known limitations related to noise, saturation and calibration that we have previously acknowledged (1, 4, 11, 19). In this study, the channels which provided physiologically consistent P-V loops were selected and averaged. However, since there was no significant drift of the volume signal during recording, any systematic offset related to calibration of the volume channels did not affect the result when the conductance volume was calibrated via ventriculography. If the two absolute measures (ESV, EDV) have slight systematic differences, resulting in a systematic volume calibration offset, the absolute values of the slopes could be inaccurate. However, comparison of slopes between subjects and groups would remain valid, because such a systemic offset would affect all measurements equally. Indeed the absolute location of the D-PVR or EDPVR in the pressure-volume axes does not affect the slope of the pressure volume relation.

While the multiple beat D-PVR or EDPVR approach relies more on relative measures of pressures and volumes, the single beat method is sensitive to absolute measured volume. The steady state value for V_{ED} in NSR and V_D in AF was calibrated to ventriculography determined EDV. Thus an equivalent method for determination of V_D in NSR would have been determining a conductance catheter measured average ratio of V_D to V_{ED} , and then multiplying ventriculography measured EDV by that scaling factor.

4.5.2 Subjects as Their Own Controls

Ideally, to determine the effect of AF on chamber properties one would determine the stiffness in a chamber in NSR, then induce chronic AF, and determine the stiffness in the same chamber after an appropriate interval. Since this idealized scenario is unattainable in humans, we opted for the closest practical, *in vivo* method of investigating the consequences of AF on chamber stiffness by comparing the D-PVR determined stiffness in NSR vs. chronic AF groups.

4.5.3 Load Variation Approach

An average of 7 beats per subject in the NSR patients and 19 beats per subject in the AF patients were used to construct the D-PVR because in NSR patients, the load was varied primarily through respiration, PVC or Valsalva maneuver. For PVC and Valsalva the D-PVR was measured during the compensatory period. Although the amount of load variation after these maneuvers is modest, the P-V relationship constructed from an average of 7 beats in NSR is sufficient (19). In contrast to NSR, only respiratory variation was utilized in AF patients to construct D-PVR, so a greater number of cardiac cycles per subject was included in the analysis to generate the D-PVR. In previous work on D-PVR (19), we demonstrated that even though the heart may respond differently to Valsalva maneuver and PVC, the D-PVR and EDPVR measurements using the two load-varying methods do not differ significantly. Ideally one would prefer a single method consistently utilized in inducing the load change, however, that would limit the range of load variation.

In P-V relationship determining physiology experiments, not only volumes are conventionally varied to generate P-V loop variation, but inotropic state may be varied by pharmacologic means via positive and negative inotropic stimulation. Our data obtained during the course of cardiac catheterization and the associated informed consent procedure did not allow

for interventions involving external (non-physiologic) inotropic agents. This limitation is obviated somewhat by the fact that the load variation was entirely physiologic and did not include the complexities of reflex mechanisms associated with pharmacologic interventions. However, this limitation underscores the importance of carrying out similar experiments in intact, closed-chest mammals, where pharmacologic interventions are the norm and the physiology of the diastatic P-V relationship can be further elucidated.

4.5.4 HR Limitation

D-PVR analysis requires the presence of a diastatic interval, and therefore requires moderate HR. In the setting of tachycardia, diastasis may not be reached before the ECG R-wave, and thus D-PVR analysis is not possible. In the current study HR was moderate and every cardiac cycle selected for analysis had a clear flat diastatic pressure interval. In AF some cardiac cycles had short R-R intervals in which diastasis was not attained, and therefore, these cycles were not utilized for analysis.

4.6 CONCLUSION

Traditionally, passive LV chamber stiffness is determined invasively via the EDPVR. However, the EDPVR cannot be used to compare the chamber stiffness in AF with that in NSR because end-diastole is equivalent to diastasis in AF, but distinguishable from diastasis in NSR. Thus the EDPVR systematically overestimates chamber stiffness in NSR relative to AF. This can only be resolved by measuring chamber stiffness relative to diastasis, not end-diastole in both groups. Diastasis is the natural choice for passive chamber stiffness determination, because it is

the in-vivo equilibrium volume of the ventricle. Both single-beat estimation technique and multiple beat P-V approaches should be performed using diastatic hemodynamics.

4.7 REFERENCES

1. Bauman L, Chung CS, Karamanoglu M, and Kovács SJ. The peak atrioventricular pressure gradient to transmitral flow relation: kinematic model prediction with in vivo validation. *Journal of the American Society of Echocardiography : official publication of the American Society of Echocardiography* 17: 839-844, 2004.
2. Bhatia RS, Tu JV, Lee DS, Austin PC, Fang J, Haouzi A, Gong Y, and Liu PP. Outcome of heart failure with preserved ejection fraction in a population-based study. *N Engl J Med* 355: 260-269, 2006.
3. Burkhoff D, Flaherty JT, Yue DT, Herskowitz A, Oikawa RY, Sugiura S, Franz MR, Baumgartner WA, Schaefer J, and Reitz BA. In vitro studies of isolated supported human hearts. *Heart Vessels* 4: 185-196, 1988.
4. Chung CS, Ajo DM, and Kovács SJ. Isovolumic pressure-to-early rapid filling decay rate relation: model-based derivation and validation via simultaneous catheterization echocardiography. *J Appl Physiol* 100: 528-534, 2006.
5. Chung CS and Kovács SJ. Consequences of increasing heart rate on deceleration time, the velocity-time integral, and E/A. *Am J Cardiol* 97: 130-136, 2006.
6. Kass DA. Assessment of diastolic dysfunction. Invasive modalities. *Cardiology clinics* 18: 571-586, 2000.
7. Klotz S, Dickstein ML, and Burkhoff D. A computational method of prediction of the end-diastolic pressure-volume relationship by single beat. *Nat Protoc* 2: 2152-2158, 2007.
8. Klotz S, Hay I, Dickstein ML, Yi G-H, Wang J, Maurer MS, Kass DA, and Burkhoff D. Single-beat estimation of end-diastolic pressure-volume relationship: a novel method with potential for noninvasive application. *Am J Physiol Heart Circ Physiol* 291: H403-412, 2006.

9. Kovács SJ, Barzilai B, and Pérez JE. Evaluation of diastolic function with Doppler echocardiography: the PDF formalism. *Am J Physiol* 252: H178-187, 1987.
10. Kovács SJ, Setser R, and Hall AF. Left ventricular chamber stiffness from model-based image processing of transmitral Doppler E-waves. *Coronary Artery Disease* 8: 179-187, 1997.
11. Lissauskas JB, Singh J, Bowman AW, and Kovács SJ. Chamber properties from transmitral flow: prediction of average and passive left ventricular diastolic stiffness. *J Appl Physiol* 91: 154-162, 2001.
12. Little WC. Diastolic dysfunction beyond distensibility: adverse effects of ventricular dilatation. *Circulation* 112: 2888-2890, 2005.
13. Little WC, Ohno M, Kitzman DW, Thomas JD, and Cheng CP. Determination of left ventricular chamber stiffness from the time for deceleration of early left ventricular filling. *Circulation* 92: 1933-1939, 1995.
14. Pozzoli M, Cioffi G, Traversi E, Pinna GD, Cobelli F, and Tavazzi L. Predictors of primary atrial fibrillation and concomitant clinical and hemodynamic changes in patients with chronic heart failure: a prospective study in 344 patients with baseline sinus rhythm. *Journal of the American College of Cardiology* 32: 197-204, 1998.
15. Redfield MM. Understanding "diastolic" heart failure. *N Engl J Med* 350: 1930-1931, 2004.
16. Senzaki H, Chen CH, and Kass DA. Single-beat estimation of end-systolic pressure-volume relation in humans. A new method with the potential for noninvasive application. *Circulation* 94: 2497-2506, 1996.

17. Shmuylovich L and Kovács SJ. E-wave deceleration time may not provide an accurate determination of LV chamber stiffness if LV relaxation/viscoelasticity is unknown. *Am J Physiol Heart Circ Physiol* 292: H2712-2720, 2007.
18. Takagaki M, McCarthy PM, Inoue M, Chung M, Connor JT, Dessoffy R, Ochiai Y, Howard M, Doi K, Kopcak M, Mazgalev TN, and Fukamachi K. Myocardial compliance was not altered after acute induction of atrial fibrillation in sheep. *Med Sci Monit* 11: BR147-153, 2005.
19. Zhang W and Kovacs S. The diastatic pressure-volume relationship is not the same as the end-diastolic pressure-volume relationship. *AJP-Heart and Circulatory Physiology*, 294: H2750-60, 2008.

CHAPTER 5.

STIFFNESS AND RELAXATION/VISCOELASTICITY JOINTLY

DETERMINE DECELERATION TIME

5.1. INTRODUCTION

5.1.1 One to One Stiffness to Deceleration Time Relation

The instantaneous slope of the left ventricular (LV) pressure-volume relation dP/dV defines chamber stiffness and serves as one of the two main parameters (the other is relaxation) by which diastolic function (DF) is conventionally quantitated(14, 28, 34, 35). Because the instantaneous slope dP/dV varies throughout the cardiac cycle and increases with increasing end diastolic volume (EDV), many investigators(10, 22, 23, 25, 26, 32) estimate chamber stiffness by defining ratios of pressure differences to volume differences over relevant portions of filling. A convenient and common choice is to take the pressure and volume rise from minimum pressure to end diastolic pressure, thereby defining a lumped diastolic chamber stiffness called $\Delta P/\Delta V_{AVG}$. The determination of $\Delta P_{AVG}/\Delta V_{AVG}$ via high-fidelity, micromanometric pressure recording defines the invasive ‘gold-standard’. Because $\Delta P_{AVG}/\Delta V_{AVG}$ is a ‘relative’, rather than ‘absolute’ index, the requirement to use invasive methodology for its determination is not absolute. Accordingly, non-invasive methods for estimation of LV stiffness have been proposed (9, 10, 19, 22, 23, 25, 29). Previous work by Little et al. has predicted and experimentally validated a strong inverse correlation between the E-wave deceleration time (DT) and the square of invasively determined LV hemodynamic operating stiffness $\Delta P/\Delta V_{AVG}$ (23). The basis for Little et al’s approach was an energy loss free model of wave-deceleration based on the following differential equation:

$$\ddot{v} = \left(K_{LV}\right)^2 v \quad \text{Equation 5.1}$$

, where v is flow velocity, K_{LV} is an effective chamber stiffness constant, and $v(0)=E_{\text{peak}}$ (the model begins at the peak of the E-wave). The solution to Eq. 5.1 is a cosine function with

frequency K_{LV} , and this is identical (within a phase shift) to the lossless oscillator ($c=0$ limit of the PDF model) in Chapter 1. Using this solution, Little showed that the chamber stiffness can be expressed trivially in terms of model parameters and multiplicative constants:

$$K_{LV} = \frac{\Delta P}{\Delta V_{AVG}} = \frac{\rho L}{A_{MV}} \left(\frac{\pi}{2DT} \right)^2 \quad \text{Equation 5.2}$$

, where DT is the time from peak flow to zero velocity, ρ is the density of blood, L is the effective mitral plug-flow length, and A_{MV} is the constant effective mitral valve area (MVA). This equation provides a simple connection between stiffness, an invasive measure, and the non-invasively determined DT . Furthermore, starting with the lossless oscillator or simply inverting Eq 5.2, one can solve for DT in terms of chamber stiffness:

$$DT_k \propto \frac{\pi}{2\sqrt{k}} \quad \text{Equation 5.3}$$

, where k can be either the Little et al defined stiffness constant or the PDF defined stiffness constant. Note that DT_k is the deceleration time defined by a ‘stiffness only’ model of diastolic filling.

Little et al validated the inverse of Eq. 5.2 in a study of 8 dogs undergoing catheterization and echocardiography. Little et al found a strong linear relationship between chamber stiffness predicted by DT and chamber stiffness measured from $\Delta P/\Delta V_{AVG}$. Further validation of Eq. 5.2, for humans undergoing open-heart surgery, and for humans undergoing catheterization, was achieved by Garcia et al (10) and Marino et al (25), respectively. Thus Eq 5.2 and its inverse represent a significant step forward in the noninvasive determination of traditionally invasively determined indexes.

5.1.2 Challenging The One to One Stiffness and Deceleration Time Relation

While Eq. 5.3 is useful because of its simplicity and applicability, the one-to one relation between DT and chamber stiffness implied by Eq. 5.3 is fairly restrictive. This one-to-one relation implies that two LVs with E-waves having indistinguishable DTs should have indistinguishable left ventricular stiffness ($\Delta P_{AVG}/\Delta V_{AVG}$), assuming similar chamber volumes and that the constant lumped coefficient in Eq. 5.3 is the same for both. Therefore, subjects

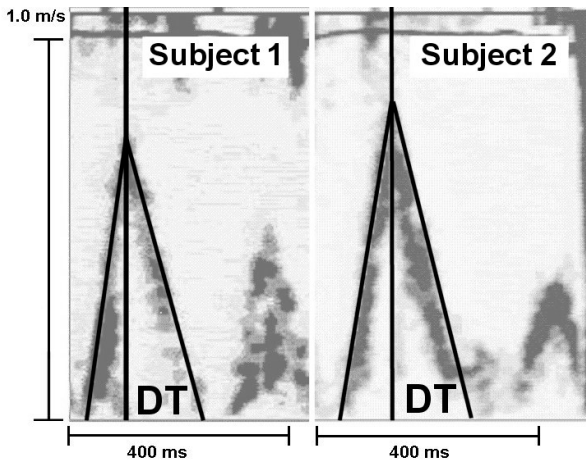


Table 5.1 Comparison of hemodynamic stiffness and DT between two subjects

	Subject 1	Subject 2
DT, s	0.147 (0.01)*	0.146 (0.02)
k , $1/s^2$	343 (36)†	276 (55)
$\Delta P_{AVG}/\Delta V_{AVG}$, mmHg/cm ³	0.34 (0.07)‡	0.22 (0.04)
$\Delta P_E/\Delta V_E$, mmHg/cm ³	0.27 (0.08)§	0.19 (0.05)
EDV, cm ³	95	106

Figure 5.1 E-waves of two subjects having indistinguishable DTs, but significantly different values for E-wave derived stiffness k and catheterization-derived stiffness $\Delta P_{AVG}/\Delta V_{AVG}$. Measured DTs of 10 beats from subject 1 and 7 beats from subject 2 are indistinguishable. Measured k and $\Delta P_{AVG}/\Delta V_{AVG}$ of 9 beats from subject 1 and 7 beats from subject 2 are significantly different via ANOVA. Values in the table are means (SD). DT, deceleration time; k , E-wave derived stiffness; $\Delta P_{AVG}/\Delta V_{AVG}$, catheterization-determined average chamber stiffness; $\Delta P_E/\Delta V_E$, catheterization-determined early rapid filling stiffness; EDV, end-diastolic volume. P values determined by ANOVA * $P=0.93$. † $P=0.011$. ‡ $P=0.0015$. § $P=0.037$. See text for details.

having similar MVA, blood density, and chamber volumes, and having indistinguishable DTs by Doppler echo but significantly different $\Delta P_{AVG}/\Delta V_{AVG}$ by catheterization, would suggest that although Eq. 5.3 is an excellent correlate of chamber stiffness, it is incomplete.

We motivate our work through a specific example (Figure 5.1) from two subjects, with similar end-diastolic volumes (EDV), undergoing elective diagnostic catheterization in whom simultaneous micromanometric LV pressure (Millar) and transmitral flow (E-waves) were recorded. For both subjects, catheterization determined stiffness $\Delta P_{AVG}/\Delta V_{AVG}$, as well as the

PDF model E-wave derived kinematic LV stiffness analog (19, 22) (k), were calculated for several consecutive beats (see Methods). Although the DTs in Figure 5.1 are indistinguishable, all the invasive and noninvasive stiffness indexes were significantly different between the two subjects.

To resolve the ‘indistinguishable DT, but distinguishable measured stiffness ($\Delta P_{AVG}/\Delta V_{AVG}$)’ dilemma we investigated the functional relationship between DT and $\Delta P_{AVG}/\Delta V_{AVG}$. We employ the PDF formalism (see Chapters 1 and 2), to derive a general expression for chamber stiffness that depends on both measured DT and c , the PDF relaxation/viscosity parameter. Because the general expression for DT is not solely stiffness (k) dependent, two subjects with indistinguishable DT need not have equivalent stiffness. We validate the model-predicted hypothesis that DT is determined jointly by chamber stiffness and chamber relaxation/ viscoelasticity through analysis of 400 E-waves recorded from 79 subjects undergoing simultaneous echocardiography-catheterization.

5.2 METHODS

5.2.1 Mathematical Derivation

Model Comparison

In the Little et al model of diastolic filling, inertial forces are opposed solely by elastic ventricular forces. This model is mathematically equivalent to the lossless simple harmonic oscillator described in Chapter 1, has the following equation of motion (per unit mass):

$$\ddot{x} + kx = 0 \qquad \text{Equation 5.4}$$

where x is displacement (cm), k is stiffness per unit mass(g/s^2), and \ddot{x} is the second time derivative of displacement (cm/s^2).

In contrast, the PDF model accounts for the role of the LV as a mechanical suction pump in early diastole and predicts E-wave contours through a damped simple harmonic oscillator, having the following equation of motion:

$$\ddot{x} + c\dot{x} + kx = 0 \quad \text{Equation 5.5}$$

where c is the damping constant (g/s); \dot{x} is the velocity (cm/s); and x , k , and \ddot{x} are defined as in Eq. 5.4. Apart from the choice of initial conditions for the two models, the damping parameter c is the primary difference between the PDF formalism and the Little et al. model. Thus, in deriving a PDF formalism based equivalent to the period of oscillation vs. DT relation (Eq 5.3), we expect the PDF formalism derived formula to be a function of both stiffness (k) and relaxation/viscosity (c).

Underdamped E-waves

The general expression for DT in terms of PDF parameters was derived in Chapter 2, and we summarize the approach here. We begin with the underdamped form of the PDF derived E-wave velocity contour.

$$v(t) = \frac{kx_o}{\omega} e^{-\alpha t} \sin(\omega t) \quad \text{Equation 5.6}$$

with $\alpha = \frac{c}{2}$ and $\omega = \frac{\sqrt{4k - c^2}}{2}$. The duration of the wave, E_{dur} , is the sum of the

acceleration time (AT) and deceleration time (DT), and can be found when the sine term vanishes:

$$DT + AT = \frac{\pi}{\omega} \quad \text{Equation 5.7}$$

Furthermore, one can find the time from start to peak of the wave (AT) by solving for the time at which acceleration vanishes:

$$AT = \frac{1}{\omega} \tan^{-1}\left(\frac{\omega}{\alpha}\right) \quad \text{Equation 5.8}$$

To simplify further analysis we can define a new variable $y = \frac{c}{2\sqrt{k}}$, and then combine Eq. 5.7 and 5.8 to obtain a simplified expression for DT:

$$DT = \frac{1}{\sqrt{k}} \cdot \left[\frac{\pi - \cos^{-1}(y)}{\sqrt{1-y^2}} \right] \quad \text{Equation 5.9}$$

Equation 5.9 is complex and may be simplified by considering appropriate limits.

Because this analysis is based on the underdamped regime of the PDF model, it is reasonable to expand Eq. 5.9 in the $y \ll 1$ limit. Taylor's theorem allows a continuous function to be approximated around 0 as:

$$g(x) = g(0) + g'(0)(x) + \frac{g''(0)}{2!}(x)^2 + \dots \quad \text{Equation 5.10}$$

We focus on the bracketed expression in Eq. 5.9, and first note that:

$$\frac{d}{dy}\left(-\cos^{-1}(y)\right) = \frac{1}{\sqrt{1-y^2}} \quad \text{Equation 5.11}$$

Thus if we define $q = -\cos^{-1}(y)$, the bracketed expression in Eq. 5.9 becomes:

$$f = q'(\pi + q) \quad \text{Equation 5.12}$$

Now applying the product rule, we can quickly determine derivatives of f :

$$\begin{aligned}
f' &= q''(\pi + q) + (q')^2 \\
f'' &= q'''(\pi + q) + 3(q'q'') \\
f''' &= q''''(\pi + q) + 4(q'q''') + 3(q'')^2
\end{aligned}
\tag{Equation 5.13}$$

Furthermore, $q(0) = -\pi/2$, and higher even derivatives of q vanish at $y=0$. Thus, the derivatives in 5.13 may be simplified at $y=0$:

$$\begin{aligned}
f(0) &= q'(0) \cdot \left(\frac{\pi}{2}\right) = \frac{\pi}{2}, \quad f'(0) = (q'(0))^2 = 1 \\
f''(0) &= q'''(0) \cdot \left(\frac{\pi}{2}\right) = \frac{\pi}{2}, \quad f'''(0) = 4(q'(0)q'''(0)) = 4
\end{aligned}
\tag{Equation 5.14}$$

Plugging in the values in Eq. 5.14 into 5.10 and 5.9, we obtain the following Taylor expansion around $y=0$ for DT :

$$DT = \frac{1}{\sqrt{k}} \cdot \left[\frac{\pi}{2} + y + \frac{\pi y^2}{4} + \frac{2y^3}{3} + \dots \right]
\tag{Equation 5.16}$$

and if we take just the first two terms in the expansion and rewrite y in terms of c and k , we obtain a simplified expression for DT :

$$DT_{k,c} = \frac{\pi}{2\sqrt{k}} + \frac{c}{2k}
\tag{Equation 5.17}$$

where $DT_{k,c}$ is the DT predicted by a ‘stiffness and viscoelasticity’ model of filling. This equation is valid in the $y < 1$ or $c^2 < 2 \cdot k$ limit. Note that DT_k , the DT in Eq 5.3 derived from a stiffness only model of filling, is recovered from Eq 5.17 in the $c=0$ limit. Eq. 5.17 can be inverted to have similar form as Eq. 5.2, thereby expressing stiffness as a function of DT and c :

$$\frac{\Delta P}{\Delta V_{AVG}} \propto k = \frac{1}{8DT^2} \left(\pi + \sqrt{\pi^2 + 8DT \cdot c} \right)^2
\tag{Equation 5.18}$$

We note that Eq. 5.2 is recovered in the $c=0$ limit.

Overdamped Waves

When one encounters an E-wave whose contour corresponds to ‘overdamped’ kinematics ($y > 1$ regime), DT is no longer clearly defined, because the end of the wave can not be easily determined. However, as described in Chapter 2, the effective deceleration time may be approximated from the base of the triangle defined by the E-wave peak and inflection point in the deceleration portion. The key to the derivation is that the inflection point occurs at twice the acceleration time, and therefore the slope of the deceleration line may be calculated and equated between the E-wave peak and the inflection point and E-wave peak and E-wave end. This results in the following relationship for overdamped deceleration time:

$$DT_{over} = AT \cdot \left(\frac{v(AT)}{v(AT) - v(2AT)} \right) \quad \text{Equation 5.19}$$

, where AT and $v(t)$ are given by Equations 2.32 and 2.36. Evaluating the velocities in Eq. 5.19 and simplifying, one obtains the following expression for overdamped DT :

$$DT_{over} = \frac{1}{\sqrt{k}} f(\varphi) \quad \text{Equation 5.20}$$

, where $\varphi = 1 - y^{-2}$, $f(\varphi) = \frac{(1-\varphi)\Phi(\varphi)}{2 \cdot e^{\Phi(\varphi)} - \sqrt{1-\varphi}}$, and $\Phi(\varphi) = -\frac{\ln(1+\sqrt{\varphi}) - \ln(1-\sqrt{\varphi})}{2\sqrt{\varphi}}$.

The overdamped limit corresponds to $\varphi > 0$ limit, and therefore we can expand Eq. 5.22 around $\varphi = 0$ to obtain an expression for DT :

$$DT_{over} = \frac{1}{\sqrt{k}} (f(0) + \varphi \cdot f'(0) + \dots) \quad \text{Equation 5.21}$$

To simplify Eq. 5.21, we need to find the derivative of $\Phi(\varphi)$:

$$\Phi'(\varphi) = \frac{1}{2\varphi} \left(\frac{\ln(1+\sqrt{\varphi}) - \ln(1-\sqrt{\varphi})}{2\sqrt{\varphi}} - \frac{1}{1-\varphi} \right) \quad \text{Equation 5.22}$$

Applying expansions of $\ln(1\pm\varphi)$ and $(\varphi-1)^{-1}$ at $\varphi=0$ to Eq. 5.21 and 5.22 yields:

$$\Phi(0) = -1, \quad \Phi'(0) = -\left(\frac{1}{3}\right) \quad \text{Equation 5.23}$$

We can find the derivative of $f(\varphi)$:

$$f'(\varphi) = \frac{((1-\varphi)\Phi'(\varphi) - \Phi(\varphi))\left(2 \cdot e^{\Phi(\varphi)} - \sqrt{1-\varphi}\right) - \left(2 \cdot \Phi'(\varphi)e^{\Phi(\varphi)} + \frac{1}{2\sqrt{1-\varphi}}\right)(\Phi(\varphi)(1-\varphi))}{\left(2 \cdot e^{\Phi(\varphi)} - \sqrt{1-\varphi}\right)^2} \quad \text{Equation 5.24}$$

Armed with these expressions, we can evaluate $f(\varphi)$ and $f'(\varphi)$:

$$f(0) = \frac{e}{e-2}, \quad f'(0) = -\frac{(4e-e^2)}{6(2-e)^2} \quad \text{Equation 5.25}$$

Plugging Eq. 5.25 into Eq. 5.21, we can express DT_{over} in terms of c and k .

$$DT_{\text{over}} \approx \frac{1}{\sqrt{k}} \left(\frac{e}{e-2} + \left(1 - \frac{1}{y^2}\right) \frac{4e-e^2}{6(2-e)^2} \right) \quad \text{Equation 5.26}$$

$$DT_{\text{over}} \approx \frac{1}{\sqrt{k}} \left(\frac{5e^2-8e}{6(2-e)^2} - \frac{4e-e^2}{6(2-e)^2} \frac{4k}{c^2} \right)$$

The kinematic dependence of DT on c and k in both overdamped and underdamped cases (Eq 5.9 and 5.20) can be visualized with isochrones in the c vs k plane (Figure 5.2).

5.2.2 EXPERIMENTAL VALIDATION

Inclusion Criteria

Seventy nine subjects were selected from an existing Cardiovascular Biophysics Laboratory database of simultaneous Doppler echocardiographic transmitral flow recordings and micromanometric catheter-derived LV pressures obtained during diagnostic cardiac catheterization (2, 22). Our methodology for simultaneous micromanometric LV pressure-

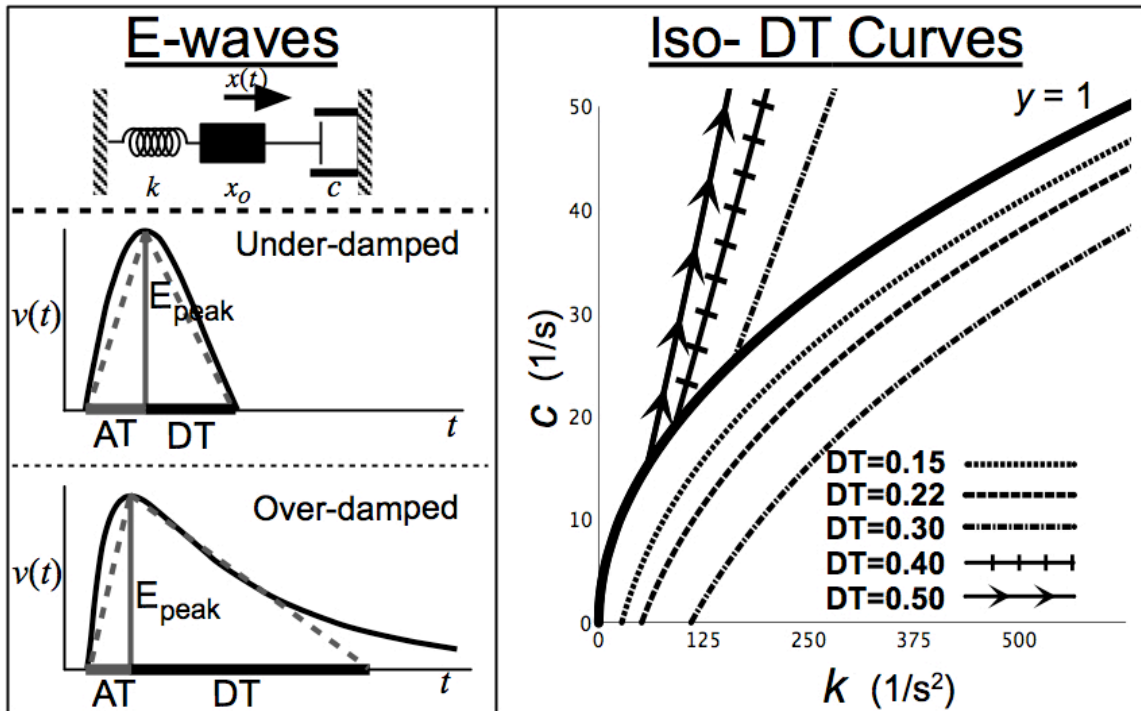


Figure 5.2. The PDF model reveals how E-wave deceleration time (DT) is determined jointly by stiffness and relaxation. The model re-expresses DT in terms of PDF parameters (c , k) for both ‘overdamped’ and ‘underdamped’ contours. Taylor series approximation simplifies expressions for DT . The right panel shows lines of constant DT in the c vs. k plane. Note that a constant value of DT can be generated by a range of c and k values. The $y=1$ curve separates overdamped (top) and underdamped (bottom) regimes. See text for details.

transmitral flow acquisition has been previously described (2, 22), and is reviewed in Chapter 2.

All subjects underwent elective cardiac catheterization at the request of their referring physician.

Prior to data acquisition and cardiac catheterization, all subjects provided signed, informed consent approved by Washington University Medical Center Human Studies Committee (IRB).

Selection criteria from the database required that subjects have normal sinus rhythm, normal valvular function, and clearly identifiable E- and A-waves. Subjects with significant merging between E- and A-waves were excluded. Nineteen of the seventy nine subjects had ejection fraction (EF) less than 55%, while thirty-five of the eight subjects had LVEDP \geq 19 mmHg.

Table 5.2 summarizes the demographic information for the group.

Table 5.2. Subject Demographics

Age, yr	55(10)
Gender	57 M, 23 F
Height, m	1.59(0.51)
Weight, kg	83(33)
EF	64(15)
EDV, mL	183(65)
LVEDP, mmHg	19 (6.5)
DT, s	0.19(0.04)

Values are mean(SD); $n=79$ subjects. 19 subjects showed evidence of systolic dysfunction ($EF < 55\%$). 35 subjects showed evidence of diastolic dysfunction ($LVEDP \geq 19\text{mmHg}$).

Doppler Analysis Methods:

At least 5 under-damped E-waves were acquired and analyzed from each subject. DT was measured manually as defined by standard criteria (1) as the base of the triangle approximating the deceleration portion of the E-wave. In addition, for each beat, the parameterized diastolic filling (PDF) formalism was used to fit the E-wave contour (12, 17) and extract model-based stiffness (k) and damping (c) parameters (see Chapter 2 for details on triangle and PDF-model fitting). In total 400 E-waves were analyzed.

As in prior work(22), diastolic volume differences (ΔV) were calculated by multiplying mitral valve area by the VTI over the relevant portion of the diastolic period. Effective (constant) mitral valve area was estimated by dividing the ventriculography determined (calibrated) stroke volume by the average total VTI (sum of E- and A-wave VTI).

Calculation of Left Ventricular Hemodynamic Operating Stiffness

Two subjects with similar EDV from the group (Fig. 5.1), exhibiting clear diastasis intervals between E- and A-waves, were chosen for a preliminary analysis. For each subject, DT

and hemodynamic stiffness $\Delta P_{AVG}/\Delta V_{AVG}$ were measured in 7-10 consecutive beats. In addition, E- waves were fit by the parameterized diastolic filling (PDF) formalism for each beat. Beats from each subject having indistinguishable DT were grouped together. To test whether subjects with indistinguishable DT had indistinguishable LV stiffness values, hemodynamically determined stiffness values ($\Delta P_{AVG}/\Delta V_{AVG}$, $\Delta P_E/\Delta V_E$ as described below), as well as PDF model-derived LV stiffness (k) were compared between beats having indistinguishable DT. In addition to comparing mean values between subjects for stiffness parameters and DT, all measured values (DT, hemodynamic stiffness, PDF stiffness) for each beat from subject 1 (9 beats analyzed) were compared to measured values for subject 2 (7 beats) by ANOVA analysis using Microsoft Excel (Microsoft Corp, Redmond, WA).

The method for determining LV hemodynamic operating stiffness has been previously detailed (22). Briefly, early rapid filling stiffness ($\Delta P_E/\Delta V_E$), and average chamber stiffness ($\Delta P_{AVG}/\Delta V_{AVG}$) were calculated from ratios of LV pressure (LVP) changes and volume changes over appropriate time intervals. In accordance with the Little et al definition (23), average chamber stiffness was defined as the ratio of the change in pressure to the change in volume during the time interval from minimum LVP to LV end-diastolic pressure (LVEDP)

($\Delta P_{AVG}/\Delta V_{AVG} = \frac{P_{EndDiastolic} - P_{minimum}}{V_{EndDiastolic} - V_{P(minimum)}}$). Early rapid-filling stiffness, the effective E-wave LV

stiffness, was defined as the ratio of the change in pressure to the change in volume during the

time interval from minimum LVP to diastasis LVP ($\Delta P_E/\Delta V_E = \frac{P_{Diastasis} - P_{minimum}}{V_{Diastasis} - V_{P minimum}}$).

Comparative Analysis Between DT_k and $DT_{k,c}$

Previous work by Lissauskas et al showed for a large sample size ($n=131$) that the E-wave derived kinematic stiffness k is strongly linearly correlated with catheterization determined $\Delta P_{AVG}/\Delta V_{AVG}$ (22). Additional work by Kovács et al (19) has shown that k is equal to a constant multiple of the Little et al DT-determined stiffness for low c -valued E-waves. Thus, instead of calculating $\Delta P_{AVG}/\Delta V_{AVG}$ (as we did for the preliminary work presented in Figure 1) for all 79 subjects in the comparative analysis, we used PDF-derived k as a surrogate for invasively determined stiffness. To ensure the validity of this approximation we independently tested the

correlation between PDF derived stiffness parameter k and catheterization determined $\Delta P_{AVG}/\Delta V_{AVG}$ in a subgroup of our patients ($n=20$) using methods analogous to those presented in Lissauskas et al (22). In accordance with previous work by Lissauskas et al, a strong linear correlation ($r^2=0.59$) between PDF derived parameter k and catheterization determined $\Delta P_{AVG}/\Delta V_{AVG}$ was observed for the subgroup of subjects (Figure 5.3).

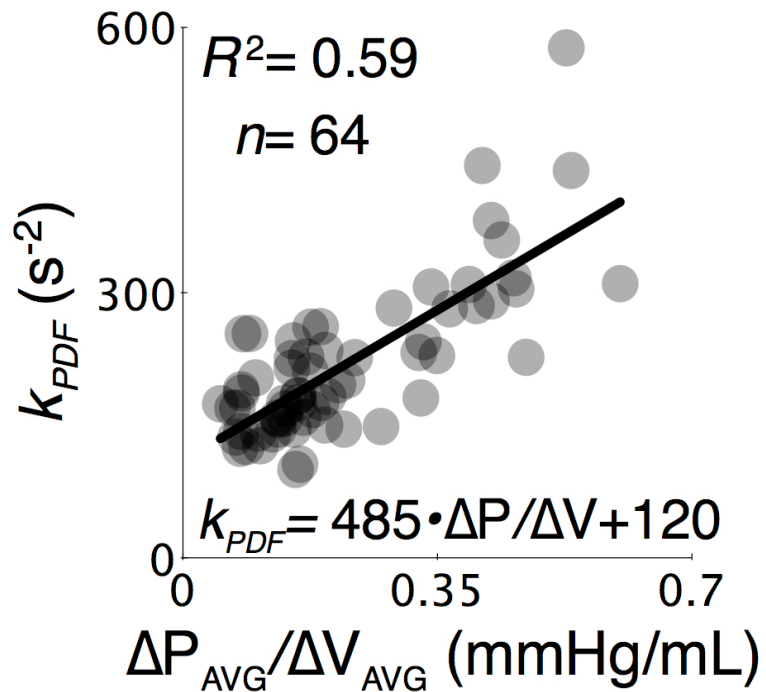


Figure 5.3. Data for 64 beats from $n=20$ subjects. For each beat $\Delta P_{AVG}/\Delta V_{AVG}$ was calculated using invasively derived high fidelity pressure and simultaneous transmitral flow derived volume change in a manner analogous to the methods presented in Lissauskas et al and by others. Least squares linear regression of k_{PDF} to $\Delta P_{AVG}/\Delta V_{AVG}$ yielded an $r=0.76$. This result provides additional support for using k_{PDF} as a surrogate for $\Delta P_{AVG}/\Delta V_{AVG}$.

$DT_{k,c}$ and DT_k values were computed for a total of 400 E-waves by substituting model based stiffness k and relaxation/viscosity c into equations 5.3 and 5.17. Clinically measured triangle-based DT was compared to the model-predicted $DT_{k,c}$ and DT_k by least mean square (LMS) regression. Paired t -test analysis of the difference between measured and predicted DT values was performed using Microsoft Excel (Microsoft Corp, Redmond, WA).

5.3 RESULTS

For illustrative purposes representative E-waves from two subjects with indistinguishable DTs and similar MVA and chamber volumes, are presented in Figure 5.1. Invasively derived stiffness $\Delta P_{AVG}/\Delta V_{AVG}$, $\Delta P_E/\Delta V_E$, as well as PDF determined stiffness k were calculated for 7 beats in subject 2 and 10 beats in subject 1. While DT values were indistinguishable between the two subjects ($p=0.89$), both invasively derived and kinematically derived stiffness values were

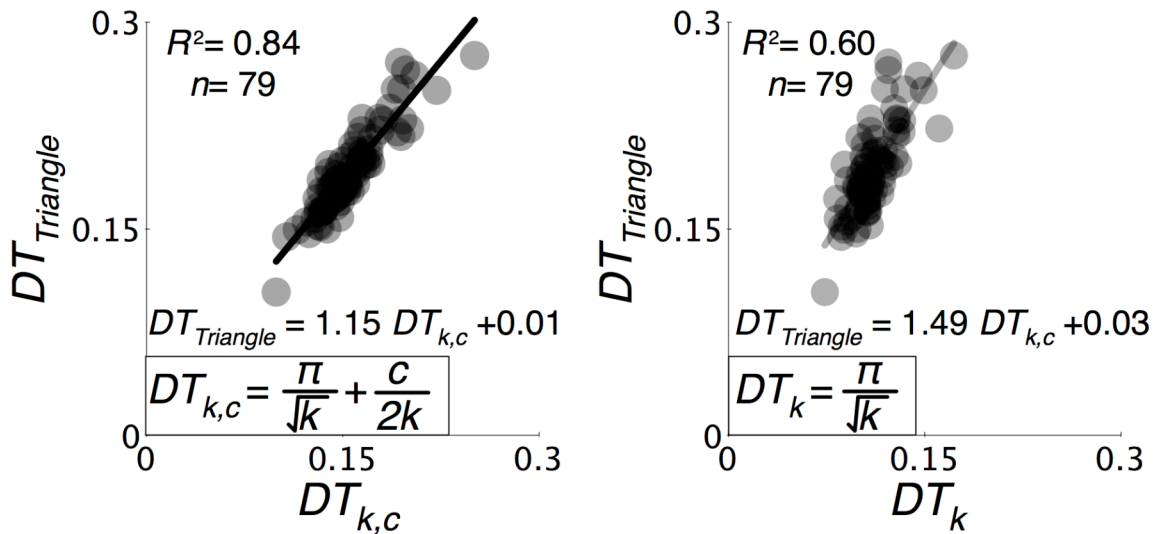


Figure 5.4. Comparison of measured vs predicted values for DT by the ‘stiffness only, DT_k ’ and ‘stiffness and viscoelasticity, $DT_{k,c}$ ’ models in 79 subjects. Five E-waves per subject were analyzed and averaged to generate each patient’s data point. The $DT_{k,c}$ model incorporating both stiffness and relaxation/viscoelasticity attains a much stronger correlation coefficient ($r^2 = 0.84$ vs 0.60) via least mean-square regression. See text for details.

significantly different by ANOVA ($p < 0.001$).

The predicted relationship between DT, k , and c was compared to the established (inverted) stiffness-only relationship of Little et al. Figure 5.4 plots the raw data of measured DT vs. model-predicted $DT_{k,c}$ using Eq. 5.17 and by Little's model, Eq. 5.3. LMS regression yields: $(DT = 1.15DT_{k,c} + 0.01, r^2 = 0.84)$ vs. $(DT = 1.48DT_k + 0.03, r^2 = 0.60)$. The average difference between the measured DT and Little et al model predicted DT ($DT - DT_k$) was 0.082(0.022) sec, while the average difference between measured DT and Kovács et al model predicted DT ($DT - DT_{k,c}$) was 0.036(0.031) sec. Paired t-test analysis of the difference between measured and predicted DT ($DT - DT_{k,c}$ vs $DT - DT_k$) at a significance level of $\alpha = 0.05$, yields $t = 32$, and $p \approx 10^{-47}$ for a two-tailed test.

5.4 DISCUSSION

5.4.1 Summary

Average left ventricular (LV) chamber stiffness, $\Delta P_{AVG}/\Delta V_{AVG}$, is an important diastolic function (DF) determinant. An E-wave based determination of $\Delta P_{AVG}/\Delta V_{AVG}$ by Little et al predicted that deceleration time (DT) determines stiffness according to $\Delta P_{AVG}/\Delta V_{AVG} = A/(DT)^2$. This implies that if the DTs of two LVs are indistinguishable, so is their stiffness. We observed that LVs having indistinguishable DTs may have markedly different values for $\Delta P_{AVG}/\Delta V_{AVG}$ determined by simultaneous echocardiography-catheterization.

To solve the problem of why two subjects having indistinguishable DTs and chamber volume can have different catheterization determined values of chamber stiffness, we used the PDF formalism to derive the general expression between DT, ventricular stiffness, and

relaxation/viscoelasticity (Eq. 5.17). We compare clinically measured DT to the general expression for DT ($DT_{k,c}$), containing both stiffness and relaxation components, and to the Little et al stiffness only expression for DT (DT_k), in 79 subjects. The results demonstrate that DT is jointly determined by stiffness and relaxation, and suggest that accurate determination of chamber stiffness requires measuring both DT and chamber relaxation properties.

5.4.2 Kinematic Model Comparison

In 1995, Little independently posited that, starting from the E-wave peak, the deceleration portion can be modeled kinematically as an undamped oscillation (i.e. a cosine function) (23). Expressed differently, Little et al's independent derivation, based on chamber stiffness as the mechanism which opposes inertia to decelerate the E-wave, is a special ($c=0$) limit of the solution to the suction-initiated transmitral flow problem, solved via the 1987 proposed PDF formalism (18). It is reassuring that totally different and independent lines of physiologic argument, invoking different initial conditions, lead, via Newton's Law, to essentially the same mathematical expression for the E-wave contour.

There is, however a significant limitation to the stiffness only approach. While an undamped oscillator provides an excellent approximation to the deceleration portions of many E-wave contours, for deceleration portions of E-waves exhibiting an inflection point or the 'delayed relaxation' pattern, a cosine function has limited applicability. Indeed, a cosine (quarter wavelength, 'concave-down') can not fit an E-wave deceleration contour having an inflection point, ('concave-down' changing to 'concave-up'). Thus the cosine model works best for ventricles where relaxation/viscoelastic effects are negligible relative to stiffness. Furthermore, the stiffness only approach predicts that ventricles with identical deceleration times will have

indistinguishable stiffness. This prediction is not consistent with experimental findings (Figure 5.1), and resolution of this inconsistency requires additional parameters.

5.4.3 Resolving the “Indistinguishable DT , Distinguishable stiffness dilemma”

Equation 5.17 and 5.26 resolves the “same DT , different chamber stiffness dilemma” through the parameter c . In cases where viscous losses are small, the second term can be neglected and DT will have a one-to-one correspondence with chamber stiffness as Little et al predicted. However, in cases where viscous losses are significant, DT is determined by **both** stiffness (k) and viscoelasticity/relaxation effects (c). Thus two ventricles with identical DT may have different stiffness values if they also have different c values. This is clear by following lines of constant DT in Figure 5.2, where the exact expressions for DT are determined. The previous discussion makes clear that an additional damping parameter (c) mathematically resolves a limitation of the stiffness-only model. However, in order to be a valid approach, the incorporation of c must be grounded in basic physiology and experimental findings. Thus it is important to consider the experimental basis for chamber viscoelasticity.

5.4.4 Experimental Evidence For Significance of Tissue Viscoelasticity

The simplest model for the material properties of the chamber assumes that the tissue is a linear elastic material. This approach lumps complex cellular and extracellular interactions into a single stiffness parameter that relates stress to strain (pressure differences to volume differences). Though some models treat tissue as purely elastic, many studies have shown that tissue is viscoelastic (8, 13, 16, 20, 30, 32, 36). The connection between a simple elastic model and a viscoelastic model for the LV is subtle, but was elucidated in the pioneering work of Templeton

et al (32). They dynamically filled canine ventricles with a sinusoidally varying volume and measured the resulting chamber pressures changes as well as the operating chamber stiffness. They found that the peak of the chamber pressure perturbation was offset (in time) from the peak of the driving volume perturbation, indicating the presence of viscous effects. Importantly, any offset introduced by the coupling of regional pressure gradients to regional ventricular dimension (6, 21, 26) can not account for the observed offset, since volume changes were measured precisely from calibrated driving piston motion, and not from ventricular dimensions. To account for viscous effects, Templeton used a three component (stiffness, damping, and inertia) linear model for the pressure contour. Inversion of the model allowed determination of the elastic stiffness and the “viscous stiffness” for each ventricle from the pressure-volume data. Thus, Templeton showed that ventricular stiffness could be divided into elastic and viscous components, elastic components being those measured by instantaneous dP/dV measurements, and viscous components being measured by phase differences between hemodynamic pressures and volumes. Thus ventricular stiffness is best approximated by elastic dP/dV stiffness only if viscous effects are negligible.

Several studies, however, have shown viscous effects to be significant both in animal models and in humans, particularly in those with pathology. For example, Rankin et al found that a viscoelastic, rather than a purely elastic, model of the ventricle was required to fit observed stress strain data obtained in open chest dogs (30). Hess et al extended these results to humans, and showed that for patients with myocardial hypertrophy, a model that included both viscous and elastic parameters, provided a better fit to ventricular stress-strain relationships than a simple elastic model. Hess concluded that “it is important for the assessment of diastolic myocardial stiffness to evaluate the viscous influences during filling, because the simple elastic constants

reflect a composite of elastic and viscous forces and may be misleading, especially in patients with myocardial hypertrophy.” (13)

5.4.4 Clinical Utilization of Stiffness and Viscosity

In current practice, Templeton’s elastic stiffness component (due to collagen, titin, and a myriad of other factors (15)) can be invasively measured from hemodynamics, and the “viscous stiffness” component is referred to as viscosity/relaxation effects. In fact, general consensus has developed that diastolic dysfunction is associated with pathophysiology related to stiffness and relaxation (15, 28, 34, 35).

Relaxation is intuitively appealing as a parameter that determines diastolic function and it is a term that has both clinical and physiologic interpretations. From a physiological perspective it includes viscoelastic effects, and involves processes related to the reuptake of Ca^{2+} after crossbridge-cycling and force generation, intracellular components including microtubules, and actin-titin interactions (15, 16, 20). Clinically, impaired relaxation can be characterized by two dominant phenomena. First, prolonged τ determined by (invasive) catheterization or prolonged IVRT determined by (noninvasive) echocardiography often indicates impaired Ca^{2+} handling and poor relaxation of the ventricle during isovolumic relaxation.

Relaxation effects are also visible during filling, both in the velocity contour and in the pressure contour (see Chapter 6 for details regarding relaxation and the pressure contour). Relaxation/viscoelastic effects during filling declare themselves in the damped oscillatory features of the velocity contour, transforming a pure sine wave (no damping) shaped E-wave to an asymmetric E-wave with a prolonged deceleration time. Prolonged $\text{DT} > 220\text{ms}$ is one of the

hallmarks of the E-wave ‘delayed relaxation pattern’, and this finding has been associated with the progression of diastolic dysfunction (see Chapter 1).

5.4.5 Unifying Abnormal Relaxation Indices Through One Parameter

Through mathematical modeling and experimental validation, we have advocated the use of a lumped ‘damping’ parameter c to account for all viscous effects during filling, including both prolonged τ effects and viscous effects of the tissue and blood. Two studies, one animal and one human, found that damping factor c was significantly higher in E-waves acquired from diabetics compared to non-diabetic controls (7, 31). Higher c values implied that the diabetic hearts had dynamic force relationships during diastole that differ from diastolic force relationships found in normal controls, and these differing relationships reliably generated distinguishable transmitral velocity profiles between the two groups. Furthermore, a recent study using simultaneous echo-cath data predicted and validated a significant linear correlation between the E-wave derived c and $1/\tau$, the invasively derived time constant of isovolumic relaxation (4).

5.4.6. Stiffness Only vs Stiffness and Relaxation Models in a Clinical Context

The main difference between the two models presented in Figure 5.3 resides in the relative significance of relaxation/viscosity effects on filling. When relaxation/viscosity effects are small, then equations 5.3 and 5.17 predict the same value for DT, and the two models are virtually equivalent. Such a scenarios would correspond to a fairly symmetric E-wave. As relaxation effects become more pronounced, the symmetry of the E-wave is lost, and the DT grows. It is important to note, however, that in clinical situations where E-waves have a

“restrictive pattern” ie tall and narrow waves with short DT, the waves necessarily have high PDF k values, but that does not imply that $c=0$. Nevertheless, in such cases the value of $c/2k$ in equation 5.17 is much smaller than $\pi/(2\sqrt{k})$, and the predicted $DT_{k,c}$ value is very close to the predicted DT_k value. In other words, for patients with restrictive E-wave, using DT to estimate stiffness by Little et al’s equation will not introduce a significant error. However for patients with a “delayed relaxation” (long DT) E-wave, the parameter c is significant, and the ratio $c/2k$ cannot be ignored. In this case the use of the Little et al equation to estimate stiffness from DT alone will underestimate LV stiffness significantly.

5.4.7 Impact of Viscous Damping on Pressure Gradients

An interesting kinematic consequence of the presence of relaxation/viscoelastic effects relates to the AV pressure gradient. If damping were absent, the elastic recoil of the ventricle would be completely converted to fluid motion, and the AV pressure gradient would vanish when blood acceleration is zero i.e. at the E-wave peak. However, if viscosity is present, zero AV-pressure gradient implies that the damping forces opposing flow equal the inertial force, and therefore the AV pressure gradient would be expected to vanish after the peak of the E-wave. This analysis is similar to the work of Templeton et al, because it predicts that viscous effects will introduce a phase shift between the pressure gradient and the resulting flow. Previous work utilizing frequency based (Fourier) analysis of in-vivo pressure-volume data has also characterized such a phase difference during the E-wave (33).

To make this analysis more precise, we may apply the PDF model to the analysis of the pressure gradient. The analog pressure gradient according to the PDF model is the force per unit area, expressed as $\Delta P=kx(t)$. Thus, the AV pressure gradient vanishes when the displacement

$x(t)=0$. From Chapter 2, we know that in the underdamped ($y<1$) limit, the displacement of the oscillator as a function of time is:

$$x = x_0 e^{-\alpha t} \left(\cos \left(t \sqrt{k} \sqrt{1-y^2} \right) + \frac{y}{\sqrt{1-y^2}} \sin \left(t \sqrt{k} \sqrt{1-y^2} \right) \right) \quad \text{Equation 5.27}$$

We solve for the time when $x=0$:

$$-\frac{\sqrt{1-y^2}}{y} = \tan \left(t \sqrt{k} \sqrt{1-y^2} \right) \quad \text{Equation 5.28}$$

Inverting Eq. 5.28 for time yields:

$$\frac{1}{\sqrt{k} \sqrt{1-y^2}} \tan^{-1} \left(-\frac{\sqrt{1-y^2}}{y} \right) = (t) \quad \text{Equation 5.29}$$

The following identities are useful in simplifying Eq. 5.29:

$$\tan^{-1} \left(-\frac{\sqrt{1-y^2}}{y} \right) = \cos^{-1}(y), \quad \cos^{-1}(y) + \cos^{-1}(-y) = \pi \quad \text{Equation 5.30}$$

Applying 5.30 and 5.9 to 5.29 yield the following expression for the time at which displacement vanishes:

$$t = \frac{1}{\sqrt{k}} \left(\frac{\pi - \cos^{-1}(y)}{\sqrt{1-y^2}} \right) = DT \quad \text{Equation 5.31}$$

Thus, for underdamped waves, the pressure crossover point occurs at a time $t=DT$ after the start of the E-wave. This prediction is of course only valid in the underdamped case, because $x(t)=0$ only at $t=\infty$ in the overdamped case! Furthermore, the PDF model requires that $DT \geq AT$ for all waves, and therefore Eq. 5.31 predicts that the atrioventricular crossover point always occurs on

($c=0$ case) or after ($c>0$ case) the peak of the E-wave. This prediction has yet to be tested directly.

5.5 LIMITATIONS

5.5.1 Appropriateness of A Simplified Approach to Diastolic Function

We acknowledge that ventricular diastolic properties are nonlinear, and nonlinear models of filling, as compared to linear models such as the Little et al model or the PDF model employed in the current study, have the advantage that they can more completely characterize the complex underlying physiology. However, the more complex models cannot be inverted and often are unable to generate a unique set of parameters that fit the clinical data. Therefore these models cannot be employed in the clinical setting (27). Furthermore, previous work in our lab has demonstrated that the PDF model generates a fit to the clinical E-wave contour that is numerically indistinguishable from well-established complex and non-linear models (27). In addition, experiments clearly show that the giant protein titin, which causes myocytes to ‘spring-back’ and ‘push’ as they re-lengthen, while generally non-linear, behaves as a linear, bidirectional spring when evaluated in the usual working range of sarcomere lengths (11).

While a more complex model is sure to yield further insights into the connection between transmitral flow parameters and individual ventricular properties, the simplified kinematic approach presented in the current Chapter elucidates fundamental physiologic components (stiffness/viscoelasticity) that determine filling, and provides an important next step (a higher order correction) to the initial pioneering work of Little et al (23).

5.5.2 Mathematical Interdependence of Parameters

A potential limitation may be that k , c , and DT are all E-wave derived parameters. Therefore one may suspect that k and c are algebraically related, and therefore, one of the variables in Eq. 5.17 can be eliminated, resulting in a one-to-one correspondence between k and DT. While physiology constrains the range of observed values for c and k , we note that k and c are mathematically independent. Apart from the restriction that the wave-shape is underdamped ($\gamma < 1$), and that the parameters are non-negative, there is no explicitly known functional relationship between the two parameters.

5.5.3 Appropriateness of k as a Surrogate for Invasive Stiffness

While a highly linear relationship between stiffness parameter k and $\Delta P_{AVG}/\Delta V_{AVG}$ has been demonstrated in a large sample $n=131$ by Lissauskas (22) and independently repeated for a smaller sample $n=20$ in the current work, one may surmise, from Figure 5.3, that a more appropriate comparison would be in equation 5.17 to utilize catheterization determined $\Delta P_{AVG}/\Delta V_{AVG}$ in place of k . However, our use of k as a surrogate for $\Delta P_{AVG}/\Delta V_{AVG}$ would only be inappropriate if it resulted in a tautology, in the sense of not being able to differentiate one hypothesis from another. If viscoelasticity were not an important determinant of DT, and the E-wave contour were purely the result of elastic and inertial forces, then all E-waves would have concave down deceleration portions and DT and LV stiffness would have a one-to-one correspondence. If resistive forces could be neglected for the entire E-wave, then all E-waves would be symmetric. In this case, the PDF c parameter would vanish, and the k parameter would be exactly equal to Litte et al's $K_{LV} \sim 1/(DT^2)$ (as demonstrated in Kovács et al.(19)). Furthermore, in such a scenario the panels of Figure 5.3 would yield indistinguishable plots for

DT vs. DT_k and DT vs. $DT_{k,c}$. In contrast, if viscoelastic/resistive forces play a discernible role in determining the E-wave contour, then we expect a better fit to the data in the $DT_{k,c}$ panel compared to the DT_k panel, and this is what Figure 5.3 shows. Indeed, the model fit to the data using k and c is significantly better ($p=10^{-42}$) compared to use of k alone, as assessed by a paired t-test of the differences (see results). Thus using the stiffness parameter k rather than $\Delta P_{AVG}/\Delta V_{AVG}$ for comparative analysis is both reasonable and appropriate.

5.5.4 Defining Stiffness From the Average Pressure Volume Slope

While there are numerous definitions for chamber stiffness, physiologists and clinicians routinely define ventricular stiffness as a ratio of pressure changes to volume changes. However, defining chamber stiffness as the slope of the pressure-volume loop introduces a variety of conceptual challenges, because the slope of the P-V loop during diastole varies. Indeed, at mitral valve opening, the instantaneous dP/dV slope is negative (indicating mechanical ventricular suction), and only after minimum pressure has been achieved, does the slope become positive. During isovolumic relaxation or contraction, $dV=0$, which implies a further conceptual hurdle, namely infinite chamber stiffness (5).

To overcome these conceptual challenges, either a multiple beat or an average single beat approach is applied. In the multiple beat approach (see Chapter 4) a pressure volume relationship is constructed from end-diastolic or diastatic pressure volume coordinates over varying load. In the average single beat approach an average of the pressure volume slope, called the operating chamber stiffness and defined as $\Delta P_{AVG}/\Delta V_{AVG} = (P_{EDP}-P_{min})/(V_{EDV}-V_{Pmin})$, is used to estimate ventricular stiffness. Due to a lack of significant load variation in the subject hemodynamics, we utilized the operating chamber stiffness definition in the current work.

Another average pressure volume slope that was utilized in the current Chapter was $\Delta P_E/\Delta V_E$, the slope defined by pressure volume points at minimum pressure and the end of the E-wave. It is important to note that $\Delta P_E/\Delta V_E$ is calculated over a shorter duration (by about a factor of 2) than $\Delta P_{AVG}/\Delta V_{AVG}$ and as such, is more sensitive to exact temporal alignment of the pressure and echo waveform than $\Delta P_{AVG}/\Delta V_{AVG}$. This sensitivity manifests in Figure 5.1 as a larger standard deviation present in the DP_E/DV_E values, and this contributes to the higher p value. However, the differences in invasive chamber stiffness between subjects in Figure 5.1 are significant regardless of which specific regime is chosen to calculate average operating chamber stiffness, and it is this significant difference that serves as the conceptual basis for the work presented in this Chapter.

5.5.5 Inclusion of Low Ejection Fraction Subjects

The subjects in the current Chapter were not chosen with the intent of determining the effects of particular disease states on deceleration time and its dependence on stiffness and relaxation. In fact, a heterogeneous group of subjects was chosen so as to demonstrate that the dependence of deceleration time on both stiffness and relaxation applies independent of systolic or diastolic dysfunction. It may be the case, however, that the inclusion of subjects with systolic dysfunction (ejection fraction <55%) is responsible for the dramatic differences observed in Figure 5.3. However, an sub analysis excluding lower EF patients does not change the results. If the 19 subjects with low EF are removed, the DT vs $DT_{k,c}$ regression becomes $DT=1.18(DT_{k,c})+0.009$, $r^2=0.80$, while the DT vs DT_k regression becomes $DT=1.57(DT_k)+0.02$, $r^2=0.53$. This analysis further bolsters the claim that the connection between DT, stiffness, and relaxation depends on underlying physical principles, and not on specific pathophysiology.

5.5.6 Mitral Valve Area and Atrial Properties

Another minor limitation is the use of E and A-wave velocity time integrals and a constant mitral valve area multiplier for ΔV determination in $\Delta P_{AVG}/\Delta V_{AVG}$ and $\Delta P_E/\Delta V_E$ in the place of conductance catheter data. Indeed, mitral valve area has been shown to vary during diastole (3), and conductance catheter volumes may avoid the error introduced in multiplying the VTI by a constant effective mitral valve area. However, use of constant effective MVA is inherent in the derivation of the expression by Little et al Eq. 5.2. Specifically, expressing ΔV as $VTI \cdot MVA$ the mitral valve area cancels from Eq. 5.2 leaving only ΔP and VTI:

$$\frac{\Delta P}{VTI_{AVG}} = \rho L \left(\frac{\pi}{2DT} \right)^2 \quad \text{Equation 5.32}$$

Finally, left atrial properties, particularly left atrial stiffness, may play a role in determining DT. While some studies suggest that DT is affected jointly by left ventricular and atrial stiffness, during the E-wave the atrium is a conduit and is passive. Indeed, a recent study by Marino et al(24) measured atrial stiffness during diastole in relation to ventricular stiffness and concluded that its role was minor and did not significantly affect DT.

5.6 CONCLUSIONS

Different LVs having the same duration of E-wave DT and similar chamber volume, can have different catheterization determined values for chamber stiffness ($\Delta P_{AVG}/\Delta V_{AVG}$). Model-based analysis of E-waves provides unique values for chamber stiffness ($k \propto \Delta P_{AVG}/\Delta V_{AVG}$) and chamber viscoelasticity (c). For E-waves which are very nearly symmetrically shaped ($AT \cong DT$) about E-wave peak, DT and chamber stiffness are related according to $DT_k = \pi/(2\sqrt{k})$. Once

asymmetry is present and $AT \neq DT$, the E-wave deceleration portion manifests an inflection point and lengthens. The general expression for DT applicable to all E-waves depends on chamber stiffness but also requires inclusion of chamber relaxation/viscoelastic effects according to $DT_{k,c} = \pi/(2\sqrt{k}) + c/(2k)$ in the underdamped limit.

We conclude that quantitative diastolic function assessment warrants consideration of viscoelastic effects in addition to those of stiffness, because E-wave DT is determined by both. This is a general finding for all ventricles, but is most significant for ventricles possessing relaxation abnormalities.

5.7 REFERENCES

1. Appleton CP, Firstenberg MS, Garcia MJ, and Thomas JD. The echo-Doppler evaluation of left ventricular diastolic function. A current perspective. *Cardiology clinics* 18: 513-546, ix, 2000.
2. Bauman L, Chung CS, Karamanoglu M, and Kovács SJ. The peak atrioventricular pressure gradient to transmitral flow relation: kinematic model prediction with in vivo validation. *Journal of the American Society of Echocardiography : official publication of the American Society of Echocardiography* 17: 839-844, 2004.
3. Bowman AW, Frihauf PA, and Kovács SJ. Time-varying effective mitral valve area: prediction and validation using cardiac MRI and Doppler echocardiography in normal subjects. *Am J Physiol Heart Circ Physiol* 287: H1650-1657, 2004.
4. Chung CS, Ajo DM, and Kovács SJ. Isovolumic pressure-to-early rapid filling decay rate relation: model-based derivation and validation via simultaneous catheterization echocardiography. *J Appl Physiol* 100: 528-534, 2006.
5. Chung CS, Strunc A, Oliver R, and Kovács SJ. Diastolic ventricular-vascular stiffness and relaxation relation: elucidation of coupling via pressure phase plane-derived indexes. *Am J Physiol Heart Circ Physiol* 291: H2415-2423, 2006.
6. Courtois M, Kovács SJ, and Ludbrook PA. Transmitral pressure-flow velocity relation. Importance of regional pressure gradients in the left ventricle during diastole. *Circulation* 78: 661-671, 1988.
7. Dent CL, Bowman AW, Scott MJ, Allen JS, Lissauskas JB, Janif M, Wickline SA, and Kovács SJ. Echocardiographic characterization of fundamental mechanisms of abnormal diastolic filling in diabetic rats with a parameterized diastolic filling formalism. *Journal of the*

American Society of Echocardiography : official publication of the American Society of Echocardiography 14: 1166-1172, 2001.

8. Ewert D, Wheeler B, Doetkott C, Ionan C, Pantalos G, and Koenig SC. The effect of heart rate, preload, and afterload on the viscoelastic properties of the swine myocardium. *Ann Biomed Eng* 32: 1211-1222, 2004.

9. Flachskampf FA, Weyman AE, Guerrero JL, and Thomas JD. Calculation of atrioventricular compliance from the mitral flow profile: analytic and in vitro study. *Journal of the American College of Cardiology* 19: 998-1004, 1992.

10. Garcia MJ, Firstenberg MS, Greenberg NL, Smedira N, Rodriguez L, Prior D, and Thomas JD. Estimation of left ventricular operating stiffness from Doppler early filling deceleration time in humans. *Am J Physiol Heart Circ Physiol* 280: H554-561, 2001.

11. Granzier H and Labeit S. The Giant Protein Titin A Major Player in Myocardial Mechanics, Signaling, and Disease. *Circ Res*, 2004.

12. Hall AF and Kovács SJ. Automated method for characterization of diastolic transmitral Doppler velocity contours: early rapid filling. *Ultrasound in medicine & biology* 20: 107-116, 1994.

13. Hess OM, Grimm J, and Krayenbuehl HP. Diastolic simple elastic and viscoelastic properties of the left ventricle in man. *Circulation* 59: 1178-1187, 1979.

14. Kass DA. Assessment of diastolic dysfunction. Invasive modalities. *Cardiology clinics* 18: 571-586, 2000.

15. Kass DA, Bronzwaer JGF, and Paulus WJ. What mechanisms underlie diastolic dysfunction in heart failure? *Circ Res* 94: 1533-1542, 2004.

16. Koide M, Hamawaki M, Narishige T, Sato H, Nemoto S, DeFreyte G, Zile MR, Cooper G IV, and Carabello BA. Microtubule depolymerization normalizes in vivo myocardial contractile function in dogs with pressure-overload left ventricular hypertrophy. *Circulation* 102: 1045-1052, 2000.
17. Kovács SJ, Barzilai B, and Pérez JE. Evaluation of diastolic function with Doppler echocardiography: the PDF formalism. *Am J Physiol* 252: H178-187, 1987.
18. Kovács SJ, Rosado J, Manson McGuire AL, and Hall AF. Can transmitral Doppler E-waves differentiate hypertensive hearts from normal? *Hypertension* 30: 788-795, 1997.
19. Kovács SJ, Setser R, and Hall AF. Left ventricular chamber stiffness from model-based image processing of transmitral Doppler E-waves. *Coronary Artery Disease* 8: 179-187, 1997.
20. Kulke M, Fujita-Becker S, Rostkova E, Neagoe C, Labeit D, Manstein DJ, Gautel M, and Linke WA. Interaction between PEVK-titin and actin filaments: origin of a viscous force component in cardiac myofibrils. *Circ Res* 89: 874-881, 2001.
21. Ling D, Rankin JS, Edwards CH, McHale PA, and Anderson RW. Regional diastolic mechanics of the left ventricle in the conscious dog. *Am J Physiol* 236: H323-330, 1979.
22. Lisauskas JB, Singh J, Bowman AW, and Kovács SJ. Chamber properties from transmitral flow: prediction of average and passive left ventricular diastolic stiffness. *J Appl Physiol* 91: 154-162, 2001.
23. Little WC, Ohno M, Kitzman DW, Thomas JD, and Cheng CP. Determination of left ventricular chamber stiffness from the time for deceleration of early left ventricular filling. *Circulation* 92: 1933-1939, 1995.
24. Marino P, Faggian G, Bertolini P, Mazzucco A, and Little WC. Early mitral deceleration and left atrial stiffness. *Am J Physiol Heart Circ Physiol* 287: H1172-1178, 2004.

25. Marino P, Little WC, Rossi A, Barbieri E, Anselmi M, Destro G, Prioli A, Lanzoni L, and Zardini P. Can left ventricular diastolic stiffness be measured noninvasively? *Journal of the American Society of Echocardiography : official publication of the American Society of Echocardiography* 15: 935-943, 2002.
26. Nikolic SD, Feneley MP, Pajaro OE, Rankin JS, and Yellin EL. Origin of regional pressure gradients in the left ventricle during early diastole. *Am J Physiol* 268: H550-557, 1995.
27. Nudelman S, Manson AL, Hall AF, and Kovács SJ. Comparison of diastolic filling models and their fit to transmitral Doppler contours. *Ultrasound in medicine & biology* 21: 989-999, 1995.
28. Oh JK, Appleton CP, Hatle LK, Nishimura RA, Seward JB, and Tajik AJ. The noninvasive assessment of left ventricular diastolic function with two-dimensional and Doppler echocardiography. *Journal of the American Society of Echocardiography : official publication of the American Society of Echocardiography* 10: 246-270, 1997.
29. Ohno M, Cheng CP, and Little WC. Mechanism of altered patterns of left ventricular filling during the development of congestive heart failure. *Circulation* 89: 2241-2250, 1994.
30. Rankin JS, Arentzen CE, McHale PA, Ling D, and Anderson RW. Viscoelastic properties of the diastolic left ventricle in the conscious dog. *Circ Res* 41: 37-45, 1977.
31. Riordan MM, Chung CS, and Kovács SJ. Diabetes and diastolic function: stiffness and relaxation from transmitral flow. *Ultrasound in medicine & biology* 31: 1589-1596, 2005.
32. Templeton GH and Nardizzi LR. Elastic and viscous stiffness of the canine left ventricle. *Journal of Applied Physiology* 36: 123-127, 1974.

33. Wu Y and Kovács SJ. Frequency-based analysis of the early rapid filling pressure-flow relation elucidates diastolic efficiency mechanisms. *Am J Physiol Heart Circ Physiol* 291: H2942-2949, 2006.
34. Zile MR, Baicu CF, and Gaasch WH. Diastolic heart failure--abnormalities in active relaxation and passive stiffness of the left ventricle. *N Engl J Med* 350: 1953-1959, 2004.
35. Zile MR and Brutsaert DL. New concepts in diastolic dysfunction and diastolic heart failure: Part I: diagnosis, prognosis, and measurements of diastolic function. *Circulation* 105: 1387-1393, 2002.
36. Zile MR, Richardson K, Cowles MK, Buckley JM, Koide M, Cowles BA, Gharpuray V, and Cooper G. Constitutive properties of adult mammalian cardiac muscle cells. *Circulation* 98: 567-579, 1998.

CHAPTER 6.

THE E-WAVE DELAYED RELAXATION PATTERN TO LV PRESSURE
CONTOUR RELATION: MODEL-BASED PREDICTION WITH *IN-VIVO*
VALIDATION

6.1 INTRODUCTION

6.1.1 Noninvasive Diastolic Function Parameters and Relaxation

Echocardiography is the preferred method by which diastolic function is noninvasively assessed (17), and much effort has been devoted to the analysis of Doppler-echo determined transmitral flow velocity contours (E- and A-waves) (1). An established Doppler-echo hallmark of diastolic dysfunction is the ‘delayed relaxation’ pattern, which is characterized by an E-wave that simultaneously has a prolonged deceleration time ($DT > 220\text{ms}$) and a lower peak velocity than the A-wave peak ($E/A < 1$) (14). As we demonstrated in the Chapter 1 and Chapter 2, when one models the E-wave kinematically through the PDF damped simple harmonic oscillator model, the delayed relaxation pattern corresponds to an E-wave with increased damping parameter c .

Because meaningful noninvasive invasive parameters must have invasive hemodynamic analogues, it is important to explore the hemodynamic analogues of noninvasive diastolic function parameters. The hemodynamic analogues of the PDF stiffness parameter k , which is also a determinant of the E-wave deceleration time, have already been explored in previous work (27) and were discussed in the previous chapter. The delayed relaxation pattern and the PDF parameter c , however, have not been fully explored from the hemodynamic perspective.

6.1.2 Challenges With Current Hemodynamic Surrogates of Delayed Relaxation

The connection between the delayed relaxation pattern and diastolic dysfunction has been supported by invasive catheterization studies that report that subjects with a delayed relaxation pattern tend to have a prolonged time-constant of isovolumic relaxation (τ) (2, 29). Similarly, previous work has demonstrated a modest inverse correlation between the PDF determined

damping constant c and $1/\tau$ (5) suggesting that E-waves with elevated PDF c values have prolonged τ .

However, τ is measured before mitral valve opening, when ventricular pressures are elevated and are rapidly changing. The delayed relaxation pattern and the effects of c , however, are observed during filling (E-wave), when pressures are much lower and are slowly changing. These fundamental physiologic differences provide a clue regarding the variable mechanistic and causal relation between τ and the delayed relaxation pattern. Indeed, well-matched subjects with E-waves having delayed relaxation patterns and elevated c values but normal τ can be often encountered (Figure 6.1).

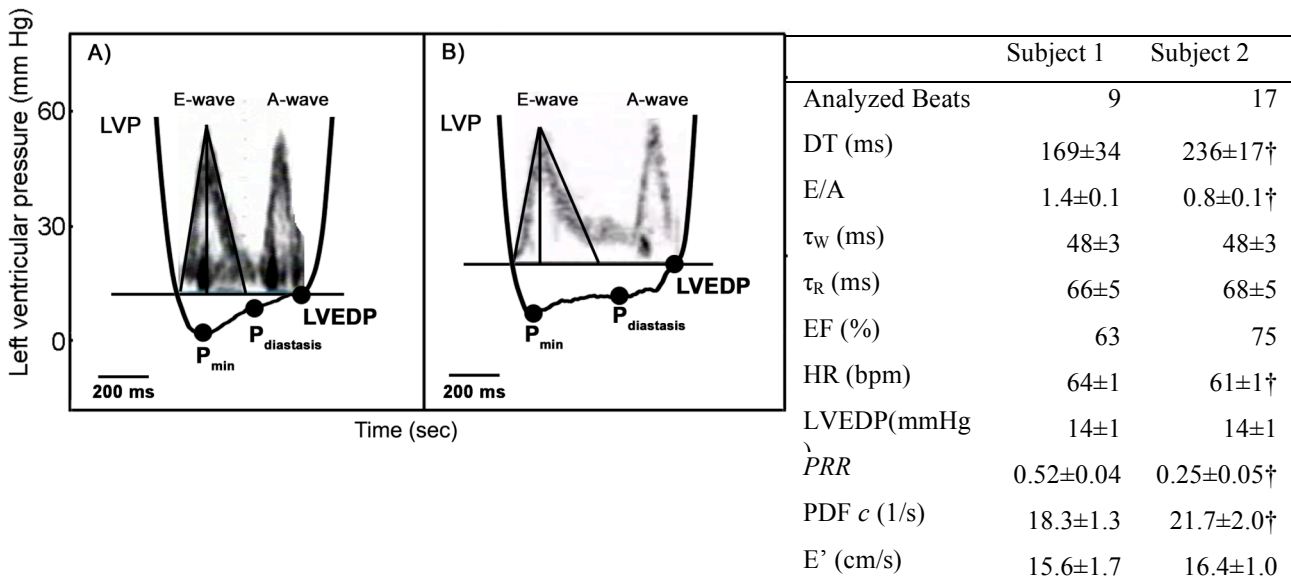


Figure 6.1 and Table 6.1. Simultaneous transmitral flow (Doppler echo) superimposed with LV pressure from two subjects with different E-wave shapes and pressure contours (one representative beat from each patient). Subject 1 had a normal filling pattern while subject 2 had a delayed relaxation pattern. Despite the dramatic difference in E-waves, the time constant of isovolumic relaxation is indistinguishable between the subjects. DT, deceleration time; E/A, E-wave to A-wave peak velocity ratio; τ_w , Weiss model defined isovolumic relaxation time constant; τ_R , Non-zero pressure intercept defined isovolumic relaxation time constant; EF, ejection fraction; HR, heart rate; LVEDP, left ventricular end-diastolic pressure; PRR, pressure recovery ratio, E' - early filling tissue Doppler peak velocity; LVP, left ventricular pressure. †, $p < 0.001$. All other results not significant. See Results for details.

Thus τ is not an accurate hemodynamic analogue of the delayed relaxation pattern or the PDF parameter c and therefore the search for a pressure contour based analogue of filling-related relaxation is warranted. One easily visualized filling-related feature of the pressure contour is the recovery of pressure from the minimum pressure to diastasis. We hypothesize that, in the setting of a normal mitral valve, normalizing this pressure rise to the difference between the minimum pressure and a fiducial filling pressure provides a novel and causal analogue of the delayed relaxation pattern. We call this dimensionless hemodynamic index the pressure recovery ratio (PRR), and validate our hypothesis by comparing the PRR between subjects with and without a delayed relaxation pattern. In addition, we apply mathematical methods to derive a causal connection between PRR and the E-wave PDF model based damping constant c , and validate the predicted correlation in subjects with and without a delayed relaxation pattern.

6.2 METHODS

6.2.1 Mathematical Derivation

Applying Bernoulli's Equation To Filling

To gain insight into the hemodynamic analogue of c , one needs to apply the PDF model to cardiovascular pressures. A natural starting point is the Bernoulli equation for non-steady flow:

$$LAP = LVP + \frac{1}{2}\rho v^2 + \rho \int_{LA}^{LV} \frac{\partial v(s,t)}{\partial t} ds \quad \text{Equation 6.1}$$

where we assume that blood flow velocity in the atrium is small compared with the blood flow velocity in the ventricle, and fluid viscous energy losses are negligible. The assumption that fluid viscous energy losses is warranted (12), but importantly does not eliminate tissue energy losses

from the model. Tissue energy losses will simply be reflected in the damping components of the velocity and acceleration terms.

In Equation 6.1, ρ is the density of blood, v is the transmitral velocity and is a function of both location along the streamline and time, LAP is the left atrial pressure, and LVP is the left ventricular pressure. The integral is the acceleration term, and can be approximated as $MI \cdot (dv/dt)$, (41) where MI (*constant*) is the mitral inertiance. This approximation applied to Equation 6.1 yields:

$$\Delta P = \frac{1}{2} \rho v^2 + MI \cdot \dot{v} \quad \text{Equation 6.2}$$

, where ΔP is LAP-LVP.

Determining a PDF Model Consistent Expressions for Mitral Inertiance

Both $v(t)$ and $\dot{v}(t)$ can be expressed in terms of the PDF parameters, but the value of MI at first glance seems to be a free parameter. This parameter can be set to a specific value consistent with the PDF model, however, when one considers the time at which $\Delta P=0$. Both theoretical considerations and experimental findings (10) have shown that ΔP must be positive to drive initial suction mediated filling, and must be negative towards the end of filling in order to decelerate the blood and tissue. Because the net force associated with filling is equal to $k \cdot x(t)$ by the PDF model, and is physiologically proportional to ΔP , it is reasonable to define the $\Delta P=0$ crossover point as the time at which $x(t)=0$. In the previous Chapter we showed that $x(DT)=0$. Thus, we can plug $t=DT$ into Equation 6.2, and because $\Delta P(DT)$ must vanish, we can find a simple expression for MI :

$$MI = -\frac{\rho v^2(DT)}{2\dot{v}(DT)} \quad \text{Equation 6.3}$$

In the analysis that follows we will work out the under-damped case. From Chapter 2, we have the following expression for transmitral velocity:

$$v(t) = \frac{kx_o}{\omega} e^{-\alpha t} \sin(\omega t) \quad \text{Equation 6.4}$$

with $\alpha = \frac{c}{2}$ and $\omega = \frac{\sqrt{4k - c^2}}{2}$. Taking the derivative of Eq. 6.4 yields the necessary

acceleration equation:

$$\dot{v}(t) = v(t) \cdot (\omega \cot(\omega t) - \alpha) \quad \text{Equation 6.5}$$

Putting Eq. 6.5 together with Eq. 6.4 and Eq. 6.3 gives us a more complete expression for MI :

$$MI = -\frac{1}{2} \rho \frac{v(DT)}{(\omega \cot(\omega DT) - \alpha)} \quad \text{Equation 6.6}$$

In the Chapter 5 we found an expression for DT in terms of k and $y = \frac{c}{2\sqrt{k}}$. This equation may

be applied to evaluate $\cot(\omega t)$:

$$\cot(\omega DT) = \cot\left(\pi - \cos^{-1}(y)\right) = \frac{-\cos\left(\cos^{-1}(y)\right)}{\sqrt{1 - \cos^2\left(\cos^{-1}(y)\right)}} = -\frac{\alpha}{\omega} \quad \text{Equation 6.7}$$

Applying Eq. 6.7 to 6.6 provides a far simpler expression for MI :

$$MI = \frac{1}{2} \rho v(DT) \cdot \frac{1}{2\alpha} \quad \text{Equation 6.8}$$

Thus we have solved for the mitral intertiance factor MI and ensured that the Bernoulli equation is internally consistent with the assumptions of the PDF model.

Determining and Applying a PDF Consistent Bernoulli Equation

With Eq 6.8 and 6.2, we may write the pressure gradient at any given time t as:

$$\Delta P(t) = \frac{1}{2} \rho v(t) \cdot \left[v(t) + \frac{1}{2} v(DT) \left(\frac{\omega}{\alpha} \cot(\omega t) - 1 \right) \right] \quad \text{Equation 6.9}$$

We plot Eq 6.8 with representative values for ω and α in Figure 6.2 below. Consistent with experimental findings (10) the ΔP plot is a damped oscillator with a pressure crossover at $t = DT$.

The dependence of ΔP on c in Eq 6.9 is not apparent, though the effect of c can be readily

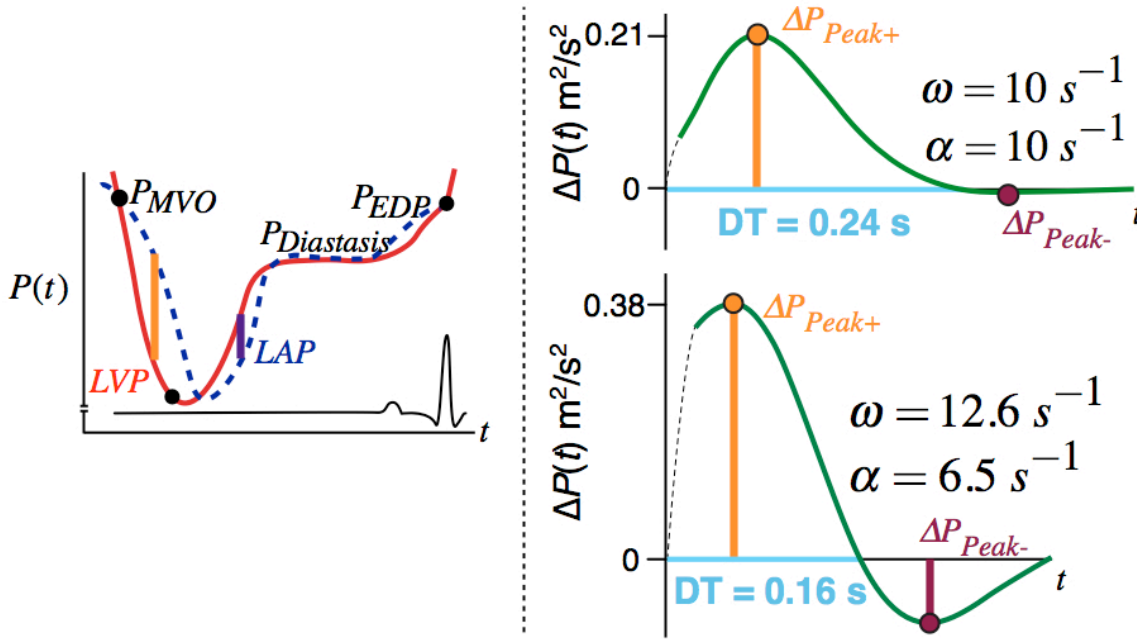


Figure 6.2: Left panel: Left ventricular pressure (LVP) contour between mitral valve opening and end diastole, with a schematic atrial pressure (LAP) signal superimposed. P_{MVO} - pressure at mitral valve opening, P_{EDP} - pressure at end diastole. Right panel: ΔP from equation 6.9 with different ω and α values. DT - deceleration time. ΔP_{Peak+} - peak positive pressure gradient; ΔP_{Peak-} - peak negative pressure gradient.

appreciated by comparing the peak positive ΔP with the peak negative ΔP . Clearly larger values of c lead to relatively smaller values of peak negative ΔP (Figure 6.2). Thus, to focus our analysis on c and ΔP , it is useful to define a new parameter, the peak pressure-gradient ratio ($PPGR$):

$$PPGR = \left| \frac{\Delta P_{PeakNegativeGradient}}{\Delta P_{PeakPositiveGradient}} \right| \quad \text{Equation 6.10}$$

Simplification of PPGR

To simplify, we note that the positive ΔP portion and negative ΔP portion of the graph are nearly symmetric, and therefore the peak positive ΔP occurs near a time $t = DT + \frac{1}{2}AT$, and the peak negative ΔP occurs near $t = \frac{1}{2}DT$. Numerical simulation with 180 randomly picked physiologic c and k values was performed to confirm this simplification. The result showed that the peak pressure gradient recovery ratio measured at these two estimated time points is a very good approximation to the value of the peak pressure gradient recovery ratio at the actual peaks of the gradients (see Figure 6.3).

With this approximation, the peak pressure gradient recovery ratio becomes:

$$PPGR \approx \left| \frac{\Delta P_{t=DT+\frac{1}{2}AT}}{\Delta P_{t=\frac{1}{2}DT}} \right| = e^{-\frac{y}{\sqrt{1-y^2}}\pi} \left| \frac{\frac{1}{1+y} - \frac{1+2y}{y\sqrt{2+2y}} e^{\frac{y\cos^{-1}(y)}{2\sqrt{1-y^2}}}}{\frac{1}{1-y} + \frac{1-2y}{y\sqrt{2-2y}} e^{-\frac{y(\pi-\cos^{-1}(y))}{2\sqrt{1-y^2}}}} \right| \quad \text{Equation 6.11}$$

, where $y = \frac{c}{2\sqrt{k}}$. For the clinical data analyzed, underdamped E-waves had y values between 0.3 and 1.0. Thus $PPGR$ becomes a function of y , and a MATLAB numerical simulation was performed whereby the relationship of $PPGR$ to y was visually assessed. Figure 6.3B shows the strong linear relationship between $PPGR$ and y . Thus, the $PPGR$, is predicted to be linearly related to $y = \frac{c}{2\sqrt{k}}$. To assess the relationship between $PPGR$ and c alone, we picked 180 random combinations of c and k and calculated the expression in Eq. 6.11. Figure 6.3C shows the strong linear relationship between $PPGR$ and c for these random (k, c) combinations.

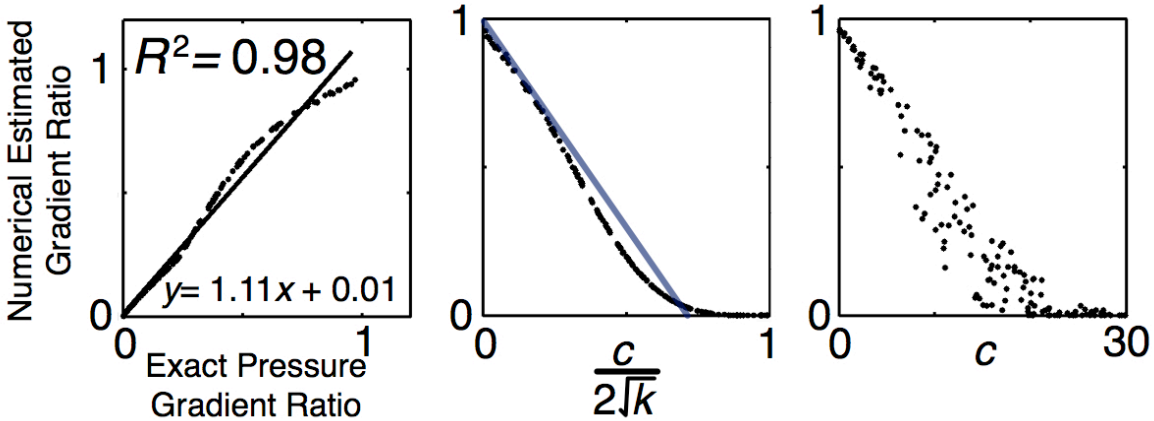


Figure 6.3. Results of numerical experiments demonstrating the linear relationship between theoretically calculated pressure gradient recovery ratio (*PPGR*) and c , derived from Bernoulli's equation. A) Correlation between the simulated pressure gradient peak ratio and the numerically estimated pressure gradient peak ratio. B) Relationship between the numerically estimated peak pressure gradient ratio and $y = \frac{c}{2\sqrt{k}}$. The linear Taylor expansion approximation is shown in blue. C) Relationship between the numerically estimated peak pressure gradient ratio and the E-wave derived relaxation/viscoelastic parameter c . See text for details.

Approximating PPGR in the $y \ll 1$ limit

While the numerical approach provides insight into the relationship between *PPGR* and y , a more analytic approach may provide additional insight into the slope between *PPGR* and y . Equation 6.11 appears daunting at first and not amenable to further simplification, but progress can be made by defining the numerator as a separate function:

$$f(y) = \frac{1}{1+y} - \frac{1+2y}{y\sqrt{2+2y}} e^{\frac{y \cos^{-1}(y)}{2\sqrt{1-y^2}}} \quad \text{Equation 6.12}$$

Remarkably the denominator in Eq. 6.11 is simply $f(-y)$! Expanding $f(y)$ around $y=0$ yields the following Taylor expansion:

$$f(y) = \lambda - \frac{\gamma}{y} + O(y) \quad \text{Equation 6.13}$$

$$\lambda = \frac{1}{\sqrt{2}} \left(\sqrt{2} - \frac{\pi}{4} - \frac{3}{2} \right) \quad \gamma = -\frac{1}{\sqrt{2}}$$

With Eq. 6.13 we can continue the series expansion of *PPGR* around $y=0$:

$$PPGR \approx \left| e^{-\frac{y}{\sqrt{1-y^2}}\pi} \left[\frac{f(y)}{f(-y)} \right] \right| = \left| (1 - \pi y + \dots) \left(-1 + \frac{2\lambda}{\lambda} y + \dots \right) \right| = 1 - \left(\frac{\pi}{2} + 2\sqrt{2} - 3 \right) y + O(y^2) \quad \text{Equation 6.14}$$

, where λ and γ are defined in Eq. 6.13. The blue line in Figure 6.3B above demonstrates the close agreement between a numerically determined *PPGR* by Eq. 6.11 and the linear approximation derived in Eq. 6.14. Thus both numerical and analytic techniques demonstrate the *PPGR* is linearly related to y , and because $y = \frac{c}{2\sqrt{k}}$, we can see that *PPGR* is predicted to be linearly related to c . Eq. 6.14 therefore provides the predicted connection between the noninvasively determined PDF parameter c and an invasively determined pressure-based index.

6.2.2 Clinical Application of the Derivation: The Pressure Recovery Ratio

A Clinical Surrogate for PPGR

While the derivation above is focused on ratios of pressure gradients, in clinical practice, only LVP is routinely measured. Thus to apply Eq. 6.10 in the clinical setting, another approximation must be made. It is established that both LVP and LAP decrease and then recover during early filling (10), eventually both converging at the same diastatic pressure. In fact, the LAP and LVP contours are quite similar, with the LAP contour simply being offset in time relative to the LVP contour³⁶. Thus, a symmetry argument may be applied to define a LVP based (LAP independent) equivalent to the *PPGR*. We call this the pressure recovery ratio (*PRR*), and define it as the ratio of pressure drop between mitral valve opening and minimum pressure to the pressure rise between minimum pressure and diastasis:

$$PRR = \frac{LVP_{Diastasis} - LVP_{Minimum}}{LVP_{MVO} - LVP_{Minimum}} \quad \text{Equation 6.15}$$

Thus, in analogy to the *PPGR* and in accordance with mechanical suction-initiated kinematic filling and energy conservation, Equation 6.14 implies that *PRR* is the hemodynamic surrogate of the PDF parameter *c*. This suggests that in a purely elastic ventricle with negligible energy losses, the LVP contour will take the shape of an inverted symmetric wave (i.e. such as a sine wave) between mitral valve opening (MVO) and diastasis, thereby defining a *PRR* value of 1. A chamber with significant viscous energy losses or filling-related relaxation, however, will have a pressure contour that recovers from minimum pressure (P_{MIN}) to a diastasis pressure ($P_{Diastasis}$) that is well below P_{MVO} , thereby defining a *PRR* value less than 1.

Choice of Fiducial Pressure

P_{MVO} can be reliably estimated hemodynamically using simultaneous LVP and pulmonary artery occlusive or “wedge” pressure recording, but is rarely measured during routine diagnostic left heart cath/coronary angiography procedures. Therefore a fiducial filling related pressure that is analogous to P_{MVO} must be utilized in order to allow for routine clinical application of the *PRR*. There are several fiducial pressures that one may choose, and for subjects in normal sinus rhythm (NSR) we choose the left ventricular end-diastolic pressure (LVEDP) to be a fiducial surrogate for P_{MVO} . This choice is supported by studies showing that LVEDP is a reasonable approximation to P_{MVO} in subjects with NSR and no significant pathophysiology (3, 18, 32, 33). Thus in the current study we calculated *PRR* for NSR subjects by the following equation:

$$PRR = \frac{P_{Diastatic} - P_{Min}}{LVEDP - P_{Min}} \quad \text{Equation 6.16}$$

LVEDP can not be used as the fiducial pressure for P_{MVO} in the setting of atrial fibrillation (AF). Instead, we selected LV pressure at minimum dP/dt ($P_{dP/dtMin}$) as the fiducial early-rapid filling related pressure in the setting of AF. Thus PRR in AF subjects was defined as:

$$PRR^{(AF)} = \frac{P_{Diastatic} - P_{Min}}{P_{dP/dtMin} - P_{Min}} \quad \text{Equation 6.17}$$

6.2.3 Experimental Validation of PRR

Subjects

Datasets from 40 subjects with NSR and 9 subjects with AF (total of 49 subjects) were selected from the Cardiovascular Biophysics Laboratory Database of simultaneous micromanometric catheter recorded left ventricular pressure (LVP) and echocardiographic data (26). The method of simultaneous echocardiographic transmitral flow and pressure-volume data recording was described in Chapter 2, and an example of simultaneous echocardiographic-hemodynamic data is presented in Figure 6.1.

All subjects provided informed consent prior to the procedure in accordance with a protocol approved by the Barnes-Jewish Hospital/Washington University Human Research Protection Office (HRPO). The criteria for data selection included: normal valvular function, no active ischemia, and no significant merging between echocardiographic E- and A- waves. None of the 49 subjects had previous myocardial infarction or peripheral vascular disease. Thirty nine out of 40 NSR subjects had normal ejection fraction ($EF > 55\%$) and 4 out of 9 AF subjects had an EF lower than 55%.

Subjects in NSR were divided into 3 groups related to presence or absence of an echocardiographically determined delayed relaxation pattern. Group 1, the full delayed relaxation pattern group (DR), consisted of subjects with both an $E/A < 1$ and a $DT > 220ms$ (15).

Group 2, the partially delayed relaxation group (PDR), consisted of subjects with either an $E/A < 1$, or a $DT > 220$ ms. Group 3, the normal relaxation pattern group (NMLR) consisted of subjects with normal transmitral flow patterns ($E/A > 1$ and $DT < 220$ ms) and with normal Doppler tissue E' (> 8 cm/s) or normal velocity of propagation ($V_p > 45$ cm/s) values. Table 6.2 presents demographic data for the NSR and AF subjects. Several hemodynamic indexes, including PRR , and several echocardiographic indexes were analyzed from multiple beats in each subject.

Table 6. 2

	DR	PDR	NMLR	NSR	AF
Size of the group	9	15	16	40	9
Age	65±7	60±9	52±8 ^{†††}	58±10	61±9
Sex (m/f)	6/3	11/4	8/8	25/15	8/1
Race (w/b)	7/2	12/3	12/4	31/9	7/2
HR	61±8	60±7	63±8	62±7	84±22
Systolic Blood Pressure (mmHg)	149±22	126±14 ^{**}	135±30	135±24	130±15
Diastolic Blood Pressure (mmHg)	74±7	70±9	76±16	74±12	80±10
EF (%)	67±11	71±8	76±6 [*]	72±9	51±19
LVEDV (ml)	180±51	145±32	148±39	154±41	170±50
P _{Min} (mmHg)	11±3	8±2 [*]	9±3	9±3	9±3
P _{Diastasis} (mmHg)	13±4	12±2	14±4	13±3	17±6
LVEDP (mmHg)	20±6	19±3	19±4	19±4	17±6 [‡]
PRR	0.31±0.12	0.39±0.08 [*]	0.48±0.08 ^{***††}	0.41±0.11	N.A.
PDF parameter c (1/s)	21.3±2.5	19.2±1.9 [*]	17.5±1.7 ^{***††}	19.0±2.4	17.6±3.4
PDF parameter k (1/s ²)	169±28	168±45	175±32	171±36	241.2±78.7
Isovolumic relaxation time constant (τ_w) (ms)	53±5	52±7	51±6	52±6	56±6
Isovolumic relaxation time constant (τ_R) (ms)	65±6	59±7	60±9	61±8	76±19
IVRT (ms)	112±16	74±13 ^{***}	72±13 ^{***}	82±21	79±14
E-wave acceleration time (AT) (ms)	98±9	97±16	91±11	95±13	95±17
E-wave deceleration time (DT) (ms)	239±15	225±36	185±27 ^{***††}	212±36	187±44
E-wave duration (ms)	336±22	320±49	276±34 ^{***††}	306±45	283±60
E-wave peak (cm/s)	65.9±15.2	76.3±15.9	81.3±15.7 [*]	76±16	90±35
A-wave peak (cm/s)	73.2±12.0	71.8±11.2	68.8±14.6	71±13	N.A.
E/A	0.9±0.1	1.1±0.2 [*]	1.2±0.2 ^{***}	1.1±0.2	N.A.
E-wave VTI (cm)	11.0±2.2	12.3±3.7	11.3±2.7	12±3	13±7
A-wave VTI (cm)	6.9±1.4	7.7±1.2	6.1±1.4 ^{††}	7±1	N.A.
VTI _E /VTI _A	1.6±0.2	1.6±0.3	1.9±0.3 ^{†††}	1.7±0.3	N.A.
Tissue Doppler E' peak (cm/s)	13.2±3.9	15.1±3.6	14.3±3.9	14.1±3.9	N.A.

Clinical descriptors and other physiologic measurements including invasive and noninvasive indexes in NSR and AF groups. Comparisons between three NSR groups (DR, PDR, and NMLR) are also included. *, significantly different ($p < 0.05$) from delayed relaxation group. **, significantly different ($p < 0.01$) from delayed relaxation group. ***, significantly different ($p < 0.001$) from delayed relaxation group. †, significantly different ($p < 0.05$) from PDR group. ††, significantly different ($p < 0.01$) from PDR group. †††, significantly different ($p < 0.001$) from PDR group. ‡, LVEDP=P_{diastasis} in AF. PRR in AF group is calculated using Eq. 3. DR, delayed relaxation pattern group. PDR, partial delayed relaxation pattern group. NMLR, normal relaxation group. NSR, normal sinus rhythm group including all patients in DR, PDR, and NMLR groups. AF, atrial fibrillation. VTI, velocity time integral. LVEF determined by ventriculography. Data are presented as mean ± standard deviation.

Hemodynamic Analysis

Hemodynamic values and parameters (P_{Min} , $P_{dP/dt\text{Min}}$, $P_{\text{Diastasis}}$, LVEDP, τ) were determined from the high-fidelity Millar LVP data for each beat. Diastatic pressure and LVEDP values were measured at the peaks of the P- and R- waves on the simultaneous ECG, respectively using a custom LABVIEW (National Instruments, Austin, TX) program. Isovolumic relaxation time constant (τ) was calculated from the isovolumic pressure decay contour for all measured beats in each patient according to two methods, a zero pressure asymptote method (τ_{W}) and a floating asymptote method (τ_{R}) (See Chapter 2)

The *PRR* was calculated according to Equation 6.16 for each beat in each NSR subject, and according to Equation 6.17 for each beat in each AF subject.

Because LVEDP may not be a strong correlate of P_{MVO} in subjects with diastolic dysfunction, we determined the sensitivity of *PRR* to the particular choice of fiducial P_{MVO} pressure. Instead of choosing LVEDP as the fiducial filling pressure, we considered 11 additional choices of fiducial pressures. We considered 4 *PRR* definitions (PRR^{1-4}) where the fiducial pressure was chosen 0ms, 10ms, 30 ms, and 60ms after P_{Max} , respectively. In addition we considered 7 alternate *PRR* definitions (PRR^{5-11}) where the fiducial pressure was chosen -20ms, -10ms, -5ms, 0ms, 10ms, 20ms, and 30 ms after the minimum dP/dt , respectively. See Figure 6.4A for a pictorial representation of these alternative fiducial pressure values. *PRR* values defined by the 11 alternative fiducial pressure choices described above were calculated for all beats in all NSR subjects. We note that these alternative choices for the fiducial pressure were employed to serve only as a test of the dependence of *PRR* on the choice of initial diastolic

fiducial pressure. Each alternative choice was compared to the preferred PRR defined by Equation 6.16 in NSR, and Equation 6.17 in AF.

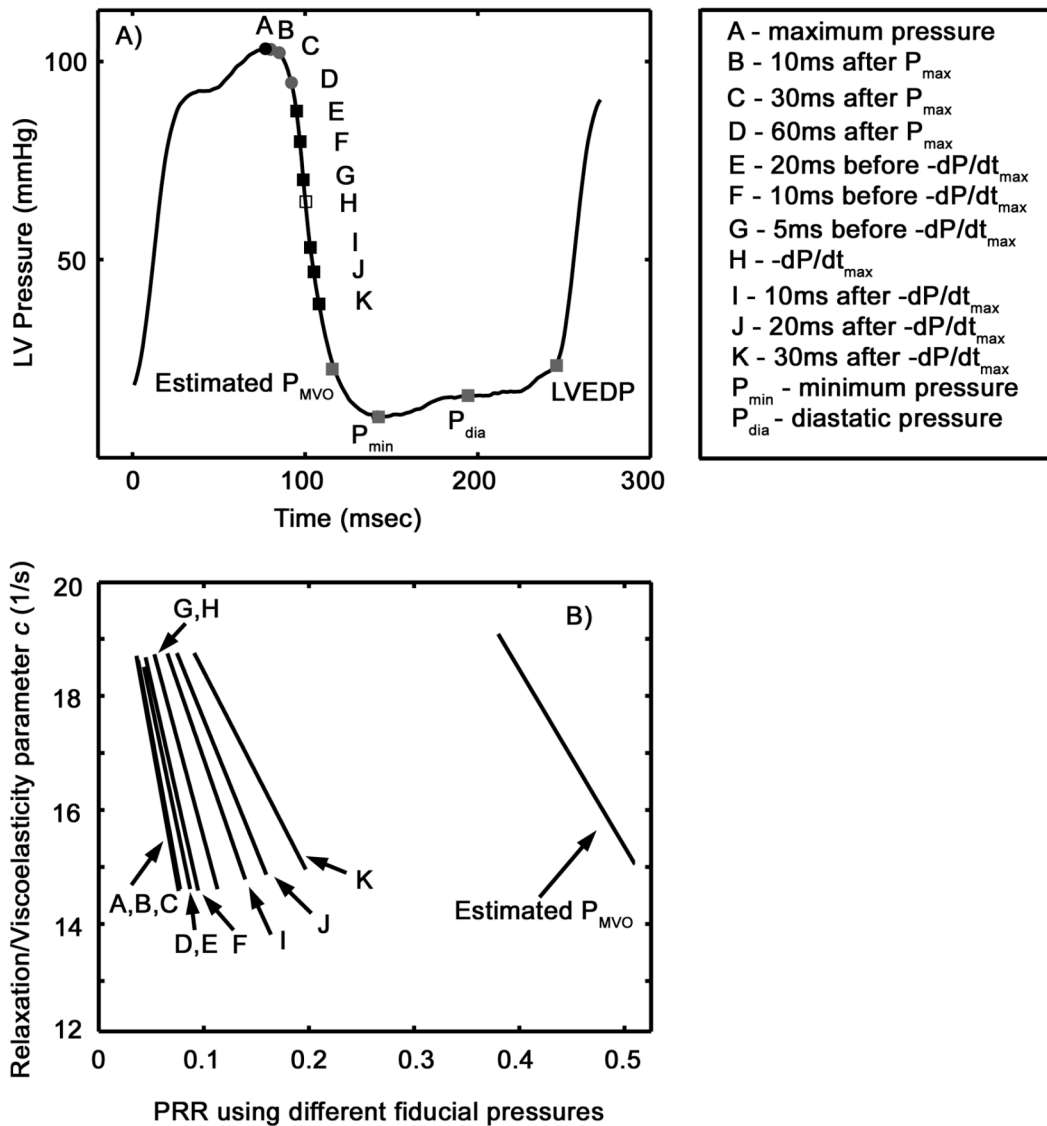


Figure 6.4. A) Pressure tracing showing 12 different choices of fiducial pressures. B) Linear correlations between relaxation/viscoelasticity parameter c and PRR using different fiducial pressures. The letters next to the lines represent the fiducial pressures used to generate the lines. See text for details.

Doppler E-wave Analysis

For each subject, an average of 9 cardiac cycles were analyzed (354 heart beats total for 40 NSR subjects, 113 heart beats for 9 AF patients, total of 467 heart beats). Conventional, triangle approximations of E- and A-wave shapes provided peak E-wave velocity (E_{peak}), E-wave acceleration and deceleration times (AT and DT), E-wave duration and velocity-time integral (E_{dur} and VTI_E), peak A-wave velocity (A_{peak}), and A-wave velocity-time integral (VTI_A). Furthermore the ratios of E_{peak} to A_{peak} ($E_{\text{peak}}/A_{\text{peak}}$) and VTI_E to VTI_A ($\text{VTI}_E/\text{VTI}_A$) were calculated for all beats. The isovolumic relaxation time (IVRT) was also measured. Doppler tissue imaging (DTI) lateral E'- and A'-waves was available in 39 out of 40 NSR patients. Flow propagation velocity (V_p) was determined according to conventional method (13) for the one subject without DTI E'- and A'-wave data.

In addition, all E-waves were subjected to Parametrized Diastolic Filling (PDF) model-based image processing (MBIP) to yield E-wave specific kinematic model parameters (relaxation/viscoelasticity parameter c , stiffness parameter k , initial load parameter x_0) for each E-wave. See Chapter 2 for triangle based and PDF-model based fitting details.

Comparison of Invasive and Noninvasive Relaxation Parameters

All invasive and noninvasive parameters of interest (E/A , $\text{VTI}_E/\text{VTI}_A$, DT, PRR , c , τ_w , τ_R) were averaged for each of the 49 subjects and several comparisons were performed.

First, values of interest were compared between Group 1 (DR), Group 2 (PDR), and Group 3 (NMLR) NSR subjects. Student's t-tests were utilized to assess whether the PRR , defined by Eq. 6.16 or by one of the alternate fiducial pressures (PRR^{1-11}), was significantly different between the three NSR groups. Similar analysis was performed for DT, E/A , τ_w , τ_R , and LVEDP.

Second, values of interest were compared in a continuous fashion through linear regressions. Linear regressions between c , DT, E/A, VTI_E/VTI_A , and PRR were performed. For each variable of interest, two types of linear regressions were calculated. First, linear regressions between each variable of interest and PRR for all 354 beats pooled from all NSR subjects were performed. Second, linear regression of the variables averaged over each of the 40 NSR subjects was also performed relative to a similarly averaged PRR value. Equivalent analysis was undertaken for the 9 subjects with AF.

In addition, 11 separate linear regressions between c and the PRR^{1-11} values defined by each of the alternative fiducial pressure choices were performed. All statistical analyses utilized MS-Excel (Microsoft, Redmond, WA).

6.3 RESULTS

6.3.1 Comparisons of conventional and novel indexes between groups

In the delayed relaxation group ($n=9$), 3 (33%) subjects had normal τ_w values ($\tau_w < 50$ ms). In the PDR group ($n=15$), 9 (60%) subjects had normal τ_w values. In the NMLR group ($n=16$), 7 (44%) subjects had normal τ_w values. The τ_w values in the three groups did not differ from each other significantly ($p=0.86$ between delayed relaxation and PDR, $p=0.64$ between PDR and NMLR, $p=0.52$ between delayed relaxation and NMLR) by unpaired Student's t-test. Similar to τ_w , τ_R was also statistically indistinguishable among the three groups ($p=0.07$ between delayed relaxation and PDR, $p=0.75$ between PDR and NMLR, $p=0.20$ between delayed relaxation and NMLR). Figure 6.1 shows two representative subjects, one from the delayed relaxation group and one from the NMLR group respectively, to illustrate the variable relationship between delayed relaxation pattern and τ_w . Although the two subjects had similar,

normal τ_w values, subject 1 had a normal filling pattern and subject 2 had a delayed relaxation pattern. Detailed data from these two subjects is given in Table 6.1. As shown in Table 6.2 and Figure 6.5, DT did not differentiate the delayed relaxation from the PDR group, but did differentiate the delayed relaxation and the PDR groups from the NMLR group ($p < 0.001$, $p < 0.01$, respectively). E-wave duration differentiated the delayed relaxation and PDR groups from the NMLR group ($p < 0.001$, $p < 0.01$, respectively), but not the delayed relaxation from the

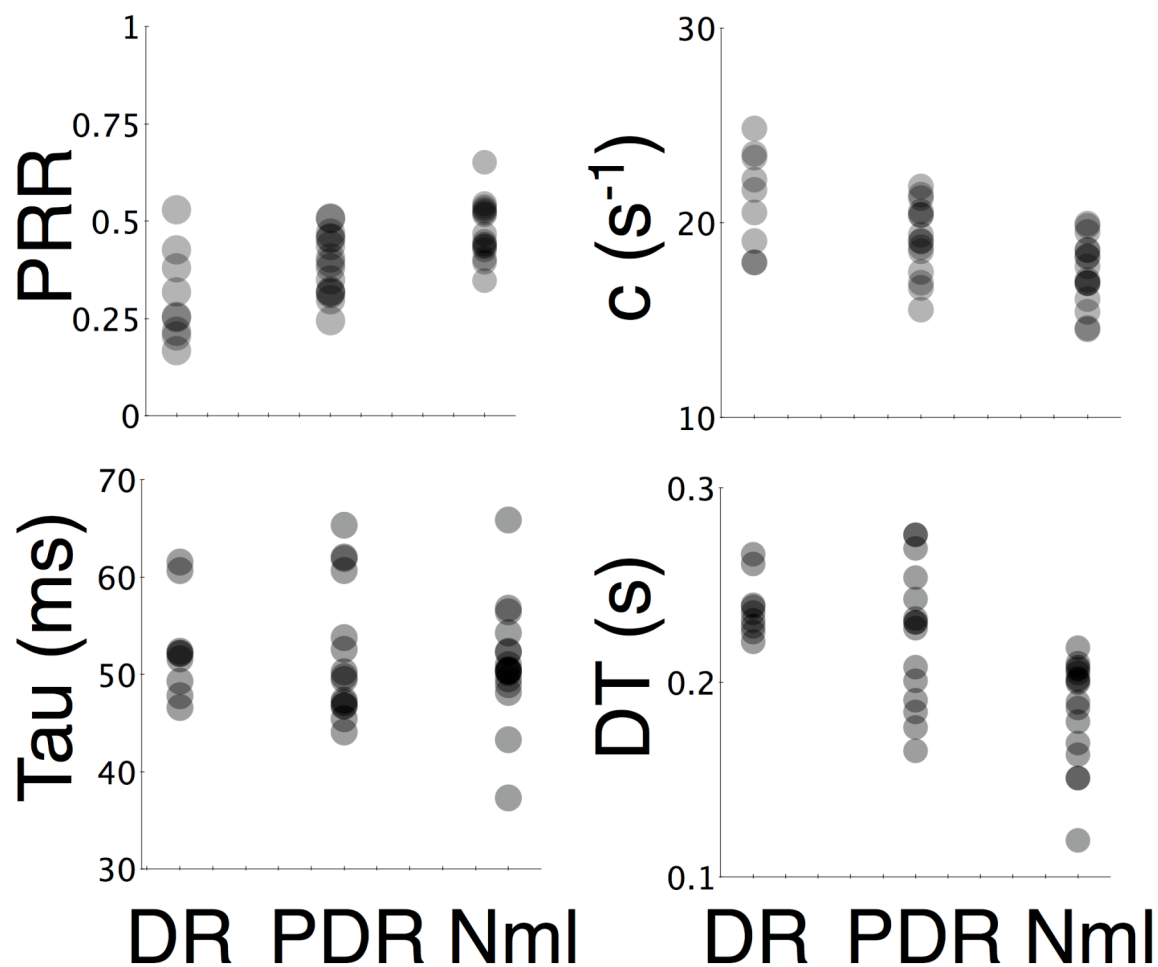


Figure 6.5. Comparison of pressure recovery ratio (PRR), E-wave damping parameter (c), deceleration time (DT) and τ among delayed relaxation (DR), partially delayed relaxation (PDR) and normal relaxation filling pattern (NMLR) groups. (A) pressure recovery ratio. (B) Parametrized diastolic filling (PDF) relaxation/viscoelastic parameter c . (C) time constant of isovolumic relaxation τ . (D) E-wave DT. Detailed comparisons are also provided in Table 6.2. See text for details.

PDR group. E_{peak} failed to differentiate both the delayed relaxation group from the PDR group and the PDR group from the NMLR group, but did differentiate the delayed relaxation from the NMLR group ($p < 0.05$). A_{peak} was indistinguishable between groups. E/A , however, differentiated the delayed relaxation group from both the PDR group ($p < 0.05$) and the NMLR group ($p < 0.001$), but not the PDR group from the NMLR group. The PDF parameter c was significantly different between the three groups ($p < 0.05$ between the delayed relaxation and PDR groups, $p < 0.01$ between the PDR and NMLR groups, $p < 0.001$ between the delayed relaxation and NMLR groups).

6.3.2 Sinus Rhythm Group – *PRR* with LVEDP as Fiducial Pressure

The clinical descriptors of the 40 NSR subjects and their hemodynamic and echocardiographic indexes are shown in Table 6.2.

As predicted by the algebraic derivation above, *PRR* and c were found to be strongly linearly correlated ($c = -20.2 \times PRR + 27.2$, $R^2 = 0.77$) over all analyzed NSR beats (Figure 6.6A). The individual regressions in all NSR subjects were similar (Figure 6.6 B) and collinear with the overall regression. The averaged *PRR* vs. c R^2 across 40 NSR subjects was 0.82 ± 0.13 . When average values for each subject were compared, *PRR* and c maintained the expected strong linear correlation ($c = -19.7 \times PRR + 27.0$, $R^2 = 0.79$).

PRR did not significantly correlate with typical conventional indexes of diastolic function such as E/A ($R^2 = 0.14$), VTI_E/VTI_A ($R^2 = 0.11$), and DT ($R^2 = 0.01$) across all beats in NSR subjects.

Unlike average τ_w and τ_R values, average PRR values were significantly different between the delayed relaxation and PDR groups ($p<0.05$), the PDR and NMLR group ($p<0.01$), and delayed relaxation and NMLR groups ($p<0.001$) (shown in Table 6.1, and Figure 6.5).

E' velocities in 39 of the 40 NSR subjects were determined. E' was similar in all three groups (13.2 ± 3.9 cm/s in delayed relaxation group, 15.1 ± 3.6 cm/s in PDR group, and 14.3 ± 3.9 cm/s in the NMLR group, $p=0.25$ between delayed relaxation and PDR, $p=0.56$ between PDR and NMLR, $p=0.52$ between delayed relaxation and NMLR).

PRR had very weak correlations with end systolic volume (ESV) ($R^2=0.10$, $p=0.43$), end diastolic volume (EDV) ($R^2=0.06$, $p>0.05$), systolic blood pressure ($R^2=0.03$), and diastolic blood pressure ($R^2=0.01$).

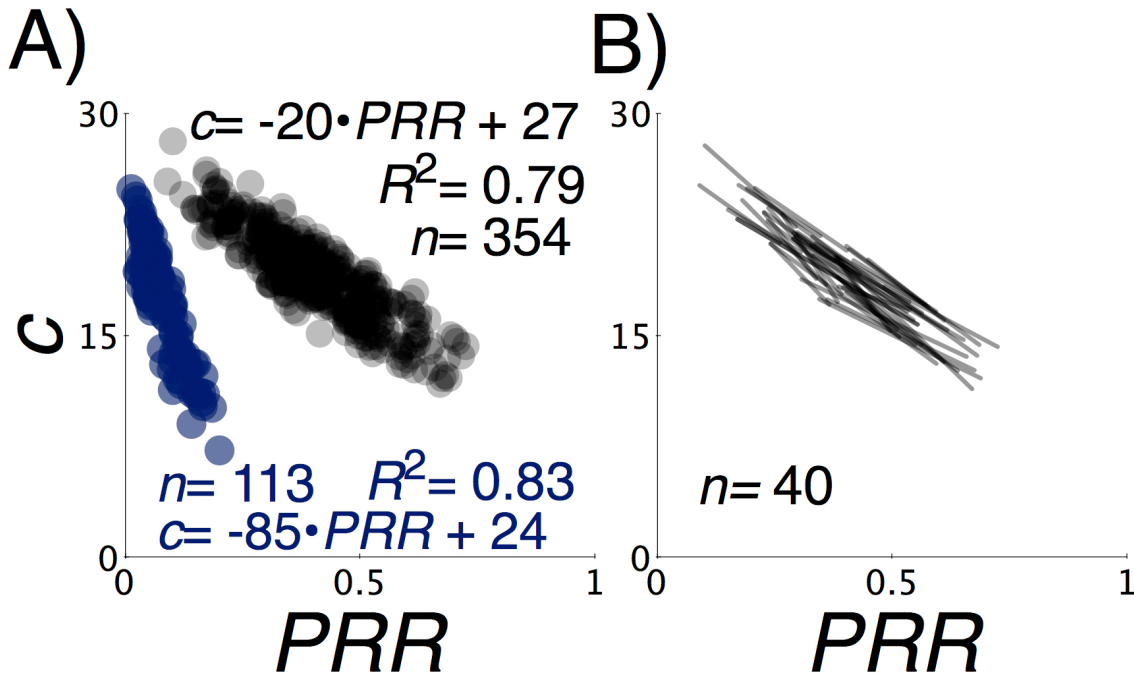


Figure 6.6. A) Pressure recovery ratio (PRR) vs. the E-wave derived relaxation/viscoelasticity parameter c for all 40 normal sinus rhythm subjects (black circles, 354 heart beats) and nine atrial fibrillation (AF) patients (blue circles, 113 heart beats). B) Linear regressions between PRR and c in all 40 NSR subjects. See text for details.

6.3.3 Sinus Rhythm- *PRR* Calculated Using Multiple Alternative Fiducial Pressures

For any particular choice of fiducial pressure, the associated *PRR* values (PRR^{1-11}) remained moderately well correlated to the noninvasive relaxation parameter *c* across all beats (see Table 6.3). The *PRR* vs. *c* regressions, with different choices of fiducial pressure, are shown for one representative subject in Figure 6.4B.

Among the 11 *PRR* values defined by 11 different choices for fiducial pressures (PRR^{1-11}), 8 can differentiate the delayed relaxation group from the PDR group ($p < 0.05$), and 10 can differentiate the delayed relaxation group from the NMLR group ($p < 0.05$).

If the pressure recovery from minimum pressure to diastatic pressure was not normalized relatively to any fiducial pressure, the correlation between the magnitude of this pressure difference and *c* was weaker ($R^2 = 0.29$) than the observed correlation between *PRR* and *c*. Like the *PRR*, the un-normalized pressure difference between minimum and diastatic pressure can differentiate the delayed relaxation from the PDR group ($p < 0.01$) and the delayed relaxation from the NMLR group ($p < 0.001$).

However, while the *PRR* was also found to be significantly different between PDR and NMLR groups ($p < 0.01$), the un-normalized pressure difference between minimum and diastatic pressure was not able to significantly distinguish between the PDR and NMLR groups ($p = 0.45$).

Table 6.3. R^2 values of the linear correlations between alternately defined *PRR* values and *c* across 363 NSR beats.

<i>PRR</i> Value	Fiducial Pressure	R^2
PRR^1	P_{max}	0.50
PRR^2	10 ms after P_{max}	0.50
PRR^3	30 ms after P_{max}	0.48
PRR^4	60 ms after P_{max}	0.39
PRR^5	20 ms before $-dP/dt_{max}$	0.48
PRR^6	10 ms before $-dP/dt_{max}$	0.48
PRR^7	5 ms before $-dP/dt_{max}$	0.46
PRR^{AF}, PRR^8	$-dP/dt_{max}$	0.45
PRR^9	10ms after $-dP/dt_{max}$	0.41
PRR^{10}	20ms after $-dP/dt_{max}$	0.38
PRR^{11}	30ms after $-dP/dt_{max}$	0.31
<i>PRR</i>	LVEDP	0.77

All *PRR* values are calculated for each beat according to Eq. 6.15, with alternative values for fiducial pressure as indicated above. *PRR*, pressure recovery ratio; LVEDP, left ventricular end diastolic pressure; $-dP/dt_{max}$, maximum rate of pressure decay; P_{max} , maximum pressure.

6.3.4 Results in the AF Group

The clinical descriptors of the 9 AF subjects and their hemodynamic and echocardiographic indexes are shown in Table 1. Equation 3 defined *PRR* was strongly correlated ($R^2=0.83$) with *c* for the 9 AF subjects (Figure 6.6A).

6.4 DISCUSSION

The connection between the E-wave delayed relaxation pattern and the LV pressure contour has not been fully characterized, although the physiologic details, including atrio-ventricular hemodynamics for a normal E-wave have been experimentally elucidated (9). As we have shown, subjects with an echo-determined delayed relaxation pattern may have normal τ_w , and subjects with prolonged τ_w may have normal E- and A-wave patterns and normal E' velocities (Figure 6.1). The laws of fluid mechanics, however, require that the shapes of the E-wave contour and the LV pressure contour be causally related (9). Thus in the current work, we derived and validated the *PRR*, a hemodynamic index defined after mitral valve opening that is causally related to the E-wave contour and therefore provides a hemodynamic measure of the echo-determined delayed relaxation pattern (Figure 6.7).

6.4.1 Delayed and Prolonged Relaxation

Effective diastolic function requires the ventricular myocardium to rapidly and uniformly relax from the previous systolic cramp. The relaxing tissue allows for the chamber to liberate its stored elastic recoil to spring back toward its diastatic (equilibrium) volume and aspirate blood

from the atrium (38, 45). Therefore, diastolic function and dysfunction involves stiffness and relaxation properties of the chamber. Measures of tissue relaxation are often derived from different aspects of the relaxation processes. A patient having prolonged relaxation during catheterization has a prolonged τ or duration of isovolumic pressure decay, whereas a patient with a ‘delayed relaxation’ pattern has a prolonged E-wave velocity contour. While both findings reflect the process of ventricular relaxation, isovolumic relaxation occurs primarily through calcium cycling and cross-bridge uncoupling (30, 44), whereas E-wave related relaxation is governed primarily by viscoelastic tissue properties (40). Indeed, the relaxation processes that

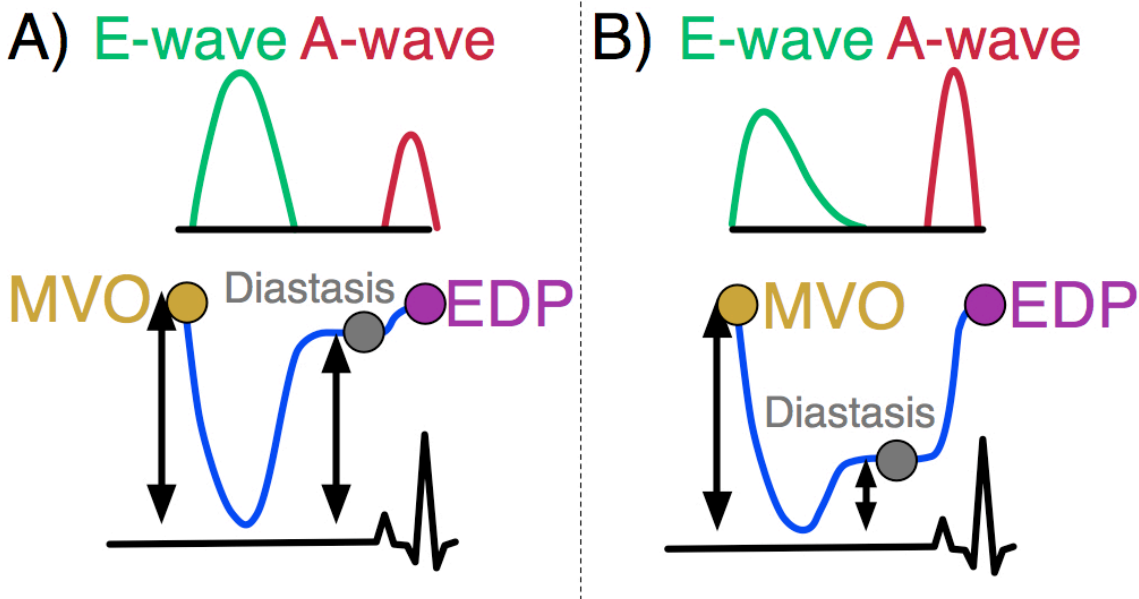


Figure 6.7. Schematic summary of the connection between the pressure contour (lower plot) defined pressure recovery ratio and noninvasively measured transmitral contour (upper plot) shape. A more symmetric E-wave contour (A) is associated with greater pressure recovery beyond minimum pressure, and a value of *PRR* closer to 1, while a delayed relaxation E-wave contour (B) is associated with poor pressure recovery and a value of *PRR* closer to 0. MVO- mitral valve opening; EDP- end diastolic pressure.

dominate isovolumic relaxation are typically complete within 3 or 4 τ intervals (42). It therefore should not be surprising that in the current study, τ (floating or fixed asymptote) was not able to differentiate between the DR, PDR and NMLR groups. Indeed, while τ is a useful clinical index, it is important to consider that the delayed relaxation pattern provides clinical information that

may be independent of τ . Indeed, as demonstrated by the *PRR*, the delayed relaxation pattern reflects, in a causal sense, the level of pressure recovery after P_{Min} relative to the pressure drop after MVO.

6.4.2 Previous Filling-related Indexes

Others have proposed invasive indexes of viscoelasticity (relaxation) beyond the isovolumic interval. For example, Templeton *et al.* (40) applied a sinusoidal volume variation to an isolated chamber and measured its viscoelastic property by the phase-delay of the resulting pressure response. Other investigators have observed viscoelastic chamber properties in various experimental settings (11, 21, 22, 25, 35, 39, 47). Though these studies did not involve simultaneous echocardiography, one would expect that the invasive relaxation indexes that these studies propose would likely relate to the echo-determined delayed relaxation pattern. However, the clinical applicability of these studies is limited because few of them were carried out in closed-chest, *in-vivo* chambers under normal physiologic conditions using routine clinical data acquisition methods.

6.4.3 The connection between c and *PRR*

Fluid mechanics dictates that the *PRR* is related to energy loss and the relative efficiency of filling. We have shown in previous work that the E-wave transmitral velocity contour may be modeled causally as the result of lumped tissue recoil and resistance forces (23, 24). The energy loss in the model is accounted for by a damping parameter, called c . A ventricle with no energy loss during filling would have a symmetric E-wave with a c value of 0, whereas a ventricle with significant energy losses during filling would have a blunted E-wave with a prolonged

deceleration portion, and an elevated value of c . Therefore, $c = 0$ theoretically corresponds to $PRR = 1$, where the pressure recovery between minimum and diastasis equals the initial pressure drop between mitral valve opening and minimum pressure. While the strongest correlation between c and PRR predicts a c value of 7.1/s at a PRR value of 1 ($R^2=0.7$), one observes a slightly weaker correlation ($R^2=0.75$) if the regression is set to cross the PRR axis at $PRR=1$.

It is interesting to compare the experimentally determined PRR vs. c correlation with the predicted correlation in Eq. 6.14. However, we must adjust the predicted relationship in Eq. 6.14 in order to make the comparison. Recalling that PRR is defined as the clinical surrogate for $PPGR$ due to the difficulty of determining atrial and ventricular pressures simultaneously, and that $y=c/(2\sqrt{k})$, we can rewrite Eq. 6.14 in terms of PRR and c :

$$PRR \approx 1 - \frac{(\pi + 4\sqrt{2} - 6)}{4\sqrt{k}} c \quad \text{Equation 6.18}$$

Among the 40 NSR subjects that we analyzed, the average PDF k value was $171 \pm 36 \text{ s}^{-1}$, and thus the predicted relationship between PRR and c would be $PRR = -0.0535 \cdot c + 1$. As we can see in (Figure 6.8), this is remarkably close to the experimentally determined relationship.

The results of Figure 6.6 and 6.8, where a strong linear relationship is observed between c and the PRR , support the conclusion that the PRR represents an invasive analog for the E-wave extracted damping parameter c . In other words, the PRR provides a measure of the relaxation

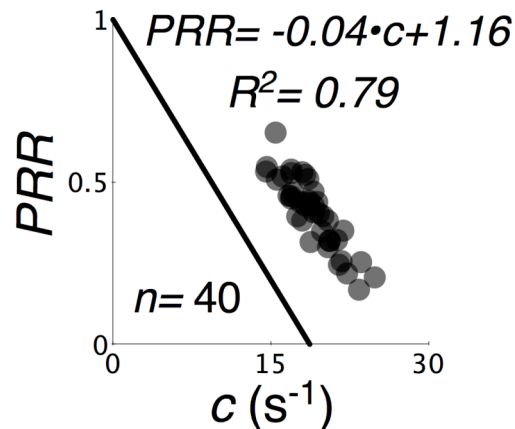


Figure 6.8. Plot of PRR vs c for 40 subjects, showing both raw data (black circles) and the theoretically predicted relationship from Equation 6.18. See text for details.

portion of the filling-related pressure contour, while c provides a measure of the relaxation portion of the E-wave.

6.4.4 Clinical and Physiologic Significance of *PRR*

The validation of the *PRR* as the only available invasive index of filling related relaxation sheds new light on how to characterize the relaxation properties of the chamber. The existence of a relaxation index that is not a strong correlate of τ suggests that there are different tissue relaxation mechanisms before and after MVO. A chamber may have adequate or inadequate isovolumic relaxation and adequate or inadequate pressure recovery, thus the observed range of relaxation abnormalities encountered requires additional information beyond a normal or abnormal τ . The demonstrated low correlation between τ and *PRR* further supports the conclusion that τ and *PRR* characterize variable mechanisms of relaxation. This is not surprising, because relaxation during the isovolumic interval (measured by τ) primarily reflects rates of calcium sequestration and crossbridge detachment in the face of stored elastic strain, whereas filling related relaxation (measured by *PRR*) is primarily determined by macroscopic chamber viscoelasticity in addition to the waning effects of calcium sequestration.

Beyond the conceptual value and physiologic significance of the *PRR*, clinical utility resides in the catheterization laboratory, where the *PRR*, and therefore filling related chamber relaxation may be quickly estimated by visual inspection of pressure contours. While this information could be extracted from the E-wave contour (parameter c), it is not routine to have an echocardiographic machine available during catheterization, and therefore chamber relaxation properties during catheterization would be best estimated by a combination of τ and *PRR*. Our

work therefore suggests that to capture the full spectrum of relaxation related pathophysiology, isovolumic relaxation measures (τ) and filling related relaxation measures (*PRR*) are required.

6.4.5 Load Dependence of *PRR*

For each subject, we also included in our analysis beats following a premature ventricular contraction, as well as E-waves recorded at different phases of respiration in order to determine *PRR* in the setting of load variation. Since load variation results in E-wave shape variation (see Chapter 1 and Chapter 8), both *c* and *PRR* varied in response to load, but the *c* vs. *PRR* correlation remained unchanged (Figure 6.6B). Indeed, because the E-wave delayed relaxation pattern and pressure recovery was derived from basic physiologic principles, *PRR* should be applicable in a wide variety of pathophysiologic scenarios. The fact that *PRR* remained strongly correlated with *c* for the wide range of clinical E-wave shapes and clinical settings considered, supports the predicted robustness of the index and the generality of the method. Thus the *PRR* should be applicable in normal and pathophysiologic settings, with the proviso that load status must be considered when values of *PRR* are to be compared.

6.4.6. *PRR* in Constrictive Restrictive Filling Pattern

The analysis in the current study was limited to normal and delayed relaxation pattern E-waves. However, *PRR* applicability is not limited to these E-wave patterns alone. To demonstrate this we analyze an additional NSR subject from the Cardiovascular Biophysics Laboratory database of simultaneous pressure and echocardiography exhibiting a constrictive restrictive (i.e. short DT) E-wave pattern. This patient had LVEF = 20%, E-wave deceleration time (DT) = 134 ± 10 ms, E/A = 2.9 ± 0.2 , LVEDP = 29 ± 3 mmHg, $\tau_w = 72 \pm 4$ msec, $\tau_R = 121 \pm 12$ msec, and *PRR*

= 0.34 ± 0.07 . This lower *PRR* value is consistent with the high viscoelasticity and significant filling-related relaxation abnormalities that one would expect in a subject with constrictive restrictive filling patterns. Furthermore, in this patient for all (N=17) beats analyzed, *PRR* had a strong correlation with *c* ($c = -37.3 \times PRR + 32.6$ $R^2=0.85$), and plotting this subject's average *PRR* and *c* values on Figure 6.6 yields a point that is concordant with the observed correlation. This suggests that the *PRR* is a general index, applicable to a wide variety of E-wave filling patterns. Detailed study in a larger number of subjects with short DT (constrictive-restrictive) E-wave patterns is required to fully characterize the utility of the *PRR*. Of particular interest is how *PRR* would change in subjects with restrictive E-wave patterns that manifest as impaired relaxation patterns in response to Valsalva maneuver.

6.4.7. Independence of Fiducial Pressure

We found that *PRR* values defined by 11 other choices of fiducial pressures (PRR^{1-11}) (Figure 6.4) still maintain reasonable correlations with the parameter *c*. The majority of PRR^{1-11} value can differentiate between the delayed relaxation and PDR groups (8 out of 11), and between the delayed relaxation and NMLR groups (10 out of 11). These results demonstrated that regardless of the choice of fiducial pressure, the normalized pressure recovery concept represents the invasive analogue of the delayed relaxation pattern. While these results serve to validate the hypothesis that the critical component of filling related relaxation is the recovery of pressure from minimum to diastasis, it is important to note that the strongest correlation between *PRR* and *c* was obtained from *PRR* defined by Equation 6.16, where LVEDP serves as a surrogate for MVO. Therefore this is the only *PRR* definition that should be used for subjects in

NSR, and for simplicity, *PRR* defined by Equation 6.17 should be the exclusive *PRR* relationship used for subjects in AF.

6.4.8. Importance of Normalization

The normalization of pressure recovery relative to the pressure difference between minimum pressure and a fiducial pressure provides the strongest correlation with c and most robust differentiation between the three groups. However, the magnitude of pressure recovery (mmHg) alone had a reasonable correlation with c ($R^2=0.29$) and can differentiate the delayed relaxation group from both the PDR group ($p<0.01$) and the NMLR group ($p<0.001$), though not the PDR group from the NMLR group ($p=0.45$). This result increases our confidence that the pressure recovery feature during early filling is causally related to the delayed relaxation pattern. However, *PRR* is superior to the unnormalized pressure recovery in terms of its ability to differentiate delayed relaxation pattern and its correlation with parameter c .

6.4.9 Atrial Contribution to PRR

Equation 6.16, which involves LVEDP, was used to calculate the *PRR* for all NSR subjects. Thus one may suspect that the *PRR* must primarily reflect atrial properties, because LVEDP is partly determined by atrial contraction. However, the analysis presented in Table 6.3, as well as the strong correlation between Equation 6.17 determined *PRR* and c (Figure 6.6) in AF subjects, indicates that atrial properties are unlikely to be causal determinants of *PRR* since other fiducial pressures during IVR can be chosen to calculate *PRR*. Furthermore, we present strong evidence that the *PRR* is primarily related to the relaxation/viscoelasticity parameter c , which quantitates the curvilinearity of the deceleration portion of the E-wave. Indeed *PRR* did not

correlate strongly with conventional DF indexes that involve the atrium, such as E/A or VTI_E/VTI_A (See Figure 6.9). The strong correlation between E-wave derived c and PRR , coupled with the lack of dependence on classic indexes that rely on atrial-systole related filling, reinforces the argument that the PRR is causally unrelated to atrial properties.

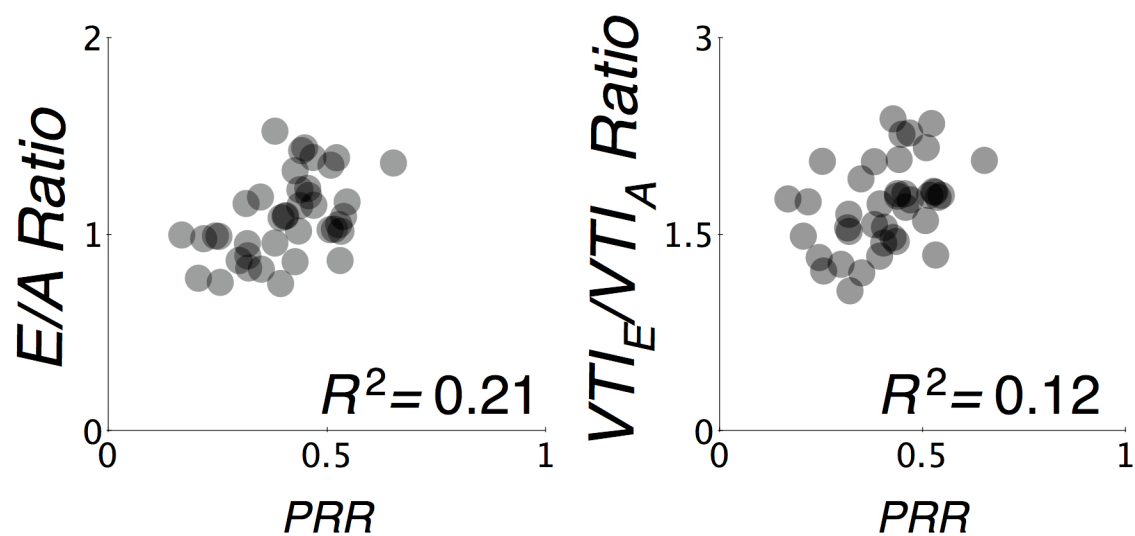


Figure 6.9. Plot of E-wave peak to A-wave peak ratio (E/A) and E-wave velocity time integral to A-wave velocity time integral ratio (VTI_E/VTI_A) vs pressure recovery ratio (PRR), demonstrating no correlation. This argues against PRR being strongly influenced by atrial properties. See text for details.

6.5 LIMITATIONS

6.5.1 Heterogeneity of the Subjects

The 40 subjects included in this study had a mixture of normal (7 patients with $LVEDP < 19\text{mmHg}$ and $\tau_w < 50\text{msec}$) and abnormal (12 patients with $LVEDP \geq 19\text{mmHg}$, and $\tau_w \geq 50\text{msec}$) diastolic function. The remaining subjects had normal pressures but abnormal relaxation (12 patients with $LVEDP < 19\text{mmHg}$ and $\tau_w \geq 50$) or elevated filling pressures with normal relaxation (9 patients with $LVEDP \geq 19\text{mmHg}$ and $\tau_w < 50$). The heterogeneity of the

subjects is by design, and is intended to demonstrate the robustness and generality of the *PRR*. This is underscored by the fact that each patient individually showed a strong correlation between the *PRR* and the Doppler echocardiographically derived *c* parameter (average $R^2=0.82\pm 0.13$). The fact that *PRR* correlated with *c* in the wide range of subjects studied supports the predicted robustness of the index and the generality of the method. Thus, for subjects with a normal mitral valve, the *PRR* should be applicable in both normal and abnormal DF.

Future suitably controlled clinical studies with well-defined patient groups will provide further insight to the clinical utility of the *PRR* index. For example, normal ejection fraction diabetic subjects have worse diastolic function than normal ejection fraction controls as a result of increased viscous losses (37) during filling. Assessing such a group via *PRR* would provide additional insight regarding the effect of diabetes on diastolic function.

6.5.2 Heart Rate Considerations

The calculation of the *PRR* requires measurement of the pressure at diastasis. At heart rates above 80 beats per minute(6, 7), the E- and A-waves merge and the conventional diastatic interval is lost. Thus in the face of tachycardia, the precise determination of the diastatic pressure can not be achieved. For this reason calculation of *PRR* can not be reliably performed in the setting of tachycardia.

6.5.3 Calculation of τ

Both the Glantz floating asymptote and Weiss zero asymptote methods were utilized to calculate τ in the current study. Consistent with previous literature (43) our results showed that the τ value measured using the Glantz method is consistently higher than the value measured by

Weiss method. Thus a potential limitation of the different methods for τ determination relates to the cutoff chosen for normal vs abnormal τ . The established cutoff for normal τ has been reported as 50 ms in major clinical studies, including those referenced by the European Heart Journal working group on diastolic function (16, 36, 46). However in those studies the Weiss method was used to calculate τ , and therefore studies that use the Glanz method may bias normal relaxation subjects with Weiss τ values less than but near 50 ms into the abnormal group. To mitigate this potential bias we used the Weiss τ value for dichotomization of isovolumic relaxation function between subjects. Furthermore, though the absolute values of the Glantz method τ are not used to dichotomize groups, the Glantz method τ remains statistically indistinguishable among the three groups (See Table 6.2).

Both floating and fixed intercept methods rely on the monoexponential model of isovolumic pressure decay. Other models of isovolumic relaxation have been proposed, including a logistic model (28) and a kinematics-based model (8). While some investigators have demonstrated the benefits of the logistic model (20), recent work in our laboratory highlights one of the challenges inherent in applying the logistic model (8). When isovolumic pressure decay is plotted in the phase (dP/dt vs. P) plane, the isovolumic contour may appear straight or curved. The logistic model only fits those contours that are curved, while the monoexponential model only fits those that are straight. Thus the logistic model requires a subjective judgment of whether the IVR portion in the phase plane is sufficiently ‘linear’ vs. ‘curved’. Because the majority of phase plane contours from the subjects in the current study possessed linear phase plane IVR contours, application of a monoexponential IVR model for determination of τ was deemed more appropriate.

6.5.4 LVEDP as the P_{MVO} Surrogate

While the validity of the assumption that LVEDP approximates MVO pressure has been demonstrated (4, 19, 31, 34), this assumption has limitations, especially in patients with severe diastolic dysfunction. However, our analysis of 354 heart beats in 40 NSR subjects, all of whom had normal mitral valves, is likely to minimize any systematic difference between MVO pressure and LVEDP. Our choice of LVEDP should be viewed as a convenient reference fiducial pressure. Figure 6.4 and Table 6.3 demonstrate that when different reference fiducial pressures are chosen, the conceptual considerations and physical underpinnings regarding the decay of the pressure and its recovery relative to some fiducial value, remain the same. Thus, the systematic error that may be introduced by the choice of fiducial pressure is mitigated by the fact that the pressure recovery is a relative rather than an absolute index because it relies on pressure differences, and not absolute pressures. We also found that if the pressure recovery from minimum to diastasis is not normalized relative to any pressure drop, the correlation between the pressure recovery and parameter c was decreased. As a result, pressure drop and recovery jointly characterize the delayed relaxation pattern.

The determination of LVEDP was achieved by determining the LVP at the ECG R-wave peak. However, in the setting of 1st degree AV block with late diastolic mitral regurgitation, we determine LVEDP at the peak pressure between diastasis and the R-wave peak.

6.5.5 Determination of Diastasis Pressure

The numerator of the PRR requires the determination of the diastatic pressure. While robust determination of diastasis pressure would require simultaneous atrial and ventricular pressures, in the current study diastasis pressure was determined by taking the pressure at the

peak of ECG P-wave in NSR. We have shown previously that diastasis period is eliminated when the heart rate is typically above 80 beats/min (6, 7). All the NSR subjects included in this study had heart rates slow enough to assure that diastasis was present.

Due to the lack of coordinated atrial contraction, diastasis and end-diastole have the same pressure in AF. In this group of patients, ‘diastatic’ pressure was measured at the peak of the ECG R-wave.

6.5.6 Application of Bernoulli’s Equation

In the derivation of the PRR dependence on c , we ignored the viscous term in Bernoulli’s equation. This simplification has been used by several investigators (12, 41). It is important to note that the PRR reflects the resistive effects of tissue and chamber relaxation, not fluid viscosity. For this reason it is appropriate to ignore the fluid viscous term in Bernoulli’s equation. Instead, by including the PDF model expression for velocity, we incorporate the effects of tissue viscosity into the equation. This is a novel approach to the Bernoulli equation, because while fluid energy losses are ignored, tissue energy losses are lumped in with the decreasing velocity. There are likely more insights, beyond the connection between PRR and c , to be gleaned from a deeper analysis of Eq. 6.9.

6.6 CONCLUSIONS

The Doppler E-wave delayed relaxation pattern is a hallmark of diastolic dysfunction. The time constant of isovolumic relaxation τ and the E-wave delayed relaxation pattern are not strongly causally related since they characterize relaxation during different diastolic time intervals. No hemodynamic measure of the E-wave delayed relaxation pattern has been

established. We demonstrate that unlike τ , the dimensionless pressure recovery ratio (*PRR*), defined by the ratio of pressure difference between minimum and diastatic LVP to the difference between MVO and minimum LVP, conveys early-rapid filling related chamber relaxation properties, and differentiates patients with delayed relaxation from patients NMLR E-wave contours. Thus *PRR* serves as the hemodynamic analogue of the E-wave delayed relaxation pattern.

Furthermore, the establishment and validation of the causal connection between *PRR* and the E-wave deceleration provides mechanistic insight into the chamber property-to-transmitral flow relation. Due to its simplicity, the *PRR* may be easily measured in the catheterization laboratory to assess filling-related chamber relaxation properties. Future work should undertake further robust clinical validation of the *PRR* in suitably selected pathophysiologic subsets.

6.7 REFERENCES

1. Appleton CP, Firstenberg MS, Garcia MJ, and Thomas JD. The echo-Doppler evaluation of left ventricular diastolic function. A current perspective. *Cardiology clinics* 18: 513-546, ix, 2000.
2. Appleton CP, Hatle LK, and Popp RL. Relation of transmitral flow velocity patterns to left ventricular diastolic function: new insights from a combined hemodynamic and Doppler echocardiographic study. *J Am Coll Cardiol* 12: 426-440, 1988.
3. Cheng C, Igarashi Y, and Little W. Mechanism of augmented rate of left ventricular filling during exercise. *Circulation Research* 70: 9-19, 1992.
4. Cheng-Baron J, Chow K, Khoo NS, Esch BT, Scott JM, Haykowsky MJ, Tyberg JV, and Thompson RB. Measurements of changes in left ventricular volume, strain, and twist during isovolumic relaxation using MRI. *Am J Physiol Heart Circ Physiol* 298: H1908-1918, 2010.
5. Chung CS, Ajo DM, and Kovács SJ. Isovolumic pressure-to-early rapid filling decay rate relation: model-based derivation and validation via simultaneous catheterization echocardiography. *J Appl Physiol* 100: 528-534, 2006.
6. Chung CS, Karamanoglu M, and Kovács SJ. Duration of diastole and its phases as a function of heart rate during supine bicycle exercise. *Am J Physiol Heart Circ Physiol* 287: H2003-2008, 2004.
7. Chung CS and Kovács SJ. Consequences of increasing heart rate on deceleration time, the velocity-time integral, and E/A. *Am J Cardiol* 97: 130-136, 2006.
8. Chung CS and Kovács SJ. Physical determinants of left ventricular isovolumic pressure decline: model prediction with in vivo validation. *Am J Physiol Heart Circ Physiol* 294: H1589-1596, 2008.

9. Courtois M, Kovacs SJ, and Ludbrook PA. Transmitral pressure-flow velocity relation. Importance of regional pressure gradients in the left ventricle during diastole. *Circulation* 78: 661-671, 1988.
10. Courtois M, Kovács SJ, and Ludbrook PA. Transmitral pressure-flow velocity relation. Importance of regional pressure gradients in the left ventricle during diastole. *Circulation* 78: 661-671, 1988.
11. Ewert D, Wheeler B, Doetkott C, Ionan C, Pantalos G, and Koenig SC. The Effect of Heart Rate, Preload, and Afterload on the Viscoelastic Properties of the Swine Myocardium. *Annals of Biomedical Engineering* 32: 1211-1222, 2004.
12. Firstenberg MS, Vandervoort PM, Greenberg NL, Smedira NG, McCarthy PM, Garcia MJ, and Thomas JD. Noninvasive estimation of transmitral pressure drop across the normal mitral valve in humans: importance of convective and inertial forces during left ventricular filling. *Journal of the American College of Cardiology* 36: 1942-1949, 2000.
13. Garcia MJ, Smedira NG, Greenberg NL, Main M, Firstenberg MS, Odabashian J, and Thomas JD. Color M-mode Doppler flow propagation velocity is a preload insensitive index of left ventricular relaxation: animal and human validation. *J Am Coll Cardiol* 35: 201-208, 2000.
14. Garcia MJ, Thomas JD, and Klein AL. New Doppler echocardiographic applications for the study of diastolic function. *J Am Coll Cardiol* 32: 865-875, 1998.
15. Garcia MJ, Thomas JD, and Klein AL. New Doppler echocardiographic applications for the study of diastolic function. *Journal of the American College of Cardiology* 32: 865-875, 1998.
16. Hirota Y. A clinical study of left ventricular relaxation. *Circulation* 62: 756-763, 1980.

17. Hogg K, Swedberg K, and McMurray J. Heart failure with preserved left ventricular systolic function; epidemiology, clinical characteristics, and prognosis. *J Am Coll Cardiol* 43: 317-327, 2004.
18. Ishida Y, Meisner J, Tsujioka K, Gallo J, Yoran C, Frater R, and Yellin E. Left ventricular filling dynamics: influence of left ventricular relaxation and left atrial pressure [published erratum appears in *Circulation* 1986 Sep;74(3):462]. *Circulation* 74: 187-196, 1986.
19. Ishida Y, Meisner JS, Tsujioka K, Gallo JI, Yoran C, Frater RW, and Yellin EL. Left ventricular filling dynamics: influence of left ventricular relaxation and left atrial pressure. *Circulation* 74: 187-196, 1986.
20. Kass DA. Assessment of diastolic dysfunction. Invasive modalities. *Cardiology clinics* 18: 571-586, 2000.
21. Kheradvar A, Milano M, Gorman R, Gorman J, and Gharib M. Assessment of Left Ventricular Viscoelastic Components Based on Ventricular Harmonic Behavior. *Cardiovasc Eng* 6: 30-39, 2006.
22. Koide M, Hamawaki M, Narishige T, Sato H, Nemoto S, DeFreyte G, Zile MR, Cooper G, IV, and Carabello BA. Microtubule Depolymerization Normalizes In Vivo Myocardial Contractile Function in Dogs With Pressure-Overload Left Ventricular Hypertrophy. *Circulation* 102: 1045-1052, 2000.
23. Kovács SJ, Barzilai B, and Pérez JE. Evaluation of diastolic function with Doppler echocardiography: the PDF formalism. *Am J Physiol* 252: H178-187, 1987.
24. Kovács SJ, Meisner JS, and Yellin EL. Modeling of diastole. *Cardiology clinics* 18: 459-487, 2000.

25. Kulke M, Fujita-Becker S, Rostkova E, Neagoe C, Labeit D, Manstein DJ, Gautel M, and Linke WA. Interaction Between PEVK-Titin and Actin Filaments: Origin of a Viscous Force Component in Cardiac Myofibrils. *Circulation Research* 89: 874-881, 2001.
26. Lissauskas JB, Singh J, Bowman AW, and Kovacs SJ. Chamber properties from transmitral flow: prediction of average and passive left ventricular diastolic stiffness. *Journal of Applied Physiology* 91: 154-162, 2001.
27. Lissauskas JB, Singh J, Bowman AW, and Kovács SJ. Chamber properties from transmitral flow: prediction of average and passive left ventricular diastolic stiffness. *J Appl Physiol* 91: 154-162, 2001.
28. Matsubara H, Takaki M, Yasuhara S, Araki J, and Suga H. Logistic time constant of isovolumic relaxation pressure-time curve in the canine left ventricle. Better alternative to exponential time constant. *Circulation* 92: 2318-2326, 1995.
29. Maurer M, Spevack D, Burkhoff D, and Kronzon I. Diastolic dysfunction Can it be diagnosed by Doppler echocardiography? *Journal of the American College of Cardiology*, 2004.
30. Maurer MS, Spevack D, Burkhoff D, and Kronzon I. Diastolic dysfunction: Can it be diagnosed by Doppler echocardiography? *Journal of the American College of Cardiology* 44: 1543-1549, 2004.
31. Miki S, Murakami T, Iwase T, Tomita T, Nakamura Y, and Kawai C. Doppler echocardiographic transmitral peak early velocity does not directly reflect hemodynamic changes in humans: importance of normalization to mitral stroke volume. *Journal of the American College of Cardiology* 17: 1507-1516, 1991.
32. Miki S, Murakami T, Iwase T, Tomita T, Nakamura Y, and Kawai C. Doppler echocardiographic transmitral peak early velocity does not directly reflect hemodynamic changes

in humans: importance of normalization to mitral stroke volume. *Journal of the American College of Cardiology* 17: 1507-1516, 1991.

33. Murakami T, Hess O, Gage J, Grimm J, and Krayenbuehl H. Diastolic filling dynamics in patients with aortic stenosis. *Circulation* 73: 1162-1174, 1986.

34. Murakami T, Hess OM, Gage JE, Grimm J, and Krayenbuehl HP. Diastolic filling dynamics in patients with aortic stenosis. *Circulation* 73: 1162-1174, 1986.

35. Nikolic S, Tamura K, Tamura T, Dahm M, Frater R, and Yellin E. Diastolic viscous properties of the intact canine left ventricle. *Circulation Research* 67: 352-359, 1990.

36. Paulus WJ, Tschöpe C, Sanderson JE, Rusconi C, Flachskampf FA, Rademakers FE, Marino P, Smiseth OA, De Keulenaer G, Leite-Moreira AF, Borbély A, Edes I, Handoko ML, Heymans S, Pezzali N, Pieske B, Dickstein K, Fraser AG, and Brutsaert DL. How to diagnose diastolic heart failure: a consensus statement on the diagnosis of heart failure with normal left ventricular ejection fraction by the Heart Failure and Echocardiography Associations of the European Society of Cardiology. *Eur Heart J* 28: 2539-2550, 2007.

37. Riordan MM, Chung CS, and Kovács SJ. Diabetes and diastolic function: stiffness and relaxation from transmitral flow. *Ultrasound in medicine & biology* 31: 1589-1596, 2005.

38. Shmuylovich L, Chung CS, Kovács SJ, Yellin EL, and Nikolic SD. Left ventricular volume during diastasis IS/IS NOT the physiologic in-vivo equilibrium volume and IS/IS NOT related to diastolic suction. *J Appl Physiol*, 2009.

39. Starc V, Yellin EL, and Nikolic SD. Viscoelastic behavior of the isolated guinea pig left ventricle in diastole. *american journal of physiology* 271: H1314-1324, 1996.

40. Templeton GH and Nardizzi LR. Elastic and viscous stiffness of the canine left ventricle. *Journal of Applied Physiology* 36: 123-127, 1974.

41. Thomas JD, Newell JB, Choong CY, and Weyman AE. Physical and physiological determinants of transmitral velocity: numerical analysis. *Am J Physiol* 260: H1718-1731, 1991.
42. Weisfeldt ML, Frederiksen JW, Yin FC, and Weiss JL. Evidence of incomplete left ventricular relaxation in the dog: prediction from the time constant for isovolumic pressure fall. *J Clin Invest* 62: 1296-1302, 1978.
43. Yamakado T, Takagi E, Okubo S, Imanaka-Yoshida K, Tarumi T, Nakamura M, and Nakano T. Effects of aging on left ventricular relaxation in humans. Analysis of left ventricular isovolumic pressure decay. *Circulation* 95: 917-923, 1997.
44. Yellin EL, Nikolic S, and Frater RW. Left ventricle filling dynamics and diastolic function. *Progress in Cardiovascular Diseases* 32: 247-271, 1990.
45. Zhang W, Chung CS, Shmuylovich L, and Kovács SJ. Is left ventricular volume during diastasis the real equilibrium volume, and what is its relationship to diastolic suction? *J Appl Physiol* 105: 1012-1014, 2008.
46. Zile MR, Baicu CF, and Gaasch WH. Diastolic heart failure--abnormalities in active relaxation and passive stiffness of the left ventricle. *N Engl J Med* 350: 1953-1959, 2004.
47. Zile MR, Richardson K, Cowles MK, Buckley JM, Koide M, Cowles BA, Gharapuray V, and Cooper G, IV. Constitutive Properties of Adult Mammalian Cardiac Muscle Cells. *Circulation* 98: 567-579, 1998.

CHAPTER 7.

APPLICATION OF PRR: IN SILICO ECHOCARDIOGRAPHY

7.1. INTRODUCTION

In the previous chapter we demonstrated derived a robust connection between PRR , an index derived from the invasively measured pressure contour, and the PDF parameter c , a parameter that is extracted from noninvasively measured early filling transmitral velocity contours. In previous work other connections have been validated between noninvasive PDF parameters and invasive hemodynamic parameters. Taken together these results may be used to derive the invasive contour from hemodynamic data alone, and we demonstrate that approach in the current chapter with a theoretical analysis and proof of concept using clinical data. We first briefly summarize the noninvasive and invasive data below.

7.1.1 Summary of Doppler Echocardiography Transmitral Flow

One of the most powerful tools readily available to clinical and research cardiologists is noninvasive Doppler echocardiography. Doppler echocardiography allows for the rapid measurement and visualization of the transmitral blood velocity contour. In conjunction with numerous clinical findings, cardiologists use features of a patient's transmitral blood velocity contour to help diagnose and treat numerous cardiovascular disorders (see Chapter 1). Examples of typical transmitral blood flow velocity contours were discussed in Chapter 1 and are presented in Figure 7.1.

Figure 7.1B demonstrates a variety of E- and A- wave contour patterns. These patterns are used in practice for phenotypic characterization of cardiovascular physiology, especially diastolic pathophysiology. Current clinical methodology for analysis of E- and A-waves however is quite coarse grained; finer details of E- and A-wave features such as curvature are discarded

and simple triangular geometric approximations to the E- and A-wave shapes are instead employed (1).

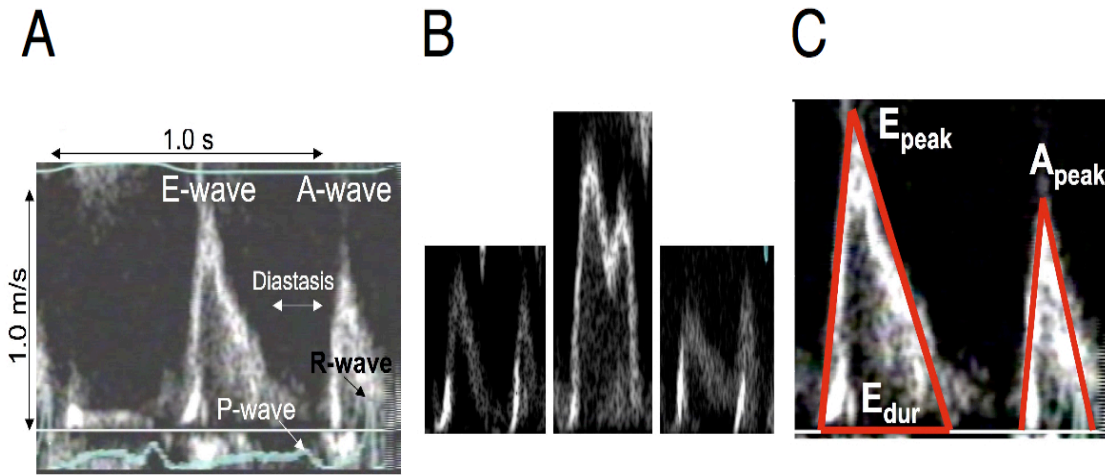


Figure 7.1. Summary of noninvasive Doppler echocardiography transmitral flow contours. A) Transmitral velocity measured by Doppler echocardiography with 3-lead ECG signal. Notice that the signal consists of 3 phases. The first positive wave is called the early filling velocity wave, or simply E-wave. The second phase of the transmitral velocity profile is defined by the interval between the first and second velocity waves, and is called the diastasis interval. For filling beats occurring at high heart rates (>90 beats per min) the first and second velocity waves may merge together, thereby eliminating the diastasis interval. The third phase of the transmitral velocity profile consists of the second distinct positive velocity wave, and is called the atrial filling, or A-wave. B) Transmitral velocity contours vary in shape with changes in load and diastolic function. The middle panel shows highly merged E- and A-waves, while the right panel demonstrates the “delayed-relaxation” pattern. Clinicians routinely use the transmitral contour shape as part of the diagnosis and management of diastolic dysfunction. C) Transmitral contours are typically quantitated as triangles in the clinical setting, and triangle widths and heights are compared to clinically established standards in the diagnosis and management of diastolic dysfunction. The width of the E-wave is called E_{dur} , and the peak height of the E-wave is called E_{peak} . See Chapter 1 for further details.

7. 1.2 Pressure Measurement By Catheterization

While echocardiography is widely employed in the evaluation of cardiac patients, invasive catheterization represents another widely employed tool available to cardiologists. In fact, the gold standard for determining diastolic function is the determination of the left ventricular end diastolic pressure (LVEDP) by means of left ventricular catheterization (7). Ventricular catheterization involves the introduction of a pressure recording catheter into a patient’s left ventricle (see Chapter 2). A typical real-time catheterization determined left

ventricular pressure profile is presented in Figure 7.2. Just as with the E- and A-waves, specific measures derived from the left ventricular pressure profile are used by cardiologists for diagnosis and treatment of cardiac disease including diastolic dysfunction (12).

Figure 7.2 indicates several of the clinically relevant measures derived from the left ventricular pressure profile. As discussed in previous Chapters, these measures include the end diastolic pressure (LVEDP) and the time constants of isovolumic relaxation, τ or τ_L . Taken

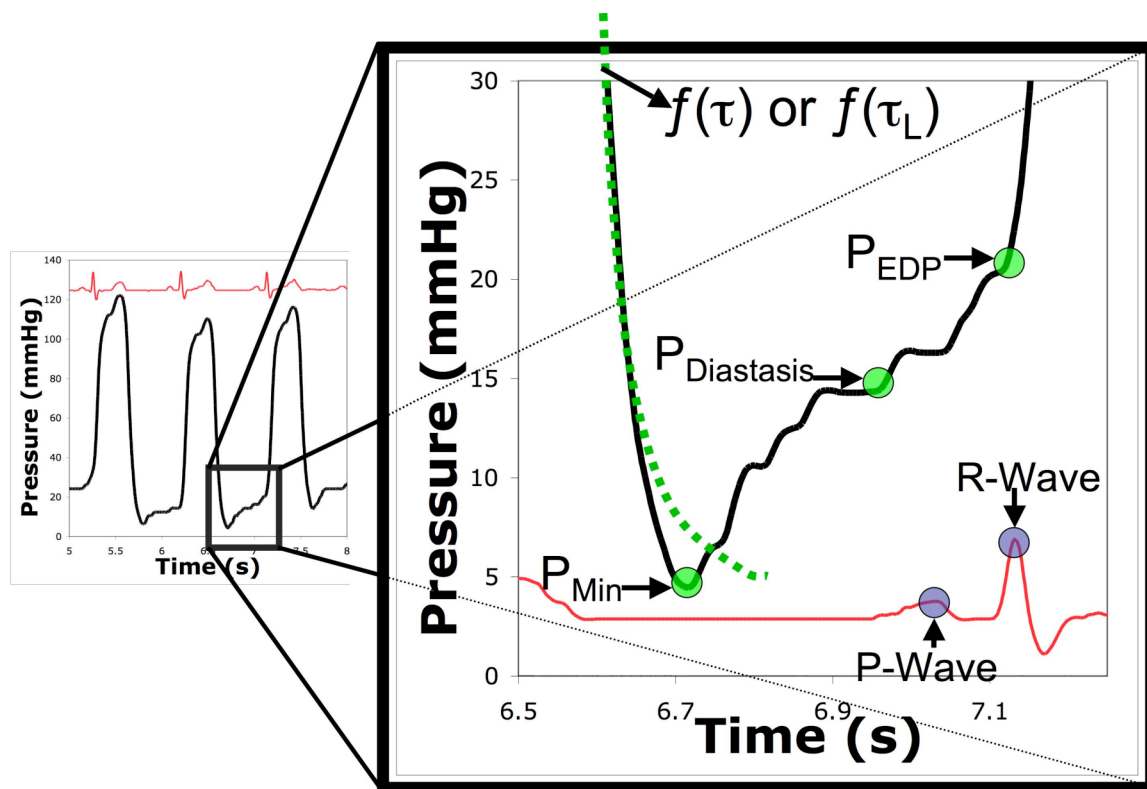


Figure 7.2. A typical real time left ventricular pressure (LVP) and simultaneous ECG signal seen in the catheterization lab during a procedure. The diastolic (filling) portion of the LVP contour is enlarged and several important indexes are shown for reference. The peak of the ECG P-wave corresponds to the beginning of atrial contraction mediated LV filling, or the Doppler A-wave. The peak of the R-wave, or by some conventions the start of the R-wave positive upward deflection, corresponds to the LV end diastolic pressure (LVEDP). The decreasing portion of the LVP contour is often fit to an exponential or logistic equation as a function of isovolumic time constants called τ and τ_L respectively.

together, Doppler echocardiography and left ventricular catheterization can provide a more complete assessment of a particular patient's cardiac function and, in particular, the patient's diastolic function.

7.1.3 Simultaneous Application of Clinical Modalities

Though simultaneous Doppler-echocardiography and left-ventricular catheterization is possible and forms the basis for the Cardiovascular Biophysics Database described in Chapter 2, it is rarely performed in clinical practice because of the desire to reduce catheterization time. However, the E-wave can provide additional information about diastolic function that is not available from catheterization alone. Thus, a method by which an E-wave could be estimated from a left ventricular pressure (LVP) profile alone in real time would be of great benefit. We call this method “In-Silico Echocardiography”, and we describe the mathematical details below.

7.2. IN SILICO ECHOCARDIOGRAPHY THEORETICAL DERIVATIONS

Previous work in our laboratory has demonstrated that the E- and A-wave velocity contours can be modeled and accurately predicted by the physics of damped simple harmonic motion. The physical underpinnings (parameterized diastolic filling, or PDF model) and numerical methods (model based image processing or MBIP) needed to extract damped harmonic motion parameters from E- and A-wave were described in Chapter 2, and have been extensively published and validated (2, 4, 6, 8-10). Most patients have E-wave velocities that exhibit the underdamped regime of damped simple harmonic motion:

$$v(t) = \frac{kx_o}{\omega} e^{-\frac{c}{2}t} \sin(\omega t) \quad \text{Equation 7.1}$$

where k is a spring constant, c is a damping constant, x_0 is a multiplicative initial spring

displacement, and $\omega = \sqrt{k - \frac{c^2}{4}}$.

Figure 7.3 provides a plot of Eq. 7.1. As described in Chapter 2, the initial upslope, or mass normalized initial driving force, is numerically given by the product kx_0 . Furthermore, the width of the wave (E_{dur}) is related to the frequency ω simply by π/ω .

We notice that Equation (7.1) is fully determined if one can determine the quantities ω , kx_0 , and c . Thus, to estimate

the E-wave from the LVP contour, we need to find methods by which kx_0 , ω , and c can be easily determined. In Figure 7.4 we present a general flowchart for the determination of E-wave contours from LVP contours. Previous and current work suggests that the E-wave parameters of interest (kx_0 , ω , c) can be determined if one can find the following hemodynamic parameters from the LVP contour and ECG : the LV end-diastolic time and pressure (t_{EDP} , P_{EDP}), the diastasis pressure ($P_{Diastasis}$), the mitral valve opening time and pressure (t_{MVO} , P_{MVO}), the LV minimum pressure and time (t_{Min} , P_{Min}), and the E-wave end time or time at which diastasis begins ($t_{DiastasisStart}$). In what follows, we discuss specific methods that can be automated by which the relevant hemodynamic parameters can be determined and used to generate kx_0 , ω , and c values for various physiological cases. Note that this analysis applies requires that subjects do

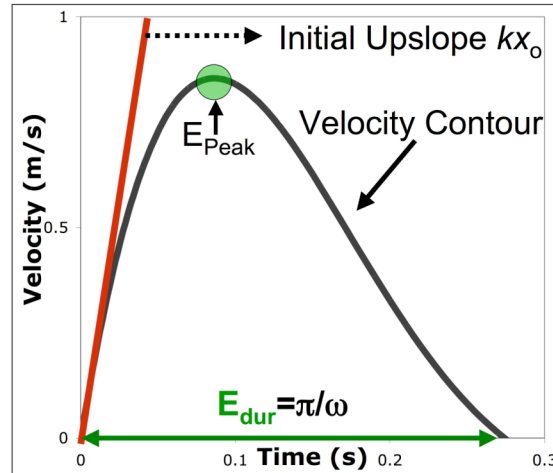


Figure 7.3. A plot of Equation 1 vs. time for arbitrarily chosen k , c , and x_0 values in the underdamped regime. The width of the E-wave, or duration of the E-wave is called E_{dur} and is related to the frequency of the E-wave ω . The peak velocity of the E-wave is called E_{peak} . The initial upslope the E-wave is numerically equivalent to the product of the parameters k and x_0 .

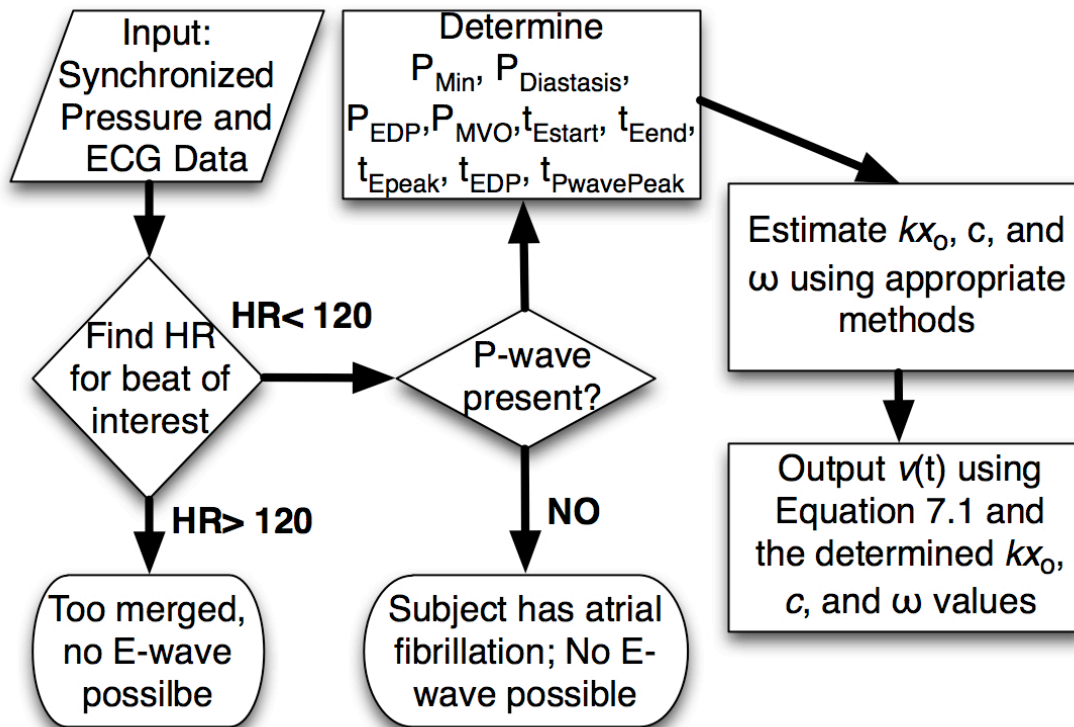


Figure 7.4. A flowchart for generation of a simultaneous E-wave velocity contour given synchronized LVP and ECG data. If the heart rate (HR) is too high, then the E- and A-waves will be merged and it is not possible to generate an E-wave velocity contour. If the HR is within normal limits then one must consider whether the subject has a P-wave or not. If the P-wave is not present then one must abandon the analysis. The general method requires the estimation of kx_0 , ω , and c from specific hemodynamic variables, as described in the text.

not have significantly elevated heart rates, and that subjects possess P -waves in their ECG signal.

Thus, subjects in atrial fibrillation can not be analyzed using these methods.

7.2.1 Estimation of c

To estimate the E-wave from the LVP contour, we first employ the PRR to determine the damping constant c of the E-wave. In Chapter 6, a strong linear relationship is presented between the PRR and the damping constant c . This regression allows for calculation of c given the PRR:

$$c = -19.2(\text{PRR}) + 26.6 \quad \text{Equation 7.2}$$

As described in Chapter 6, the PRR can be easily and in a real-time fashion calculated from the LVP profile (11), and therefore the damping constant c may be simply calculated from Eq. 7.2.

7.2.2 Estimation of kx_0

The next step in estimation of the E-wave involves the estimation of the initial E-wave upslope, kx_0 . Previous published work (2) has demonstrated a strong linear relationship between the echocardiographically determined kx_0 value and the (simultaneously) catheterization determined pressure difference between LVEDP and minimum LVP⁵. This regression provides an equation for determining kx_0 (in units of m/s^2) from LVP profile measures alone:

$$kx_0 = 0.407(P_{EDP} - P_{min}) + 15.40 \quad \text{Equation 7.3}$$

7.2.3 Estimation of ω

The final step involves the calculation of the frequency ω . Because $E_{dur} = \pi/\omega$, the frequency can be easily calculated if we estimate the E-wave duration, E_{dur} . There are several methods by which the duration of the E-wave may be approximated. The ideal method for E_{dur} determination would consist of placing a pressure catheter in the atrium and ventricle. Figure 7.5 gives representative hemodynamic pressure and flow data from such a procedure. As is evident from Figure 5, the E-wave start corresponds to the first atrioventricular pressure crossover, and the end of E-wave flow is causally coupled with the third equalization of atrial and ventricular pressures after mitral valve opening. The impracticality of obtaining atrial pressures in the cath lab were discussed briefly in Chapter 1, and therefore while the method embodied by Figure 7.5 would be ideal, different methodology must be applied.

To aid in analysis we may employ previous results regarding the duration of diastole as a function of heart rate. Previous work by Chung et al. demonstrated a robust correlation ($r^2=0.98$) between the mechanical duration of diastole (MDD) in ms and heart rate (HR) (3).

$$MDD = -549 + 2.13HR + \frac{61500}{HR} \quad \text{Equation 7.4}$$

The HR, in beats per minute can be determined by dividing 60 by the particular beat's R-peak to R-peak time interval (in seconds), and this value can be plugged into Equation 7.4 to determine the MDD. Finally if we take the time of the R-wave peak to be the particular beat's end diastolic time, then we may determine the start of the E-wave and the mitral valve opening time by subtracting the MDD from the R-wave peak time. With this tool in hand we move on to describe the details of the method.

An effective strategy for determination of E_{dur} involves determining the E-wave start- and end-times, and simply taking the difference of these two time points.

7.2.3 Step 1: Determine the E-wave start time

Method 1:

Two simple methods may be employed to determine the E-wave start-time. First, as discussed in Chapter 6, the pressure at mitral valve opening and E-wave start is nearly equivalent

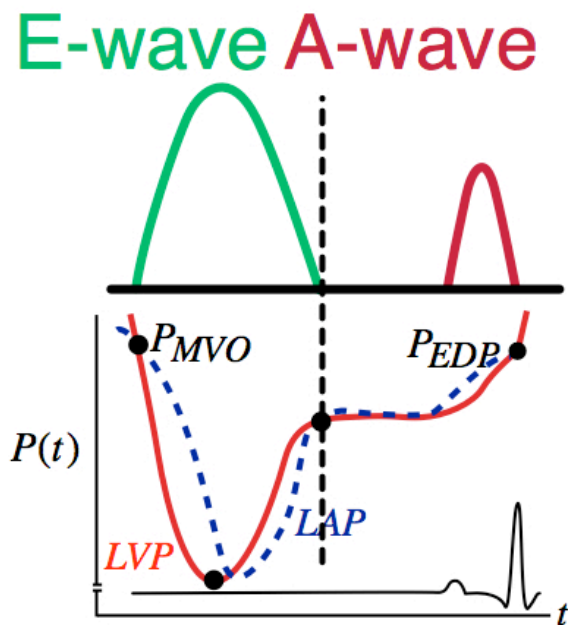


Figure 7.5. Schematic left ventricular pressure, left atrial pressure, Doppler E- and A-wave, and ECG data for one beat. Notice the E-wave ends, and diastasis begins, at the 2nd atrio-ventricular pressure crossover after mitral valve opening. In addition, diastasis begins approximately when the flat portion of the LVP contour commences.

to the end-diastolic pressure. Thus, the time of mitral valve opening and therefore start of the E-wave can be taken to be the time at which the decreasing LVP profile is equal to the ensuing LVEDP.

Method 2:

A second possible method for determining the E-wave start time takes advantage of the strong correlation between MDD and HR presented in Equation 7.4. As discussed above, the E-wave start time is then given by the MDD subtracted from the R-wave peak-determined or otherwise-determined LVEDP time. Once the start of the E-wave is determined, the only task remaining is the determination of the E-wave end-time.

7.2.3 Step 2: Determining the E-wave End Time

Method 1:

Cardiac cycles with RR intervals above 800 ms (<90 beats per minute) typically have a clear diastasis interval separating E- and A-waves. Previous published work has demonstrated a strong correlation between HR and time duration of the diastasis interval. This relationship holds even for slightly merged E- and A-waves (heart rates between 100-120), where the diastasis time interval is negative. Thus, one can easily estimate the interval between E- and A-wave employing the relationship in Chung et al(3):

$$\Delta t_{Diastasis} = 4.40(HR) + 65500\left(\frac{1}{HR}\right) - 1150 \quad \text{Equation 7.5}$$

where $\Delta t_{Diastasis}$ is the duration of diastasis, defined by the time between E-wave end and A-wave start.

Furthermore, the start of the A-wave occurs simultaneously with the ECG P-wave (see Figure 7.5). Current catheterization labs routinely employ automated ECG pattern detection algorithms to detect, among other things, P- and R-waves. Because the ECG signal and the LVP profile are synchronized in the catheterization lab, automated detection of and P- and R-waves allows for automated determination of A-wave start times, as well as diastasis pressures and LVEDP (as described in Chapter 2).

Thus, the E-wave end-time is calculated by traveling backwards in time on the pressure contour, that is, by determining the time of the P-wave peak and subtracting the diastasis interval time determined from Equation 7.5. Once we have the E-wave end-time, the E-wave duration is calculated as simply the difference between E-wave end-time and E-wave start time. Finally, with the E_{dur} calculated, we can easily determine the frequency ω . Putting this together we have:

$$\omega = \frac{\pi}{(t_{ECG\ P-wave} - \Delta t_{Diastasis}) - t_{E-wave\ start}} \quad \text{Equation 7.6}$$

Method 2:

Another possible estimate of the E-wave-end time can be made by considering the flat (i.e. diastatic) portion of the LVP profile. To be sure, the flat portion of the LVP profile does not necessarily represent the full diastatic interval, because diastasis requires the absence of a pressure gradient, and the atrioventricular pressure gradient crossover may not occur until after the LVP profile flattens out or may occur before some major flat regime begins. However, the use of multiple methods to estimate the E-wave end time is advantageous because it provides upper and lower limits to the resulting E-waves. The simplest method for determining the start of the LVP flat interval is a basic thresholding procedure. With this method, the start of the LVP flat interval is the time at which the LVP recoils to a pressure within a 1-2mmHg, or some

suitable threshold, of the previously determined diastasis pressure ($P_{\text{Diastasis}}$). See Chapter 2 for detailed discussion of the methods by which a diastasis pressure may be determined in an automated fashion.

Method 3:

Alternatively, one can determine the LVP flat interval start through an iterative approach. We create a first guess of the LVP flat interval start as the midpoint time between LV minimum pressure and P-wave peak. The iterative approach creates 1 least squares best fit line to the pressure contour between the minimum pressure and previous guess point, and a second least squares best fit line to the pressure contour between the previous guess point and the P-wave peak. The next guess for the time of the start of the LVP flat interval is then taken to be the intersection of the two best fit lines created in the previous step. This process is iterated until one converges on one point, or on a stable cycle of a set of points. If the convergence is toward a set of points, then the start of the LVP flat interval is taken to be the average of these points. This process is visually detailed in Figure 7.6.

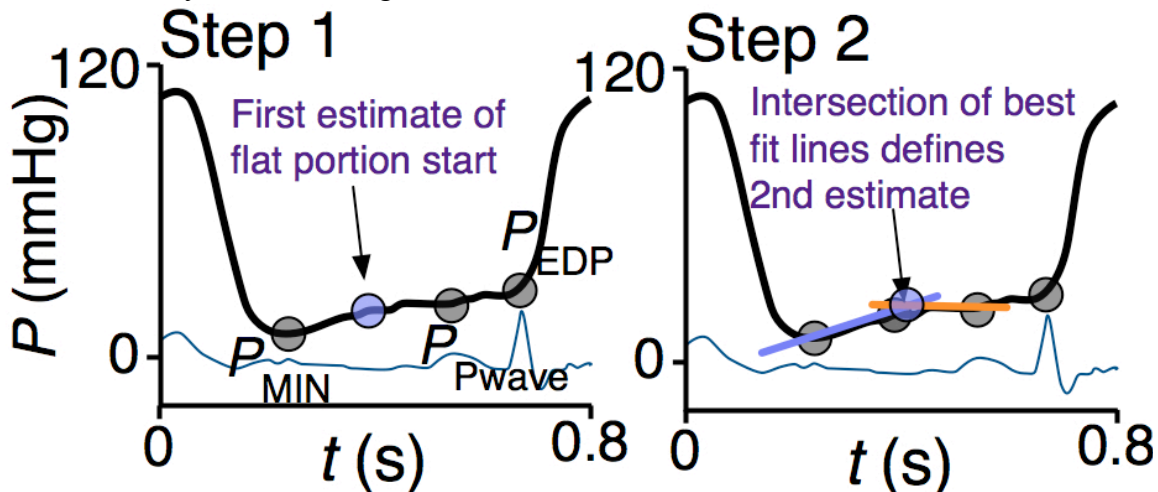


Figure 7.6. In this figure the iterative approach for determining the start of the LVP contour is presented. Initially we take the LVP minimum pressure (P_{MIN}), the P-wave LV pressure (P_{Pwave}), and the halfway point between those two points as initial markers. Best-fit lines are then created between the endpoints and the midpoint, and the intersection point of these lines is taken to be the next estimation of the start of the LVP flat portion. The process is completed once we converge upon a solution.

The iterative approach is a more robust method than simply applying a threshold of 1-2 mmHg relative to a determined diastasis pressure, because in certain cases the so called “flat LVP portion” may not be completely flat, and instead may show a gradual change of 1-5 mmHg with respiration. For example, a large inspiration during a diastasis interval will tend to slightly increase the LV pressures, thereby making the thresholding procedure less reliable, and the iterative approach more favorable. In addition, often clinical data may possess several small regions that appear to be flat, and therefore it is not obvious as to which flat region to pick. This is seen somewhat in the data presented in Figure 7.2, and in such cases the iterative approach to determining the end of the E-wave is preferred.

7.3. In Silico Echocardiography Proof Of Principle

We will apply the methods described above to the LVP contour presented in Figure 7.2. In other words, we will estimate the E-wave associated with the hemodynamics presented in that beat. The data presented in Figure 7.2 was acquired during a specific simultaneous catheterization-echocardiography research study, and thus the simultaneous echocardiographically measured E-wave can be superimposed with the In Silico Echocardiography derived E-wave to assess how closely our estimate fits with the real data.

First using automated ECG pattern detection techniques which are widely available in the clinical setting, we determine the R-waves that flank the filling interval. The resulting RR interval is 930 ms, which gives a HR of 65 beats per minute. This is well within the regime of unmerged waves, so we proceed with the flow chart presented in Figure 7.4.

Next we determine various hemodynamic parameters, and much of the methods for this are discussed in Chapter 2. We notice that the particular beat contains a P-wave, and therefore we may proceed in our analysis.

First we determine the end-diastolic pressure P_{EDP} . Because there is no evidence of AV block, we take P_{EDP} to be the pressure at the peak of the R-wave, which is 23.7 mmHg, or the pressure at the start of the R-wave, which is 20.3 mmHg. In the presence of AV block one would have to calculate the maximum pressure between the R-wave peak and the minimum pressure point to determine P_{EDP} . By maintaining two estimates for P_{EDP} we allow for the determination of lower and upper bounds for the resulting E-wave. Now we make the assumption that mitral valve opening pressure equals end-diastolic pressure, and therefore determine that the E-wave start time must be either at $t_{Estart}=6.624s$, or $t_{Estart}=6.622s$, depending on if we use the peak R-wave or start of R-wave determined P_{EDP} pressure as a reference. Furthermore, we can use the determined HR and plug into Equation 7.6 to determine the MDD. We thus determine the MDD to be 542 ms. Again, if we know that diastole ends at either the peak of the R-wave or the start of the R-wave, then subtracting MDD we find that the E-wave start and mitral valve opening occurs at $t_{Estart}=6.564s$ or $t_{Estart}=6.594s$ respectively. Thus we have multiple estimates for the E-wave start time.

Next we can easily determine the minimum pressure, because it is the minimum pressure found in the chosen R-R interval. We find that the minimum pressure is $P_{Min}=4.5$ mmHg and that this minimum occurs at $t_{Min}=6.716s$.

Next we determine the diastasis pressure $P_{Diastasis}$. We may take advantage of the presence of a P-wave, and through ECG detection algorithms we can determine the peak of the P-wave to be at $t_{PwavePeak}=7.031s$, with a simultaneous LV pressure of $P_{PwavePeak}=16.3$ mmHg. Because the

P-wave peak marks the beginning of A-wave flow, we may estimate the diastasis pressure as simply being the pressure at the P-wave peak, and thus a first estimate of $P_{\text{Diastasis}}$ is $P_{\text{Diastasis}}=16.3$ mmHg. Also we may back off the P-wave peak and only take the pressure at the start of the P-wave, which is $P_{\text{Diastasis}}=14.4$ mmHg. We can apply next the iterative approach detailed above for determination of E-wave end time. This method converges on $t_{\text{End}}=6.851$ s, and a concurrent diastasis pressure of $P_{\text{Diastasis}}=12.5$ mmHg. If we apply the iterative method with the P-wave start as a reference point instead of the P-wave peak then we converge on $t_{\text{End}}=6.856$ s, and a $P_{\text{Diastasis}}=12.6$ mmHg. The refined diastasis pressure is then the average of these values, and is therefore $P_{\text{Diastasis}}=14.0$ mmHg. Averaging over multiple values only serves to overdetermine and average out any systematic errors or biases associated with one particular method. It is not in general necessary to calculate so many approximations to the diastasis pressure, and in practice only one or two estimations may be necessary. Alternatively, one may simply calculate the $\Delta t_{\text{Diastasis}}$ as defined in Equation 7.5, and determine the start of diastasis by simply subtracting $\Delta t_{\text{Diastasis}}$ from the P-wave peak time. Plugging in for HR we find that $\Delta t_{\text{Diastasis}} = 149.12$ ms, and this yields $t_{\text{End}}=6.882$ s. Then the diastasis pressure may be simply estimated as the average pressure between t_{End} and $t_{\text{PwavePeak}}$. The average pressure between $t=6.882$ s and $t=7.031$ s is 15.0 mmHg, and thus another estimate is $P_{\text{Diastasis}} = 15.0$ mmHg.

With these calculations we can now determine c , kx_o , and ω . First, we determine c . To do this we must calculate the PRR, which is described in more detail in Chapter 6. Using the value for P_{Min} and the various estimates for P_{EDP} and $P_{\text{Diastasis}}$ we obtain that PRR may be 0.49, 0.60, 0.55, or 0.67, and, using Equation 3, we find that c is either 17.1 1/s, 15.1 1/s, 16.1 1/s, or 13.8 1/s respectively. The average PRR is 0.58 and the average c is 15.5 1/s.

Next we determine the kx_0 value. Using the value for P_{Min} and the possible values for P_{EDP} we determine that the ΔP may be 19.3 mmHg or 15.8 mmHg. These pressure differences correspond, using Equation 7.3, to kx_0 values of 23.2 mN or 21.8 mN, with an average value of 22.5 mN.

Finally we determine the frequency ω . In determining the diastasis pressure we have already found estimates of t_{End} , and in the first few calculations we determined several estimates for t_{Start} . Taking the difference between the estimated E-wave end and start times results in possible values for E_{dur} , and, by Equation 2, possible values for ω . Using only estimates for t_{End} that employ the P-wave peak, we find that E_{dur} may be 0.258s, 0.26, 0.288s, or 0.318s. The corresponding ω values are 12.2 1/s, 12.1 1/s, 10.9 1/s or 9.9 1/s.

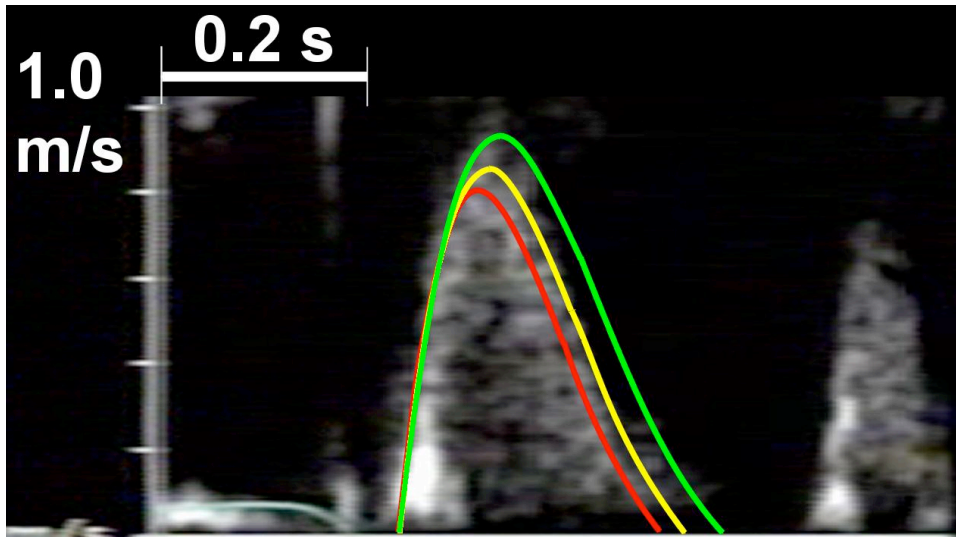


Figure 7.7 The actual transmitral Doppler velocity contour measured simultaneously during catheterization for the beat presented in Figure 7.2 is shown here. Upper bound, lower bound, and average E-waves derived from the LVP profile alone are superimposed in green, red and yellow curves respectively. Notice the close agreement between predicted average E-wave (yellow curve), and the actual measured E-wave contour. See text for details.

With all of this in hand, we may create upper bounds, lower bounds, and average values for all the E-wave parameters of interest. The lower bound E-wave has $\omega=9.9$ 1/s, $kx_0=21.8$ and

$c=14.3$ 1/s. The upper bound E-wave has $\omega=12.2$ 1/s, $kx_0=23.2$ and $c=16.7$ 1/s. Finally, the average E-wave has $\omega=11.18$ 1/s, $kx_0=22.5$ and $c=15.3$ 1/s.

To display any of these E-waves we plug in the estimated ω , kx_0 , and c values into Equation 1. This leaves still the variable t in Equation 7.1. We simply take t to be between 0 and E_{dur} , where E_{dur} is given by the estimated ω value, and plot the resulting function with appropriate scale on the LVP contour or in a separate display.

For comparison, the resulting upper bound, lower bound, and average E-wave estimated from the LVP contour alone is superimposed on the actual measured Doppler E-wave in Figure 7.7. Notice that the average E-wave, colored in yellow, predicts the true E-wave contour extremely well. Furthermore the

upper and lower bound E-wave effectively demarcate the location of the true E-wave, and track the deceleration portion curvature fairly well. Thus Figure 7.7 demonstrates how closely an invasively derived E-wave analogue can predict the actual noninvasive Doppler E-wave.

To independently assess the closeness of fit, a blinded observer applied the PDF formalism to the raw E-wave image from Figure 7.7, in order to derive a best-fit velocity contour. Figure 7.8 shows the best-fit velocity contour (5), derived by the blinded investigator (green), as well as the LVP-contour derived

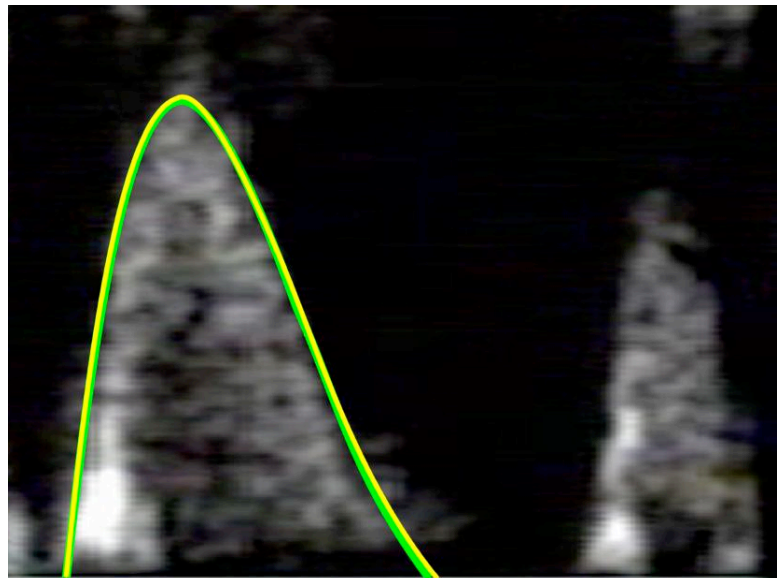


Figure 7.8 An independent assessment of the close agreement between the In Silico Echocardiography determined E-wave and measured Doppler E-wave.

average E-wave that we showed in Figure 7.7 (yellow). The two waves are virtually indistinguishable. Thus, “In Silico Echocardiography” gives the clinician the ability to see, in real-time, a very close analogue to the actual E-wave without ever having to separately order an echocardiographic study.

The results in this Chapter provide methodological details and demonstrate the potential of the In Silico Echocardiography method with a selected example. Further work extending these results to more subjects, including those with diastolic dysfunction is warranted.

7.4 REFERENCES

1. Appleton CP, Firstenberg MS, Garcia MJ, and Thomas JD. The echo-Doppler evaluation of left ventricular diastolic function. A current perspective. *Cardiology clinics* 18: 513-546, ix, 2000.
2. Bauman L, Chung CS, Karamanoglu M, and Kovács SJ. The peak atrioventricular pressure gradient to transmitral flow relation: kinematic model prediction with in vivo validation. *Journal of the American Society of Echocardiography : official publication of the American Society of Echocardiography* 17: 839-844, 2004.
3. Chung CS, Karamanoglu M, and Kovács SJ. Duration of diastole and its phases as a function of heart rate during supine bicycle exercise. *Am J Physiol Heart Circ Physiol* 287: H2003-2008, 2004.
4. Hall AF, Aronovitz JA, Nudelman SP, and Kovács SJ. Automated method for characterization of diastolic transmitral Doppler velocity contours: late atrial filling. *Ultrasound in medicine & biology* 20: 859-869, 1994.
5. Hall AF and Kovács SJ. Automated method for characterization of diastolic transmitral Doppler velocity contours: early rapid filling. *Ultrasound in Medicine and Biology* 20: 107-116, 1994.
6. Hall AF, Nudelman SP, and Kovács SJ. Beat averaging alternatives for transmitral Doppler flow velocity images. *Ultrasound in medicine & biology* 24: 971-979, 1998.
7. Kass DA. Assessment of diastolic dysfunction. Invasive modalities. *Cardiology clinics* 18: 571-586, 2000.
8. Kovács SJ, Barzilai B, and Pérez JE. Evaluation of diastolic function with Doppler echocardiography: the PDF formalism. *Am J Physiol* 252: H178-187, 1987.

9. Lisauskas JB, Singh J, Bowman AW, and Kovács SJ. Chamber properties from transmitral flow: prediction of average and passive left ventricular diastolic stiffness. *J Appl Physiol* 91: 154-162, 2001.
10. Shmuylovich L and Kovács SJ. E-wave deceleration time may not provide an accurate determination of LV chamber stiffness if LV relaxation/viscoelasticity is unknown. *Am J Physiol Heart Circ Physiol* 292: H2712-2720, 2007.
11. Zhang W, Shmuylovich L, and Kovacs SJ. The pressure recovery ratio: The invasive index of LV relaxation during filling. Model-based prediction with in-vivo validation. *Conf Proc IEEE Eng Med Biol Soc* 2009: 3940-3943, 2009.
12. Zile MR and Brutsaert DL. New concepts in diastolic dysfunction and diastolic heart failure: Part I: diagnosis, prognosis, and measurements of diastolic function. *Circulation* 105: 1387-1393, 2002.

CHAPTER 8.

LOAD INDEPENDENT INDEX OF DIASTOLIC FUNCTION: DERIVATION

AND IN VIVO VALIDATION

8.1 INTRODUCTION

8.1.1 Previously Validated Load Independent Index of Systolic Function

The analysis of pressure-volume data obtained from the in-vivo heart for the purpose of determining intrinsic pump function is complex because pressures and volumes are dependent on both intrinsic variables (such as contractility and muscle stiffness) and extrinsic variables (such as preload and afterload). By viewing cardiac function mechanically, as a system having time-varying elastance, Suga and Sagawa successfully uncoupled these variables (29). They showed experimentally that the instantaneous pressure to volume ratio defines a time-varying elastance that attains the same maximum value at a fixed contractile state regardless of preload changes. This established E_{\max} as an experimentally validated, load-independent index of systolic function (27). Additional conceptual validation of E_{\max} as a load-independent index has been achieved using a kinematic, forced harmonic oscillator-based argument showing that the slope of the maximum force-displacement relationship (E_{\max} analog) depends only on the intrinsic oscillator parameters rather than the initial (load) conditions (21). While E_{\max} is a chamber property that is uncoupled from the effects of load on systolic function, no non-invasive load-independent attribute for diastole has been theoretically proposed and validated, or empirically observed in the course of experiment.

8.1.2 The Load Independent Index of Diastolic Function Problem

Doppler echocardiography is the preferred method for noninvasive diastolic function (DF) assessment. Doppler derived indexes have been used to characterize DF in numerous cardiac disorders including heart failure, myocardial infarction, hypertrophic cardiomyopathy, and hypertension (1). In current practice, most DF indexes are derived by visual inspection of

transmitral E- and A-waves. These shape-derived indexes include peak velocity of the E-wave (E_{peak}), duration of the E-wave (E_{dur}), acceleration and deceleration times of the E-wave (AT and DT) and area under the E-wave (velocity-time integral VTI). Additional indexes include the peak velocity of the A wave (A_{peak}) and the ratio of the E and A peak velocities (E/A). Most clinically relevant Doppler derived DF indexes have proved to be load-dependent in animals and humans, both in health and in disease (3, 7, 9, 11, 13, 17, 22, 24, 25, 28, 30-32, 35, 38). Several newer load-independent indexes have been empirically suggested, from velocity of propagation (V_p), to annular velocities derived from Doppler tissue imaging (E'/A' , E' , E/E'), but there is no consensus as to whether these indexes are truly load independent (8, 12, 15, 19, 20, 23, 37). This established load-dependence confounds the clinical interpretation of diastolic function indexes, because load variation may modify an E-wave shape in a pathologic setting to resemble a normal E-wave, and therefore lead to an uncertain diagnosis.

8.1.3 Approaching the Load Independent Index Problem with the PDF Model

At first glance it appears that the PDF model should solve this problem naturally, because from a purely mathematical perspective, the PDF parameters c , k , are mathematically independent of the load parameter x_0 . In the context of physiology, however, this mathematical degree of freedom is constrained, because there is physiological coupling between stiffness, relaxation, and load. Indeed because k , c , and x_0 mathematically determine the shape of the E-wave, it is not surprising that load-induced E-wave shape variation results in k , c , and x_0 variation. Even if load is varied, suction initiated filling governs the physiology and therefore the PDF model and the equation of motion apply. Therefore, in the face of load variation, the PDF model solution should continue to provide an accurate prediction for E-wave shape. This insight

suggests an approach to solving the ‘load independent index of diastolic function’ (LIIDF) problem. Because the same kinematics apply to E-waves measured at different load, we hypothesize that a load independent index of diastolic function, M , may be derived from appropriate mathematical analysis of multiple E-waves acquired at different loads. To test the load independence of M , we altered load in healthy human volunteer subjects by changing tilt-table position while recording transmitral flow. We investigated changes in traditional echo-derived indexes, changes in PDF parameters, and the load dependence of M . To assess the ability of M to differentiate between control and diastolic dysfunction (DD) states, we analyzed preexisting data from patients undergoing simultaneous catheterization-echocardiography using micromanometric (Millar) catheters.

8.2 METHODS

8.2.1 Theory

Theoretical Derivation

We begin with the underdamped form of E-wave velocity from Chapter 2:

$$v(t) = \frac{kx_o}{\omega} e^{-\frac{c}{2}t} \sin(\omega t) \quad \text{Equation 8.1}$$

To solve the LIIDF problem, we consider Equation 8.1 at two extremes. At the start of filling, velocity vanishes, and we have an expression for kx_o the peak mass-normalized force driving flow:

$$kx(0) = -\ddot{x}(0) \longrightarrow kx_o = \ddot{x}_o \quad \text{Equation 8.2}$$

At the peak of inflow, the acceleration term vanishes, and we have an expression for cE_{peak} , the peak resistive force opposing flow:

$$c\dot{x}(AT) = -kx(AT) \longrightarrow cE_{peak} = kx(t_{peak}) \quad \text{Equation 8.3}$$

This analysis demonstrates that for every E-wave fit by the PDF model, the peak resistive force that opposes flow (cE_{peak}), is equivalent to the spring force driving flow at time of E-wave peak. That is a tautological statement that is certainly load-independent, but it has little clinical value because it can not differentiate one subject from another.

To find a clinically useful LIIDF, we must apply physiological constraints to this analysis. Applying the expressions for $x(t)$ and AT from Chapter 2 to Eq. 8.3, we find that:

$$kx(t_{peak}) = kx_o \left[2y \cdot e^{-\alpha t_{peak}} \right] = kx_o \left[2y \cdot e^{-\frac{y \cos^{-1}(y)}{\sqrt{1-y^2}}} \right] \quad \text{Equation 8.4}$$

Eq 8.4 suggests a connection between $kx(t_{peak})$ and kx_o . Indeed, because E-waves reach peak velocity fairly quickly, it may be appropriate to approximate $kx(t_{peak})$ as a linear function of kx_o :

$$kx(t_{peak}) = \mu \cdot kx_o + \nu \quad \text{Equation 8.5}$$

, where μ and ν are constants. Together with Eq. 8.3, this suggests that kx_o and cE_{peak} are linearly related according to the equation:

$$kx_o = M(cE_{peak}) + B \quad \text{Equation 8.6}$$

where M and B are constants, kx_o is the mathematical analogue for the maximum AV gradient and cE_{peak} represents the resistive (viscoelastic) force opposing filling.

Each E-wave fit by the PDF model has a kx_o and cE_{peak} value, and therefore may be plotted as a point in the kx_o vs cE_{peak} plane. As load varies, E-wave shape varies, and therefore the corresponding kx_o vs cE_{peak} coordinate for the E-wave may change as well. However, the slope (M) defined by the collection of load varying E-wave kx_o vs. cE_{peak} coordinates is predicted to remain constant. This is a prediction that is derived from load-independent assumptions, and is

therefore expected to hold in the face of load variation. Therefore the slope M , and intercept B , derived from analysis of the maximum driving force and the maximum force opposing blood flow, is predicted to be a LIIDF. If M and B can be shown to differentiate subjects with and without diastolic dysfunction, then they would be the only validated solutions to the LIIDF problem.

Theoretical Analysis

Further insight may be gained by considering physiological limits in the kx_o vs cE_{peak} plane. The mathematics are somewhat easier to appreciate if we determine the quotient of kx_o and cE_{peak} from Equation 8.4:

$$\frac{kx_o}{cE_{\text{peak}}} = \frac{1}{2y} \cdot e^{\frac{y \cos^{-1}(y)}{\sqrt{1-y^2}}} \quad \text{Equation 8.7}$$

, where as before, $y=c/2\sqrt{k}$. It is interesting to note from Eq. 8.7 that lines through the origin in the kx_o vs cE_{peak} plane are lines of constant y . From a physiological perspective, it is clear that a ventricle must have the peak driving force exceed the peak resistive force if filling is to occur. Thus, the $kx_o=cE_{\text{peak}}$ line of unity represents a physiological barrier that can not be crossed. Thus E-wave kx_o vs cE_{peak} coordinates can only exist above the line of unity in the kx_o vs cE_{peak} plane. This physiological fact can be extracted mathematically by noticing that because $y \geq 0$, the minimum of Eq. 8.7 occurs when $y=\infty$ and therefore $kx_o/cE_{\text{peak}}=1$. The other extreme limit for Eq. 8.7 occurs when $y=0$ and therefore $kx_o/cE_{\text{peak}}=\infty$. This corresponds to the case where there are no resistive forces and $c=0$. There is one other interesting physiological limit that we can consider, and that is the case of critically damped E-waves. Critical damping occurs when $y=1$, and by Eq. 8.7 that yields a value of $e/2 \sim 1.36$ for kx_o/cE_{peak} . Thus the line through the origin with

slope $e/2$ defines a transition between overdamped and underdamped E-waves. Overdamped E-wave have kx_0 vs cE_{peak} coordinates below the $e/2$ line, while underdamped E-waves have kx_0 vs cE_{peak} coordinates above the $e/2$ line (Figure 8.1).

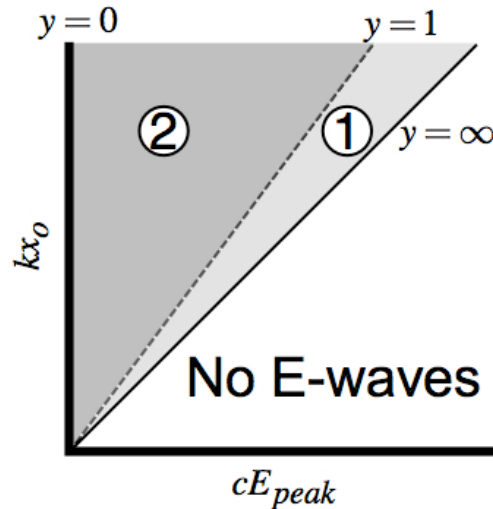


Figure 8.1. Theoretical analysis of the peak driving force (kx_0) to peak resistive force (cE_{peak}) plane, showing regimes of y , defined as $c/(2\sqrt{k})$. The $kx_0=cE_{peak}$ line corresponds to $y=\infty$, and the kx_0 -axis corresponds to $y=0$. Underdamped E-waves (2) are in the $y<1$ regime, whereas overdamped E-waves are in the $y>1$ regime. The $cE_{peak}>kx_0$ regime is not compatible with filling. See text for details.

8.2.2 Experimental Validation

Data Acquisition- Tilt Table Healthy

Volunteers

Pulsed Doppler echocardiography was

used to acquire continuous transmitral blood flow data from 16 subjects (9 male, 7 female, ages 20-30) while subjects were positioned on a tilt-table (Trex Medical Corporation, Danbury, CT). Doppler data was acquired in the apical four-chamber views with the sample volume gated at 1.5 to 2.5 mm and directed between the tips of the mitral valve leaflets orthogonal to the MV plane. The subjects were healthy medical and graduate students on no prescribed medications. None of the subjects had history of heart disease, coronary artery disease, hypertension, or diabetes. Prior to participation in the study, all subjects gave informed consent in accordance with the Washington University Human Research Protection Office guidelines.

Doppler data was obtained with a clinical echocardiographic imaging system (Acuson Sequia 256, Mountain View, CA) equipped with a 2MHz transducer. Heart rate was recorded simultaneously via ECG limb lead II and displayed on the E- and A-wave images. Blood

pressure was monitored via a digital blood pressure cuff (Medtronic LifePak 12, Minneapolis MN).

The data acquisition protocol consisted of initial (baseline) E- and A-wave recording with the subject supine and the tilt table in the horizontal position for 5 minutes such that the heart rate was in steady state. Baseline blood pressure was also obtained. After 5 minutes in horizontal position, the table, including appropriate padding and straps to assure safety, was gradually tilted to a 90° head-down position. Since the heart/diaphragm shifted during tilt, the transducer was suitably reoriented to obtain transmitral flow. After resolution of heart rate transients, typically after several minutes, transmitral flow was recorded. After several minutes the tilt-table was returned to the horizontal position. Once heart rate and blood pressure returned to baseline levels, transmitral flow was again recorded. After 5 minutes horizontally, the tilt table was moved to 90° head-up position. The transducer was adjusted to account for the heart shift during tilt, and after heart rate and blood pressure transients resolved, transmitral flow was recorded. In 2 of the 16 subjects the persistent increase in heart rate during head up tilt resulted in significant E- and A-wave merging. With significant merging the E-wave deceleration portion is lost, and thus it is not possible to reliably fit merged waves via the PDF formalism. Hence for these 2 subjects head-up E-waves were not analyzed, but the head-down and horizontal data were included in the overall analysis. After 5 minutes upright subjects were tilted to horizontal position and a concluding set of transmitral flow images were recorded. All data was recorded on VHS tape for off-line analysis using a custom editing station.

Data Acquisition- Subjects Undergoing Simultaneous Catheterization and Echocardiography

In addition to acquiring data in healthy normal subjects via tilt-table, we acquired additional data in subjects with and without diastolic dysfunction undergoing diagnostic

catheterization. This additional analysis used existing data from previous studies(2, 16) utilizing the Cardiovascular Biophysics Laboratory database of simultaneous Doppler echocardiographic transmitral flow and micromanometric (Millar) catheter-derived left ventricular pressure (see Chapter 2 for a detailed description of existing Cardiovascular Biophysics Laboratory simultaneous Doppler flow and catheter derived pressure database). We note that the original intent of the Cardiovascular Biophysics Laboratory database was not explicit testing of load-dependence. However, because some subjects manifested significant beat-to-beat respiratory variation of end diastolic pressure and simultaneously recorded E-wave contours, the data were suitable for determination of the kx_0 to cE_{peak} relationship. We therefore selected subjects who had good quality E-waves as well as significant load variation (end diastolic pressure variation > 10 mmHg) in response to the respiratory cycle. Selection criteria for inclusion in the diastolic dysfunction group required: normal sinus rhythm, no evidence of valvular disease, no active ischemia, normal ejection fraction(EF) $>60\%$, and elevated end diastolic pressure (>19 mmHg). Subjects in the control group had normal sinus rhythm, no valvular disease, no active ischemia, normal EF $>60\%$ and normal end diastolic pressure. Because subjects are referred for catheterization to establish the presence of coronary artery disease, variable degrees of coronary artery disease were present in both the control and diastolic dysfunction groups. However, no subject in either group had ongoing or active ischemia. Demographics are presented in Table 8.1.

Data Analysis

For each tilt table subject at each stage of tilt, 5 E- and A-wave contours were selected for analysis. A traditional triangle fit was applied to each wave and conventional Doppler-derived indexes (E_{peak} , AT, DT, E_{dur} , A_{peak} , A_{dur} , E/A) were determined. In addition, E- and A-wave contours were fit via the parameterized diastolic filling formalism to yield PDF c , k , and x_0

parameters. Since directly measured and model calculated

values of E_{peak} show nearly perfect agreement, E_{peak} was calculated directly from the model predicted contour for the E-wave.

For each catheterization subject, 25 consecutive E-waves and

simultaneous left ventricular pressures were analyzed. For each subject, good quality E-waves were selected and analyzed using the model-based fitting procedure described above. Left ventricular end-diastolic pressure was determined from the simultaneous left ventricular pressure data by reading off the pressure at the time of ECG R-wave peak. See Chapter 2 for detailed methods related to triangle fitting, PDF fitting, and determination of end diastolic pressure.

For each E-wave from each subject, the products $k \cdot x_0$ and $c \cdot E_{\text{peak}}$ were calculated, and the resulting coordinates were plotted in the kx_0 vs cE_{peak} plane. For each subject, the collection of E-wave kx_0 vs cE_{peak} coordinates defined a best fit linear regression, and the slope (M) and intercept (B) of the regression were calculated. M is the predicted dimensionless load independent index of diastolic function (Figure 8.2). The Pearson correlation coefficient for the kx_0 vs cE_{peak} regression was calculated for each subject and compared between subjects. The values of M and B were average and compared by ANOVA between groups (tilt-table group, normal control catheterization group, and diastolic dysfunction catheterization group).

All parameters, both conventional and model-based, were compared within each tilt-table subject between different load states. Percent change relative to supine values was calculated and

Table 8.1. *Demographics of simultaneous catheterization-echocardiography subjects analyzed retrospectively*

	Control	Diastolic Dysfunction
<i>n</i>	5	6
Age	44 ± 9	49 ± 13
Weight	156 ± 30	202 ± 48
Systolic LV Pressure	119 ± 8	147 ± 25*
Ejection Fraction	73 ± 8	68 ± 8
LVEDP	13 ± 4	26 ± 5†

Values are means (SD); *n* (no. of subjects) = 11. LV, left ventricular; LVEDP, LV end-diastolic pressure. * $P < 0.05$; † $P < 0.001$. *P* values were calculated by ANOVA.

compared across subjects. All statistical analysis was carried out using MS-Excel (Microsoft, Redmond, WA).

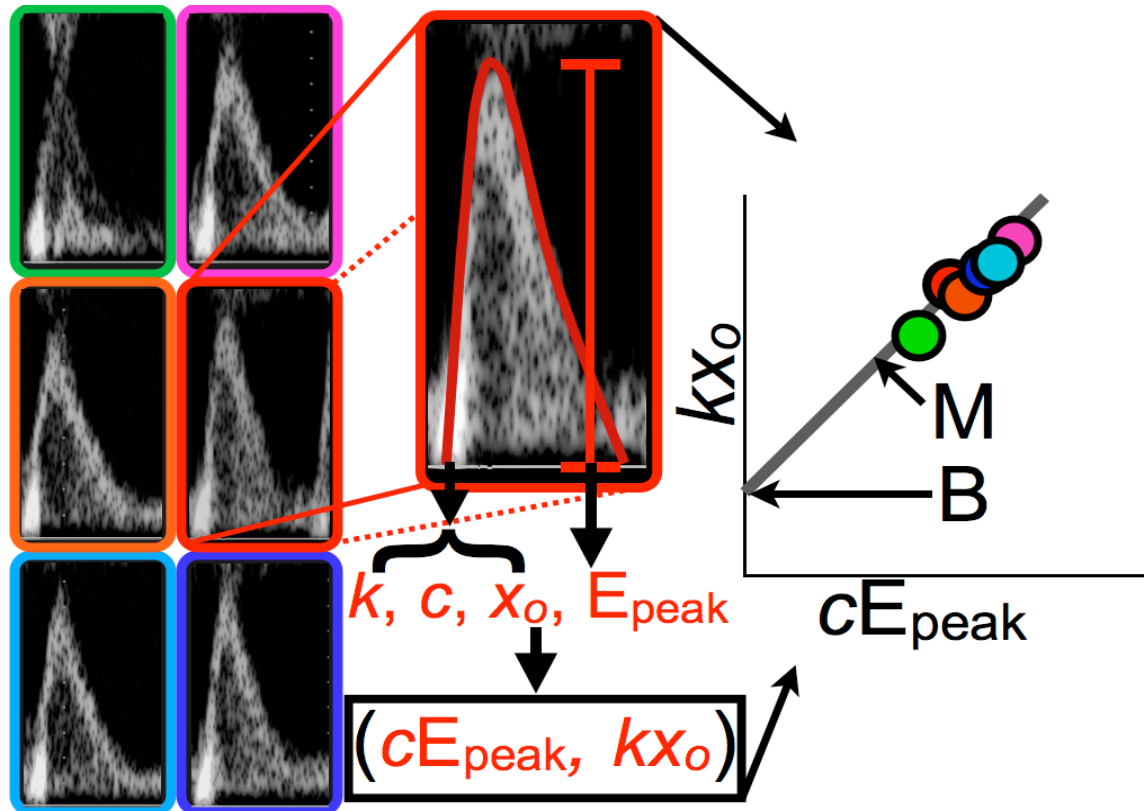


Figure 8.2. The determination of the load independent index of diastolic function (LIIDF), requires multiple E-waves with different shapes. In this case we demonstrate the method applied to 6 waves, though in practice more waves may be necessary. Each wave therefore determines one point in the kx_0 vs cE_{peak} plane, and we color code the waves and corresponding points above for clarity. The slope M of the resulting linear regression determined by the points in the kx_0 vs cE_{peak} plane a dimensionless load-independent index of diastolic function.

8.3 RESULTS

8.3.1 Variation of E-wave shape with tilt table position

In agreement with earlier studies (7, 9, 14, 22, 24, 25, 30), both E- and A- wave shapes varied in response to changes in load generated by changes in tilt table position. Since the PDF

parameters are determined from the contour of the waves, changes in load resulted in changes in the PDF parameters. Figure 8.3 shows representative Doppler waves from a subject in the head-up, supine and head-down position. Table 8.2 summarizes the average values for both traditional Doppler indexes and PDF parameters under different load states i.e. tilt-table positions.

Since subjects had a distribution of values for Doppler indexes and PDF parameter values in the horizontal tilt-table position, determining an average over all subjects required reference to a common baseline. Supine (horizontal) was chosen as the baseline tilt table position and all values were calculated as percent change from horizontal. Table 8.3 presents both PDF and traditional Doppler data as percent change from horizontal for both head-up and head-down tilt.

Table 8.2 *Average values of Doppler indexes and PDF parameters in one typical tilt table subject at three different preload states*

	Head Up	Horizontal	Head Down
<i>Average Doppler indexes, one typical subject</i>			
E_{peak} , m/s	0.50 ± 0.05	0.55 ± 0.05	0.70 ± 0.04
AT, s	0.11 ± 0.01	0.10 ± 0.01	0.09 ± 0.01
DT, s	0.16 ± 0.03	0.14 ± 0.02	0.13 ± 0.01
E_{dur} , s	0.27 ± 0.03	0.24 ± 0.03	0.22 ± 0.02
A_{peak} , m/s	0.42 ± 0.04	0.36 ± 0.04	0.39 ± 0.04
A_{dur} , s	0.13 ± 0.01	0.13 ± 0.01	0.13 ± 0.01
E/A	1.2 ± 0.1	1.5 ± 0.1	1.8 ± 0.2
HR, beats/min	58 ± 7	49 ± 2	56 ± 6
<i>Average PDF parameter values, same typical subject</i>			
$c \cdot 10^3$ (1/s)	5.6 ± 3.9	11.3 ± 3.0	16.2 ± 5.7
$k \cdot 10^3$ (1/s ²)	113 ± 24	198 ± 31	249 ± 21
x_o , m	0.06 ± 0.01	0.06 ± 0.00	0.08 ± 0.02

Values are means \pm SD. E_{peak} , peak velocity of E-wave; AT, acceleration time; DT, deceleration time; E_{dur} , duration of E-wave; A_{peak} , peak velocity of A-wave; A_{dur} , duration of A-wave; E/A ratio of E-wave to A-wave; HR

Table 8.3. *Averaged, normalized percent increase or decrease relative to baseline (horizontal tilt table position) for all tilt table subjects*

	Head Up	Head Down
<i>Doppler indexes, normalized percent change</i>		
E_{peak} , m/s	-24 ± 17^a	$+4 \pm 14^b$
AT, s	$+10 \pm 12^a$	-9 ± 13^a
DT, s	$+3 \pm 18^d$	-7 ± 17^a
E_{dur} , s	$+7 \pm 10^a$	-7 ± 11^a
A_{peak} , m/s	-2 ± 20^a	$+6 \pm 15^a$
A_{dur} , s	$+0 \pm 13^c$	-5 ± 10^a
E/A	-26 ± 20^a	-5 ± 20^c
HR (beats/min)	$+15 \pm 9^a$	$+8 \pm 9^a$
<i>PDF parameters, normalized percent change</i>		
$c \cdot 10^3$, 1/s	-33 ± 31^a	$+25 \pm 48^a$
$k \cdot 10^3$, 1/s ²	-37 ± 16^a	$+19 \pm 28^a$
x_o , m	-5 ± 26^f	$+5 \pm 26^g$

Values are means \pm SD; $n = 16$. +, increase; -, decrease. ^a $P < 0.0001$; ^b $P < 0.001$; ^c $P < 0.01$; ^d $P = 0.03$; ^e $P = 0.09$; ^f $P = 0.4$; ^g $P = 0.07$. All P values vs. baseline.

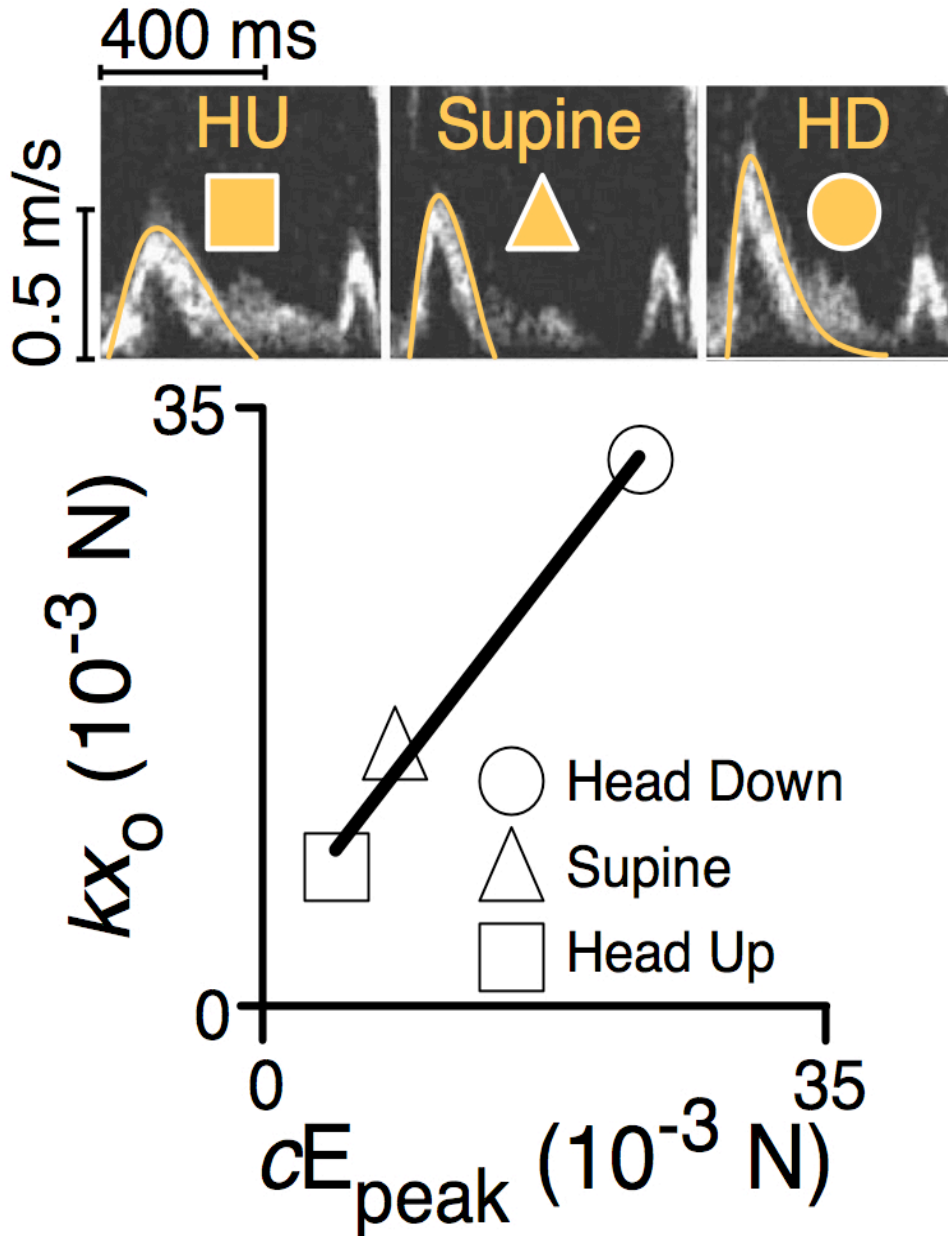


Figure 8.3. A) E- and A-waves acquired from healthy subject at 3 different tilt-table positions (HU=head up, HD= head down). Notice the E-wave shapes change with load. B) Applying MBIP to the three images to find kx_0 and cE_{peak} yields a line with constant slope that defines the ventricle's intrinsic diastolic function.

8.3.2 Determination of predicted load independence in tilt table subjects

In accordance with the prediction (see Methods 8.2.1) that the maximum driving force must be linearly related to peak viscous (resistive) force, a linear regression via least mean square error of cE_{peak} to kx_0 was performed. Figure 8.3 demonstrates the kx_0 vs cE_{peak} regression

defined by the 3 E-waves in the figure. Figure 8.4A shows a representative *maximum driving force* (kx_o) vs. *peak resistive force* (cE_{peak}) plot for another subject, showing all measured beats plotted in the kx_o vs cE_{peak} plane. Head-up data from two subjects was not included, but their head-down and horizontal data fit the *maximum driving force* (kx_o) vs. *peak resistive force* (cE_{peak}) regression with high r^2 . Among all subjects, the average slope of the *maximum driving force* (kx_o) vs. *peak resistive force* (cE_{peak}) plot was 1.27 ± 0.09 and the average intercept was 5.69 ± 1.70 . The average r^2 value for each subjects' linear regression was $r^2=0.95$. The combined

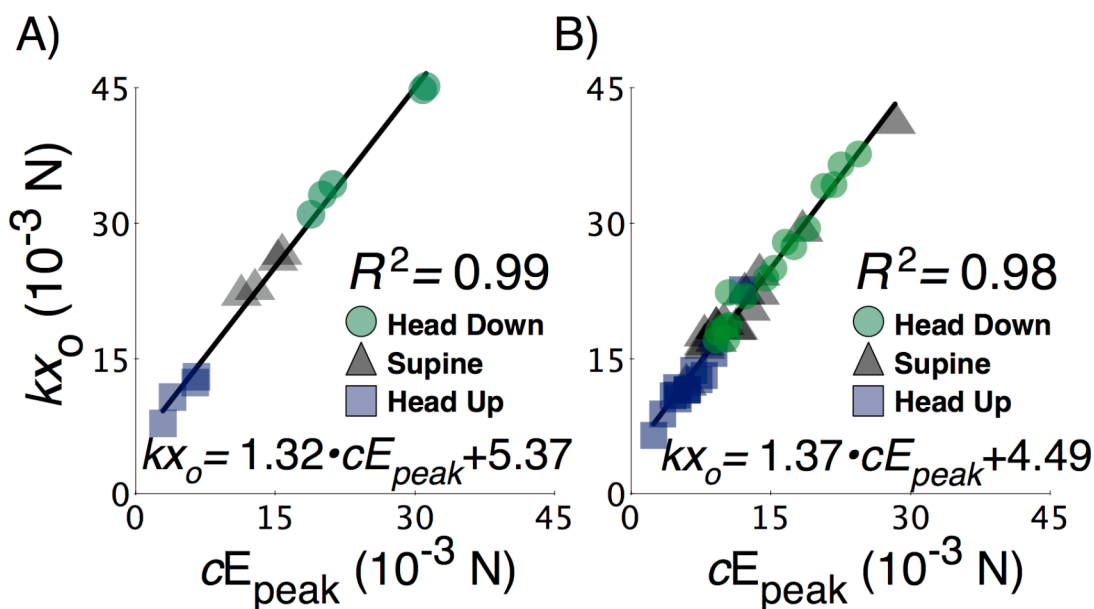


Figure 8.4. A) Maximum driving force (kx_o , peak AV gradient) vs. peak resistive force (cE_{peak}) for one subject at three different preload states. Note slope of best linear fit is independent of tilt-table position. B) Maximum driving force (kx_o , peak AV gradient) vs. peak resistive force (cE_{peak}) for all (n=16) subjects at different preload states. Reported values represent 5-beat average for kx_o and cE_{peak} for each subject at each preload state. See text for details.

data from all subjects plotted together yielded a linear regression with $r^2=0.98$ (Figure 8.4B).

8.3.3 The Effect of Diastolic Dysfunction on M

Using existing simultaneous cath-echo data, we analyzed the maximum driving force (kx_o) vs peak resistive force (cE_{peak}) relationship in subjects with significant respiratory (LVEDP)

variation. The results, including statistics, are summarized in Figure 8.5 and Table 8.4. The kx_0 vs cE_{peak} relation was highly linear for both normal (average $r^2=0.96\pm0.02$) and diastolic dysfunction groups (average $r^2=0.90\pm0.05$). The

(average

$r^2=0.90\pm0.05$). The

average slope for the

normal group was

$M=1.17\pm0.05$, and

the average value for

the diastolic

dysfunction group was $M=0.98\pm0.07$, $p<0.001$ by ANOVA. Additionally, the slope intercept of

the normal cath-echo group was $B=6.69\pm0.91$, while the slope intercept of the diastolic

dysfunction cath-echo group was $B=10.67\pm3.35$, $p=0.03$ by ANOVA. The difference in M

Table 8.4. Comparison of the slope (M), intercept (B), and LVEDP for all ($n=27$) subjects comprised of the tilt table group ($n=16$) and the catheterization-echocardiography group ($n=11$)

	Catheterization- Echocardiography Normal	Catheterization- Echocardiography Diastolic Dysfunction	Tilt Table Normals
LVEDP, mmHg	13.69 ± 3.87^a	26.47 ± 4.54	
Slope M	1.17 ± 0.05^b	0.98 ± 0.07^d	1.27 ± 0.09
Intercept B	6.69 ± 0.91^c	10.67 ± 3.35^e	5.69 ± 1.70
r^2	0.96 ± 0.02	0.90 ± 0.05	0.95 ± 0.04

Values are means \pm SD. Single paired ANOVA performed between all groups. ^a $P < 0.0001$; ^b $P < 0.001$ compared with diastolic dysfunction (DD), $P = 0.02$ compared with tilt table; ^c $P = 0.03$ compared with DD, $P = 0.22$ compared with tilt table; ^d $P < 0.00001$ compared with tilt table; ^e $P < 0.001$ compared with tilt table.

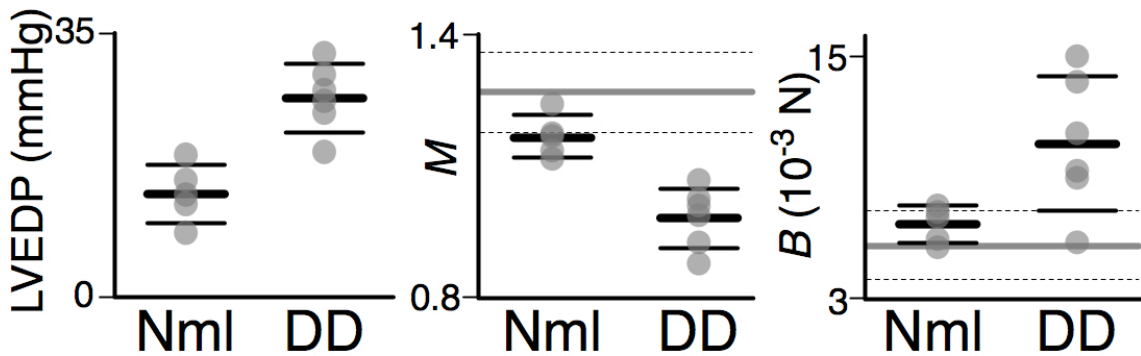


Figure 8.5 A) The heavier lines denote average values, lighter lines above and below denote one standard deviation relative to the mean LVEDP. B) Regression slope (M) comparison between groups. The thick-line is the average value from the tilt-table study. Dotted lines are one standard-deviation relative to the mean value. C) Intercept (B) comparison between groups. The thick-line is average value from the tilt-table study. Dotted lines are one standard deviation relative to the mean intercept value. Nml- normal group. DD- diastolic dysfunction group. See text for details.

between the cath-echo diastolic dysfunction subjects and the healthy tilt-table subjects showed stronger statistical significance ($p < 0.00001$) compared to the difference in M between the cath-echo normal subjects and the healthy tilt-table subjects ($p = 0.02$). The difference in intercept B is also statistically significant between diastolic dysfunction subjects and tilt-table subjects, $p < 0.0001$. There was no statistically significant difference, however, between the intercept of the normal cath-echo subjects and the tilt-table subjects.

8.4 DISCUSSION

8.4.1 Summary of Initial Results

Maximum elastance is an experimentally validated, load-independent systolic function index stemming from the time-varying elastance paradigm that decoupled extrinsic load from (intrinsic) contractility. Although Doppler-echocardiography is the preferred method of diastolic function assessment, all echo-derived indexes are load-dependent and no invasive or non-invasive load-independent index of filling exists. In this study, we used a kinematic filling paradigm (the Parameterized Diastolic Filling formalism) to predict and derive the load-independent (dimensionless) index M , defined by the slope of the peak-driving force ($kx_{o \infty \text{peak}}$ atrio-ventricular gradient) to maximum viscoelastic resistive force (cE_{peak}) relation. To validate load-independence, we analyzed E-waves recorded while load was varied via tilt-table (head up, horizontal, and head down) in 16 healthy volunteers. The effect of diastolic dysfunction on M was assessed by analysis of preexisting simultaneous cath-echo data in 6 diastolic dysfunction vs. 5 control subjects. M was found to be independent of load variation in all subjects and capable of differentiating between normal subjects and subjects with diastolic dysfunction.

8.4.2 Doppler Echocardiography and Load Dependence

A major challenge facing interpretation of echo-derived DF indexes is that the indexes in current clinical use (E_{peak} , AT, DT, E/A, VTI...) are load-dependent (3, 7, 9, 11, 13, 17, 24, 25, 30-32, 34, 35, 38). Despite this uncertainty, it is often assumed that changes observed in the indexes represent changes in pathological processes. Studies have clearly established, however, that traditional transmitral flow-derived diastolic indexes are load-dependent and therefore changes in DF indexes could be due to load variability rather than due to pathology.

Using blood pressure cuffs to non-invasively reduce preload in 12 normal subjects, Triulzi et al. (34), for example, found E_{peak} , E/A, VTI, DT and AT to change significantly with preload, and concluded that preload reduction in normal subjects produces a “pattern that mimics changes in left ventricular diastolic dysfunction”. By altering preload with postural changes, Downes et al. (7) found that though E/A ratio changed, it did not change enough for normal values to migrate into the abnormal range and concluded that “simple changes in venous return do not ‘normalize’ an abnormal pattern, nor do they ‘abnormalize’ a normal pattern”. Kmetzo et al. (13) however, found that 80 degree head up tilt produced abnormal relaxation patterns in 22 normal heart healthy volunteers.

Newer load independent Doppler-derived indexes of DF have been proposed (V_p , E' , E/E') but all have been shown to have load dependence. E' has been noted to be load independent in patients with chronic ischemic syndrome (37), but has shown variability with changing preload in normal subjects (22, 23), in animals (12), and in patients undergoing hemodialysis (20). V_p has shown load independence and strong correlation to τ (time constant of isovolumic relaxation) in patients undergoing cardiac surgery (8) but proven to be load

dependent in normal volunteers (22). Even E/E' , which many studies find to be load independent (15, 20, 22), has proved in animal experiments to be preload dependent (12).

Despite studies that have shown diastolic function indexes to be load-dependent, no studies have derived diastolic indexes that compensate for load. Recent studies (10, 33) have shown however that intrinsic properties of the ventricle may correlate better with load-induced changes in the Doppler indexes rather than the Doppler indexes themselves. For example Tanabe et al. (33) found that the change in E/A ratio following a decrease in preload correlated strongly with an invasively derived intrinsic property of the ventricle.

In contrast, Hasegawa et al. (10) observed peak volumetric flow to be linearly related to the peak AV pressure gradient ($r^2 = 0.94$) in accordance with the Bernoulli relation relating pressure gradient to flow velocity. Although load was not explicitly altered, the observed change in peak AV gradient is consistent with a variable load. Interestingly, the slope of the observed relation is highly linear and is nearly indistinguishable between the control and HF groups. Though superficially similar in appearance, the relationship of kx_o to cE_{peak} differs importantly from previous work by Hasegawa et al. (10) who compared peak volumetric flow to peak AV gradient ($[\text{mitral valve area}] \cdot E_{peak}$ vs. kx_o using our terminology) at different loading conditions. First, unlike the slope of the Hasegawa et al. relationship, the slope of the peak AV gradient (kx_o) to peak resistive force (cE_{peak}) relationship is dimensionless. Second and more importantly, the relation in the current study accounts for the resistive (viscoelastic) component of the filling process, whereas the Hasegawa et al. relation has no explicit term accounting for resistive forces. The maximum driving force (peak AV gradient kx_o) to peak resistive force (cE_{peak}) relationship presented in this study can therefore be viewed as complementary to, but independent of, the prior work of Hasegawa et al. Finally, it is important to note that while the Hasegawa et al.

relation remains linear in the face of load variation, it also does not change in the setting of heart failure and therefore in our view reflects the applicability of the Bernoulli equation but does not serve as a useful load independent index of diastolic function.

8.4.3 Applying the PDF model to the Load Independent Index Problem

The PDF model helps elucidate the connection between the Hasegawa et al. relation between peak flow rate and peak pressure gradient (10) and the current study. In agreement with Hasegawa et al., a plot (not shown) of E_{peak} vs. kx_o (the peak AV gradient equivalent) using our data also generates a linear relation. The slope has units of (s/kg); the linear regression relation is $E_{peak} = 0.017(kx_o) + 0.39$ $r^2=0.78$. The fact that an approximately linear relation is observed is predictable in part from the non-steady Bernoulli relation which relates pressure gradient to flow velocity.

A stronger and more meaningful correlation is achieved by the maximum driving force (peak AV gradient kx_o) vs. peak resistive force (cE_{peak}) relation which attains $r^2 = .98$ as compared to the $r^2= 0.78$ for the E_{peak} vs. peak AV gradient (kx_o) relation. In addition to attaining a stronger correlation, the slope of the maximum driving force (peak AV gradient, kx_o) vs. peak resistive force (cE_{peak}) relation is dimensionless. It complements the Hasegawa et al. observation by explicitly including the effect of damping. A high value for cE_{peak} implies a large peak resistive force must be generated to achieve the observed flow. This higher resistive force indicates that conversion of (maximum A-V gradient) potential energy into kinetic energy (flow) is less efficient. The PDF (viscoelastic) parameter c is important because it has been shown to be significantly different from normal in pathophysiologic states with delayed relaxation patterns such as diabetes(5, 26). A higher value of the parameter c in diabetic (human,

and rat) hearts implies that diabetic hearts, compared to normal hearts, are less efficient in being able to convert potential energy (pressure gradient) into kinetic (flow) energy. Therefore one would expect that unlike the E_{peak} vs. peak AV gradient (kx_o) relationship, the maximum driving force (peak AV gradient kx_o) vs. peak resistive force (cE_{peak}) relationship will have quantifiable differences between normal and abnormal LV function states.

Indeed Figure 8.5 demonstrates compelling evidence that both slope M and intercept B , of the kx_o vs cE_{peak} linear regression, change in LV diastolic dysfunction states. The diastolic dysfunction group had lower M values and higher B values compared to the normal cath-echo group and the healthy tilt-table group. The normal cath-echo group had the same B values as the healthy tilt-table group and slightly lower M values. This difference in M between the normal

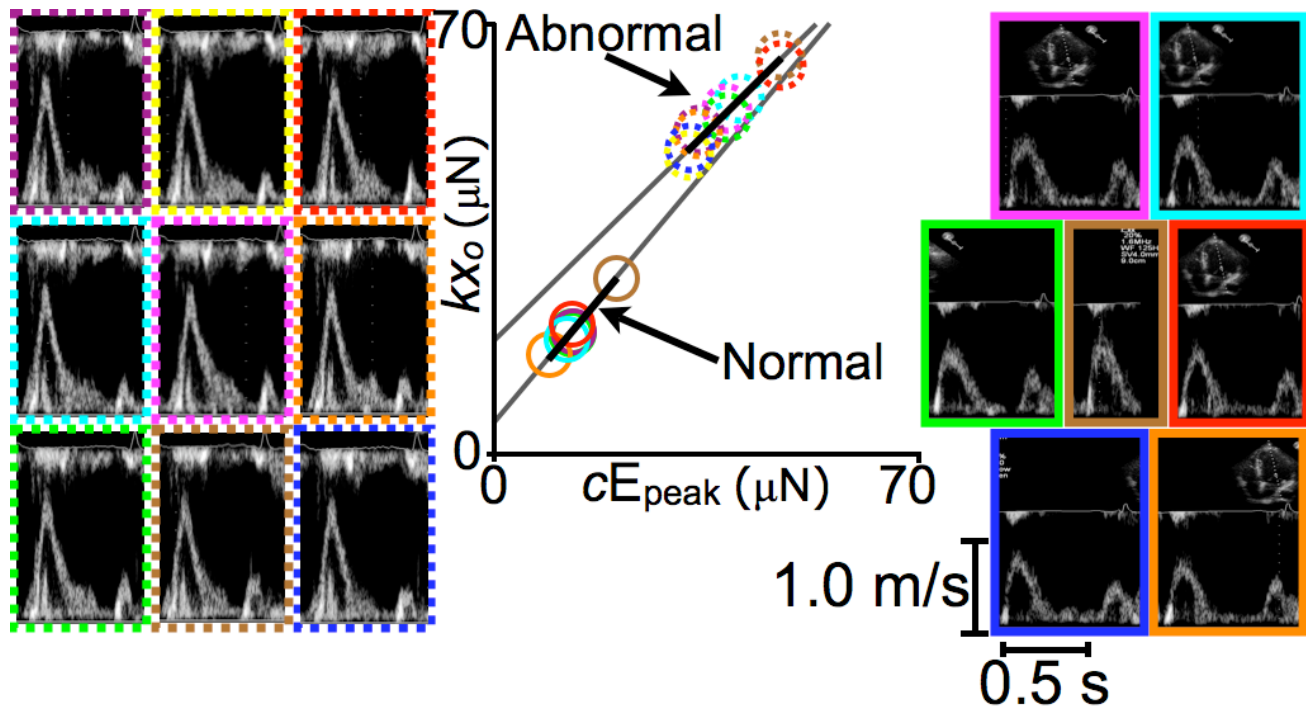


Figure 8.6. The left panel shows 9 E- and A- wave pairs from a subject with an end-diastolic pressure (EDP) of 35 mmHg (abnormal diastolic function). The right pane shows 7 E- and A- wave pairs from a subject with an EDP=12mmHg (normal diastolic function). For each E-wave a corresponding cE_{peak} and kx_o value was determined and plotted on the kx_o vs cE_{peak} plot, as described in figure 2. Thus the 9 E-waves with dotted borders defined 9 points, shown with dotted circles. Similarly the 7 E-waves with solid borders defined 7 points, shown with solid circles. The kx_o vs cE_{peak} regression for 9 dotted points was $M=0.95$, $B=19.0$, $r^2=0.98$, while the regression for the 7 solid points was $M=1.15$, $B=5.10$, $r^2=0.99$. Notice both regressions are highly linear, but the subject with abnormal diastolic function has a lower slope and higher intercept compared to the normal subject.

cath-echo subjects and the tilt-table subjects may be due to the higher average age of the normal cath-echo subjects (44 yo) relative to the healthy tilt-table group (25 yo).

These retrospective data, particularly because they were **not** acquired with the specific intent of determining load independence, strongly support the view that M and B can differentiate between normal and pathologic states. Recently we analyzed a series of transmitral contours from 2 additional subjects undergoing simultaneous catheterization and echocardiography, as described in Chapter 2. The subjects had normal and abnormal diastolic function (EDP of 12 mmHg vs 35 mmHg respectively), and plotting measured E-waves for both subjects in the kx_o vs cE_{peak} plane shows a clear difference in both M and B for the two subjects (See Figure 8.6).

8.4.4 Analysis of the kx_o vs. cE_{peak} relation: the role of randomness

While the fact the $cE_{peak}=kx(t_{peak})$ for all E-wave may suggest that Eq. 8.6 is a tautology, that claim may be easily invalidated by analysis of randomly generated E-waves. While randomly generated E-waves have identical cE_{peak} and $kx(t_{peak})$ values, they do not in general fall on a single line in the kx_o vs cE_{peak} plot. If our observations were a tautology, these E-waves would show a linear relationship between k , x_o and c . The graph of maximum driving force (peak AV gradient kx_o) vs. peak resistive force (cE_{peak}) using such random values (within the physiologic range) is shown in Figure 8.7.

Figure 8.7 shows that not all values of k , x_o and c generate a linear relationship between maximum driving force (peak AV gradient kx_o) and peak resistive force (cE_{peak}). Therefore the observed linear relation between maximum driving force (kx_o) and peak resistive force (cE_{peak}) is not a general property of a damped spring model assembled from arbitrary components.

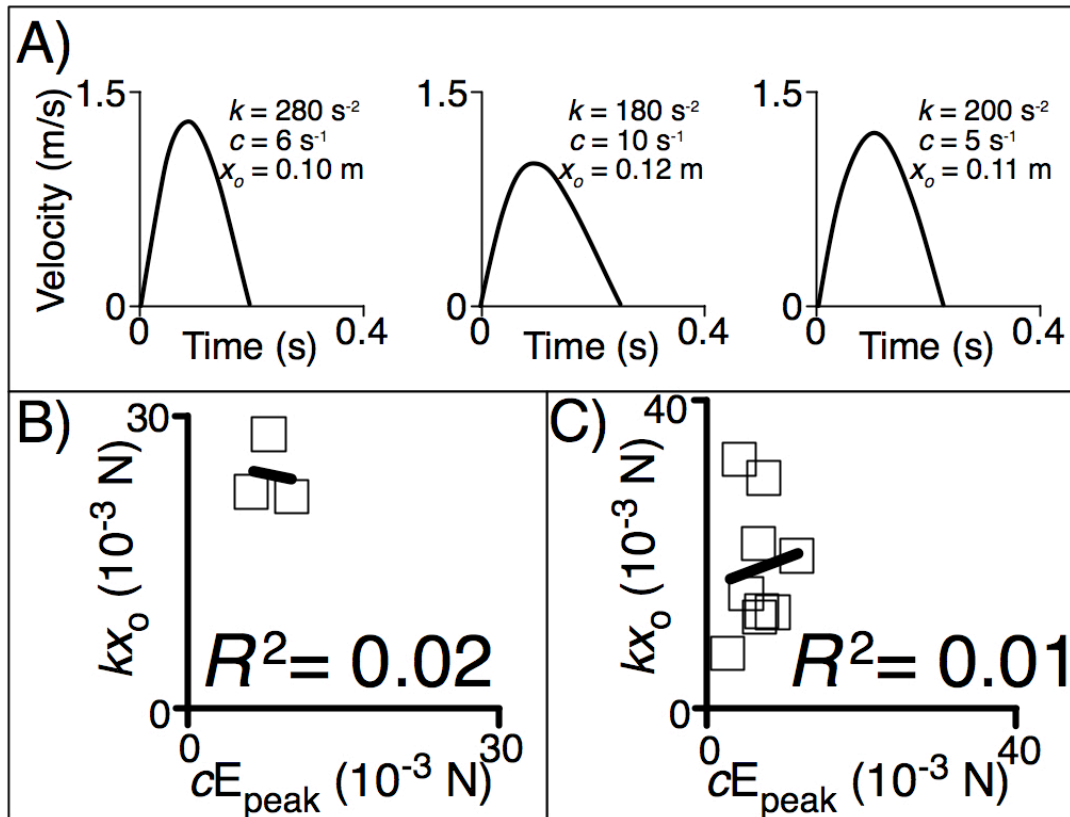


Figure 8.7 A) Three typical model-generated E waves created by randomly picking values for x_o , c , k , known to be in the physiologic range. B) Maximum driving force (kx_o) vs. peak resistive force (cE_{peak}) for the three random E-waves shown in a). Note deterioration of r^2 . C) Increase in randomly generated E-wave sample size to $n=10$ indicates further, substantial deterioration ($r^2=0.01$) of the observed, highly linear, maximum driving force (kx_o , peak AV gradient) to peak resistive force (cE_{peak}) relationship. See text for details.

It should be noted that k , c , and x_o are, from a mathematical standpoint, independent parameters. There is therefore no a-priori correlation between k , c , x_o , or any combination of the parameters that can be predicted. These parameters become physiologically coupled, and their magnitudes are constrained, once they are fit to clinical data (the E-wave). Once determined by fitting to actual E-waves, several correlations can be seen, such as E_{peak} to kx_o , k to cE_{peak} , and c to kx_o . However, kx_o to cE_{peak} is the strongest observed correlation, and is the only one with a dimensionless slope amenable to a simple physiological interpretation.

8.4.5 Physiological Meaning and Application of the Load Independent Index

The previous analysis and results provide a useful framework for understanding the meaning of M and B . In the kx_0 vs cE_{peak} plane, each E-wave is represented as a point, and multiple E-waves define curves in the plane. Conceptually speaking, kx_0 is the analogue for the peak atrioventricular pressure gradient driving flow. Similarly, cE_{peak} quantifies the lumped maximum resistive force opposing flow. As load increases, greater force is required to drive filling, and kx_0 is expected to rise. Because of the linear relationship in Eq. 8.6, cE_{peak} is expected to rise as well. A ventricle with E-waves that define a kx_0 vs cE_{peak} regression with low slope M would have a fairly large increase in cE_{peak} for a given increase in kx_0 . A ventricle with a high value for M would on the other hand have a lower increase in cE_{peak} for a given increase in kx_0 (see Figure 8.8). Thus ventricles with high M values are expected to more efficiently accommodate increasing load because they have a comparably less significant rise in resistive forces as load and driving forces increase. This suggests that ventricles with high M values would be expected to have normal intrinsic diastolic function, whereas ventricles with low M values would be expected to have intrinsic diastolic dysfunction. Furthermore, ventricles with M values lower than 1 would have kx_0 vs cE_{peak} regression lines that intersect the $kx_0=cE_{\text{peak}}$ physiological barrier.

Ventricles constrained to a kx_0 vs cE_{peak} regression with low M would therefore have a limit placed on the amount of load variation that their ventricles could accommodate. Indeed the only method for accommodating more load would be to increase the intercept B , so as to have more room in the physiological region of the kx_0 vs cE_{peak} regression. This would also have the effect of shifting E-waves from the overdamped region into the underdamped region. Thus a theoretical analysis predicts that B may serve a compensatory role in diastolic dysfunction. Given that the

units of B are also those of kx_0 , it is not unreasonable to suspect that B may be a surrogate of average filling pressures. Indeed, in diastolic dysfunction subjects, elevated LVEDP is thought to be a compensatory mechanism that allows effective filling to continue in the face of relaxation or stiffness abnormalities.

This compensatory increase in LVEDP is also thought to cause a shift in E-wave pattern from delayed relaxation (over-damped) back to pseudonormal (under-damped) in subjects with progressive diastolic dysfunction. In the kx_0 vs cE_{peak} plane, this would be analogous to increasing the kx_0 coordinate so that an E-wave coordinate moves from the over-damped to the under-damped regime. Clinically the pseudonormal pattern is unmasked (it shifts back to delayed

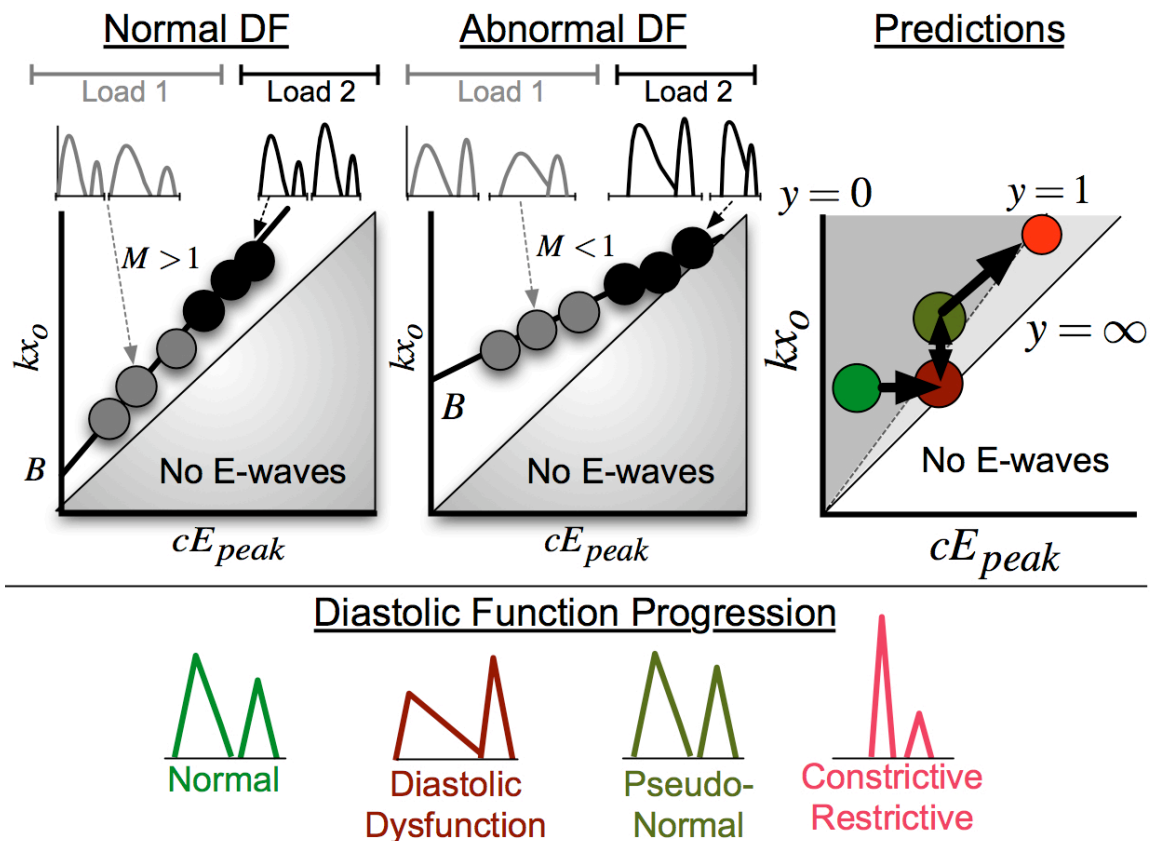


Figure 8.8. Theoretical kx_0 vs cE_{peak} relations for subjects with normal and abnormal diastolic function. As demonstrated in the results, diastolic dysfunction leads is associated with higher intercept and lower slope. The classic clinical progression of diastolic dysfunction, shown in the lower panel, can be visualized in the kx_0 vs cE_{peak} plane (right panel). See text for details.

relaxation) in response to preload reduction by Valsalva maneuver (18), and this would be equivalent to shifting an E-wave from the underdamped regime back down into the over-damped regime in the kx_0 vs cE_{peak} plane. The constrictive restrictive pattern does not have a clear over-damped or under-damped pattern, but certainly would be associated with higher kx_0 and cE_{peak} values and would be a shift vertically and to the right from the pseudonormal E-wave. It is encouraging that predictions from the kx_0 vs cE_{peak} plane are consistent with known physiology and can be mapped onto the clinically established progression of diastolic dysfunction spectrum.

8.5 LIMITATIONS

A minor limitation is the absence of end-diastolic volume (EDV) data as a correlate of preload alteration at different stages of tilt. EDV could not be reliably calculated, because only a 4-chamber view was archived. Transthoracic echocardiographic studies have shown that EDV calculated from 4-chamber views alone achieve only an $r=0.61$ correlation with true EDV (36). Though exact preload change with tilt alteration is not reported, many studies have altered preload using tilt table methodology(7, 9, 13, 22, 24, 25, 30, 37), and it is certain that preload is highest in head-down tilt and lowest in head-up tilt(6, 9).

A second limitation is that the PDF formalism is most applicable to E-waves having both ascending and descending portions. E- and A-waves become difficult to separate and discern when the A-wave merges with the E-wave and covers more than 2/3 of the E-wave deceleration(4) which typically occurs at $HR > 100\text{bpm}$. Thus M values for subjects with high hearts rates (> 100 bpm) were not computed. In the current study, only 2 of 16 subjects during head-up tilt had limited E-wave deceleration portions. Hence head-up data from these two subjects were not fit by the PDF formalism.

Finally, in our tilt-table study, all data was acquired from heart healthy volunteers and so a detailed comparison of the maximum driving force (peak A-V gradient kx_o) vs. peak resistive force (cE_{peak}) relation between normal and pathologic states cannot be made. We predict, and results from analysis of previously acquired data obtained for other purposes in a modest sample size show that the slope and intercept of the maximum driving force (peak AV gradient kx_o) vs. peak resistive force (cE_{peak}) relation changes (decreases) in the setting of dysfunction. The full potential of the index resides in performance of follow-up echocardiographic studies, where each person is their own control, showing alteration of E-wave morphology in response to pharmacologic therapy. Whether observed E-wave changes are due to load, or due to intrinsic changes in the LV in response to therapy (LV remodeling), could be addressed via slope M and intercept B . Because no prediction regarding the existence of any LIIF or its noninvasive validation in normal subjects has been previously achieved, the proposed approach is a reasonable first step.

8.6 Additional Results

8.6.1 Diastolic Reserve

Introduction

Because the left ventricle (LV) is a suction pump the kinematics of LV filling obey the laws of damped simple harmonic oscillatory (SHO) motion. Thus echocardiographic early transmitral flow velocity contours (E-waves) manifest underdamped or overdamped patterns. As we show in the current Chapter, E-wave shape changes with changing load due to respiratory variation or body tilt angle. However, the transition from overdamped to underdamped filling pattern is difficult to predict in practice. The results of the current Chapter suggest that E-wave

shape variation is constrained by a constant kx_0 vs cE_{peak} regression, and further analysis of this regression is likely to yield insights regarding the transition of E-wave filling patterns from overdamped to underdamped regimes.

Approach and Hypothesis

In Figure 8.1 we demonstrate that the transition from underdamped to overdamped kinematic filling may be easily visualized in the kx_0 vs cE_{peak} plane, which we call for convenience the forces of filling plane, by a line through the origin with a slope of $e/2$. Thus, for any E-wave, one can determine a distance between the E-wave (cE_{peak} , kx_0) coordinate and the $e/2$ line. Furthermore, because a set of E-wave determines a linear kx_0 vs cE_{peak} regression, one can determine the distance from the end of the linear regression to the $e/2$ overdamped to underdamped transition line. Thus, for subjects with only underdamped waves, we define diastolic reserve as the distance by which the kx_0 vs cE_{peak} line must be extended in order to enter

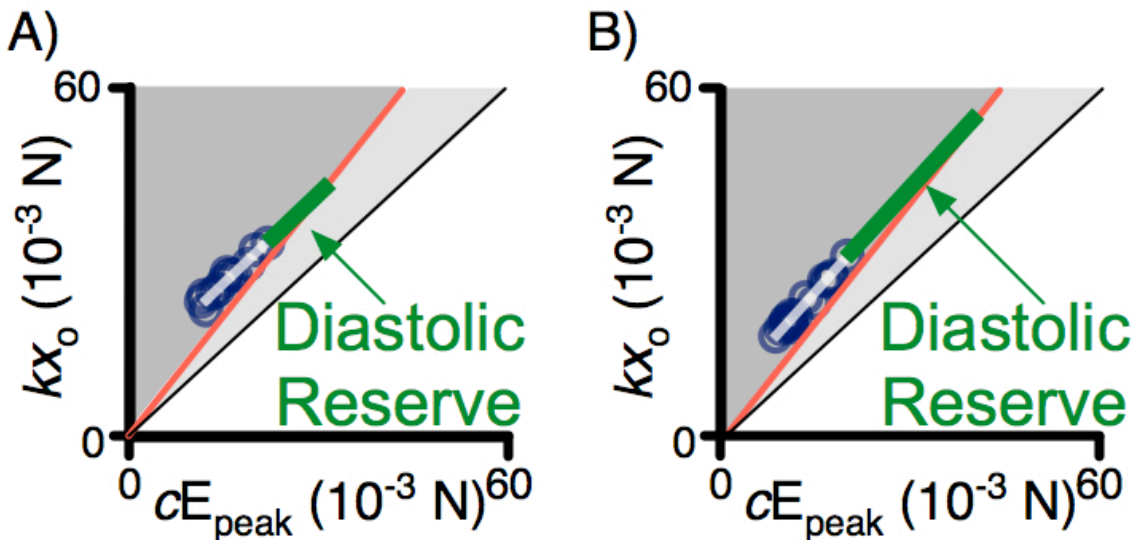


Figure 8.9. The forces of filling plane for a subject with diastolic dysfunction (left) and for a subject with normal diastolic function (right). The length of the line with slope M , starting at the maximum point on the kx_0 vs. cE_{peak} plot, and ending on the critically damped border line (red), defines a subject's diastolic reserve.

the overdamped regime. To test this approach, we use the E-waves measured from the 10 catheterization subjects in the current study (5 diastolic dysfunction (DD) (LVEDP>19), 5 controls). We calculate diastolic reserve and plot it in the forces of filling plane.

Results

Figure 8.9 shows example results from 2 subjects. Notice that a lower slope in the subject with diastolic dysfunction leads to a smaller distance between the kx_0 vs cE_{peak} regression and the overdamped/underdamped transition line. The results in Figure 8.10 were consistent across all subjects. Indeed subjects with diastolic dysfunction exhibited significantly less diastolic reserve ($p<0.05$) than controls (Figure 8.10). We conclude that the transition between underdamped and overdamped kinematics in response to load variation provides a physiologic limit from which diastolic reserve can be determined.

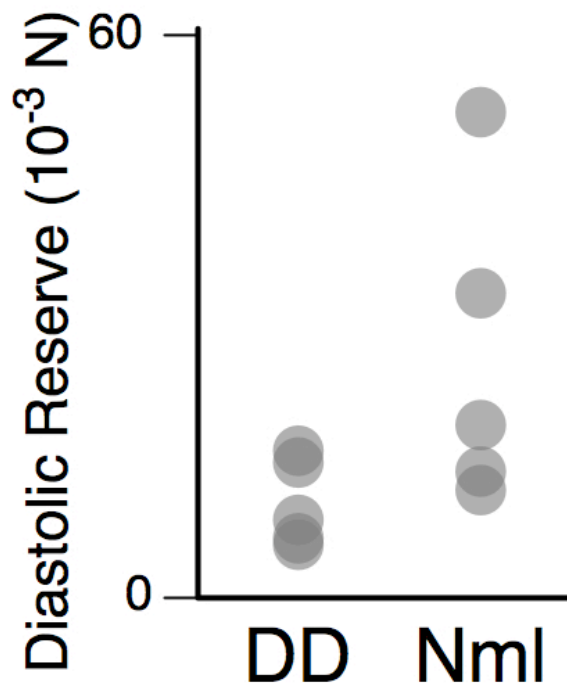


Figure 8.10. Subjects with diastolic dysfunction (DD) exhibited significantly decreased diastolic reserve ($p<0.05$) compared to normal controls (Nml).

8.6.2 Kinematic Filling Efficiency in the kx_0 vs cE_{peak} Plane

Introduction

In previous work (39) we have described a novel index of diastolic filling efficiency called the kinematic filling efficiency index (KFEI). KFEI is a dimensionless index defined by

the ratio of measured E-wave area to the idealized lossless E-wave area. KFEI varies between 1 (for undamped waves) and 0.5 (for critically or overdamped waves) (Figure 8.11). In one study (39) KFEI was calculated in diabetic and non-diabetic subjects and found to differentiate between groups, even though conventional indexes like E-

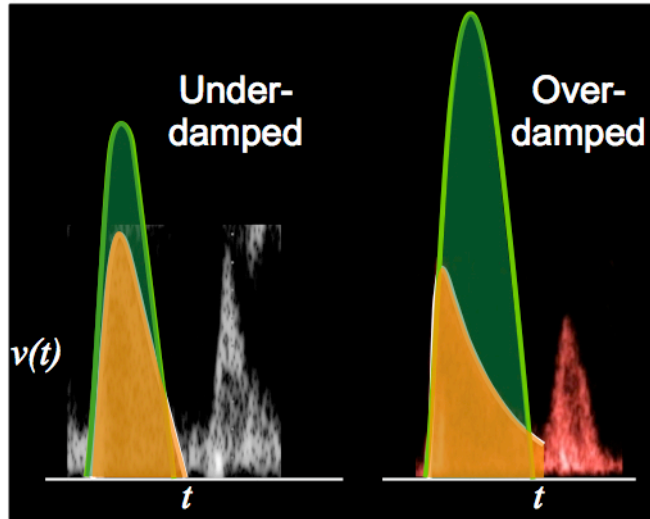


Figure 8.11. Comparison of KFEI between E-wave with low damping (left) and high damping (right). Green areas represent the equivalent E-wave assuming zero damping. KFEI is defined as the ratio of orange area to green area, and is expected to be lower in subjects with higher E-wave damping.

wave deceleration time could not. KFEI has an intriguing connection to the forces of filling plane that can be appreciated by a more detailed mathematical analysis of the KFEI index.

Theoretical Derivation

In Chapter 2 we derived a general expression for E-wave area :

$$VTI_E = x(E_{dur}) - x(0) = x_o \left(1 + e^{-\frac{\pi y}{\sqrt{1-y^2}}} \right) \quad \text{Equation 8.8}$$

, where y is defined as in Eq 8.7 above. We also noted that in the undamped limit ($y=c=0$), the E-wave area was equal to $2x_o$. Thus, KFEI, the ratio of E-wave area to idealized undamped E-wave area is simply:

$$KFEI = \frac{1 + e^{-\frac{\pi y}{\sqrt{1-y^2}}}}{2} \quad \text{Equation 8.9}$$

Thus, KFEI is a function of y , and can be inverted to yield the following expression:

$$y = \frac{\ln(2KFEI - 1)}{\sqrt{\pi^2 + \ln^2(2KFEI - 1)}} \quad \text{Equation 8.10}$$

Applying Equation 8.10 above, we may determine the ratio of kx_o to cE_{peak} in terms of KFEI and plot the resulting expression in Figure 8.12:

$$\frac{kx_o}{cE_{peak}} = -\frac{\sqrt{\pi^2 + \ln^2(2KFEI - 1)}}{2 \ln(2KFEI - 1)} \cdot e^{\frac{\ln(2KFEI - 1) \tan^{-1}\left(\frac{\pi}{\ln(2KFEI - 1)}\right)}{\pi}} \quad \text{Equation 8.11}$$

Thus the location on an E-wave in the kx_o vs cE_{peak} plane determines the KFEI index exactly, and all E-waves along lines going through the origin in the kx_o vs cE_{peak} plane have equal KFEI.

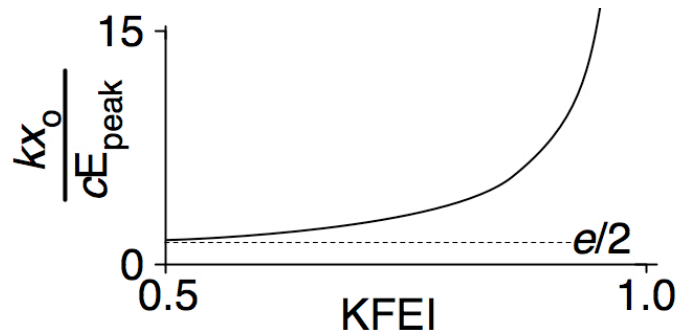


Figure 8.12. Theoretical plot of kx_o/cE_{peak} vs the kinematic filling efficiency index (KFEI). The critically damped E-wave has KFEI of 0.5 and kx_o to cE_{peak} ratio of $e/2$, whereas the undamped E-wave has KFEI equal to 1 and infinite kx_o to cE_{peak} ratio.

Application to Previous Results

In previous work diabetic and non-diabetic patients were compared using both the KFEI index and more conventional parameters like E-wave deceleration time. The results showed clearly that KFEI was significantly different between groups, even though deceleration time was not distinguishable. Given the connection between KFEI and the forces of filling plane, it is intriguing to visualize the KFEI results of the previous study in the context of Equation 8.11. In Figure 8.13 we show the average (cE_{peak} , kx_o) coordinates for 15 diabetic (red) and 18 matched non-diabetic subjects (blue) in the forces of filling plane. Lines of constant KFEI are superimposed in the forces of filling plane using measured average KFEI values from diabetic

and non-diabetic subjects. The difference in average KFEI can be clearly visualized in the forces of filling plane because the diabetic subjects fall along a constant KFEI line that is shallower than the constant KFEI line that non-diabetic subjects follow. It is encouraging to see that multiple lines of inquiry lead to consistent and complimentary methods for assessment of diastolic function, and further inquiry towards the load dependence of KFEI is warranted.

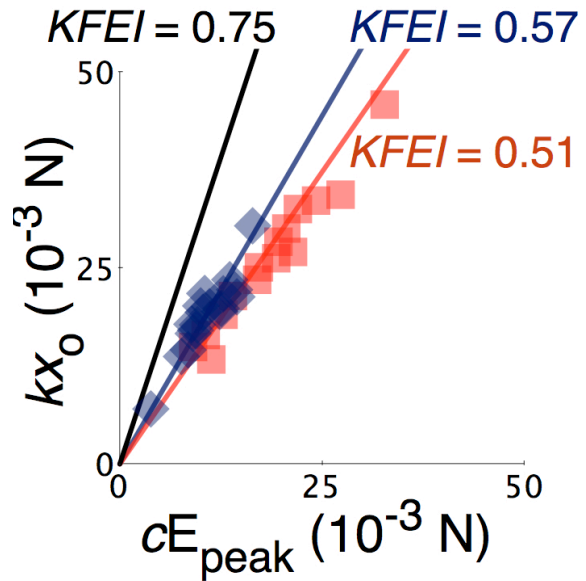


Figure 8.13. Plot of diabetic (red) and nondiabetic (blue) subjects in the kx_o vs cE_{peak} plane, showing lines of constant KFEI. In agreement with previous work, diabetic subjects have lower KFEI than non-diabetic subjects. See text for details.

8.6 CONCLUSIONS

It is known that changing tilt-table position alters load in a predictable manner and affects E-waves in a predictable way(3, 7, 9, 11, 13, 17, 24, 25, 28, 30-32, 34, 35, 38). Changes in load thereby affect the E-wave determined PDF parameters (k , x_o , and c). The observed E-wave variation reflects the physiologic mechanisms that respond to changes in load. Because the slope M of the maximum driving force (peak AV gradient kx_o) vs. peak resistive force (cE_{peak}) relationship remains constant in response to alteration of tilt-table induced load we conclude that M represents a load-independent index of filling in normal subjects. To determine if M differentiates between control and diastolic dysfunction states, we analyzed previously acquired cath-echo data. Results show M to be significantly lower in diastolic dysfunction states (6 subjects with increased LVEDP and normal EF), compared to control states (5 subjects with normal LVEDP and normal EF). Taken together, these results suggest that analysis of transmitral

flow in the kx_0 vs cE_{peak} plane may decouple changes in load from changes in intrinsic function, and allow for more robust clinical determination of diastolic dysfunction. In addition, there are numerous intriguing mathematical insights that may be appreciated from further analysis of kinematic filling in the kx_0 vs cE_{peak} plane. New indexes may be extracted from E-wave location in the plane, and previously determined indexes may be mapped onto the kx_0 vs cE_{peak} plane in novel and enlightening ways.

8.8 REFERENCES

1. Appleton CP, Firstenberg MS, Garcia MJ, and Thomas JD. The echo-Doppler evaluation of left ventricular diastolic function. A current perspective. *Cardiology clinics* 18: 513-546, ix, 2000.
2. Bauman L, Chung CS, Karamanoglu M, and Kovács SJ. The peak atrioventricular pressure gradient to transmitral flow relation: kinematic model prediction with in vivo validation. *Journal of the American Society of Echocardiography : official publication of the American Society of Echocardiography* 17: 839-844, 2004.
3. Choong C, Herrmann H, Weyman A, and Fifer M. Preload dependence of Doppler-derived indexes of left ventricular diastolic function in humans. *J Am Coll Cardiol* 10: 800-808, 1987.
4. Chung CS and Kovács SJ. Consequences of increasing heart rate on deceleration time, the velocity-time integral, and E/A. *Am J Cardiol* 97: 130-136, 2006.
5. Dent C, Bowman A, Scott M, and Allen J. Echocardiographic characterization of fundamental mechanisms of abnormal diastolic filling in *Journal of the American Society of Echocardiography*, 2001.
6. Dirschedl P, Gregull A, and Lollgen H. Volume loading of the heart by "leg up" position and head down tilting (-6 degrees) (HDT). *Acta Astronaut* 27: 41-43, 1992.
7. Downes TR, Nomeir AM, Stewart K, Mumma M, Kerensky R, and Little WC. Effect of alteration in loading conditions on both normal and abnormal patterns of left ventricular filling in healthy individuals. *Am J Cardiol* 65: 377-382, 1990.
8. Garcia MJ, Smedira NG, Greenberg NL, Main M, Firstenberg MS, Odabashian J, and Thomas JD. Color M-mode Doppler flow propagation velocity is a preload insensitive index of left ventricular relaxation: animal and human validation. *J Am Coll Cardiol* 35: 201-208, 2000.
9. Guazzi M, Maltagliati A, Tamborini G, Celeste F, Pepi M, Muratori M, Berti M, and Guazzi MD. How the left and right sides of the heart, as well as pulmonary venous drainage, adapt to an increasing degree of head-up tilting in hypertrophic cardiomyopathy: differences from the normal heart. *Journal of the American College of Cardiology* 36: 185-193, 2000.
10. Hasegawa H, Little WC, Ohno M, Brucks S, Morimoto A, Cheng H-J, and Cheng C-P. Diastolic mitral annular velocity during the development of heart failure. *J Am Coll Cardiol* 41: 1590-1597, 2003.
11. Hurrell DG, Nishimura RA, Ilstrup DM, and Appleton CP. Utility of preload alteration in assessment of left ventricular filling pressure by Doppler echocardiography: a simultaneous catheterization and Doppler

echocardiographic study. *J Am Coll Cardiol* 30: 459-467, 1997.

12. Jacques DC, Pinsky MR, Severyn D, and Gorcsan J. Influence of alterations in loading on mitral annular velocity by tissue Doppler echocardiography and its associated ability to predict filling pressures. *Chest* 126: 1910-1918, 2004.
13. Kmetzo JJ, Plotnick GD, and Gottdiener JS. Effect of postural changes and isometric exercise on Doppler-derived measurements of diastolic function in normal subjects. *Chest* 100: 357-363, 1991.
14. Kovács SJ, Meisner JS, and Yellin EL. Modeling of diastole. *Cardiology clinics* 18: 459-487, 2000.
15. Lissauskas J, Singh J, Courtois M, and Kovács SJ. The relation of the peak Doppler E-wave to peak mitral annulus velocity ratio to diastolic function. *Ultrasound in medicine & biology* 27: 499-507, 2001.
16. Lissauskas JB, Singh J, Bowman AW, and Kovács SJ. Chamber properties from transmitral flow: prediction of average and passive left ventricular diastolic stiffness. *J Appl Physiol* 91: 154-162, 2001.
17. Masuyama T, St Goar FG, Alderman EL, and Popp RL. Effects of nitroprusside on transmitral flow velocity patterns in extreme heart failure: a combined hemodynamic and Doppler echocardiographic study of varying loading conditions. *Journal of the American College of Cardiology* 16: 1175-1185, 1990.
18. Nagueh SF, Appleton CP, Gillebert TC, Marino PN, Oh JK, Smiseth OA, Waggoner AD, Flachskampf FA, Pellikka PA, and Evangelista A. Recommendations for the evaluation of left ventricular diastolic function by echocardiography. *Journal of the American Society of Echocardiography : official publication of the American Society of Echocardiography* 22: 107-133, 2009.
19. Nagueh SF, Lakkis NM, Middleton KJ, Spencer WH, Zoghbi WA, and Quiñones MA. Doppler estimation of left ventricular filling pressures in patients with hypertrophic cardiomyopathy. *Circulation* 99: 254-261, 1999.
20. Oğuzhan A, Arınç H, Abacı A, and Topsakal R. Preload dependence of Doppler tissue imaging derived indexes of left ventricular diastolic function. ..., 2005.
21. Oommen B, Karamanoglu M, and Kovacs S. Modeling Time Varying Elastance: The Meaning of “Load-Independence”. *Cardiovascular Engineering*, 2003.
22. Paelinck BP, van Eck JWM, De Hert SG, and Gillebert TC. Effects of postural changes on cardiac function in healthy subjects. *European journal of echocardiography : the journal of the Working Group on Echocardiography of the European Society of Cardiology* 4: 196-201, 2003.
23. Pelà G, Regolisti G, Coghi P, Cabassi A, Basile A, Cavatorta A, Manca C, and Borghetti A. Effects of the

reduction of preload on left and right ventricular myocardial velocities analyzed by Doppler tissue echocardiography in healthy subjects. *European journal of echocardiography : the journal of the Working Group on Echocardiography of the European Society of Cardiology* 5: 262-271, 2004.

24. Pepi M, Guazzi M, Maltagliati A, Berna G, and Tamborini G. Diastolic ventricular interaction in normal and dilated heart during head-up tilting. *Clin Cardiol* 23: 665-672, 2000.

25. Plotnick GD, Kmetzo JJ, and Gottdiener JS. Effect of autonomic blockade, postural changes and isometric exercise on Doppler indexes of diastolic left ventricular function. *Am J Cardiol* 67: 1284-1290, 1991.

26. Riordan MM, Chung CS, and Kovács SJ. Diabetes and diastolic function: stiffness and relaxation from transmitral flow. *Ultrasound in medicine & biology* 31: 1589-1596, 2005.

27. Sagawa K. The end-systolic pressure-volume relation of the ventricle: definition, modifications and clinical use. *Circulation* 63: 1223-1227, 1981.

28. Stoddard MF, Pearson AC, Kern MJ, Ratcliff J, Mrosek DG, and Labovitz AJ. Influence of alteration in preload on the pattern of left ventricular diastolic filling as assessed by Doppler echocardiography in humans. *Circulation* 79: 1226-1236, 1989.

29. Suga H, Sagawa K, and Shoukas AA. Load independence of the instantaneous pressure-volume ratio of the canine left ventricle and effects of epinephrine and heart rate on the ratio. *Circ Res* 32: 314-322, 1973.

30. Suzuki T, Sato K, and Aoki K. Influence of postural change on transmitral flow velocity profile assessed by pulsed Doppler echocardiography in normal individuals and in patients with myocardial infarction. *American Heart Journal* 120: 110-115, 1990.

31. Sztajzel J, Ruedin P, Monin C, Stoermann C, Leski M, Rutishauser W, and Lerch R. Effect of altered loading conditions during haemodialysis on left ventricular filling pattern. *Eur Heart J* 14: 655-661, 1993.

32. Takahashi T, Iizuka M, Sato H, Serizawa T, Momomura S, Mochizuki T, Kohmoto O, Aoyagi T, Matsui H, and Ikenouchi H. Doppler echocardiographic-determined changes in left ventricular diastolic filling flow velocity during the lower body positive and negative pressure method. *Am J Cardiol* 65: 237-241, 1990.

33. Tanabe M, Onishi K, Dohi K, Funabiki K, Koji T, Kitamura T, Ito M, Nobori T, and Nakano T. Change in filling pattern with preload reduction reflects left ventricular relaxation. *Int J Cardiol* 98: 67-72, 2005.

34. Triulzi MO, Castini D, Ornaghi M, and Vitolo E. Effects of preload reduction on mitral flow velocity pattern in normal subjects. *Am J Cardiol* 66: 995-1001, 1990.

35. Völler H, Uhrig A, Spielberg C, von Ameln H, Schröder K, Brüggemann T, and Schröder R. Acute alterations of pre- and afterload: are Doppler-derived diastolic filling patterns able to differentiate the loading condition? *Int J Card Imaging* 9: 231-240, 1993.
36. Weyman A. *Principles and Practice of Echocardiography*. Philadelphia: Lea & Febiger, 1994.
37. Yalçın F, Kaftan A, Muderrisoğlu H, Korkmaz ME, Flachskampf F, Garcia M, and Thomas JD. Is Doppler tissue velocity during early left ventricular filling preload independent? *Heart* 87: 336-339, 2002.
38. Yamamoto K, Masuyama T, Tanouchi J, Uematsu M, Doi Y, Mano T, Hori M, Tada M, and Kamada T. Peak early diastolic filling velocity may decrease with preload augmentation: effect of concomitant increase in the rate of left atrial pressure drop in early diastole. *Journal of the American Society of Echocardiography : official publication of the American Society of Echocardiography* 6: 245-254, 1993.
39. Zhang W, Chung CS, Riordan MM, Wu Y, Shmuylovich L, and Kovács SJ. The kinematic filling efficiency index of the left ventricle: contrasting normal vs. diabetic physiology. *Ultrasound in medicine & biology* 33: 842-850, 2007.

CHAPTER 9.

LOAD INDEPENDENT INDEX OF DIASTOLIC FUNCTION: VALIDATION IN THE FACE OF EXTENDED LOAD VARIATION

9.1 INTRODUCTION

Diastolic function is defined by dynamic interactions between load, ventricular stiffness and relaxation (9). While cardiac catheterization is the “gold-standard” for diastolic function assessment, echocardiography is preferred in the clinical and research setting.

Historically, geometric features of the echo-determined transmitral flow velocity contours during early rapid-filling and atrial systole (E- and A-waves) have been used to assess intrinsic diastolic function (stiffness and relaxation). Yet all echo-based indexes are known to depend on both intrinsic diastolic function and load (1, 3, 10, 12, 19-21, 23) and thus echo-based diastolic function indexes are all load-dependent.

In the Chapter 1 we hypothesized that load can be decoupled from intrinsic diastolic function by analyzing a set of *multiple* E-waves acquired at varying loads (17). The proposed load-independent index of diastolic function, called M , was validated in both healthy volunteers subjected to tilt-table maneuvers and cardiac catheterization patients with significant respiratory variation. We found that M was load-independent, correlated with diastolic function, and provided patient specific constraints for possible E-wave shapes.

While these initial results are promising, application of M in a wide variety of pathophysiologic states is premature. Indeed, it may be the case that M , in analogy to all previously reported load independent indexes of diastolic function (7, 10, 11, 13-15, 22) is load-independent over a narrow range but manifests load-dependence under a broader range of load variation.

In this work we consider the physiologic response to premature ventricular contractions (PVC), and the effect of PVCs on M . It is known that the physiologic response to PVCs generates a broad range of E-wave shapes (6, 18, 24). We capitalize on this extended range of E-

wave shapes and assess whether E-waves following a PVC generate a value for M that is consistent with the value for M generated by steady state beats.

9.2 METHODS

9.2.1 Patient Selection

Fifteen subjects were selected from the existing Cardiovascular Biophysics Laboratory database (see Chapter 2) of simultaneous high-fidelity (Millar) left ventricular (LV) pressure, aortic root pressure, and Doppler echocardiographic recordings of transmitral flow (Table 9.1).

Table 9.1. Demographics of simultaneous catheterization-echocardiography subjects analyzed retrospectively.

Subject	Age (y)	Height	Weight (lbs)	LVEF (%)	EDV (mL)	LVEDP (mm Hg)
1	59	5'8"	192	55	255	35 (3)
2	40	6'0"	220	62	167	17 (2)
3	66	5'2"	135	80	139	23 (2)
4	37	5'6"	138	84	120	18 (2)
5	60	5'9"	170	80	160	21 (1)
6	53	5'2"	156	81	173	18 (3)
7	77	5'5"	192	65	125	22 (2)
8	56	5'5"	220	82	167	26 (4)
9	46	5'11"	242	85	146	11 (5)
10	58	5'11"	185	63	127	21 (2)
11	72	5'5"	135	76	68	31 (3)
12	52	5'11"	275	75	161	19 (2)
13	74	5'11"	196	75	146	14 (1)
14	69	5'2"	178	62	165	15 (4)
15	53	5'9"	135	74	160	15 (1)

LVEF = ventriculographic left ventricular ejection fraction; EDV = end-diastolic volume; LVEDP = left ventricular end-diastolic pressure, values reported as means (SD)

Inclusion criteria for data set selection included the presence of at least one PVC (spontaneous or catheter induced) during data acquisition, normal sinus rhythm, no significant merging between E- and A- waves (defined as any transmitral profile where more than two-thirds of the E-wave is obscured), no evidence of valvular disease, no evidence of substantial coronary arteries

narrowing (>50% stenosis) or active ischemia, no evidence of 1st degree AV block on ECG (PR interval >200 msec), and normal ejection fraction (EF)>50%.

9.2.2 Simultaneous echocardiographic and high-fidelity pressure data acquisition

See Chapter 2 for a detailed description of the method by which simultaneous echocardiographic and high-fidelity pressure data is acquired. Representative data for subjects analyzed in the present study is shown in Figure 9.1 and Table 9.2. The first two beats following PVCs represented ‘perturbed load’ beats and defined Group-1 and Group-2 beats respectively. Remaining beats represented ‘baseline’ beats and were placed into Group-3. Furthermore the 2 or 3 analyzable beats that directly follow each group-1 and -2 perturbed beat defined a subset of Group-3 and called the “matching beats”.

9.2.3 Doppler E-wave Analysis and Hemodynamic Analysis

For each subject, approximately 14-34 beats of transmitral flow data, including the PVC beat(s), were recorded and analyzed. Conventional triangle shape approximations of E- and A-waves provided peak velocities (E_{peak} and A_{peak}), E-wave acceleration and deceleration times (AT and DT), and E-wave duration and velocity-time integral (E_{dur} and E_{VTI}). In addition, E-waves were subjected to parametrized diastolic filling (PDF) model-based image processing to yield E-wave specific kinematic parameters c , k , and x_0 . These parameters reflect ventricular relaxation/viscoelasticity, stiffness, and initial load, respectively. Methods for determining PDF parameters and triangle parameters are presented in greater detail in Chapter 2.

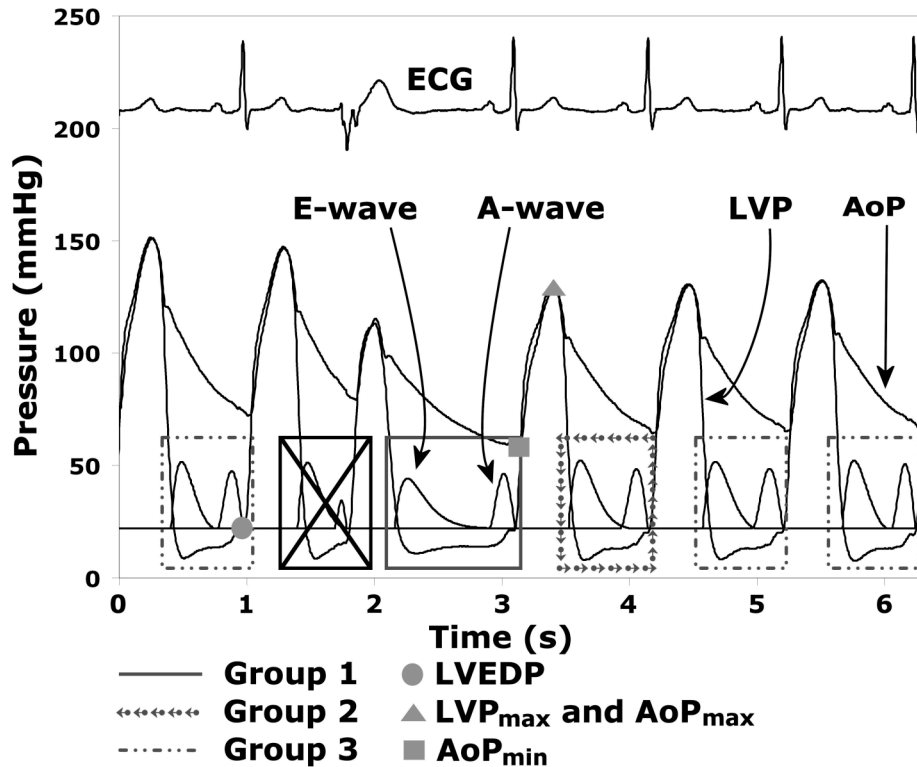


Figure 9.1. Typical data showing six consecutive beats from one subject. Relevant parameters and definitions shown. Left ventricular pressure, aortic pressure, ECG tracing, and model-fit E- and A-waves were all temporally synchronized as detailed in methods. Note the ejecting premature ventricular contraction (PVC) before $t = 2$ s. Group-1 (first post-PVC beat), Group-2 (second post-PVC beat) and Group-3 (control beats) are shown. The two Group-3 beats at $t=5$ s and 6 s represent “matching beats” for the preceding post-PVC beats. Pre-PVC filling beats (crossed off), were not included in analysis. LVEDP = end diastolic pressure; LVP_{max} = maximum left ventricular pressure of fourth beat; AoP_{max} = maximum aortic pressure associated with the fourth beat; AoP_{min} = minimum aortic pressure associated with the fourth beat. See text for details.

End-diastolic (LVEDP) and peak-systolic (LVP_{max}) pressures, aortic minimum and maximum (AoP_{min} and AoP_{max}) pressures, pulse pressure ($PP = AoP_{max} - AoP_{min}$), and peak pressure derivative ($+dP/dt_{max}$) were measured for all beats (Figure 9.1). For 3 patients with no aortic pressure data, only LV measures were assessed.

9.2.4 Statistical Analysis and Inter-Group Comparisons

The mean and standard deviation of all measured variables was determined for the Group-3 beats. In addition, the overall average Group-3 E-wave contour was determined by aligning (at $t=0$) and averaging (over $\Delta t=0.5$ s) all steady-state PDF contours. Additionally, a

mean square error (MSE) for a given E-wave was determined by calculating the square root of the residual between the E-wave of interest and the (aligned) Group-3 average E-wave.

To account for steady-state physiological beat to beat variation, a modified z-score, z_{n-3} , was defined relative to steady state for each variable of interest (i.e. E_{peak} , DT, etc) as:

$$z_{n-3} = \frac{x_n - \langle x \rangle_3}{\sigma_3} \quad \text{Equation 9.1}$$

, where $n=1$ or 2 and x_n , $\langle x \rangle_3$, and σ_3 is the value, Group-3 average, and standard deviation, respectively, for the variable of interest. For example, a DT $z_{1-3} > 1$ would imply that DT from a Group-1 beat exceeded the Group-3 mean in excess of 1 Group-3 standard deviation.

Intersubject comparison of z_{n-3} values was achieved by determining z_{n-3}^* , which is defined as the average of all z_{n-3} positive magnitudes across all beats. For example, a subject having 2 beats with $E_{\text{peak } z_{1-3}}$ values of (-1) and (+2), would have an $E_{\text{peak } z_{1-3}^*}$ value of 1.5.

Finally, $(z_{n-3}^*)_{\text{AVG}}$, defined as the overall effective z-score, was calculated (for each variable of interest) by averaging the individual z_{n-3}^* values across all subjects. For example, a DT $(z_{1-3}^*)_{\text{AVG}} > 2$ would indicate that across all subjects, the average Group 1 DT value deviated from its respective Group 3 mean by more than 2 respective Group 3 deviations. Microsoft Excel (Microsoft, Redmond WA) was utilized for all statistical analysis and calculations.

9.2.5 Calculation of Load Independent Index of Filling (M)

The method described in Chapter 8 was applied to plot and determine the kx_0 vs cE_{peak} regression with slope M and intercept B . For each subject, $M_{\text{SteadyState}}$, $B_{\text{SteadyState}}$, and $r^2_{\text{SteadyState}}$ defined the slope, intercept, and r^2 of the Group-3 (without “Matching Beats”) kx_0 vs. cE_{peak} regression. The kx_0 vs. cE_{peak} plot using all E-waves defined M_{AllBeats} , B_{AllBeats} , and r^2_{AllBeats} . The kx_0 vs. cE_{peak} plot generated from Group-1 -2 and associated “matching beats” as described

above defined $M_{\text{LoadPerturbed}}$, $B_{\text{LoadPerturbed}}$, and $r^2_{\text{LoadPerturbed}}$. Extended load-independence of M was tested in each patient by paired two-tailed t -tests between perturbed ($M_{\text{LoadPerturbed}}$) and steady-state ($M_{\text{SteadyState}}$, M_{AllBeats}) slopes. E-wave analysis and subsequent calculation of M was performed by two independent observers.

Table 9.2. Summary of M and r^2 values for all subjects for load-perturbed, steady-state and all beats combined

Sub.	n_1	n_2	n_3	n_{Match}	E/A_1	E/A_2	E/A_3	M_{Steady}	M_{All}	$M_{\text{Load-}}$	r^2_{Steady}	$r^2_{\text{All-}}$	$r^2_{\text{Load-}}$
								-State	-Beats	Perturbed	-State	Beats	Perturbed
1	1	1	25	4	0.9	0.82	1.01	1.01	1.05	1.22	0.98	0.95	0.98
2	1	0	19	3	1.32	NA	1.14	1.02	1.02	1.09	0.98	0.97	0.96
3	2	2	10	4	0.89	0.76	0.85	0.99	1.18	1.24	0.94	0.95	0.92
4	1	0	23	3	1.52	NA	1.21	1.15	1.14	1.11	0.95	0.97	1.00
5	1	1	15	3	0.89	1.10	1.02	0.88	0.93	0.86	0.98	0.95	0.93
6	1	0	13	3	0.77	NA	1.26	1.10	1.11	1.20	1.00	0.99	0.94
7	2	3	11	4	1.29	1.02	1.02	1.18	1.19	1.15	0.99	0.97	0.88
8	2	1	13	4	1.21	1.07	1.08	1.05	1.07	1.15	0.98	0.93	0.85
9	3	3	27	6	0.78	0.99	0.93	1.04	1.10	1.18	0.99	0.99	1.00
10	2	2	14	6	1.13	1.20	1.00	1.21	1.10	0.91	0.98	0.93	0.85
11	10	6	18	4	1.03	1.17	1.20	0.89	0.97	0.97	0.96	0.91	0.90
12	2	2	16	4	1.14	1.35	1.20	1.09	1.16	1.18	0.99	0.99	0.99
13	1	1	14	2	0.57	0.63	0.75	1.14	1.15	1.15	0.99	0.99	0.98
14	3	2	20	2	1.36	0.80	0.75	1.16	1.13	1.16	0.95	0.97	0.98
15	3	2	16	5	1.65	1.65	1.48	1.09	1.12	1.18	0.99	0.99	0.99

NA = Not Available. Sub.- Subject

n_1 , n_2 , n_3 and n_{Match} are the number of beats in Groups-1, -2, -3 and “matching group” respectively. E/A_n is the Group- n $E_{\text{peak}}/A_{\text{peak}}$ average ratio. See text for M and r^2 naming conventions.

* $M_{\text{LoadPerturbed}}$ vs M_{AllBeats} $p=0.34$.

** $M_{\text{LoadPerturbed}}$ vs $M_{\text{SteadyState}}$ $p=0.18$.

*** $M_{\text{SteadyState}}$ vs M_{AllBeats} $p=0.14$ (all p -values reflect two-tailed paired t -test).

9.3 RESULTS

On average, 17 Group-3, 2 Group-1 and 2 Group-2 beats were analyzed per subject. In some subjects unequal numbers of Group-1 and -2 beats were analyzed because of poor data. The ratio of load-perturbed group-1 and -2 beats to “matched beats” ranged from 1:3 for subjects with only 1 load-perturbed E-wave to 4:1 for subjects with multiple load-perturbed E-waves. See Table 9.2 for details.

9.3.1 Comparison of E-wave shapes between Group-1 and Group-3

Figure 9.2 shows representative beats from one subject with marked Group-1 and -2 E-wave shape alterations relative to steady-state. 9 subjects had Group-1 beats with lower E_{peak} ($E_{\text{peak}} z_{1-3} < 0$) and higher DT values relative to averaged Group-3 values. The remaining 6 subjects had beats with $E_{\text{peak}} z_{1-3} > 0$. Averaged over all 11 subjects, $E_{\text{peak}} (z_{1-3}^*)_{\text{AVG}}=2.38$, $\text{DT} (z_{1-3}^*)_{\text{AVG}}=2.41$, $E_{\text{peak}}/A_{\text{peak}} (z_{1-3}^*)_{\text{AVG}}=2.27$, $E_{\text{VTI}} (z_{1-3}^*)_{\text{AVG}}=2.13$, and $\text{MSE} (z_{1-3}^*)_{\text{AVG}}=3.71$.

9.3.2 Comparison of E-wave shapes between Group-2 and Group-3

Among the 12 subjects with analyzable Group-2 beats, $E_{\text{peak}} (z_{2-3}^*)_{\text{AVG}}=1.09$, $\text{DT} (z_{2-3}^*)_{\text{AVG}}=1.48$, $E_{\text{peak}}/A_{\text{peak}} (z_{2-3}^*)_{\text{AVG}}=1.35$, $E_{\text{VTI}} (z_{2-3}^*)_{\text{AVG}}=1.40$, and $\text{MSE} (z_{2-3}^*)_{\text{AVG}} = 2.31$. Significant deviation from steady-state was seen for one

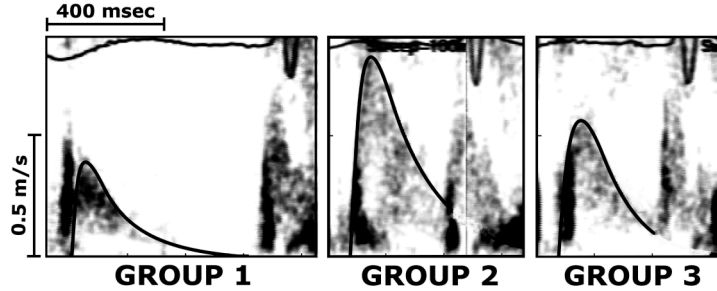


Figure 9.2 Representative Group-1, Group-2 and Group-3 pulsed wave transmitral flow-velocity images from a single patient with a superimposed parametrized diastolic filling (PDF) model-predicted fit to each E-wave. All E-waves are acquired in the same individual, but E-wave shapes are strikingly different. See text for details.

subject presented in Figure 9.2, where $E_{\text{peak}} (z_{2-3}^*)_{\text{AVG}} = 1.72$, $\text{DT} (z_{2-3}^*)_{\text{AVG}} = 2.02$, $E_{\text{peak}}/A_{\text{peak}} (z_{2-3}^*)_{\text{AVG}} = 1.97$, and $\text{MSE} (z_{2-3}^*)_{\text{AVG}}=10.08$. The remaining 11 subjects had modest PVC-related deviations in E-wave shape, though 4 of the subjects had significantly increased early filling volumes ($E_{\text{VTI}} (z_{2-3}^*)_{\text{AVG}} > 2$).

9.3.3 InterGroup Hemodynamic Comparison

Coupling ratio, defined as the PVC coupling interval divided by a normal RR interval, varied among the subjects from 0.28 to 0.83. Surprisingly, post-PVC LVEDP showed no

significant deviation from steady-state: LVEDP (z_{1-3}^*)_{AVG}=1.15 and LVEDP (z_{2-3}^*)_{AVG}=0.91.

The $+dP/dt_{\text{Max}}$ was elevated for Group-2 beats, with $+dP/dt_{\text{max}}$ (z_{2-3}^*)_{AVG} = 2.96. Finally, Group-2

LVP_{max} showed significant deviation, with LVP_{max} (z_{2-3}^*)_{AVG} = 3.06.

9.3.4 Calculated Load Independent Index and Inter-Group Comparison

Significant kx_0 deviation from steady-state was observed for 6 subjects (kx_0 (z_{n-3}^*)>2).

The kx_0 vs. cE_{peak} relationship was strongly linear in all subjects (see Figure 9.3) with nearly all

$r^2 > 0.9$. The M and B interobserver variability was 8%. The $B_{\text{LoadPerturbed}}$ value was nearly

distinguishable from B_{AllBeats} ($p = 0.08$) and distinguishable from $B_{\text{SteadyState}}$ ($p = 0.03$). The

$M_{\text{LoadPerturbed}}$ value was indistinguishable from M_{AllBeats} ($p = 0.34$) and $M_{\text{SteadyState}}$ ($p = 0.18$).

M_{AllBeats} was also indistinguishable from $M_{\text{SteadyState}}$ ($p = 0.14$). M_{AllBeats} was indistinguishable

from $M_{\text{SteadyState}}$ ($p = 0.14$). The r^2 values remained above 0.85. See Table 9.2 for details.

9.4 DISCUSSION

All noninvasive indexes of diastolic function are load dependent (4, 7, 8, 10-15, 19, 21-23). Our solution to the load independent index of diastolic function problem, presented in

Chapter 1, is based upon physical principles and causality, and is therefore promising.

Nevertheless, it may be that M is a load independent index of diastolic function over only a

narrow range of loads. To extend the range of load variation and study the global linearity of the

kx_0 vs. cE_{peak} relation, we tested whether M remains constant in the face of post- PVC related

load and E-wave shape variation.

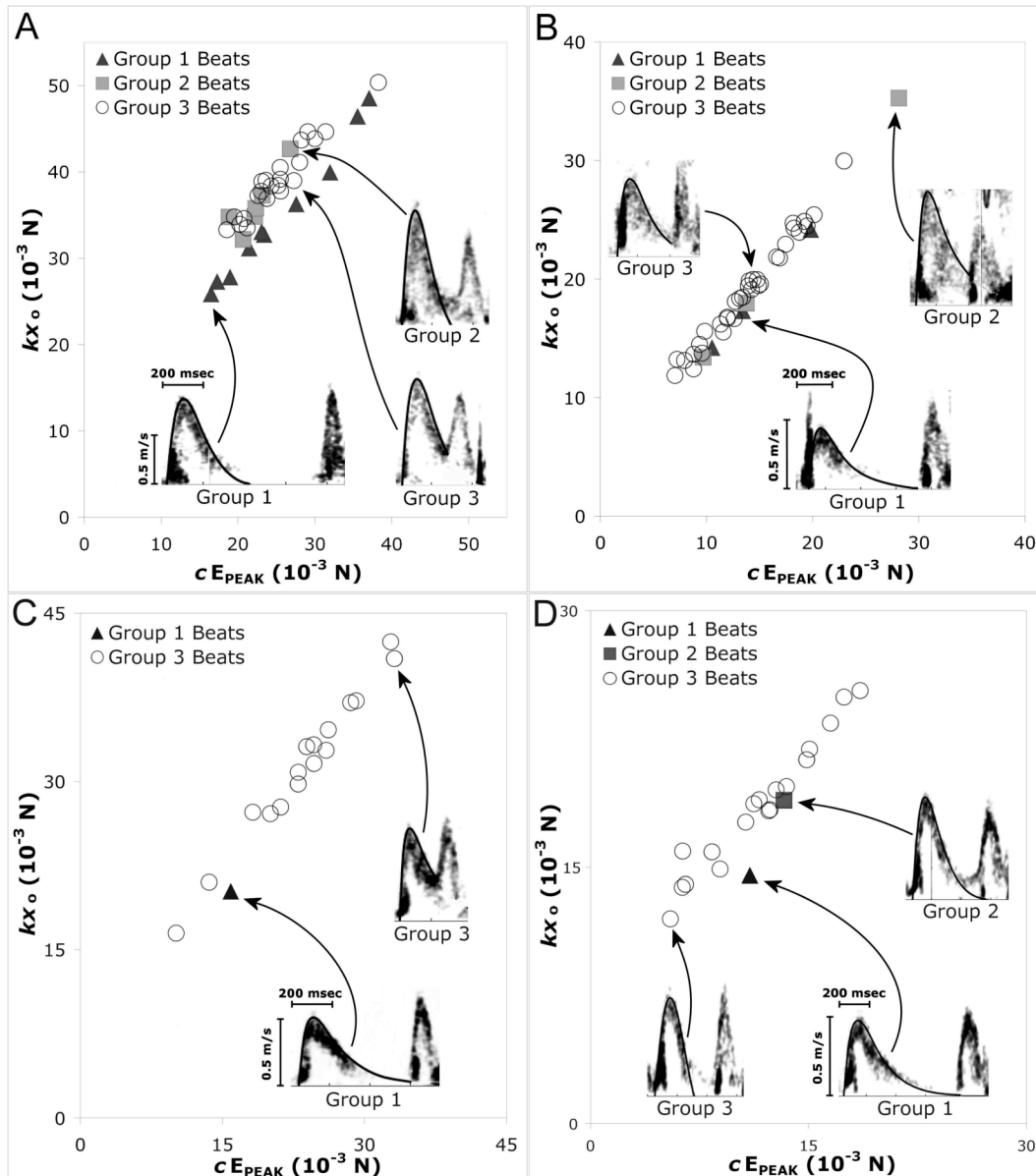


Figure 9.3 Maximum driving force [kx_0 , peak atrioventricular (AV) gradient] vs. peak resistive force (cE_{peak}) for 4 subjects. Raw Doppler images with superimposed PDF model fits to E-wave contours are shown for representative Group-1, Group-2 and Group-3 beats in each panel. Despite significant E-wave contour variations in Groups-1 and -2 relative to Group-3, kx_0 vs. cE_{peak} plots remain linear. Notice the range of kx_0 and cE_{peak} variation is increased in panels A and B above the variation seen in Group-3 beats alone. See text for details.

9.4.1 Diastolic Function and Premature Ventricular Contractions

The effect of PVCs on relaxation has been extensively studied (5), and studies have demonstrated a prolonged time constant of relaxation (τ) in Group-1 beats compared to steady state (2, 5). Carroll et al. (2) compared Group-1 and Group-3 pressure-volume loops in 6

patients. They found that while Group-1 beats had prolonged t values, the diastolic portions of the pressure-volume loops (intrinsic diastolic function) remained unchanged. Thus while filling dynamics were altered after a PVC, intrinsic diastolic function was conserved.

Consistent with Carroll's observation, several investigators have found altered filling patterns for Group-1 beats relative to Group-3 steady-state beats (18, 24). In agreement with these studies, we observed significantly different E-wave shapes for Group-1 and -2 E-waves compared to Group-3 E-waves. While Stoddard et al (18) found that Group-1 E_{peak} values were significantly lower compared to steady-state values, we found this to be true for 6 of the subjects, while the remaining 5 subjects had significantly higher Group-1 E_{peak} values relative to steady state. The mechanisms responsible for the varied E-wave responses following a PVC are not yet fully characterized. However, regardless of whether the Group-1 E_{peak} value increased or decreased relative to steady-state, we consistently found that the degree of variation was significant relative to steady state, and this is all that we require in order to test the extended load and E-wave shape dependence of M .

9.4.2 PVC effect on the Index M

Since load-perturbed E-wave shapes varied, the location of the Group-1 and -2 beats on the kx_o vs. cE_{peak} plot also varied. Figure 9.3A-D shows the kx_o vs cE_{peak} relation for subject 11, 9, 6 and 5, respectively. In Figure 9.3A we note that the slope M defined by the 15 Group-1 and -2 beats is 0.97, virtually parallel to the line defined by just Group-3 beats ($M=0.91$). Notice that in both Figures 9.3A and 9.3B, the kx_o vs. cE_{peak} relation retains the same linear character as it is extended over a wider range of shape variation. Indeed we found that perturbed beats (including "matching beats") visually extended the length of the kx_o vs. cE_{peak} regression in 9 of the 15

subjects. In Figure 9.3C and 9.3D, the Group-1 E-waves are outliers relative to steady-state beats, but their kx_o and cE_{peak} values in combination with kx_o and cE_{peak} values from only 3 matching beats generate a regression that is indistinguishable from the Group-3 regression. Indeed for all subjects the load-perturbed beats combined with a modest number of “matching beats” generated kx_o vs. cE_{peak} regressions whose slopes were indistinguishable from the kx_o vs. cE_{peak} regression slopes generated by steady-state alone and by all beats taken together. Thus although E-wave shapes change drastically in the beats that follow a PVC, the altered E-wave shapes generate a value for slope M that is consistent with the value generated by steady-state beats. Indeed, in all subjects, the slope of the specific kx_o vs. cE_{peak} relation constrains the filling ventricle and is conserved in the face of drastic post-PVC E-wave shape alteration.

9.4.3 Must All Measured Waves Be Collinear in the kx_o vs cE_{peak} plane?

The results suggest that load variation by PVC results in E-waves that are still constrained by the same kx_o vs cE_{peak} regression as other E-waves measured in the same subject. This may lead to the suspicion that all clinically measured E-waves must be collinear. While Chapter 8 showed clearly that randomly generated E-waves are not collinear, a striking example is provided in the current data. Subject 7 possesses a beat where the E- and A-waves are completely merged, thus appearing as one large velocity contour. When this merged wave is fit as an assumed E-wave, it generates kx_o and cE_{peak} values that appear as outliers relative to the Group-3 determined kx_o vs. cE_{peak} regression (Figure 9.4). Thus, it is not guaranteed that any set of E-waves will be collinear in the kx_o vs cE_{peak} plane.

9.4.4 The Connection between Relaxation, Restoring Forces, and M

The plot of kx_o vs cE_{peak} may be interpreted conceptually as a stiffness vs. relaxation (resistive effect) plot, and the slope M describes how effectively stiffness compensates for changes in relaxation. Thus the findings of Carroll et al. (2) where it was postulated that maintenance of DF following PVCs was achieved through enhanced restoring forces compensating for prolonged relaxation effects, can be understood in the context of the current study. If relaxation is prolonged following a PVC then the resulting E-wave will have a higher cE_{peak} value.

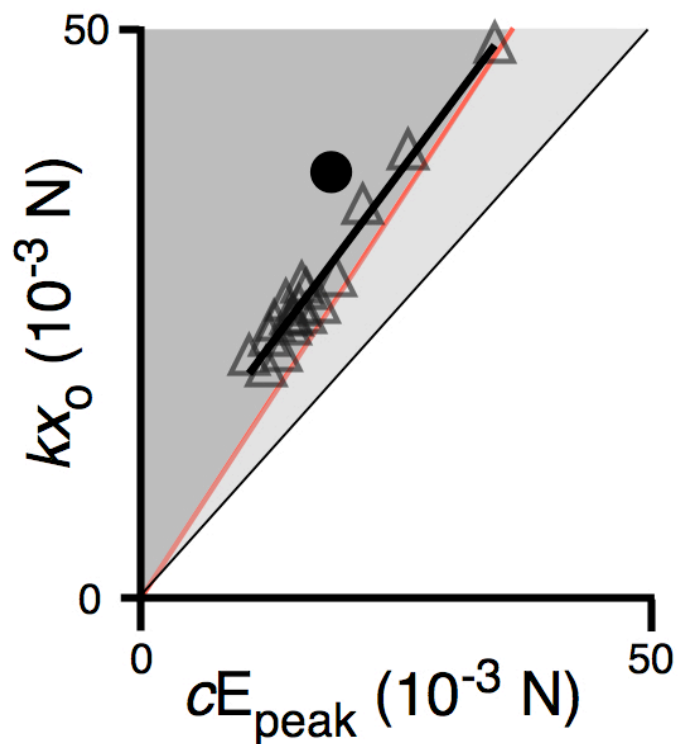


Figure 9.4. Maximum driving force (kx_o) vs. peak resistive force (cE_{peak}) for subject 7. Unmerged E-waves are represented by triangles. A filling wave consisting of completely merged E- and A-waves was fit as an “E-wave” and the corresponding kx_o vs cE_{peak} point is represented by the solid circle. Notice that the false E-wave falls significantly off of the linear relation defined by the true E-waves. Overdamped and Underdamped regions are shaded light gray and dark gray respectively.

Because the E-wave is constrained to a specific kx_o vs cE_{peak} relation, the elastic restoring forces, quantified by kx_o , will in turn be elevated. Despite the fact that the E-wave will be visually different, the balance between the forces that determine the E-wave and define M will be conserved.

9.5 LIMITATIONS

E-waves were analyzed off-line using digitized, frame-captured images. This makes automated edge detection algorithms and post processing less useful and could be viewed as a minor technical limitation to our study. Furthermore, subjects in the study were chosen retrospectively based on presence of PVC beats and high quality images amenable to analysis. Given the retrospective nature of the study, its aims, and the lack of specific clinical selection criteria, it may be inappropriate to compare clinical correlates with M values in these patients. While this represents a clear limitation, the purpose of the study is to investigate the robustness of M for the same subject when computed in the setting of varying loading conditions.

The calculation of a load independent index of diastolic function requires E-waves with clearly discernible contours. In addition, significant merging of E- and A-waves, leading to a loss of more than two-thirds of the E-wave deceleration contour, makes PDF and subsequently load independent index of diastolic function analysis less robust. To avoid significant E- and A-wave merging, subjects with high heart rate (>90 bpm) or prolonged PR intervals must be excluded from analysis. While the limitation of high heart rate may be overcome with pharmacologic agents, the results of the current study suggest an alternative approach. Because PVC's are often followed by a compensatory pause, Group-1 beats tend to have clear diastatic intervals, even if the Group-3 beats have significant E- and A-wave merging. For example, in our work we encountered a subject with merged Group-3 beats that precluded standard load independent index of diastolic function computation. However, this subject had several Group-1 beats with clearly discernible diastatic intervals that yielded a highly linear kx_0 vs. cE_{peak} relationship (data not shown). Since the results of this study suggest that the load independent index of diastolic function is independent of PVC related perturbations, it may be clinically appropriate to

overcome the E- and A-wave merging limitation by utilizing unmerged post-PVC beats for load independent index of diastolic function calculation.

Calculation of the M requires the construction of a linear regression based on extracted parameters from multiple varying E-waves. For this reason, we were not able to effectively calculate the M in all subjects using Group-1 and Group-2 beats alone, and therefore we added a modest number of subsequent Group-3 beats in order to increase the number of points on the line. A possible limitation may be that the matching beats had a dominant effect in determining the $M_{\text{LoadPerturbed}}$ values. However, only 3 of the subjects had 3 matching beats combined with only 1 Group-1 beat and the remaining subjects had at most 3 matching beats for every 2 perturbed beats. Thus, matching beats and perturbed beats had comparable weight in determining M . Furthermore, matching beats directly followed the Group-1 and -2 beats and the ventricle may not be fully back to steady state after only 2 filling beats following a PVC (16). Thus it may be appropriate to include some of the matching-beats in the ‘perturbed’ beat category, and at worst they represent a balanced, not dominant, effect relative to Group-1 and -2 beats.

An additional limitation of the current study may be the limited range of LVEDP variation introduced with the inclusion of post-PVC beats. Possible explanations for this may be the effects of respiratory variation, variable intravascular volume status and variable inotropic state. Significant respiratory variation may mask the pressure response following PVC’s because the PVC may occur at end-inspiration. and second, z -scores defined by Eq. 1 are lower when the baseline variation is significant.

It may seem that the ventricular response following PVCs was not dramatic enough to extend our confidence in the load-independence of M . It is important to stress that for Doppler-echo data load-dependence refers to the observed changes in E-wave morphology in the face of

physiological variation. Thus, the key test of any E-wave derived load independent index of diastolic function is how the index changes in the face of changing E-wave morphology. All geometric E-wave shape-based indexes change dramatically with changing E-wave morphology, and indeed, we observed significant deviation from steady state for all geometrically based E-wave indexes. Furthermore, 9 subjects possessed Group-1, -2 or “matching beats” that visually increased the range of the kx_o vs cE_{peak} line. Thus we can be sure that whatever physiological mechanisms underlie the hemodynamic response following PVCs, these mechanisms are consistently responsible for dramatic E-wave shape changes, and therefore provide a serious challenge to any proposed load independent index of diastolic function.

9.6 CONCLUSIONS

In Chapter 8 we showed that changes in E-wave shape caused by respiration alone obey a linear driving-force to resistive-force (kx_o vs. cE_{peak}) relation whose slope M is independent of load. In the current Chapter the load dependence of the kx_o vs cE_{peak} regression was tested under a wider range of E-wave shapes and associated loads. We found that although E-wave shape can change markedly in post-PVC beats, the numerical value for the load-independent index M remains unchanged in a given subject. Indistinguishable values for M using different *in-vivo*, physiologic methods of load-variation in the same subjects (post-PVC and respiratory variation) underscores the robustness of M as a load independent index of diastolic function.

9.7 REFERENCES

1. Appleton CP, Firstenberg MS, Garcia MJ, and Thomas JD. The echo-Doppler evaluation of left ventricular diastolic function. A current perspective. *Cardiology clinics* 18: 513-546, ix, 2000.
2. Carroll JD, Widmer R, Hess OM, Hirzel HO, and Krayenbuehl HP. Left ventricular isovolumic pressure decay and diastolic mechanics after postextrasystolic potentiation and during exercise. *Am J Cardiol* 51: 583-590, 1983.
3. Choong C, Herrmann H, Weyman A, and Fifer M. Preload dependence of Doppler-derived indexes of left ventricular diastolic function in humans. *J Am Coll Cardiol* 10: 800-808, 1987.
4. Choong CY, Herrmann HC, Weyman AE, and Fifer MA. Preload dependence of Doppler-derived indexes of left ventricular diastolic function in humans. *Journal of the American College of Cardiology* 10: 800-808, 1987.
5. Cooper MW. Postextrasystolic potentiation. Do we really know what it means and how to use it? *Circulation* 88: 2962-2971, 1993.
6. Courtois M, Barzilai B, and Fischer A. Augmentation of early diastolic filling by left ventricular postextrasystolic contraction. *Coronary Artery ...*, 1990.
7. Firstenberg MS, Greenberg NL, Main ML, Drinko JK, Odabashian JA, Thomas JD, and Garcia MJ. Determinants of diastolic myocardial tissue Doppler velocities: influences of relaxation and preload. *J Appl Physiol* 90: 299-307, 2001.
8. Jacques DC, Pinsky MR, Severyn D, and Gorcsan J. Influence of alterations in loading on mitral annular velocity by tissue Doppler echocardiography and its associated ability to predict filling pressures. *Chest* 126: 1910-1918, 2004.

9. Kass DA. Assessment of diastolic dysfunction. Invasive modalities. *Cardiology clinics* 18: 571-586, 2000.
10. Kmetzo JJ, Plotnick GD, and Gottdiener JS. Effect of postural changes and isometric exercise on Doppler-derived measurements of diastolic function in normal subjects. *Chest* 100: 357-363, 1991.
11. Lin S-K, Hsiao S-H, Lee T-Y, Huang W-C, Hsu T-L, Mar G-Y, and Liu C-P. Color M-mode flow propagation velocity: is it really preload independent? *Echocardiography (Mount Kisco, NY)* 22: 636-641, 2005.
12. Masuyama T, St Goar FG, Alderman EL, and Popp RL. Effects of nitroprusside on transmitral flow velocity patterns in extreme heart failure: a combined hemodynamic and Doppler echocardiographic study of varying loading conditions. *Journal of the American College of Cardiology* 16: 1175-1185, 1990.
13. Oğuzhan A, Arınç H, Abacı A, and Topsakal R. Preload dependence of Doppler tissue imaging derived indexes of left ventricular diastolic function. ..., 2005.
14. Paelinck BP, van Eck JWM, De Hert SG, and Gillebert TC. Effects of postural changes on cardiac function in healthy subjects. *European journal of echocardiography : the journal of the Working Group on Echocardiography of the European Society of Cardiology* 4: 196-201, 2003.
15. Pelà G, Regolisti G, Coghi P, Cabassi A, Basile A, Cavatorta A, Manca C, and Borghetti A. Effects of the reduction of preload on left and right ventricular myocardial velocities analyzed by Doppler tissue echocardiography in healthy subjects. *European journal of echocardiography : the journal of the Working Group on Echocardiography of the European Society of Cardiology* 5: 262-271, 2004.

16. Shimizu J, Araki J, Iribe G, Imaoka T, Mohri S, Kohno K, Matsubara H, Ohe T, Takaki M, and Suga H. Postextrasystolic contractile decay always contains exponential and alternans components in canine heart. *Am J Physiol Heart Circ Physiol* 279: H225-233, 2000.
17. Shmuylovich L and Kovács SJ. Load-independent index of diastolic filling: model-based derivation with in vivo validation in control and diastolic dysfunction subjects. *J Appl Physiol* 101: 92-101, 2006.
18. Stoddard MF, Pearson AC, Kern MJ, and Labovitz AJ. The effect of premature ventricular contraction on left ventricular relaxation, chamber stiffness, and filling in humans. *American Heart Journal* 118: 725-733, 1989.
19. Sztajzel J, Ruedin P, Monin C, Stoermann C, Leski M, Rutishauser W, and Lerch R. Effect of altered loading conditions during haemodialysis on left ventricular filling pattern. *Eur Heart J* 14: 655-661, 1993.
20. Thomas J and Weyman A. Echocardiographic Doppler evaluation of left ventricular diastolic function. Physics and physiology. *Circulation* 84: 977-990, 1991.
21. Triulzi MO, Castini D, Ornaghi M, and Vitolo E. Effects of preload reduction on mitral flow velocity pattern in normal subjects. *Am J Cardiol* 66: 995-1001, 1990.
22. Yalçın F, Kaftan A, Muderrisoğlu H, Korkmaz ME, Flachskampf F, Garcia M, and Thomas JD. Is Doppler tissue velocity during early left ventricular filling preload independent? *Heart* 87: 336-339, 2002.
23. Yamamoto K, Masuyama T, Tanouchi J, Uematsu M, Doi Y, Mano T, Hori M, Tada M, and Kamada T. Peak early diastolic filling velocity may decrease with preload augmentation: effect of concomitant increase in the rate of left atrial pressure drop in early diastole. *Journal of*

the American Society of Echocardiography : official publication of the American Society of Echocardiography 6: 245-254, 1993.

24. Yellin EL, Kennish A, Yoran C, Laniado S, Buckley NM, and Frater RW. The influence of left ventricular filling on postextrasystolic potentiation in the dog heart. *Circ Res* 44: 712-722, 1979.

CHAPTER 10.

THE LOAD INDEPENDENT INDEX AND END DIASTOLIC PRESSURE
RELATION: THEORETICAL DERIVATION AND EXPERIMENTAL
VALIDATION

10.1 INTRODUCTION

While Doppler-echocardiography is the preferred method of non-invasive diastolic function (DF) assessment, the gold-standard is invasive left ventricular (LV) end diastolic pressure (EDP) determination. Chronically elevated EDP or acute elevation in response to physiologic load is a clinical sign of intrinsic diastolic dysfunction, often associated with increased chamber stiffness and volume overload (19-21). In current clinical practice E/E' , the ratio of pulsed Doppler derived peak transmitral blood flow velocity to Tissue Doppler derived peak annular tissue recoil velocity, is used as a noninvasive EDP correlate. While E/E' has been validated as an EDP surrogate in selected patient groups with abnormal systolic function, the correlation between EDP and E/E' in subjects with normal systolic function has been modest at best (10, 11, 18). All echo-derived indexes are known to be load-dependent, including E/E' (10, 14), and this may contribute to the weak correlation to EDP.

Using a damped harmonic oscillatory kinematic model of early diastolic transmitral blood flow velocity contours (E-waves), we have solved the load independent index of diastolic function (LIIDF) problem (see Chapter 8). The load-independent linear relation can be mathematically extracted from a set of load varying E-waves by plotting the (model-derived) maximum force driving flow (kx_o) vs the peak resistive force opposing flow (cE_{peak}), i.e. $kx_o = M(cE_{peak}) + B$, M and B constants. The load independence of the slope M and its ability to differentiate between control and diastolic dysfunction groups has been described (17), but the proper interpretation and clinical utility of the intercept B has not been fully elucidated.

We hypothesize that physiological and mathematical modeling allows derivation of an algebraic relation between the (noninvasive) intercept B of the kx_o vs cE_{peak} relation (a relative index) and invasively determined, average EDP (an absolute index). We validate the predicted

relationship between B and EDP in 46 subjects undergoing simultaneous echocardiography and high-fidelity catheterization, and compare the experimentally determined relationship to the E/E' vs EDP relationship in the same subjects.

10.2 METHODS

10.2.1 Theoretical Derivation

Kinematic Modeling of Diastolic Filling

Suction initiated filling governs the physiology of diastole. Therefore, independent of load, the kinematics of filling and the equation of motion that determined the E-wave always applies. Hence all the E-wave velocity contours are well characterized by the PDF model, a damped simple harmonic oscillator with relaxation/damping constant c , stiffness k , and initial conditions $v(0)=0$, $x(0)=x_o$ (initial spring displacement) (see Chapter 1 and 2). In Chapter 8, we showed that a load-independent index of filling can be obtained through PDF model-based analysis of E-waves under varying loads as the slope M of the linear (model-derived) maximum force driving flow (kx_o) vs peak resistive force (cE_{peak}) relation. In previous work, and as outlined in Chapter 8, the slope M was found to differentiate between subjects with diastolic dysfunction and subjects with normal diastolic function. However, the intercept B was found to also be different between groups, with a higher intercept found among subjects with diastolic dysfunction. It is intriguing to consider, therefore, whether a causal connection between elevated B and elevated end-diastolic pressure (EDP), a gold standard marker for diastolic dysfunction, exists.

Mathematical Analysis of EDP

The end diastolic pressure can be calculated approximately by considering the pressure volume loop during diastole (Figure 10.1). While the pressure volume loop is curvilinear between minimum pressure and end-diastolic pressure, a linear approximation is routinely applied to define average operating chamber stiffness, as described in Chapters 4 and 5. The average operating chamber stiffness is therefore given by:

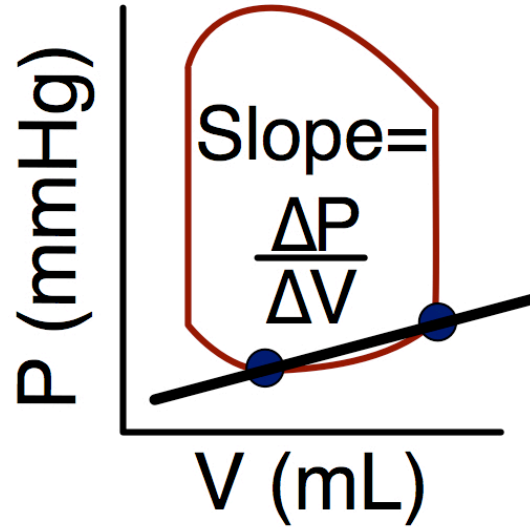


Figure 10.1 The slope of the line in the pressure-volume plane between minimum pressure and end diastolic pressure is routinely used to estimate average operating chamber stiffness. End diastolic pressure can therefore be estimated from stiffness, minimum pressure, and change in volume (ΔV) between minimum pressure and end-diastole. See text for details.

an

$$\frac{\Delta P}{\Delta V_{AVG}} = \frac{P_{EDP} - P_{Min}}{V_{EDP} - V_{P_{Min}}} \quad \text{Equation 10.1}$$

where P_{EDP} and V_{EDP} are the pressures and volumes at end-diastole, and P_{MIN} and $V_{P_{MIN}}$ are the pressures and volumes at the time of minimum pressure (9). Eq. 10.1 may be solved for end diastolic pressure:

$$P_{EDP} = P_{Min} + (V_{EDP} - V_{P_{Min}}) \frac{\Delta P}{\Delta V_{AVG}} \quad \text{Eq 10.2}$$

In order to derive a noninvasive surrogate for end diastolic pressure, we must incorporate noninvasive surrogates for each of the terms on the right side of Equation 10.2.

Previous work (9) has predicted and demonstrated a linear correlation between average operating stiffness $\Delta P / \Delta V_{AVG}$ and the PDF stiffness parameter k across 131 subjects with a large range of invasive and noninvasive measured stiffness values. Thus, Equation 10.2 may be

simplified to:

$$P_{EDP} = P_{Min} + (V_{EDP} - V_{P_{Min}})(Ck + D) \quad \text{Equation 10.3}$$

where $C=7.1 \cdot 10^{-4}$ (mmHg \cdot s²)/cm³ and $D=-0.042$ (mmHg)/cm³ are constant values as described in previously published work (9)

The volume increase between minimum pressure and end-diastole may be calculated from E-wave and A-wave areas multiplied by a constant effective mitral valve area:

$$(V_{EDP} - V_{P_{Min}}) = MVA \cdot \left(\int_{P_{min}}^{E_{dur}} v_E(t) dt + \int v_A(t) dt \right) \quad \text{Equation 10.4}$$

Where v_E and v_A are the E-wave and A-wave velocities, and E_{dur} is the E-wave duration. Note that the E-wave integral limit must begin at the time of minimum pressure, and not at the start of the E-wave. It is reasonable to assume that the peak of the E-wave and minimum in pressure occur simultaneously, and therefore, using expressions for velocity from Chapter 2, the E-wave integral may be simplified in terms of x_o and y :

$$\int_{AT}^{E_{dur}} v_E(t) dt = x_E(E_{dur}) - x_E(AT) = x_o \left(e^{-\frac{\pi y}{\sqrt{1-y^2}}} - \frac{y^2}{\sqrt{1-y^2}} e^{-\frac{\cos^{-1} y}{\sqrt{1-y^2}}} \right) \quad \text{Equation 10.5}$$

which is equal to x_o in the $y=0$ (or $c=0$) limit.

Considering the undamped ($c=0$) case is interesting, especially given the results of Chapter 5, where we showed that pressure is predicted to recover completely to mitral valve opening pressure, which is approximately equivalent to end diastolic pressure, by the end of the E-wave. In other words, in the undamped limit, the A-wave is expected to play an insignificant role in filling. It is certainly the case that as damping increases and E-waves take on a delayed relaxation pattern, A-waves tend to become more prominent so as to conserve stroke volume.

Indeed this is why atrial fibrillation can be so dangerous in older individuals with delayed relaxation E-wave patterns, because the A-wave is so critical for maintenance of stroke volume when early filling is impaired. Thus in the theoretical undamped limit, the A-wave area is expected to be insignificant, and therefore , in the $c=y=0$ limit, Eq. 10.4 becomes:

$$\left(V_{EDP} - V_{P_{Min}} \right) \Big|_{c=0} = MVA \cdot (x_o) \Big|_{c=0} \quad \text{Equation 10.6}$$

Plugging into Eq. 10.3 we find:

$$P_{EDP} = P_{Min} + MVA \left(C \cdot kx_o \Big|_{c=0} + D x_o \Big|_{c=0} \right) \quad \text{Equation 10.7}$$

The linearity of the kx_o vs cE_{peak} regression, described in Chapter 8, suggests that a given subject is constrained to have E-wave filling contours consistent with the measured kx_o vs cE_{peak} regression. Therefore intercept B of the regression is the predicted value of kx_o in the $c=0$ limit.

Thus, Equation 10.7 may be simplified as:

$$P_{EDP} = (C \cdot MVA) \cdot B + \left(P_{Min} + MVA \cdot D x_o \Big|_{c=0} \right) \quad \text{Equation 10.8}$$

While Equation 10.8 predicts a non-zero intercept, it demonstrates clearly that there is a linear relationship expected between end-diastolic pressure and kx_o vs cE_{peak} regression intercept B . If minimum pressure is fairly consistent across subjects, and k is greater than D/C , then the nonzero intercept in Eq. 10.8 would be expected to be relatively constant, and the predicted linear relationship between end diastolic pressure and B would be expected to hold.

10.2.2 Experimental Methodology

Subject Demographics and Data Acquisition

42 normal systolic function subjects (ejection fraction > 50%), with significant load variation by respiration, were chosen from our preexisting simultaneous catheterization-echo

database. Selection criteria for inclusion included: normal sinus rhythm, no evidence of valvular disease, no active ischemia, and normal ejection fraction. Subject demographics for the 42 subjects are presented in Table 10.1.

See Chapter 2 for a description of the simultaneous echocardiography-catheterization data acquisition protocol. In each subject multiple beats of Pulsed Doppler transmitral flow, as well as Tissue Doppler flow are acquired with simultaneous high fidelity catheterization. Both septal and annular velocities are

recorded, but only lateral velocities are recorded during the catheterization portion.

Table 10.1 Subject demographics.

<i>Age (years)</i>	56 ± 12
<i>End Diastolic Volume (mL)</i>	135 ± 43
<i>Systolic LV Pressure (mmHg)</i>	140 ± 37
<i>Ejection Fraction</i>	72 ± 8
<i>Male vs Female</i>	20 vs 22

Data for 42 subjects showing mean ± standard deviation.

Data Analysis

For each subject, 8-15 E-waves were analyzed. A traditional triangle fit was applied to each wave and conventional Doppler-derived indexes (E_{peak} , AT, DT, E_{dur} , A_{peak} , A_{dur} , E/A) were determined (see section ## for discussion of conventional transmitral contour indexes). In addition, E- and A-wave contours were fit via the parameterized diastolic filling formalism (see Chapter 2) to yield PDF c , k , and x_o parameters. As described in Chapter 8, linear regression between kx_o and cE_{peak} for each subject, yielded the slope M and intercept B .

As described in Chapter 2, left ventricular end-diastolic pressure was determined from the simultaneous left ventricular pressure data by reading off the pressure at the time of ECG R-wave peak.

Determination of the E/E' ratio is challenging because simultaneous measurement of E-wave and E' waves is not possible with conventional echocardiography imagers, and therefore E

and E'-waves must be measured independently. Thus E-wave and E'-waves were matched according to heart rate, and the peak velocities of heart rate matched waves were subsequently used to determine an average E/E' ratio in each subject.

The correlations of EDP vs. B and EDP vs. E_{peak}/E' were investigated by linear regression. Linear regressions were assessed by Pearson correlation coefficient. All statistical analysis was carried out using MS-Excel (Microsoft, Redmond, WA).

10.3 RESULTS

10.3.1 Load Independent Index and EDP

As in Chapter 8, the linear regression between kx_0 and cE_{peak} was found to be strong for each individual subject (average $r^2=0.94$). Across all subjects, M varied from 0.84 to 1.39, and B varied from 3.5 to 15.7. The average catheterization determined end diastolic pressure (EDP) was 18 mmHg, and varied from 8 to 40 mmHg across all subjects. The average catheterization determined minimum pressure was 9 mmHg, and varied from 1 to 26 mmHg. The average M value for subjects with $\text{EDP}<20$ was 1.10 ± 0.11 , while the average M value for subjects with $\text{EDP}\geq 20$ was 1.03 ± 0.11 ($p=0.03$ by 2-tailed t -test between groups). In accordance with the predicted algebraic relationship (Eq. 10.8), we observe a linear correlation between B and catheterization determined end diastolic pressure ($r^2=0.43$) (Figure 10.2).

10.3.2 Conventional E/E' Ratio

Transmitral and Tissue Doppler images were matched according to heart rate (RR interval) in each subject. A simple t -test of heart rates between matched beats showed no significant difference in matched beat heart rates ($p=0.68$). The resulting E/E' ratio across

subjects varied between 2.5 and 11.1, with an average value of 5.6. Furthermore, invasively derived end diastolic pressure was linearly correlated ($r^2=0.14$) to noninvasive E/E' (Figure 10.2).

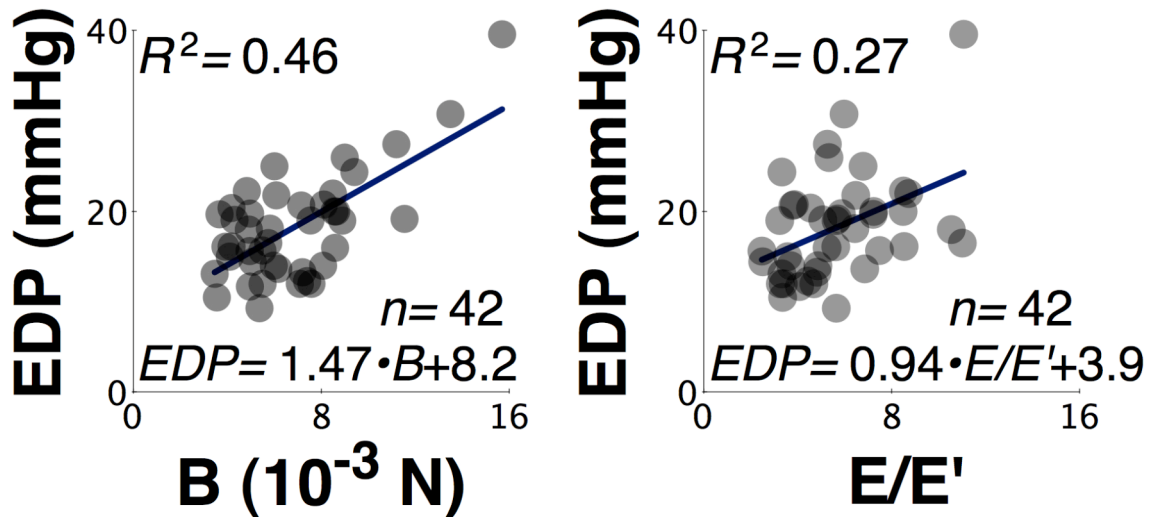


Figure 10.2 .Comparison of the correlation between invasively determined end diastolic pressure (EDP), and two noninvasive surrogates of end diastolic pressure in 42 subjects with a variety of filling pressures. The left panel shows the correlation of EDP to B , the intercept of the load independent index of diastolic function relation, and the right panel shows the correlation of EDP to E/E' , the ratio of peak transmitral early filling velocity to peak early filling annular tissue velocity.

10.4 DISCUSSION

10.4.1 Summary

While noninvasive echocardiography is the preferred method by which diastolic function is assessed, invasively determined end-diastolic pressure remains a gold standard for clinical decision making and diagnosis of diastolic dysfunction. Noninvasive surrogates for end-diastolic pressure exist, but they have limited applicability, and their load dependence makes them unreliable as indexes of diastolic function. In Chapter 8 and published work we have described a novel load-independent index of diastolic function, defined as the slope of a regression between peak driving forces and peak resistive forces of diastolic filling. In the current Chapter we derive

a linear relationship between the intercept of the load independent index linear regression and invasively determined end-diastolic pressure. We validate this linear relationship and compare it to an established end diastolic pressure surrogate, calculated from the ratio of peak filling velocity to peak tissue recoil velocity.

10.4.2 Current Application of E/E'

In current clinical practice, the ratio of peak filling velocity to peak annular tissue recoil is routinely used to assess diastolic function. Peak annular tissue velocity has been shown to be blunted in subjects with impaired relaxation (10) and to be preload dependent in subjects with normal relaxation (3, 4, 6, 13). Subjects with impaired relaxation have a blunted E-wave pattern, and dividing peak E-wave height by peak annular tissue velocity is seen to 'correct' the effect of relaxation on the E-wave. Thus, the E/E' ratio is expected to increase with progressive diastolic dysfunction, and because progressive diastolic dysfunction is associated with increased end-diastolic pressure, the E/E' ratio is expected to correlate with end-diastolic pressure. Indeed in subjects with poor systolic function, E/E' has proven to be a useful end diastolic pressure surrogate (11). Early studies in subjects with normal diastolic function did not show as promising results, however (18). Studies have shown however that using septal vs lateral annular tissue velocities makes a significant impact on the resulting correlations with EDP, especially when septal and lateral velocities are significantly different. While some studies advocate the use of septal E' velocities, studies in subjects with normal ejection fraction suggest that better results are obtained when lateral E' velocities are utilized (16). According to American Society of Echocardiography recommendations, a septal E/E' < 8 suggests normal end diastolic pressure while a septal E/E' > 15 or lateral E/E' > 12 suggests increased end diastolic pressure. The results

for E/E' between 8 and 15 are unequivocal, and further echocardiographic measures must be obtained in order to approximate filling pressures [REF]. Thus an E/E' between 8 and 15 (or 8 and 12 for lateral E/E') has limited clinical utility. This is particularly relevant to the current study because 8 of the 41 subjects had lateral E/E' values between 8 and 12. Interestingly, removing these subjects from the analysis does not improve the correlation between E/E' and end diastolic pressure.

10.4.3 Previous Modeling of E/E'

Previous theoretical analysis by Lisuaskas et al predicted a linear correlation between E/E' and LVEDP, and the theoretical basis for this predicted was the constant volume property of the 4 chamber and 2 chamber heart. (2). Previous work demonstrated that atrial and ventricular chamber volumes reciprocate during the heart cycle. Based on this physiological constraint, and applying the fact that tissue volume is conserved during the heart cycle, Lisauskas et al derived an expression between the ratio of peak blood flow velocity to peak annular tissue velocity and the ratio of peak valve to peak annular cross sectional area (8). Furthermore, arguing that the chamber behaves, to a first approximation, as an elastic chamber, they showed that cross sectional area would be expected to correlate with end diastolic pressure, and therefore predicted a linear relationship between end diastolic pressure and E/E'.

This prediction may also be appreciated by considering longitudinal vs radial modes of filling. The ventricle fills primarily by accommodating volume longitudinally, as seen by Doppler Tissue recoil velocities (15). A second mode of filling is radial filling by radial epicardial expansion. The existence of radial expansion is easiest to appreciate when one considers an oscillatory Doppler Tissue velocity waveform (see Chapter 2). The first oscillation

is the E' wave, and this represents longitudinal expansion during E-wave filling. The 2nd hump on the velocity contour, the E'' wave, on the other hand represents longitudinal contraction, and this occurs during the E-wave deceleration portion. Increasing volume from continued E-wave filling coupled with longitudinal contraction can only occur in the presence of simultaneous radial expansion. The extent of radial expansion is limited however, because within 5% the outside dimension of the heart does not change due to a physical pericardial constraint. Thus filling by radial expansion represents a higher resistance path for diastolic recoil, and is associated with elevated filling pressures. Maintenance of stroke volume ensures that a significantly blunted E' velocity, and therefore an increased E/E' ratio, is associated with increased reliance on the radial mode of filling, and therefore a likely increase in end-diastolic pressure. Thus at the extreme limit of significantly elevated E/E' , the connection to increased end-diastolic pressure is reasonable from basic physiological properties and modeling. In the absence of blunted E' , however, constant volume pump considerations do not make a strong prediction regarding the dependence of E' on LVEDP.

10.4.5 Comparing B vs. EDP and E/E' vs. EDP

As Figure 10.2 demonstrates, the intercept B of the regression across multiple beats between E-wave derived peak driving force and peak resistive force correlates linearly with end-diastolic pressure, and has a stronger degree of correlation to end diastdolic pressure than E/E' . One contributor to this difference is likely that E/E' is dimensionless, while B has units of force, or pressure per unit area. Thus from a dimensional analysis standpoint, it is not surprising that B is a more robust surrogate for end diastolic pressure than E/E' .

Both E/E' and B rely on data acquired from multiple beats. E/E' requires separate

measurements of E-wave and E'-waves followed by matching beats and averaging, whereas B relies on measuring and analyzing multiple E-wave acquired at varying load states. In accordance with first principles, load variation is accompanied by end-diastolic pressure variation, because changing end-diastolic chamber dimension is coupled, by the chamber's pressure volume relationship, to changes in end-diastolic pressure. Importantly, the EDP shown in Figure 10.2 is an average chamber end diastolic pressure, and therefore the impact of beat by beat load variation on EDP is minimal in the analysis. It is unclear if E/E' or B can predict beat by beat load-related end-diastolic pressure variation, but the results of Figure 10.2 suggest that both are reasonable surrogates for the average operation chamber end-diastolic pressure.

10.5 LIMITATIONS

10.5.1 Heart Rate

A significant limitation of PDF analysis is the inability to effectively analyze E-wave contours when E- and A-wave merging is significant (see Chapter 1 and Chapter 2). Thus, subjects with high heart rate are not amenable to PDF analysis, and determination of M and B in these subjects is not possible without heart rate lowering interventions. Determination of E-wave peak and E'-wave peak, however, is possible in the setting of tachycardia, as long as the E wave is clearly visible and distinct from the A-wave (12). If the start of the A-wave occurs before the E-wave peak then the E-wave peak velocity will have an addition contribution from the atrial kick, and this may obscure the determination of E/E' . Thus, the determination of E/E' is limited to heart rates where the P-wave occurs after the E-wave peak, but this is a far less stringent heart rate cutoff than the heart rate limitation inherent in PDF model analysis.

10.5.2 Simultaneous E and E' Determination and Location of E' Measurement

Ideally one would measure E and E' peak in the same diastolic interval, but without simultaneous and non-interfering transducers, this is not possible. Instead, E- and E'-waves must be matched as closely as possible, and one natural approach is to match beats with similar R-R intervals. In this work we performed a t-test between E-wave and matched E'-wave R-R intervals to ensure that the heart rates were indistinguishable, but there are a variety of clinical factors beyond heart rate that may affect E or E' velocities. Thus there is always some error in the determination of E/E' due to the lack of simultaneity of E and E-wave image acquisition. In addition, studies have shown marked differences in E' peak velocities at the septal vs lateral position, especially in the presence of regional dysfunction (16). In the current work lateral E' velocities were used for E/E' determination. None of the subjects in the current work had significant regional dysfunction, and recent studies have suggested better correlations between laterally defined E/E' and end diastolic pressure, and therefore our choice of lateral E' velocities was warranted. However, the regional variation in E'-wave velocity is a significant limitation to the E/E' index and must be considered with care in practice. There is always some variability in E' waveform recording depending on transducer positioning and operator skill. These issues are mitigated in this setting because of the experience of the sonographer.

10.5.3 Issue of Minimum Pressure

The derivation presented in the Methods assumes that minimum ventricular pressure is fairly constant across subjects, but in some clinical situations minimum pressure is known to be significantly elevated (7). Hypertensive episodes increase all diastolic filling pressures, including minimum pressure, and in the setting of diastolic dysfunction, this increase has been found to be

more significant. However, the derivation supporting the correlation between E/E' and end diastolic pressure also relies on the consistency of minimum pressure across multiple subjects,

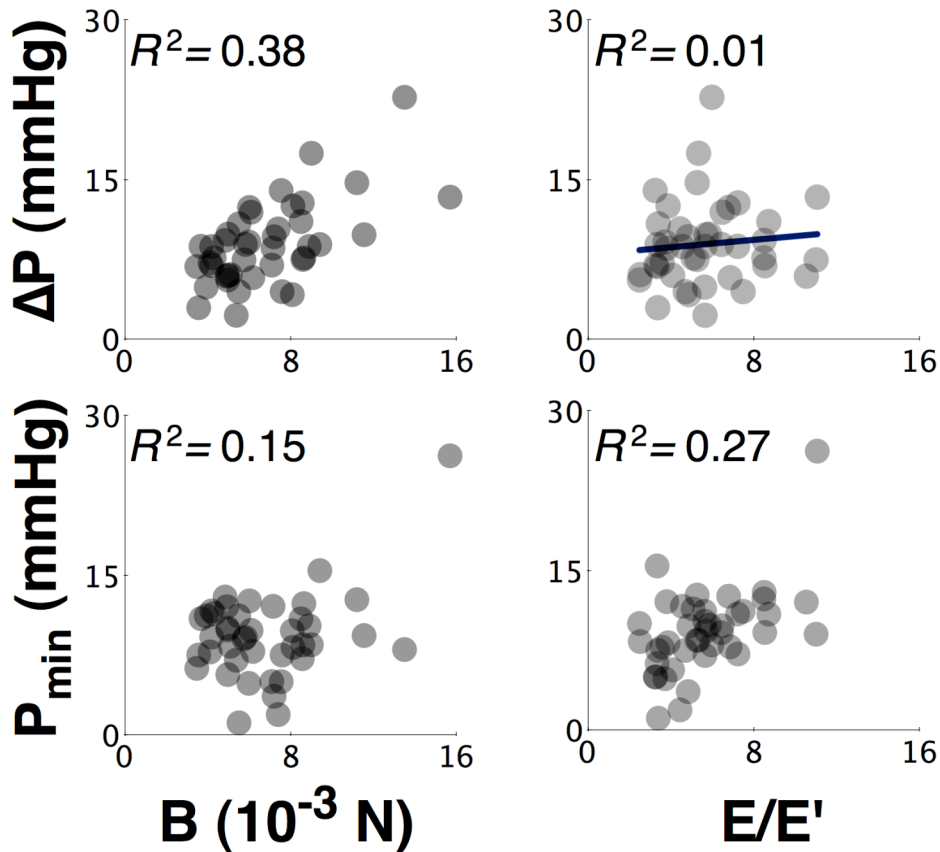


Figure 10.3. Comparison of noninvasive pressure surrogates E/E' and B to a relative pressure measure (ΔP), defined by the pressure difference between end diastole and minimum pressure, and to minimum pressure (P_{\min}). Notice that the correlation between B and ΔP is similar to the correlation between B and EDP shown in Figure 10.2, whereas the correlation between ΔP and E/E' is non-existent. The correlation between E/E' and P_{\min} is modest, but stronger than the correlations between E/E' and ΔP or EDP. See text for details.

and therefore deviations from this assumption will impact the efficacy of both E/E' and B as end diastolic pressure surrogates. In the current study minimum pressure varied between 1 and 26 across 41 subjects, with an average value of 9 ± 4 . Though the values at the extremes were significantly different than the average, the second highest minimum pressure was 15 mmHg, and only 4 subjects had minimum pressure below 5 mmHg. A more extensive analysis of minimum pressure measured in an additional 40 subjects from our simultaneous catheterization

echocardiography database, including subjects with hypertension, similarly finds a minimum pressure variation between 4 and 18 with an average value of 10 ± 3 . Thus, while in a minority of cases minimum pressure may deviate significantly from a population average, in general the assumption of fairly constant minimum pressure is reasonable.

Absolute vs Relative Measures and Minimum Pressure

It is important to note that end-diastolic pressure is an absolute measure, because it is measured and calibrated relative to a nearly constant atmospheric pressure. Doppler velocity measures, like E-waves and A-waves are relative measures however, because they are the derivatives of absolute volume measures. Thus E/E' and B are both relative indexes, while end diastolic pressure is absolute, and in general relative indexes can not accurately be surrogates for absolute measures. Indeed this is why the E/E' and B derivations rely on the assumption of fairly constant minimum pressure.

This may suggest that E/E' and B are more robust surrogates for the pressure difference between minimum pressure and end diastolic pressure, but this is not the case (see Figure 10.3). In fact, E/E' shows a stronger correlation to minimum pressure than to end diastolic pressure or the pressure difference between minimum and end diastole. *B* on the other hand shows a weaker correlation to minimum pressure than to end diastolic pressure. .

Absolute physical constraints, like the constant volume parameters of the heart, can lead to correlations between relative and absolute indexes, especially in extreme cases as is evident in the relationship between high E/E' and elevated EDP when longitudinal motion is impaired and radial expansion is the primary means for accommodating filling volume.

10.5.4 Issue of Constant Mitral Valve Area

In going from Equation 10.3 to 10.4, the assumption of constant mitral valve area was made. However, there are a variety of contributing factors to the variability of mitral valve area over time. Mitral valve leaflets open quickly in early diastole, but the cross sectional area at the leaflet tips decreases as E-wave deceleration occurs. The mitral valve leaflets connect to the mitral annulus, and during filling the annular cross sectional area increases as the slightly saddle shaped annular ring flattens with rise of the annulus and chamber distension. Indeed, previous work has demonstrated the time variation of mitral valve area (1), and therefore an exact determination of E-wave and A-wave stroke volume requires accurate incorporation of mitral valve area as a function of time. However the functional time dependence of mitral valve area is complex and not easily incorporated into routine clinical analysis. Recently we have applied the constant volume parameter of the heart to obtain a time varying expression for mitral valve area in a study of vortex formation in early diastole (5). However, for simplicity it is reasonable to assume a constant average effective mitral valve area. This value will not accurately reflect time-varying stroke volume, but is sufficient for determination of total stroke volume. Furthermore, it is unlikely that any error introduced by this approximation will be greater than the errors associated with the other assumptions applied in the derivation above.

10.6 CONCLUSIONS

We conclude that LIIDF relation-derived B is a better noninvasive estimate of EDP than E/E' , particularly in subjects with normal systolic function (ejection fraction >50%). There are clear limitations, however, to the application of a relative index to the estimation of absolute

indexes. Further work extending the B vs EDP relation to additional clinical subgroups is necessary, including subjects with systolic dysfunction.

10.7 REFERENCES

1. Bowman AW, Frihauf PA, and Kovács SJ. Time-varying effective mitral valve area: prediction and validation using cardiac MRI and Doppler echocardiography in normal subjects. *Am J Physiol Heart Circ Physiol* 287: H1650-1657, 2004.
2. Bowman AW and Kovács SJ. Assessment and consequences of the constant-volume attribute of the four-chambered heart. *Am J Physiol Heart Circ Physiol* 285: H2027-2033, 2003.
3. Caiani EG, Weinert L, Takeuchi M, Veronesi F, Sugeng L, Corsi C, Capderou A, Cerutti S, Vaida P, and Lang RM. Evaluation of alterations on mitral annulus velocities, strain, and strain rates due to abrupt changes in preload elicited by parabolic flight. *J Appl Physiol* 103: 80-87, 2007.
4. Firstenberg MS, Levine BD, Garcia MJ, Greenberg NL, Cardon L, Morehead AJ, Zuckerman J, and Thomas JD. Relationship of echocardiographic indices to pulmonary capillary wedge pressures in healthy volunteers. *J Am Coll Cardiol* 36: 1664-1669, 2000.
5. Ghosh E, Shmuylovich L, and Kovacs SJ. Determination of early diastolic LV vortex formation time (T^*) via the PDF formalism: a kinematic model of filling. *Conf Proc IEEE Eng Med Biol Soc* 2009: 2883-2886, 2009.
6. Hasegawa H, Little WC, Ohno M, Brucks S, Morimoto A, Cheng H-J, and Cheng C-P. Diastolic mitral annular velocity during the development of heart failure. *J Am Coll Cardiol* 41: 1590-1597, 2003.
7. Lavine SJ and Lavine JA. The effect of acute hypertension on left ventricular diastolic pressures in a canine model of left ventricular dysfunction with a preserved ejection fraction and elevated left ventricular filling pressures. *Journal of the American Society of Echocardiography : official publication of the American Society of Echocardiography* 19: 1350-1358, 2006.

8. Lisauskas J, Singh J, Courtois M, and Kovács SJ. The relation of the peak Doppler E-wave to peak mitral annulus velocity ratio to diastolic function. *Ultrasound in medicine & biology* 27: 499-507, 2001.
9. Lisauskas JB, Singh J, Bowman AW, and Kovács SJ. Chamber properties from transmitral flow: prediction of average and passive left ventricular diastolic stiffness. *J Appl Physiol* 91: 154-162, 2001.
10. Nagueh SF, Appleton CP, Gillebert TC, Marino PN, Oh JK, Smiseth OA, Waggoner AD, Flachskampf FA, Pellikka PA, and Evangelista A. Recommendations for the evaluation of left ventricular diastolic function by echocardiography. *Journal of the American Society of Echocardiography : official publication of the American Society of Echocardiography* 22: 107-133, 2009.
11. Nagueh SF, Lakkis NM, Middleton KJ, Spencer WH, Zoghbi WA, and Quiñones MA. Doppler estimation of left ventricular filling pressures in patients with hypertrophic cardiomyopathy. *Circulation* 99: 254-261, 1999.
12. Nagueh SF, Mikati I, Kopelen HA, Middleton KJ, Quiñones MA, and Zoghbi WA. Doppler estimation of left ventricular filling pressure in sinus tachycardia. A new application of tissue doppler imaging. *Circulation* 98: 1644-1650, 1998.
13. Nagueh SF, Sun H, Kopelen HA, Middleton KJ, and Khoury DS. Hemodynamic determinants of the mitral annulus diastolic velocities by tissue Doppler. *J Am Coll Cardiol* 37: 278-285, 2001.
14. Oğuzhan A, Arınç H, Abacı A, and Topsakal R. Preload dependence of Doppler tissue imaging derived indexes of left ventricular diastolic function. ..., 2005.

15. Riordan MM and Kovács SJ. Elucidation of spatially distinct compensatory mechanisms in diastole: radial compensation for impaired longitudinal filling in left ventricular hypertrophy. *J Appl Physiol* 104: 513-520, 2008.
16. Rivas-Gotz C, Manolios M, Thohan V, and Nagueh SF. Impact of left ventricular ejection fraction on estimation of left ventricular filling pressures using tissue Doppler and flow propagation velocity. *Am J Cardiol* 91: 780-784, 2003.
17. Shmuylovich L and Kovács SJ. Load-independent index of diastolic filling: model-based derivation with in vivo validation in control and diastolic dysfunction subjects. *J Appl Physiol* 101: 92-101, 2006.
18. Yamamoto K, Nishimura RA, Chaliki HP, Appleton CP, Holmes DR, and Redfield MM. Determination of left ventricular filling pressure by Doppler echocardiography in patients with coronary artery disease: critical role of left ventricular systolic function. *J Am Coll Cardiol* 30: 1819-1826, 1997.
19. Zile MR, Baicu CF, and Gaasch WH. Diastolic heart failure--abnormalities in active relaxation and passive stiffness of the left ventricle. *N Engl J Med* 350: 1953-1959, 2004.
20. Zile MR and Brutsaert DL. New concepts in diastolic dysfunction and diastolic heart failure: Part I: diagnosis, prognosis, and measurements of diastolic function. *Circulation* 105: 1387-1393, 2002.
21. Zile MR and Brutsaert DL. New concepts in diastolic dysfunction and diastolic heart failure: Part II: causal mechanisms and treatment. *Circulation* 105: 1503-1508, 2002.

CHAPTER 11.

**LOAD INDEPENDENT INDEX OF ISOVOLUMIC PRESSURE DECAY:
MODEL BASED DERIVATION WITH EXPERIMENTAL VALIDATION**

11.1 INTRODUCTION

Diastolic heart failure, characterized by signs and symptoms of heart failure in the face of normal ejection fraction, is an increasing clinical problem that is reaching epidemic proportions (15). Despite numerous advances in echocardiography-based noninvasive assessment of diastolic function, measurement of left-ventricular pressure (LVP) by invasive fluid filled or high-fidelity Millar catheterization, remains the gold standard by which abnormalities in diastolic function are assessed. Diastolic function assessment includes analysis of the isovolumic pressure decay contour, as well as the LVP contour from mitral valve opening to end-diastole. A monoexponential or logistic model pressure decay rate constant (τ , τ_L respectively), and the peak minimum derivative of pressure decay (P'_{MIN}) are traditionally used to characterize isovolumic physiology (14), and both parameters may be easily extracted by plotting pressure in the pressure phase plane $P(t)$ vs. $P'(t)$ (see Chapter 1). Prolonged τ and blunted P'_{MIN} are interpreted clinically as signs of relaxation abnormalities and diastolic dysfunction.

However, isovolumic pressure decay parameters such as τ and P'_{MIN} values have been found to be sensitive to both intrinsic relaxation properties, and extrinsic load (1, 3, 9, 11, 13, 21, 22, 26-28, 33). Indeed, the load-dependence of τ is well established (1, 9, 11, 13, 26, 33). Thus prolonged τ and blunted P'_{MIN} may be due to load alteration alone, and not be reflective of intrinsic chamber properties. Therefore a load-independent index of isovolumic pressure decline that overcomes load-dependent limitations of τ would be advantageous.

Recent work by Chung et al has demonstrated that isovolumic pressure decline is determined in a mathematically precise manner by the interplay of stiffness and damping/relaxation forces (5). The relative contribution of stiffness and relaxation to isovolumic pressure decline is characterized by a stiffness parameter E_k [1/s], and a damping or relaxation

parameter, τ_c [$1/s^2$]. This approach to the isovolumic pressure decay contour is analogous to the kinematic PDF model of transmitral flow described in Chapter 1. These parameters may be extracted from in-vivo isovolumic pressure decay contours by inverting the governing differential equation and applying quantitative techniques. In addition, compared to the monoexponential (τ) and logistic (τ_L) models, the τ_c, E_k model-predicted pressures and pressure derivatives provide a superior fit to the isovolumic pressure decay contour. Though τ and τ_L are typically used to assess chamber relaxation (3, 14, 20, 21), Chung et al's work predicts that relaxation (τ_c) and stiffness (E_k) effects jointly determine the physiology of isovolumic pressure decay. Furthermore, Chung et al showed that τ and τ_L could be algebraically determined from the ratio of τ_c and E_k ($\tau, \tau_L \propto \tau_c/E_k$). Thus stiffness and relaxation effects may be extracted from τ , or stiffness and relaxation may be recombined to yield a lumped isovolumic pressure decay decay constant (τ or τ_L). It is important to note, however, that τ_c and E_k may be combined in various algebraic ways to yield novel lumped isovolumic pressure decay parameters.

While the Chung model successfully unifies the previously unrelated monoexponential and logistic models of isovolumic pressure decay in a parametric limit sense, τ_c and E_k (just like τ and τ_L) are individually load-dependent. We hypothesize that certain algebraic combinations of τ_c and E_k provide a lumped isovolumic pressure decay parameter that is not subject to the load-independence of τ, τ_L, τ_c , and E_k . Guided by the load independent index of diastolic function presented in the Chapter 8, we derive a novel algebraic relation between τ_c and E_k that, unlike $\tau, \tau_L, \tau_c, E_k$, and other indexes of isovolumic pressure decay, is independent of load.

11.2 METHODS

11.2.1 Monoexponential and Logistic Models of Isovolumic Pressure Decay

The monoexponential model of isovolumic pressure decay, first proposed by Weiss (31), assumes that the time derivative of pressure decay is proportional to pressure. The governing differential equation for the monoexponential model is:

$$\tau \frac{dP}{dt} + (P - P_{\infty}) = 0 \quad \text{Equation 11.1}$$

where τ is the monoexponential time-constant of isovolumic pressure decay, and P_{∞} is the pressure asymptote. In Weiss's original formulation P_{∞} was assumed to be 0. A convenient method for determination of τ is to calculate the negative inverse of the slope of the isovolumic pressure decay contour in the pressure phase plane, where $dP(t)/dt$ is plotted against $P(t)$ (7, 26).

While the monoexponential model defines a straight line in the pressure phase plane, the logistic isovolumic pressure decay model generates a curve, and therefore has been used to accommodate nonlinear isovolumic pressure decay phase plane segments (18). The differential equation for the logistic model is

$$\frac{P^2}{P_A} + \tau_L \frac{dP}{dt} + (P - P_B) = 0 \quad \text{Equation 11.2}$$

where τ_L is the logistic time-constant of isovolumic pressure decay, and the pressure asymptote is given by the sum $P_A + P_B$. No simple geometric method for determination of τ_L has been found. Instead, nonlinear fitting algorithms are required to extract τ_L from isovolumic pressure decay contours.

11.2.2 Chung Model of Isovolumic Pressure Decay

In recent work, Chung et al unified the empiric monoexponential and logistic isovolumic pressure decay models with a general model that completely characterizes the wide range of physiologically observed isovolumic pressure decay phase plane trajectories. Based on physiologic-kinematic arguments and published experimental results (3, 10, 16, 17, 20, 24, 27, 30, 32), Chung et al(5) argued that isovolumic pressure decay is governed by the interplay of inertial, stiffness and relaxation forces. The relative values of these forces determine the resulting inertial force, and, by Newton's law, cause small-scale tissue displacements (isovolumic torsion, chamber shape change) (27). Utilizing Laplace's law to transform displacements to pressures, Chung et al proposed the following differential equation to account for isovolumic pressure decay:

$$\frac{d^2P}{dt^2} + \tau_c \frac{dP}{dt} + E_k(P - P_\infty) = 0 \quad \text{Equation 11.3}$$

where τ_c is a relaxation parameter, E_k is a stiffness parameter, and P_∞ is the pressure asymptote.

This equation can be solved in the underdamped regime ($4E_k > \tau_c$) for pressure or for the time derivative of pressure as:

$$P(t) = e^{-t \cdot \frac{\tau_c}{2}} \left[\frac{2\dot{P}_o + P_o \tau_c}{2\omega} \sin(\omega t) + P_o \cos(\omega t) \right] + P_\infty \quad \text{Equation 11.4}$$

$$\frac{dP}{dt}(t) = e^{-t \cdot \frac{\tau_c}{2}} \left[- \left(\frac{\dot{P}_o \tau_c + E_k P_o}{2\omega} \right) \sin(\omega t) + \dot{P}_o \cos(\omega t) \right] \quad \text{Equation 11.5}$$

where P_o is the initial pressure assuming zero pressure asymptote, \dot{P}_o is the initial time

derivative of pressure, and $\omega = \sqrt{E_k - \frac{(\tau_c)^2}{4}}$. The critically damped ($4E_k = \tau_c$) and overdamped

($4E_k < \tau_c$) solutions can be determined by evaluating equations 11.4 and 11.5 at $\omega=0$ (critically

damped) or $\omega=i\beta$ (overdamped) limits. The procedure for extracting E_k , and τ_c from an isovolumic pressure contour, the equivalent of solving the ‘inverse problem of isovolumic pressure decay’, is described below.

11.2.3 Human, in-vivo Hemodynamic Data

Twenty-five datasets were selected from the Cardiovascular Biophysics Laboratory Database of simultaneous micromanometric catheter recorded left ventricular pressure (LVP) and echocardiographic data. The criteria for data selection from the database included: normal sinus rhythm, normal valvular function and no wall motion abnormalities. The group was chosen to be clinically heterogeneous, so as to test the generality of our approach. Thus subjects with low ejection fraction, significantly elevated τ and τ_L , and/or significantly elevated EDP were also included. Patient demographics are presented in Table 11.1. See Chapter 2 for a detailed description of the method by which simultaneous echocardiographic and high-fidelity pressure data is acquired.

11.2.4 Hemodynamic Analysis

Hemodynamic data was analyzed using custom automated Matlab programs (Matlab 6.0; MathWorks, Natick, MA), as described in Chapter 2. For each subject, the time derivatives of pressure, left ventricular end diastolic pressure (LVEDP), mitral valve opening (MVO) time, maximum and minimum pressure and pressure derivatives (P_{MAX} , P_{MIN} , dP/dt_{MIN} , dP/dt_{MAX}) and isovolumic pressure decay contour inflection point were determined by automated Matlab scripts. LVEDP was defined by the LV pressure at the ECG R-wave peak. MVO time was

determined as the time point where the decaying pressure contour is closest to the LVEDP of the subsequent filling beat (4, 12, 19, 22).

Automated τ and τ_L fitting

The pressure phase plane was used to determine τ for each beat in each subject. The least-squares determined slope of the dP/dt vs. P plot over the interval between 5 ms after dP/dt_{Min} , and 5 ms before the estimated MVO time is equal to $-1/\tau$ (7, 14, 26). τ_L was determined for each beat according to the methods described by Matsubara et al (18), using a customized Levenberg-Marquardt algorithm (25). Automated Matlab scripts were used for both τ and τ_L determination.

11.2.5. Automated Kinematic Model Parameter Extraction

General Approach

Kinematic Model parameters τ_c , E_k , P_o , and P'_o , are extracted for each individual beat by applying a Levenberg-Marquardt (LM) Algorithm to the $P'(t)$ data defined by the extracted isovolumic pressure decays contour. The algorithm is described in detail elsewhere (25), but the salient features are described briefly below. The algorithm requires initial guesses for the kinematic parameters and the $P'(t)$ data over the isovolumic pressure decay contour.

Initial Model Parameter Estimation

Initial model parameters are determined by evaluating both Eq. 11.1 and the derivative of Eq. 11.1 at t_o , the time of the inflection point in P' , and at the time of P'_{MIN} ($t_{P\text{MIN}}$).

At t_o , the derivative of Eq. 11.1 simplifies to:

$$\frac{\tau_c}{E_k} = -\frac{(P_o^*)}{P^{**}(t_o)} \quad \text{Equation 11.6}$$

Where P_o^* and $P^{**}(t_o)$ are the values of the first and second pressure derivatives at the start of the already determined isovolumic pressure decay contour.

Similarly, at $t_{P^*_{MIN}}$, Eq. 11.1 simplifies to

$$\frac{\tau_c}{E_k} P_{MIN}^* + P(t_{P^*_{MIN}}) = P_\infty \quad \text{Equation 11.7}$$

Applying Eq. 11.6 and 11.7 provides an expression for P_∞ :

$$P_\infty = -\frac{P_o^*}{P^{**}(t_o)} P_{MIN}^* + P(t_{P^*_{MIN}}) \quad \text{Equation 11.8}$$

Applying Eq. 11.8 and Eq. 11.2 at $t=0$ yields:

$$P_o = P(t_o) + \frac{P_o^*}{P^{**}(t_o)} P_{MIN}^* - P(t_{P^*_{MIN}}) \quad \text{Equation 11.9}$$

Note that $P(t_o)$ is the pressure at the start of the automatically determined IVPD contour.

Eq. 11.1 evaluated at $t = t_o$ can be solved for E_k , in terms of P_o , P_o^* , τ_c/E_k , and $P^{**}()$.

Applying Eq. 11.6 and Eq. 11.9, we may express E_k in terms of already measured parameters:

$$E_k = \frac{[P^{**}(t_o)]^2}{[P_o^*]^2 - P^{**}(t_o) \left(P(t_o) + \frac{P_o^*}{P^{**}(t_o)} P_{MIN}^* - P(t_{P^*_{MIN}}) \right)} \quad \text{Equation 11.10}$$

Finally, from 11.6 and 11.10 we solve for τ_c :

$$\tau_c = -\frac{P^{**}(t_o) P_o^*}{[P_o^*]^2 - P^{**}(t_o) \left(P(t_o) + \frac{P_o^*}{P^{**}(t_o)} P_{MIN}^* - P(t_{P^*_{MIN}}) \right)} \quad \text{Equation 11.11}$$

Beginning with the initial parameter guesses determined from P_o^* and Eq. 11.9-11, the LM algorithm minimizes χ^2 by iterating through parameter space, where χ^2 is defined by

$\Sigma(\Delta P)/\sigma$, with ΔP defined by the error between model predicted and measured $P'(t)$ along the isovolumic pressure decay contour, and σ defined as the error in measured $P'(t)$. Iteration ends when subsequent χ^2 values change by less than a predetermined threshold value. Upon completion, the root mean square error (RMSE) between model-predicted $P'(t)$ and measured $P'(t)$ is calculated using the LM-determined best fit kinematic parameters.

Inclusion Criteria For Noisy Data

The large size of the dataset for each subject, which always includes spurious (noisy) data due to ectopy, patient cough, motion, etc, justified an automated screening procedure to exclude nonphysiologic data. The advantages of such an approach making raw data analysis observer independent and hence more robust. We demonstrate the difference between ‘clean’ and of ‘noisy’ data in Figure 11.1.

The top panel of Figure 11.1 shows typical continuous LVP and AoP data from an individual subject. Two isovolumic pressure decay contours from separate beats are highlighted. For each isovolumic pressure decay contour both pressure (P) vs. time (t) and dP/dt vs. time is plotted. Notice that the P vs. t plot for both beats looks smooth, while the dP/dt vs. t plot for the red beat on the right is noisier than the dP/dt vs. t plot for the green beat on the left.

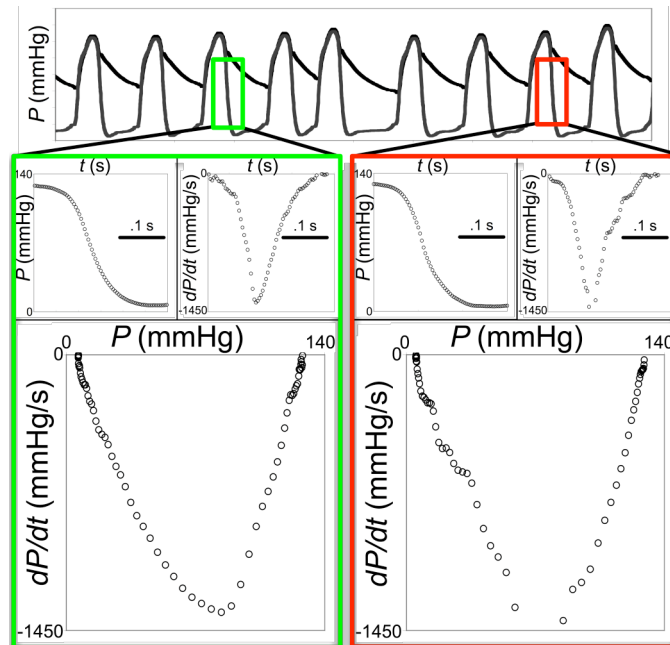


Figure 11.1 Comparison of ‘clean’ (left) and ‘noisy’ (right) left ventricular pressure data acquired in one subject. See text for details.

Indeed the root mean square error between the model fit to the dP/dt contour and the raw data is 9.24 mmHg/s for the beat on the left, and 69.0 mmHg/s for the beat on the right. At the bottom of the figure the phase-plane plot, where dP/dt is plotted vs. P , is shown for both beats. The phase plane plot illustrates in a visually dramatic manner that the beat on the right has significantly more noise than the beat on the left.

An automated approach for data selection was accomplished by determining the root mean square error (RMSE) between the model fit dP/dt and the raw dP/dt data for all beats for a given subject. As demonstrated in Figure 11.1, isovolumic pressure decay contours which are nonphysiologic and noisy generate high dP/dt RMSE values compared to acceptable physiologic dP/dt data. Accordingly, we discard beats having the largest 50th percentile of RMSE values. This approach ensures that only physiologic (smooth) data are included in the final analysis, and provides the additional advantage of being automated, thereby minimizing observer bias in beat selection.

11.2.6 The Load Independent Index of Isovolumic Pressure Decay

Derivation of the Load Independent Index of Isovolumic Pressure Decay

In Chapter 8 and previous work(29) we have derived and validated a load-independent index of diastolic function. Because the governing differential equations for early rapid filling and isovolumic pressure decay are similar, we approach the derivation of the load independent index of isovolumic pressure decay in a manner analogous to the load independent index of diastolic function derivation.

While individual isovolumic pressure decay contours vary as a result of load perturbations, Eq. 11.3 remains valid, because the governing differential equation is obeyed

independent of load. We consider this equation at the time of minimum dP/dt . At this time the second derivative term vanishes, and Eq. 11.3 becomes:

$$\tau_c \frac{dP}{dt} \Big|_{Min} = -E_k (P(t_{dP/dt_{Min}}) - P_\infty) \quad 11.12$$

Eq. 11.12 is a tautology, and is therefore true for any isovolumic pressure decay contour. Indeed, plots of $\tau_c(dP/dt_{MIN})$ vs. $E_k(P(t_{dP/dt_{MIN}})-P_\infty)$ for subjects from the current study are in close agreement with the line of unity (Figure 11.2).

It is helpful here to consider the dP/dt vs. t contour. A plot of dP/dt vs. t defined by Eq. 11.5 would yield an inverted damped sine wave. Isovolumic relaxation typically ends near the inflection point of the dP/dt vs. t downslope, but the model may be extended to the point where dP/dt_{MIN} crosses zero. This time point defines the Chung model-based maximum pressure value, and we therefore call

this value P_{MAX}^* . The time at which P_{MAX}^* occurs can be found by solving for t in Eq. 11.5 when $dP/dt=0$:

$$t_{P_{MAX}^*} = \frac{1}{\omega} \arctan \left(\frac{\omega P_o^{\ll}}{\frac{P_o^{\ll}}{2} \tau_c + E_k P_o} \right) \quad 11.13$$

Evaluating $P(t)$ in Eq. 11.4 at the time found in Eq. 11.13 yields P_{MAX}^* .

Because the time between the model predicted maximum in pressure and the model

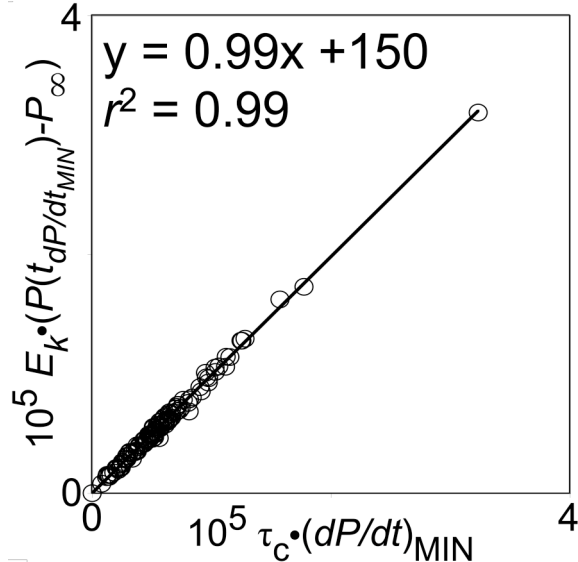


Figure 11.2. Plot of the Chung model predicted tautology (Eq. 5.12) for all beats from all subjects in the current study. Because the values of dP/dt_{MIN} and $P(t_{dP/dt_{MIN}})$ are determined directly from clinical data, the proximity of the relationship to unity demonstrates the robustness of the Chung model of isovolumic pressure decay.

predicted pressure derivative minimum is short relative to the time scale of isovolumic pressure decay, the pressure decay from maximum is nearly linear (Figure 11.3).

The linear behavior observed in Figure 11.3 suggests that P_{MAX}^* may be linearly approximated as $P(t_{dP/dt_{MIN}})$:

$$P(t_{dP/dt_{MIN}}) = \gamma \cdot (P_{MAX}^*) + \beta \quad \text{Equation 11.14}$$

However, because any individual beat may have a different rate of pressure decay, the slope γ is not expected to be the same constant for all subjects and for all beats in a given subject. In fact, the effective slope of pressure decay from P_{MAX}^* can vary, and the value of γ is expected to be akin to an ensemble average over many beats. Indeed, across all subjects and all beats (2671 beats in total), a linear relationship between $P(t_{dP/dt_{MIN}})$ and P_{MAX}^* is observed (Figure 11.4).

Thus we may apply Eq. 11.14 in Eq. 11.6 to obtain the final expression:

$$E_k(P_{MAX}^* - P_\infty) = M_{LIIIVPD} \left(\tau_c \frac{dP}{dt} \Big|_{Min} \right) + B_{LIIIVPD} \quad \text{Equation 11.15}$$

It is important to note that each individual isovolumic pressure decay contour has unique values for $E_k(P_{MAX}^* - P_\infty)$ and $\tau_c \cdot (dP/dt_{MIN})$. Thus each isovolumic pressure decay contour defines a single point in the $E_k(P_{MAX}^* - P_\infty)$ vs. $\tau_c \cdot (dP/dt_{MIN})$ plane, and a collection of isovolumic

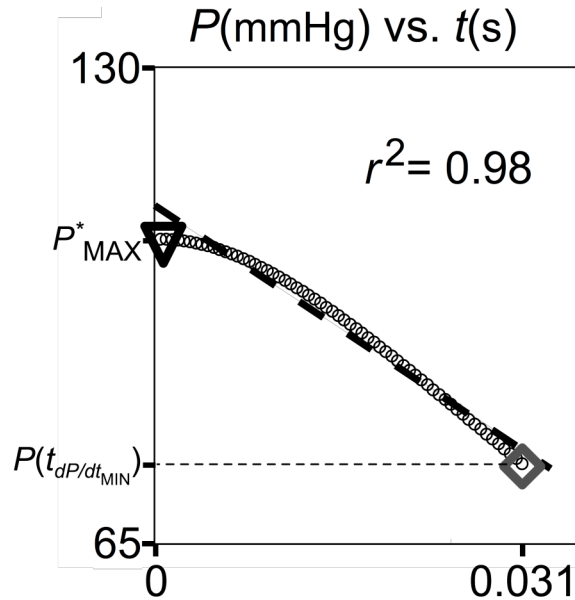


Figure 11.3 We plot the model-predicted pressure contour between the P_{MAX}^* and $P(t_{dP/dt_{MIN}})$ for subject 18 in the current study. Though the relationship is slightly curvilinear, the function over the interval is very well approximated linearly, as indicated by the linear r^2 value being near 1.00. This result justifies the derivation presented in the text (See text for details)

pressure decay contours define the regression implied by Equation 11.15. The linear relationship between $E_k \cdot (P_{MAX}^* - P_\infty)$ and $\tau_c \cdot (dP/dt_{MIN})$ is predicted to be load-independent because it is derived from equations and approximations that are general and load-independent. Thus, while τ_c , E_k , P_∞ , P_{MAX}^* , and dP/dt_{MIN} may change with load, the slope $M_{LIIIVPD}$ is predicted to remain constant in the face of load variation, and thus is the predicted load independent index of isovolumic pressure decay.

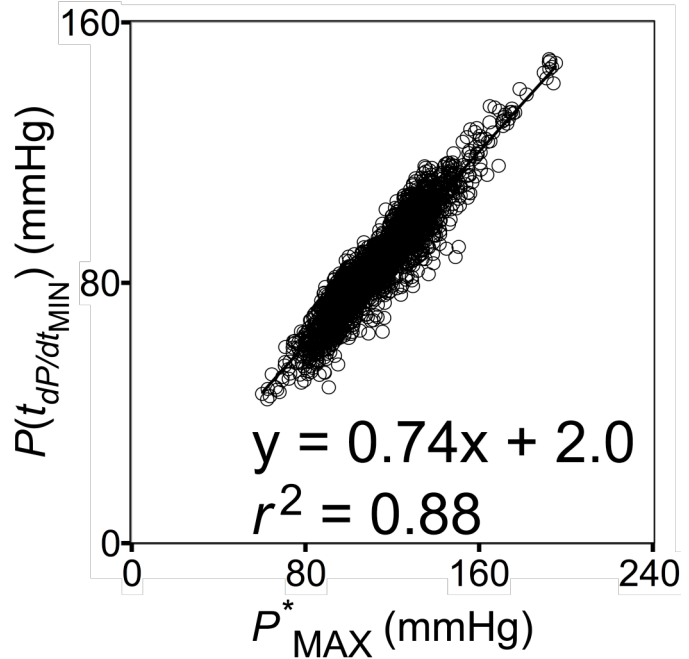


Figure 11.4. Data from all subjects and all beats in current study. This plot validates the claim that relating $P(t_{dP/dt_{MIN}})$ to P_{MAX}^* in a linear fashion is valid. Though the r^2 value is high in the correlation shown above, the plot is consistent with the notion that γ has a distribution of values. See text for details.

If all beats in a particular subject possessed a constant γ from Eq. 11.14, then $M_{LIIIVPD} = 1/\gamma$. However, the values for γ are distributed, and therefore vary enough to preclude one from calculating $M_{LIIIVPD}$ directly from γ . The value of $1/\gamma = 1.35$ does provide interesting insight however, because it provides an average estimate for $M_{LIIIVPD}$. Interestingly, beats whose IVPD contours obey critically damped kinematics lie on a line with slope $e/2 = 1.36$ in the $E_k \cdot (P_{MAX}^* - P_\infty)$ vs. $\tau_c \cdot (dP/dt_{MIN})$ plane. The critically damped regime represents a transition between overdamped (straight phase plane, τ -like isovolumic pressure decay) and underdamped (curved phase plane, τ_L -like isovolumic pressure decay) physiology, and therefore it is quite interesting that the average $M_{LIIIVPD}$ predicted from $1/\gamma$ is consistent with the critically damped regime. This

transition point is analogous to the transition between overdamped and underdamped E-wave kinematics derived in Chapter 8.

Automated Determination of $M_{LIIIVPD}$

The load-independent index of isovolumic pressure decay, $M_{LIIIVPD}$, is determined by analysis of a set of load-varying isovolumic pressure decay contours from one subject. In Figure 11.5 the steps for analyzing one IVPD contour to yield a single point in the plot of $E_k \cdot (P_{MAX}^* - P_\infty)$ vs. $\tau_c \cdot (dP/dt)_{MIN}$ are summarized. First, utilizing the methods presented above, the Chung

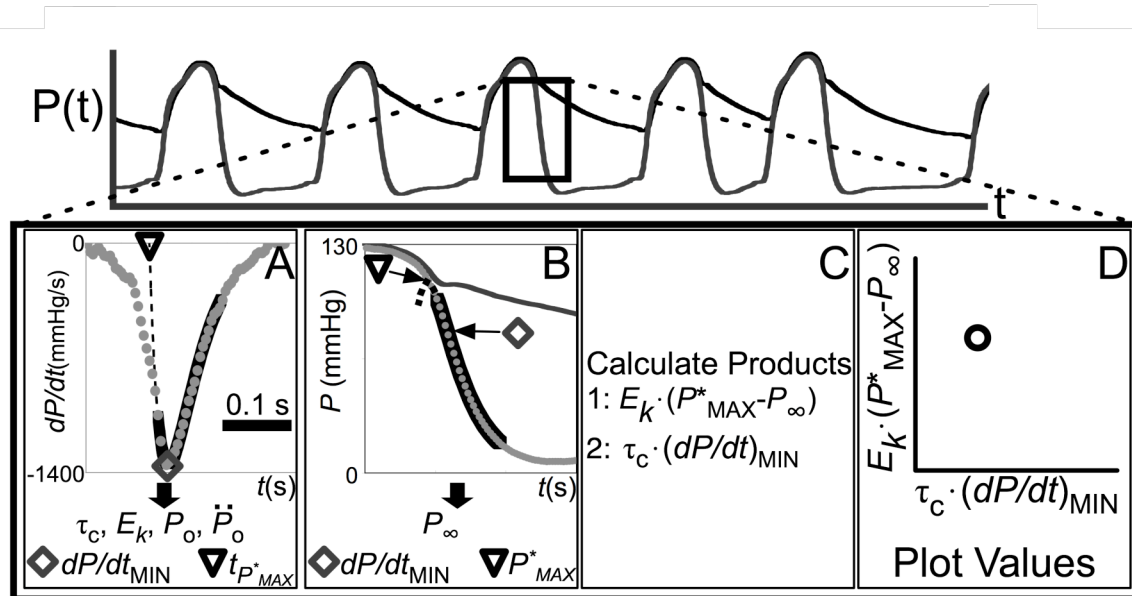


Figure 11.5 Summary of the method by which an individual IVPD contour generates a point in the $E_k(P_{MAX}^* - P_\infty)$ vs. $\tau_c(dP/dt)_{MIN}$ plane. A) IVPD contour in the dP/dt vs. t plane. IVPD data is fit to Chung IVPD model (5) by the Levenberg-Marquardt algorithm generating τ_c , E_k , P_o , and \dot{P}_o . These values are used in Eq. 11.13 to determine t_{p^*MAX} , the time when model-predicted $dP/dt=0$. B) Data in the P vs. t plane, both LV pressure and aortic pressures are shown. P_∞ is determined by minimizing the root mean square error between the Eq. 4 determined pressure and the raw data. The maximum model predicted pressure, occurring before aortic valve closure, is calculated by using t_{p^*MAX} in Eq. 4. C) With parameters determined, $E_k(P_{MAX}^* - P_\infty)$ and $\tau_c(dP/dt)_{MIN}$ are calculated. Each individual isovolumic pressure decay contour generates a single point at $[\tau_c(dP/dt)_{MIN}, E_k(P_{MAX}^* - P_\infty)]$ coordinate. D) Values plotted in the $E_k(P_{MAX}^* - P_\infty)$ vs. $\tau_c(dP/dt)_{MIN}$ plane. The steps in panels A-D are repeated for a set of isovolumic pressure decay contours for each subject, thus generating points in the $E_k(P_{MAX}^* - P_\infty)$ vs. $\tau_c(dP/dt)_{MIN}$ plane. See text for details.

isovolumic pressure decay model parameters are extracted from the isovolumic pressure decay contour of interest. This process yields unique τ_c , E_k , P_∞ , P_0 and \dot{P}_0 parameter values for each beat. If the RMSE between model prediction and clinical data is within the appropriate threshold, then P_{MAX}^* is determined for the isovolumic pressure decay contour of interest via Eq. 11.3 by using the calculated $t_{P_{MAX}}^*$ in Eq. 11.4. Subsequently dP/dt_{MIN} is determined directly from the data. Finally, the products $E_k \cdot (P_{MAX}^* - P_\infty)$ and $\tau_c \cdot (dP/dt_{MIN})$ are calculated for each beat, and these values are plotted in the $E_k \cdot (P_{MAX}^* - P_\infty)$ vs. $\tau_c \cdot (dP/dt_{MIN})$ plane.

These steps are repeated for every isovolumic pressure decay contour for every subject, thus yielding a set of points in the plot of $E_k \cdot (P_{MAX}^* - P_\infty)$ vs. $\tau_c \cdot (dP/dt_{MIN})$. In accordance with the predicted linear relationship in Eq. 11.15, a linear regression between all points in the $E_k \cdot (P_{MAX}^* - P_\infty)$ vs. $\tau_c \cdot (dP/dt_{MIN})$ plane yields the slope $M_{LIIIVPD}$, intercept $B_{LIIIVPD}$ and Pearson correlation coefficient r^2 . As the isovolumic pressure decay contour shape varies from beat to beat, the location of the point inscribed in the $E_k \cdot (P_{MAX}^* - P_\infty)$ vs. $\tau_c \cdot (dP/dt_{MIN})$ plane varies as well.

However, Eq. 11.15 predicts that for a given subject all beats should fall on the same linear regression line, with constant slope $M_{LIIIVPD}$. Thus the slope $M_{LIIIVPD}$ is the predicted load independent index of

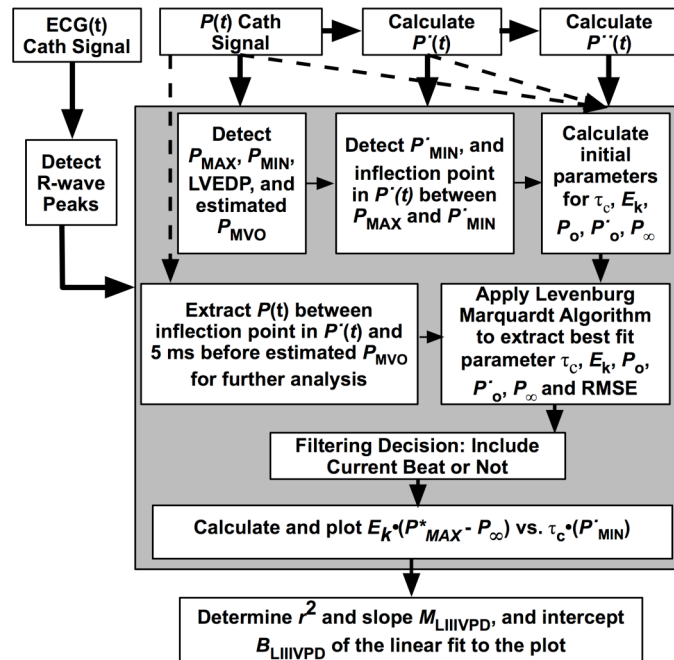


Figure 11.6. The automated process by which hemodynamic data analysis is performed is shown. The gray area contains steps that are repeated for each heart cycle, defined by successive R-wave peaks. See text for

isovolumic pressure decay. Figure 11.6 summarizes the entire automated process for hemodynamic analysis and $M_{LIIIVPD}$ determination.

Table 11.1. *Subject Demographic*

<i>Subject</i>	HR, beats/min	EDP, mmHg	EF, %	Age, yr
1	50	22	73	67
2	75	36	20	55
3	66	27	84	50
4	89	22	55	59
5	73	16	82	52
6	60	26	62	64
7	63	23	78	54
8	77	39	75	64
9	72	26	82	56
10	99	19	83	47
11	65	31	70	66
12	70	24	52	57
13	51	18	64	62
14	66	18	79	60
15	86	23	73	37
16	67	21	65	72
17	59	19	72	74
18	57	21	80	60
19	60	19	36	56
20	80	16	84	38
21	65	24	78	52
22	63	32	70	55
23	56	23	80	67
24	60	17	80	62
25	75	37	55	60

Heart rate (HR), left ventricular end-diastolic pressure (EDP), ejection fraction (EF), and age for the 25 subjects in the current study.

Validation of $M_{LIIIVPD}$

For each of the 25 subjects in the current study, $M_{LIIIVPD}$, $B_{LIIIVPD}$ and r^2 were calculated as described above via a custom Matlab script. Load independence of $M_{LIIIVPD}$ was assessed by the proximity of r^2 to 1. A low r^2 value would imply that $M_{LIIIVPD}$ is load-dependent.

To ensure that the value of $M_{LIIIVPD}$ reflects clinical and physiological information, individual $M_{LIIIVPD}$ and $B_{LIIIVPD}$ values for each subject were correlated with average EF, τ , τ_L , and dP/dt_{MIN} values from each subject.

11.3 RESULTS

11.3.1 Application of Chung Isovolumic Pressure Decay Model

An average of 284 beats were fit to the Chung IVPD model for each subject. The average RMSE (before exclusion of any beats) between the model-fit and the dP/dt vs. t contour was 19 mmHg/s (average 2% deviation between model and measured contour). Non-physiologic beats with high RMSE were excluded. Specifically, for each subject, beats with RMSE above the subject specific RMSE average value were excluded from further analysis, resulting in the

Table 11.2. *Hemodynamic Values*

Subject	τ , ms		τ_L , ms		dP/dt_{MIN} , mmHg/s		P_{MAX} , mmHg		n
	Mean (SD)	Range	Mean (SD)	Range	Mean (SD)	Range	Mean (SD)	Range	
1	57 (3)	15	45 (1)	7	-1501 (76)	452	149 (8)	51	58
2	147 (22)	127	41 (5)	27	-774 (39)	262	115 (6)	27	179
3	50 (4)	16	36 (3)	14	-1368 (97)	424	116 (10)	46	46
4	66 (4)	17	35 (1)	6	-1675 (75)	388	169 (7)	39	72
5	44 (3)	24	36 (1)	10	-1789 (86)	504	137 (7)	37	214
6	79 (9)	37	28 (3)	13	-1503 (109)	727	163 (9)	51	57
7	66 (35)	231	28 (6)	39	-1345 (230)	1072	125 (11)	61	46
8	72 (11)	62	23 (3)	15	-1662 (332)	1225	209 (39)	155	63
9	51 (7)	63	23 (2)	17	-1761 (169)	1179	170 (14)	98	121
10	33 (4)	40	34 (2)	15	-1775 (174)	1138	119 (8)	45	137
11	52 (7)	51	26 (2)	11	-1875 (240)	1335	181 (19)	98	54
12	76 (6)	39	28 (2)	10	-1308 (61)	345	143 (6)	49	100
13	58 (3)	19	30 (1)	7	-1749 (54)	386	168 (5)	49	115
14	61 (4)	27	30 (1)	8	-1249 (61)	430	119 (6)	27	102
15	67 (5)	42	29 (2)	16	-1167 (56)	480	110 (5)	23	183
16	65 (8)	54	29 (3)	20	-1433 (128)	853	144 (10)	67	74
17	72 (4)	21	26 (2)	12	-1416 (41)	275	143 (5)	24	96
18	57 (3)	22	30 (2)	16	-1440 (62)	637	133 (6)	40	175
19	113 (21)	113	28 (5)	26	-718 (25)	115	99 (2)	8	66
20	59 (3)	16	22 (1)	6	-1622 (94)	608	144 (9)	46	86
21	67 (16)	149	24 (4)	36	-1322 (197)	1152	130 (10)	68	131
22	64 (10)	75	14 (3)	16	-1157 (109)	626	110 (11)	55	161
23	65 (8)	36	22 (2)	12	-1768 (113)	788	175 (9)	77	94
24	59 (7)	55	29 (2)	15	-1194 (156)	764	124 (10)	57	118
25	114 (24)	179	27 (4)	26	-1188 (65)	675	156 (7)	57	122

Values of mean (SD) and the range of variation between minimum and maximum values are reported across all subjects for time constant (τ), logistic model time constant (τ_L), minimum first derivative of pressure (dP/dt_{MIN}), and measured maximum pressure (P_{MAX}). The number of beats (n) analyzed in each subject is also presented. Large values for range are the result of inclusion of premature ventricular contractions and Valsalva beats.

analysis of an average of 107 beats per subject. Across all subjects the average values and standard deviation for τ_c , E_k , P_o , $\overset{\ll}{P}_o$, and P_∞ were 89 1/s, 1500 1/s², 105 mmHg, -1040 mmHg/s, and 1.70 mmHg respectively. The number of beats included in analysis, as well as the P_{MAX} , dP/dt_{MIN} , τ , and τ_L average values, standard deviations, and ranges for each subject are shown in Table 11.1.

11.3.2 Physiological Variation in Isovolumic Pressure Decay Parameters

The isovolumic pressure decay contour in the pressure phase plane varied significantly with load, and therefore within any given subject, significant beat-to-beat variation was observed in τ , τ_L , P_{MAX} , and dP/dt_{MIN} . Significant variation was seen primarily in beats following PVCs or Valsalva maneuvers. Indeed, the large range of values presented in Table 11.2 reflect the significant hemodynamic variation between perturbed (PVC and Valsalva) and normal physiology. As reflected by the Table 11.2 standard deviations, steady-state hemodynamic variation was also significant in the subjects studied.

11.3.3 Determination of Predicted Load Independence

Despite the wide variation in τ , τ_L and dP/dt_{MIN} within each subject, and in accordance with the prediction (Eq. 11.15), the linear least-squares regression between $E_k \cdot (P_{MAX}^* - P_\infty)$ and $\tau_c \cdot (dP/dt_{MIN})$ yielded strong linear relationships for each subject. Figure 11.7 shows the $E_k \cdot (P_{MAX}^* - P_\infty)$ and $\tau_c \cdot (dP/dt_{MIN})$ plot for subject 5.

Below the plot, the isovolumic pressure decay portion of the phase plane is shown for three individual beats acquired in the subject. The leftmost contour shows a post PVC beat having the highest τ value among all heart cycles. The middle contour is a beat with the median τ value, and the rightmost contour is the beat with minimum τ value. The red curve shows the

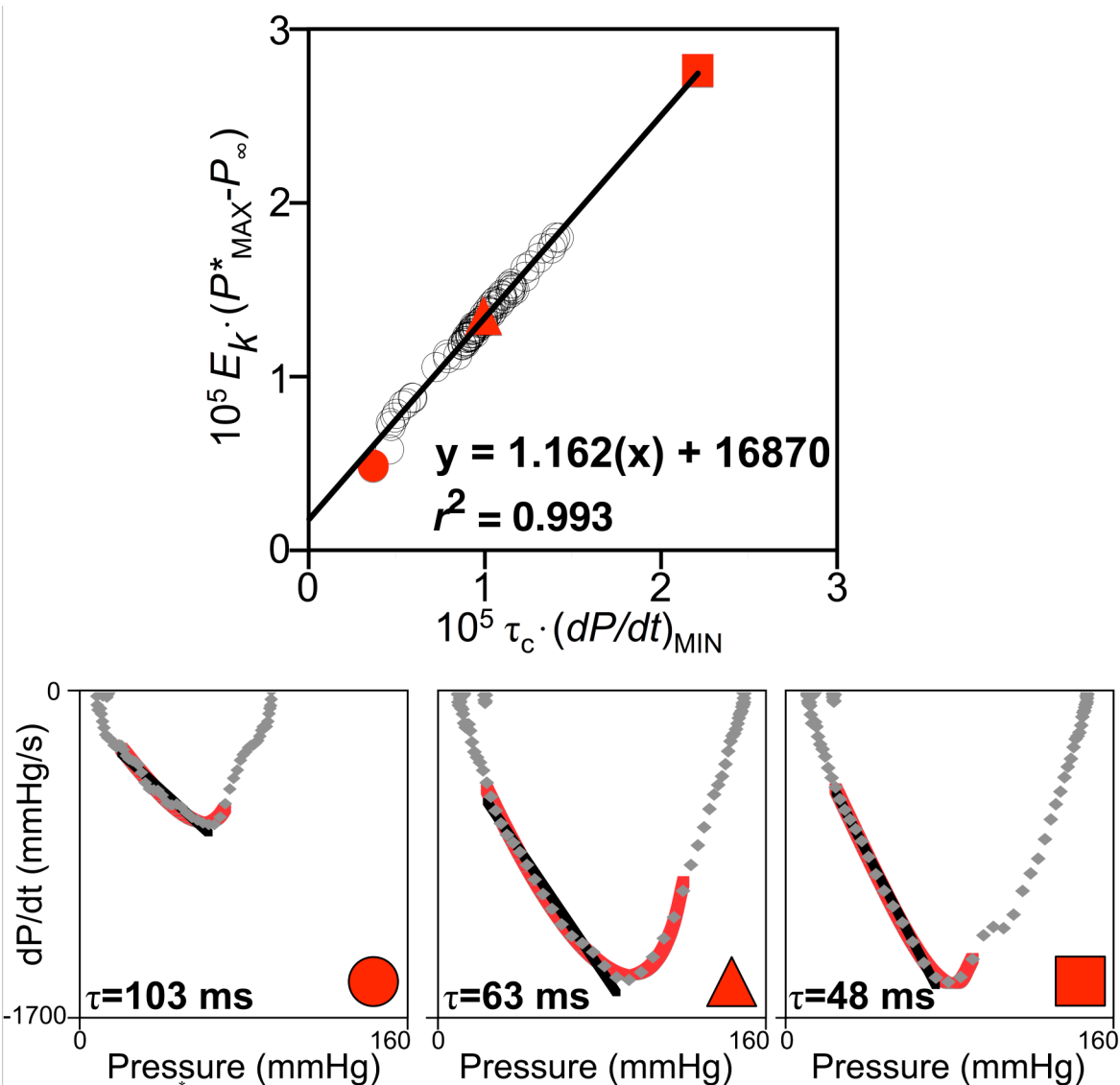


Figure 11.7. The $E_k(P_{MAX}^* - P_{\infty})$ vs. $\tau_c \cdot (dP/dt)_{MIN}$ plot for 74 beats in subject 5. Beats with highest, lowest and median τ values are detailed in the three lower panels, where the phase plane contour, as well as the linear τ fit (black) and Chung model (τ_c, E_k) fit (red) are shown. Note that each point in the top panel corresponds to one specific cardiac cycle, and the location of the beats shown in the bottom three panels are highlighted in the top plot with the circle, triangle and square labels. Despite a large degree of τ variation, the $E_k(P_{MAX}^* - P_{\infty})$ vs. $\tau_c \cdot (dP/dt)_{MIN}$ relation remains highly linear ($r^2=0.993$), with a constant M_{LHVDP} value of 1.162. See text for details.

Chung isovolumic pressure decay model fit to the phase plane contour, while the black line shows the linear τ fit. Notice that each individual beat inscribes a particular point in the

$E_k(P_{MAX}^* - P_\infty)$ vs. $\tau_c \cdot (dP/dt_{MIN})$ plot, and

these individual beats are co-linear with

the rest of the 71 beats measured in this

particular subject. Thus despite

significant changes in τ between these

three individual beats, the $M_{LIIIVPD}$

defined by these beats remains the same,

and is consistent with the $M_{LIIIVPD}$

defined by all the analyzed beats in this

subject.

$M_{LIIIVPD}$, $B_{LIIIVPD}$ and r^2 values for

each subject are presented in Table 11.3.

All subjects showed highly linear

$E_k(P_{MAX}^* - P_\infty)$ vs. $\tau_c \cdot (dP/dt_{MIN})$ relations,

with the average r^2 value equal to 0.993.

Across all subjects, $M_{LIIIVPD}$ varied

between 1.06 and 1.169, and $B_{LIIIVPD}$ varied between 10620 mmHg/s and 45990 mmHg/s. As a

further test of the consequences of the automated beat selection process, in 14 subjects whose

data were ‘clean’ in the physiologic sense, utilizing all beats (including the excluded high RMSE

beats) in the calculation of $M_{LIIIVPD}$ changed the value of $M_{LIIIVPD}$ by less than 5%. Thus, for

physiologically ‘clean’ data the beat exclusion criteria has a minimal impact on $M_{LIIIVPD}$. To

Table 11.3. *LIIIVPD Analysis*

<i>Subject</i>	$M_{LIIIVPD}$	$B_{LIIIVPD}$, mmHg/s	r^2	n
1	1.112	23008	0.994	58
2	1.006	10621	0.998	179
3	1.100	24294	0.993	46
4	1.092	23131	0.996	72
5	1.162	22959	0.989	214
6	1.081	15546	0.997	57
7	1.123	10635	0.998	46
8	1.150	19613	0.988	63
9	1.169	17183	0.990	121
10	1.145	45994	0.970	137
11	1.158	21095	0.993	54
12	1.099	17791	0.987	100
13	1.119	24760	0.997	115
14	1.105	18147	0.997	102
15	1.089	18902	0.996	183
16	1.162	16872	0.993	74
17	1.088	19447	0.997	96
18	1.091	25004	0.996	175
19	1.023	10699	0.994	66
20	1.107	23948	0.990	86
21	1.135	17261	0.990	131
22	1.069	23358	0.993	161
23	1.147	21339	0.989	94
24	1.120	16683	0.997	118
25	1.023	18559	0.994	122

The slopes, intercepts, and Pearson correlation coefficients, ($M_{LIIIVPD}$, $B_{LIIIVPD}$ and r^2) of each subjects’ $E_k(P_{MAX}^* - P_\infty)$ vs. $\tau_c \cdot (dP/dt_{MIN})$ relation are presented, where E_k is stiffness, P_∞ is pressure asymptote, and τ_c is relaxation. LIIIVPD, load-independent index of isovolumic pressure decline; n , number of beats across which the linear regressions are performed.

assure consistency in the analysis, the same RMSE-based beat exclusion criteria were applied to all subjects.

11.3.4 Clinical Correlations with $M_{LIIIVPD}$

$M_{LIIIVPD}$ values in each subject showed strong linear correlation with average EF ($r^2=0.52$), τ ($r^2=0.65$), τ_L ($r^2=0.50$), and dP/dt_{MIN} ($r^2=0.63$) values from each subject. High $M_{LIIIVPD}$ values were associated with lower τ and τ_L values, higher values for EF and more negative dP/dt_{MIN} values (see Figure 11.8). The intercept $B_{LIIIVPD}$ values from each subject did

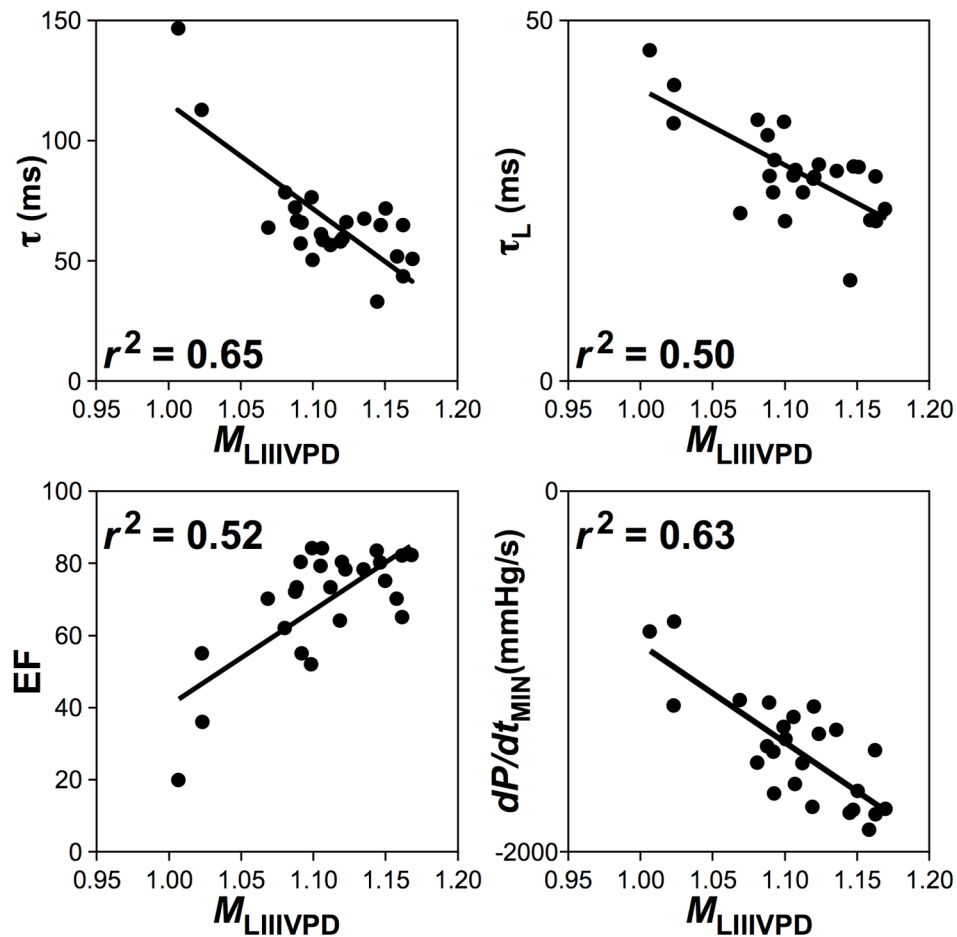


Figure 11.8. Correlation of $M_{LIIIVPD}$ with physiologic parameters. Each point in each panel represents one subject's $M_{LIIIVPD}$ value and corresponding EF, τ , τ_L , or dP/dt_{MIN} value. See text for details.

not show significant correlation to average EF ($r^2=0.22$), τ ($r^2=0.38$), τ_L ($r^2=0.55$), or dP/dt_{MIN} ($r^2=0.31$) values.

11.4 DISCUSSION

The time course of isovolumic pressure decline has been shown to depend on both intrinsic ventricular parameters and extrinsic load effects (2, 3, 9, 11, 13, 20, 24, 26, 30, 31, 33), and therefore, despite some initial claims of load-independence, both τ and τ_L have proven to be load-dependent. Previously, isovolumic pressure decay was fit by assumed and disparate logistic (τ_L) and monoexponential (τ) functions that were not derived from kinematic considerations.

Chung et al (5) proposed a novel kinematic model of isovolumic pressure decay, and demonstrated how overdamped and underdamped limits the mode corresponded with τ and τ_L generated fits to pressure data. However, the Chung model parameters E_k and τ_c are individually load-dependent, and therefore the parameters alone do not solve the ‘load independent index of isovolumic pressure decay’ problem. To solve this problem, we derive an algebraic expression that makes use of τ_c and E_k values from multiple beats in the same subject. We show that within the varying beat-to-beat pressure contours, a conserved (i.e. load-independent) relationship exists, namely the slope, of the $E_k \cdot (P_{\text{MAX}}^* - P_{\infty})$ vs $\tau_c \cdot (dP/dt_{\text{MIN}})$ relation, called M_{LIIIVPD} . Furthermore, we demonstrate clinical relevance by determining correlations between M_{LIIIVPD} and conventional parameters in a group of heterogenous subjects with varying degrees of systolic and diastolic dysfunction.

11.4.1. Known Load-Dependence of τ and τ_L

In the initial studies describing τ , investigators noted insignificant changes in τ associated with volume loading or HR variation, and concluded τ to be independent of systolic stress and end-systolic fiber length (8, 31). However, these initial studies were not performed in the intact heart, and later studies in both anesthetized and conscious dogs found τ to be significantly dependent on systolic load (9, 13, 26). In addition, τ was shown to be dependent on volume loading and end-diastolic pressure (26), pharmacologically generated increases in contractility and load (9, 13), and the timing of acute afterload perturbations (11). τ_L was suggested as an alternative to τ , and studies in human heart failure subjects, as well as in isolated canine hearts suggest that τ_L is less load-dependent than τ (21, 28). However application of τ_L may not be appropriate when the pressure phase plane trajectory is highly linear (5). Furthermore, a study in patients undergoing cardiac surgery found that load-variation due to leg lift significantly affected both τ and τ_L in a select group of patients (6).

11.4.2 Physical Interpretation of M_{LHIVPD}

The Chung IVPD model utilizes a linear damped harmonic oscillator as the kinematic analogue for chamber behavior during isovolumic pressure decay (5). The rapid decay of wall stress and associated strain directly generates pressure decay through Laplace's law, and therefore Eq. 11.3 is written in terms of pressure and pressure derivatives. However, if we consider isovolumic pressure decay kinematically and in terms of displacements, Eq. 11.3 becomes a balance of inertial, resistive, and elastic forces. Isovolumic pressure decay is governed by an elastic, mechanical recoil component that drives down the pressure, as well as a

viscoelastic resistive component related to crossbridge uncoupling that modulates pressure decay. These elastic and resistive components of isovolumic pressure decay have peak forces associated with them and, because the Chung IVPD model is linear, increased elastic (recoil) forces will be accompanied by increased peak resistive (viscoelastic) forces. The load independent index of isovolumic pressure decay is the slope of the peak elastic force driving pressure decay vs. peak resistive force opposing pressure decay. Thus Eq. 11.15 predicts that for an individual subject, peak driving force and peak resistive force maintain a constant relation, with constant slope $M_{LIIIVDP}$, in the face of load variation. As load changes, the level of peak elastic force required to drive down the pressure during isovolumic relaxation also changes. A chamber where increased peak elastic

(recoil) forces are accompanied by relatively large increases in peak resistive forces will have a low $M_{LIIIVDP}$ value, whereas increased elastic peak forces accompanied by relatively small increases in peak resistive forces will have a higher $M_{LIIIVDP}$ value. Thus $M_{LIIIVDP}$ is an index of isovolumic relaxation that is related to the efficiency with which the relaxing ventricle adapts to changes in load.

Figure 11.9 provides a theoretical plot of the peak driving

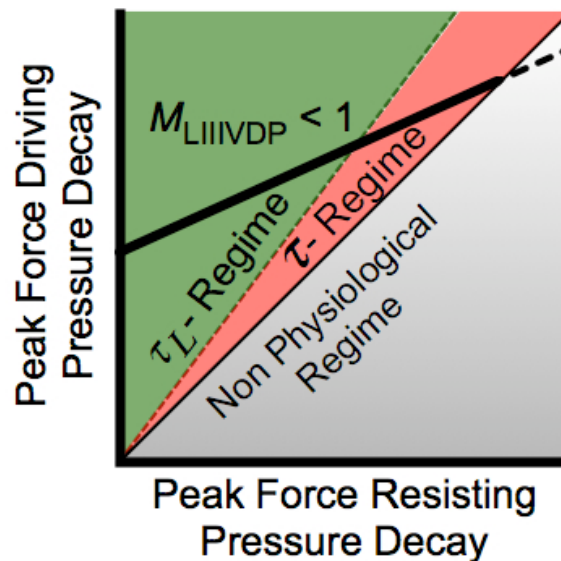


Figure 11.9. A theoretical plot of peak force driving pressure decay vs. peak force opposing pressure decay, using normalized units. As in Figure 11.5, individual beats from a particular subject will reside as points in the plot. The lower right corner of the plot is the non-physiologic regime, because then resistive forces exceed driving forces and pressure decay can not occur. Furthermore, notice that a subject with $M_{LIIIVDP} < 1$ has a limited regime over which load can vary, while subjects with $M_{LIIIVDP} > 1$ do not have such a constraint. See text for details.

force vs. peak resistive force. The area below the diagonal is theoretically restricted from occurring with normal physiology, because if peak resistive forces exceeded peak driving forces then pressure decay is prohibited. Figure 11.9 also demonstrates that a line with $M_{LIIIIVPD} < 1$ eventually crosses over to the non-physiological domain with extended load variation. Thus, when compared to subjects with $M_{LIIIIVPD} > 1$, subjects with $M_{LIIIIVPD} < 1$ will have less efficient relaxation-related beat-to-beat response to load variation, and possess a limited regime of allowed load variation compared to subjects with $M_{LIIIIVPD} > 1$. In analogy to the analysis presented in Chapter 8, the line through the origin with a slope of $e/2$ represents a transition between overdamped and underdamped physiology. Isovolumic pressure decay contours with coordinates below the $e/2$ line would be expected to have ‘straight’ pressure phase plane contours amenable to an exponential model (τ) approach, whereas pressure decay contours with coordinates above the $e/2$ line would be expected to have ‘curved’ pressure phase plane contours, between fit by a logistic model (τ_L) approach.

11.4.3 Clinical Validation of $M_{LIIIIVPD}$

The physics based derivation presented in above, as well as the results presented in Figure 11.7 and Table 11.3 demonstrate the for each subject, $M_{LIIIIVPD}$ remains constant in the face of load variation. In this manner, load-independence of $M_{LIIIIVPD}$ is both derived and validated. However, to be clinically useful, $M_{LIIIIVPD}$ must be related to real physiology, and must have the potential to differentiate between normal physiology and pathophysiology. To assess clinical validity, $M_{LIIIIVPD}$ was compared to average values of accepted, conventional measures of isovolumic relaxation.

The results of Figure 11.8 must be interpreted with care. The current study consisted of subjects with a wide range in traditional isovolumic relaxation parameters: $33\text{ms} < \tau < 147\text{ ms}$, $14 < \tau_L < 45\text{ ms}$, $-718\text{mmHg/s} < dP/dt_{\text{MIN}} < -1875\text{ mmHg/s}$. Thus, despite the fact that τ , τ_L , and dP/dt_{MIN} are known to be load-dependent, it is unlikely that load effects alone account for the large range of variation observed among the subjects. It is therefore reasonable to conclude that in the current study subjects with longer τ , τ_L , and less negative values for dP/dt_{MIN} , have relaxation-related dysfunction, whereas subjects with shorter τ , τ_L , and more negative dP/dt_{MIN} , have characteristics of normal function. Thus the correlations in Figure 11.8 between M_{LIIIVPD} and τ , τ_L , and dP/dt_{MIN} demonstrate that the values of M_{LIIIVPD} , though confined to a narrow range among the subjects studied, conveys clinical information.

We note, however, that correlating conventional indexes of isovolumic relaxation and M_{LIIIVPD} would have limited value if the subjects chosen were more homogeneous and possessed near normal average τ , τ_L , or dP/dt_{MIN} values. Indeed τ , τ_L , and dP/dt_{MIN} are load-dependent, and therefore modest variations in these parameters can be the result of load effects. By including subjects with widely different τ , τ_L , and dP/dt_{MIN} values, we insure that the subjects have significant intrinsic relaxation-related differences among them. In this manner we minimize the effects of load in the particular subject group, and therefore can conclude that the trends observed in Figure 11.8 support our view that M_{LIIIVPD} correlates with intrinsic relaxation-related function. Higher values of M_{LIIIVPD} correlate with improved function (more negative dP/dt_{MIN} , lower τ and τ_L), while lower values of M_{LIIIVPD} correlate to dysfunction (more positive dP/dt_{MIN} , prolonged τ and τ_L).

The correlation between $M_{LIIIVPD}$ and ejection fraction is interesting because conventionally ejection fraction is viewed not as an index of isovolumic relaxation, but instead as an index of global (systolic) function. However subjects with global dysfunction are likely to have relaxation abnormalities, and therefore it is not surprising that subjects with low ejection fraction's also had lower $M_{LIIIVPD}$ values compared to subjects with normal ejection fraction. The correlation between ejection fraction and $M_{LIIIVPD}$, as well as the related correlations between $M_{LIIIVPD}$ and τ , τ_L and dP/dt_{MIN} demonstrate that the variation in $M_{LIIIVPD}$ among subjects was not random, but was clinically correlated to real differences in physiology.

11.4.4 Connection to Previous Work

The derivation of $M_{LIIIVPD}$ is similar to the previously validated load independent index of diastolic function (29) presented in Chapter 8. The key physiologic difference is that the current work deals with the physiology of isovolumic pressure decay rather than transmitral flow and early-rapid filling. Thus the relevant time scales, as well as initial conditions, are different between the current study and previous load independent index of diastolic function related work. However, because both isovolumic pressure decay and transmitral flow are governed by lumped forces that can be accurately modeled kinematically, a similar derivation can be exploited in determining a load-independent index of either isovolumic relaxation or transmitral flow. The fact that the same type of conceptual and mathematical modeling works when applied to different physiology problems underscores the multi-scale power of kinematic modeling.

11.4.5 Automated Determination of $M_{LIIIVPD}$

The initial results show that $M_{LIIIVPD}$ is indeed conserved in the face of load variation and

is correlated to the intrinsic ability of the chamber to quickly and effectively relax the previous systolic cramp. Because of the broad impact that $M_{LIIIVPD}$ may have in the clinical setting, it is important to develop methods by which $M_{LIIIVPD}$ may be automatically calculated in real-time in the catheterization lab.

The Challenge With Automation

Because physiological data may contain cardiac cycles with unanticipated noise in the pressure signal, it is important for the automated methodology to detect inappropriately noisy isovolumic pressure decay contours so that they are not included in the $M_{LIIIVPD}$ analysis. The initial approach outlined in the Methods discarded beats with RMSE to $P'(t)$ above the mean RMSE value. This however required a large number of beats, which may not be practical for real time clinical application. Thus a primary challenge in automated $M_{LIIIVPD}$ calculation is determining a proper RMSE cutoff for noisy vs. clean physiological data. Calculation of $M_{LIIIVPD}$ requires a certain number of distinct isovolumic pressure decay contours, and therefore requires acquiring data from multiple cardiac cycles in a particular subject. Any selection criteria for clean data will necessarily increase the number of cardiac cycles that need to be measured in order to determine the $M_{LIIIVPD}$. Thus aggressive filtering would tend to increase the total time of data acquisition, and this is not ideal because of the invasive nature by which ventricular pressure is routinely measured. Less aggressive filtering however would lead to more significant errors in $M_{LIIIVPD}$ due to the inclusion of noisier and possibly non-physiologic isovolumic pressure decay contours. Thus to better characterize the appropriate RMSE cutoff, we perform an exploratory analysis in one of the 25 previously analyzed subjects. We apply 7 different RMSE cutoff values, and for each set of filtered beats, we calculate $M_{LIIIVPD}$ from n random beats, where n ranges

from 2 to the total number of filtered beats.

Optimizing RMSE Filtering Cutoff

Among the 340 beats analyzed in the subject of interest, RMSE varied between 10.6 mmHg/s and 66.3 mmHg/s, with the mean RMSE equal to 32.1 mmHg/s. RMSE cutoff values of 16.0, 21.4, 26.8, 32.1, 37.5, 42.9, and 48.3 were chosen. For each chosen RMSE cutoff value, n beats, where n varied from 2 to the total number of remaining beats, were chosen randomly and analyzed according to the Methods described above. Figure 11.10 shows the M_{LIIVPD} and r^2 values vs. number of beats analyzed n for the lowest 2 RMSE values, as well as the mean RMSE value. Remaining RMSE cutoff values provided similar M_{LIIVPD} vs. n plots. Note that while the lower RMSE cutoff leaves far fewer total beats with which to generate M_{LIIVPD} , it appears that fewer beats are needed to generate the appropriate M_{LIIVPD}

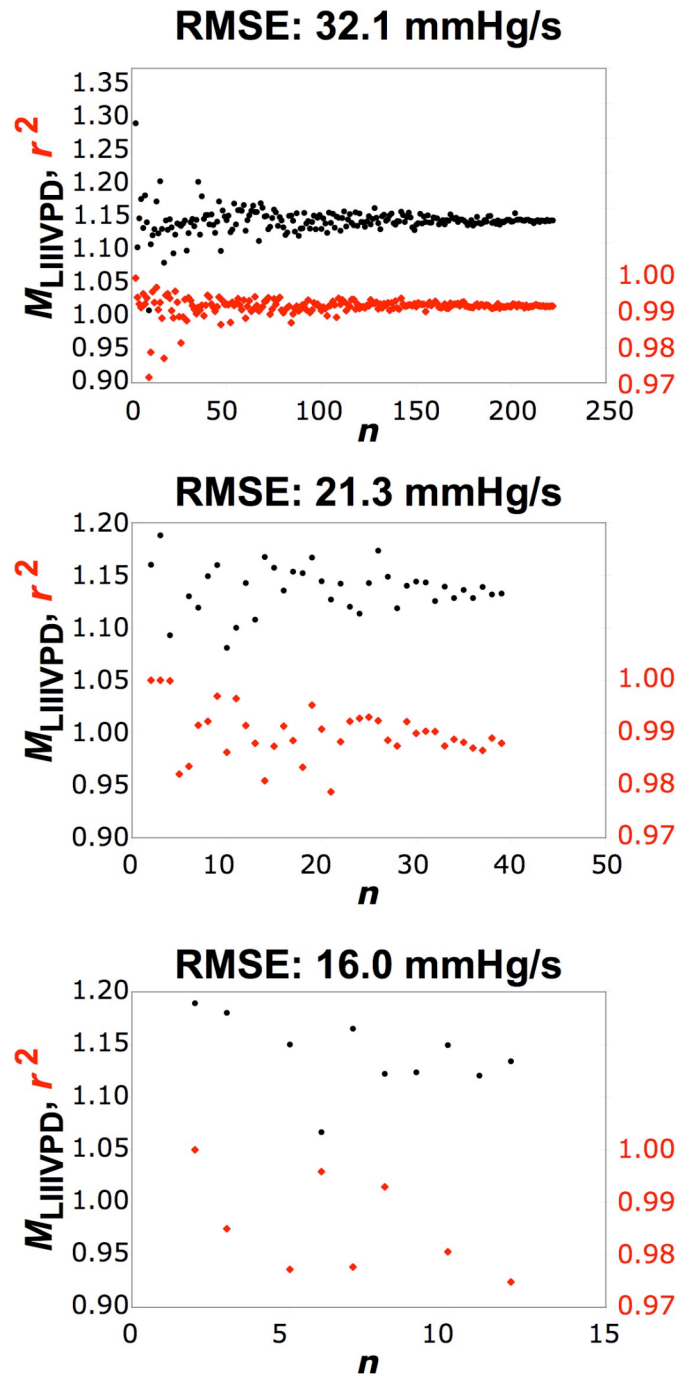


Figure 11.10. Applying the 25% (bottom) and 50% (middle) RMSE cutoff between minimum RMSE and mean RMSE, as well as the mean RMSE cutoff (top) leaves 11, 38, and 222 beats respectively. For each case the M_{LIIVPD} (black) and load independent index of isovolumic pressure decay relation r^2 (red) defined by n random beats chosen from the remaining beats is shown.

value when those beats are chosen from among the lower RMSE group.

Figure 11.10 clearly demonstrates an important trade-off that must be considered in the design of an automated process for determination of M_{LIIIVPD} in real time. The typical catheterization case has a limited number of cardiac cycles that can be measured, because arterial access time must be minimized, whereas the calculation of M_{LIIIVPD} requires numerous beats to be analyzed, especially if the data is noisy. When only data with RMSE below the mean RMSE is included, as shown in the top panel of Figure 11.10, M_{LIIIVPD} shows approximately 10% variation before the first 50 beats are analyzed. This variation decreases as more beats are analyzed, until a final value of 1.15 is reached. When a more stringent RMSE cutoff is applied, the M_{LIIIVPD} variation remains until 30 beats are analyzed, but inclusion of all 40 beats results in a convergence on an M_{LIIIVPD} value of 1.13. Finally, with the most stringent RMSE cutoff applied, only 11 beats are available and there is significant variation in M_{LIIIVPD} , but the final value is also 1.13.

A Running Average Approach

These results suggest that analyzing low RMSE data is the ideal approach. However, given data with a normal distribution of RMSE values, finding enough beats with low RMSE values may be impossible given a limited number of measured cardiac cycles. Interestingly, an interesting property emerges from the top panel of Figure 11.10, where the mean RMSE was chosen as the cutoff. It is evident that M_{LIIIVPD} shows a symmetry around the final M_{LIIIVPD} value. Indeed, a running average of M_{LIIIVPD} in the top panel stabilizes between 1.14 and 1.15 within 9 beats. For normally distributed data that would imply 18 measured cardiac cycles in total, which is a reasonable goal in the catheterization laboratory. Further work regarding the symmetry of M_{LIIIVPD} vs. n and the appropriate averaging techniques to reduce the needed number of cardiac

cycles analyzed is warranted.

11.5 LIMITATIONS

11.5.1 Kinematic Model Limitations

The lumped parameter, kinematic approach presented uses a linear differential equation with constant (i.e time-invariant) coefficients (Newton's Law) Eq. 11.3 to model events that others have modeled using time-varying ventricular properties. Past work by Nudelman (23) has compared and shown superb agreement between a time-invariant linear kinematic model and time-varying nonlinear models of transmitral flow. Although the form of the differential equation for transmitral flow and isovolumic pressure decay is the same (Newton's Law), numerical experiments comparing the kinematic model and models with time-varying coefficients for isovolumic pressure decay have not been carried out. Additional validation of the constant coefficient, kinematic modeling utilized here would require that the averaged time-varying parameters agree with the constant coefficient lumped parameters. A potential limitation of the current work is the absence of experimental data to validate time-invariant analysis in this manner. However, the ability to solve the 'inverse problem' using in-vivo data as input and unique parameter values as output, and the close agreement between the in-vivo pressure data and the time-invariant, kinematic model predicted contours, supports the conclusions of the current study.

11.5.2 Application of a Model Determined Maximum Pressure

In the derivation of the load independent index of isovolumic pressure decay, the model-based maximum pressure (P_{MAX}^*), determined by algebraically solving for the maximum value of

Eq. 11.4, was employed. It may seem inappropriate, however, to apply an isovolumic model to intervals before aortic valve closure. Indeed, P_{MAX}^* will not accurately reflect the actual P_{MAX} value, because with intact physiology, the isovolumic condition is broken at P_{MAX} . However, using P_{MAX}^* as a value in the idealized limit where the chamber is isovolumic does not violate any physical principles, or introduce any tautological conditions. In fact the use of P_{MAX}^* is analogous to the methods applied in the Doppler-echo derived load independent index of diastolic function (29) presented in Chapter 8. Furthermore, if one uses the actual P_{MAX} value instead of P_{MAX}^* , so that the y-coordinate in the regression that defines $M_{LIIIVPD}$ becomes $E_k(P_{MAX}-P_\infty)$ instead of $E_k(P_{MAX}^*-P_\infty)$, then the plots for each subject remain strongly linear, but the linear correlations between $M_{LIIIVPD}$ and τ ($r^2=0.44$), τ_L ($r^2=0.41$), dP/dt_{MIN} ($r^2=0.46$), and EF ($r^2=0.27$) decrease relative to those seen in Figure 11.8. Because $M_{LIIIVPD}$ is derived to be an index of isovolumic relaxation, it is reasonable to only use parameters derived from isovolumic data. Thus the use of P_{MAX}^* , the maximum pressure in the chamber assuming that the chamber remains isovolumic from the pressure maximum down to mitral valve opening, is preferred.

11.5.3 Clinical Utility Beyond Conventional Isovolumic Pressure Decay Indexes

A further limitation may be the concern that $M_{LIIIVPD}$ does not present information beyond what the average τ or τ_L value already provides, and therefore serves as merely a surrogate for τ . While this is reasonable, we note that $M_{LIIIVPD}$, τ , and τ_L are all determined by τ_c and E_k . In other words, all three indexes are surrogates for how stiffness and relaxation combine to determine isovolumic pressure decay. Because all three indexes represent lumped parameters

of isovolumic pressure decay and are therefore measuring the same physiological event, it is reasonable to expect these parameters to correlate with each other and to vary between subjects with different physiology. However, while each index provides information regarding isovolumic pressure decay, $M_{LIIIVPD}$ is the only one that is derived with load-independence in mind, and is validated to be load-independent.

The strong correlations presented in Figure 11.8 may suggest that inversion of these correlations would allow one to extract $M_{LIIIVPD}$ for an individual subject by measuring τ , τ_L , or dP/dt_{MIN} alone. Thus, it may appear that the load-independent $M_{LIIIVPD}$ index could be derived from load-dependent parameters. It is important to note however that Figure 11.8 consists of correlations among subjects with overt differences in τ , τ_L and dP/dt_{MIN} . While a general trend is observed between $M_{LIIIVPD}$ and relaxation-related function, a direct causal link that is appropriate for extreme and moderate values of τ , τ_L , and dP/dt_{MIN} cannot be determined from Figure 11.8. Thus inversion of the correlations in Figure 11.8 is not justified.

11.5.4 Patient Heterogeneity

Additionally the use of a non-homogeneous subject group may be seen as inappropriate because the significant physiological difference between the subjects may confound the results of the work. Had the $E_k \cdot (P_{MAX}^* - P_\infty)$ vs. $\tau_c \cdot (dP/dt_{MIN})$ relation shown to be nonlinear in some subset of the subjects, then the non-homogeneous nature of the subject group could have been invoked to explain why $M_{LIIIVPD}$ is load-independent in some cases, but load-dependent in others. However, because all subjects showed a strongly conserved $M_{LIIIVPD}$ slope in the face of load variation, the non-homogeneous nature of the subject group serves to underscore the validity and general applicability of the method.

11.5.5 Range of $M_{LIIIIVPD}$ Variation

Although the number of beats analyzed is substantial (2669) the number of subjects is modest, and therefore no claims regarding the range of normal or abnormal values for $M_{LIIIIVPD}$ are made. Although the range of variation of $M_{LIIIIVPD}$ is narrow in the absolute numerical sense, these values correlated with the underlying physiology as evidenced by Figure 11.8. Though conventional indexes of isovolumic relaxation such as τ and τ_L may exhibit a larger numerical range of variation across subjects, much of it is due to load variation. It is therefore not surprising that a load-independent index exhibits a narrower numerical range of variation than load-dependent indexes such as τ and τ_L . Thus the ‘benefit’ of a load-independent index of isovolumic pressure decay carries with it the ‘cost’ of a numerically smaller range of variation.

Future studies with carefully selected patient groups will be needed to establish clinical range for $M_{LIIIIVPD}$. In addition the variation of $M_{LIIIIVPD}$, in repeated studies where each subject serves as their own control, may provide an opportunity for phenotypic characterization that provides mechanistic insights regarding the effects of alternative (pharmacological, surgical, device based) therapeutic modalities.

11.6 CONCLUSIONS

We apply Chung’s isovolumic pressure decay model to determine (E_k and τ_c) the stiffness and relaxation components of isovolumic pressure decay respectively. Based on physical and physiologic principles, we derive a parameter that avoids the load-dependence of τ . The new index, $M_{LIIIIVPD}$, is shown to be load independent in subjects with significantly different clinical profiles. Furthermore, $M_{LIIIIVPD}$ correlates with conventional isovolumic relaxation parameters. To ensure clinical utility, we demonstrate a detailed process by which $M_{LIIIIVPD}$ is determined

from pressure and ECG data alone in a real-time automated fashion. Future work determining $M_{LIIIVPD}$ in clinical subsets having specific pathophysiology and defining proper guidelines regarding number of beats necessary for robust $M_{LIIIVPD}$ analysis is warranted.

11.7 THEMATICALLY RELATED ABSTRACT

In the work above, we have utilized a kinematic model of isovolumic pressure decay to derive a novel load independent index. We have further explored this kinematic model and present a method by which lumped τ behavior, as well as specific physiological mechanisms that determine τ , may be simultaneously assessed. This specific application of the kinematic model of isovolumic pressure decay was previously published as a conference abstract.

Our method relies upon analysis of IVPD contours in the τ_c vs E_k plane. Individual IVPD contours provide unique (E_k, τ_c) values that may be plotted in the τ_c vs E_k plane. Straight lines through the origin define lines of constant τ , and the coordinates of any beat in the τ_c vs E_k plane reveals the relative contribution of stiffness or relaxation effects that determine τ for the given beat (Figure 11.11).

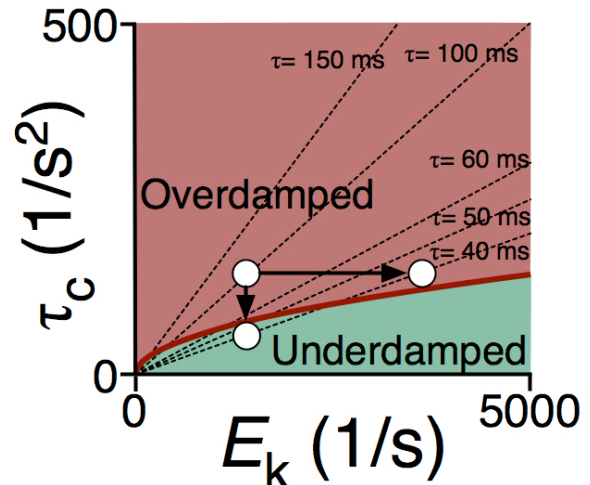


Figure 11.11. A decrease in τ from 100ms to 40ms is shown to be mediated by purely relaxation (τ_c) or stiffness (E_k) effects.

We apply the τ_c vs E_k plane to retrospective data from the 25 analyzed in the current Chapter. For each subject, an average of 107 IVPD contours were plotted in the TEP. In each subject the τ_c showed strong linear correlation to E_k ($0.65 < r^2 < 0.95$). Across all subjects, the

slope of the τ_c vs E_k plot correlated strongly with average τ , τ_L , ejection fraction (EF), and dP/dt_{MIN} ($r^2=0.94, 0.71, 0.74,$ and 0.57 respectively). Across all subjects, median τ_c vs E_k plane coordinates shifted toward decreased τ with higher EF. Interestingly, this shift was mediated primarily by increased stiffness (not relaxation) effects. We conclude that the τ_c vs E_k plane is a novel tool by which the operative mechanisms determining the physiology of isovolumic pressure decay may be more completely assessed.

11.8 REFERENCES

1. Blaustein AS and Gaasch WH. Myocardial relaxation. VI. Effects of beta-adrenergic tone and asynchrony on LV relaxation rate. *Am J Physiol* 244: H417-422, 1983.
2. Brutsaert DL and Sys SU. Relaxation and diastole of the heart. *Physiol Rev* 69: 1228-1315, 1989.
3. Camacho SA, Brandes R, Figueredo VM, and Weiner MW. Ca²⁺ transient decline and myocardial relaxation are slowed during low flow ischemia in rat hearts. *J Clin Invest* 93: 951-957, 1994.
4. Cheng CP, Igarashi Y, and Little WC. Mechanism of augmented rate of left ventricular filling during exercise. *Circ Res* 70: 9-19, 1992.
5. Chung CS and Kovács SJ. Physical determinants of left ventricular isovolumic pressure decline: model prediction with in vivo validation. *Am J Physiol Heart Circ Physiol* 294: H1589-1596, 2008.
6. De Hert SG, Gillebert TC, Ten Broecke PW, and Moulijn AC. Length-dependent regulation of left ventricular function in coronary surgery patients. *Anesthesiology* 91: 379-387, 1999.
7. Eucker SA, Lissauskas JB, Singh J, and Kovács SJ. Phase plane analysis of left ventricular hemodynamics. *J Appl Physiol* 90: 2238-2244, 2001.
8. Frederiksen JW, Weiss JL, and Weisfeldt ML. Time constant of isovolumic pressure fall: determinants in the working left ventricle. *Am J Physiol* 235: H701-706, 1978.
9. Gaasch WH, Blaustein AS, Andrias CW, Donahue RP, and Avitall B. Myocardial relaxation. II. Hemodynamic determinants of rate of left ventricular isovolumic pressure decline. *Am J Physiol* 239: H1-6, 1980.

10. Helmes M, Trombitás K, and Granzier H. Titin develops restoring force in rat cardiac myocytes. *Circ Res* 79: 619-626, 1996.
11. Hori M, Inoue M, Kitakaze M, Tsujioka K, Ishida Y, Fukunami M, Nakajima S, Kitabatake A, and Abe H. Loading sequence is a major determinant of afterload-dependent relaxation in intact canine heart. *Am J Physiol* 249: H747-754, 1985.
12. Ishida Y, Meisner JS, Tsujioka K, Gallo JI, Yoran C, Frater RW, and Yellin EL. Left ventricular filling dynamics: influence of left ventricular relaxation and left atrial pressure. *Circulation* 74: 187-196, 1986.
13. Karliner JS, LeWinter MM, Mahler F, Engler R, and O'Rourke RA. Pharmacologic and hemodynamic influences on the rate of isovolumic left ventricular relaxation in the normal conscious dog. *J Clin Invest* 60: 511-521, 1977.
14. Kass DA. Assessment of diastolic dysfunction. Invasive modalities. *Cardiology clinics* 18: 571-586, 2000.
15. Katz AM. The "modern" view of heart failure: how did we get here? *Circ Heart Fail* 1: 63-71, 2008.
16. Katz L. The role played by the ventricular relaxation process in filling the ventricle. *American Journal of Physiology*, 1930.
17. Kovács SJ, Barzilai B, and Pérez JE. Evaluation of diastolic function with Doppler echocardiography: the PDF formalism. *Am J Physiol* 252: H178-187, 1987.
18. Matsubara H, Takaki M, Yasuhara S, Araki J, and Suga H. Logistic time constant of isovolumic relaxation pressure-time curve in the canine left ventricle. Better alternative to exponential time constant. *Circulation* 92: 2318-2326, 1995.

19. Miki S, Murakami T, Iwase T, Tomita T, Nakamura Y, and Kawai C. Doppler echocardiographic transmitral peak early velocity does not directly reflect hemodynamic changes in humans: importance of normalization to mitral stroke volume. *Journal of the American College of Cardiology* 17: 1507-1516, 1991.
20. Mizuno J, Araki J, Mikane T, Mohri S, Imaoka T, Matsubara H, Okuyama H, Kurihara S, Ohe T, Hirakawa M, and Suga H. Logistic time constant of isometric relaxation force curve of ferret ventricular papillary muscle: reliable index of lusitropism. *Jpn J Physiol* 50: 479-487, 2000.
21. Mizuno J, Mohri S, Shimizu J, Suzuki S, Mikane T, Araki J, Matsubara H, Morita T, Hanaoka K, and Suga H. Starling-effect-independent lusitropism index in canine left ventricle: logistic time constant. *Anesth Analg* 102: 1032-1039, 2006.
22. Murakami T, Hess OM, Gage JE, Grimm J, and Krayenbuehl HP. Diastolic filling dynamics in patients with aortic stenosis. *Circulation* 73: 1162-1174, 1986.
23. Nudelman S, Manson AL, Hall AF, and Kovács SJ. Comparison of diastolic filling models and their fit to transmitral Doppler contours. *Ultrasound in medicine & biology* 21: 989-999, 1995.
24. Opitz CA, Kulke M, Leake MC, Neagoe C, Hinssen H, Hajjar RJ, and Linke WA. Damped elastic recoil of the titin spring in myofibrils of human myocardium. *Proc Natl Acad Sci USA* 100: 12688-12693, 2003.
25. Press ST, WT Vetterling. *Numerical Recipes: the art of scientific computing*. New York: Cambridge University Press, 1986.
26. Raff GL and Glantz SA. Volume loading slows left ventricular isovolumic relaxation rate. Evidence of load-dependent relaxation in the intact dog heart. *Circ Res* 48: 813-824, 1981.

27. Rosen BD, Gerber BL, Edvardsen T, Castillo E, Amado LC, Nasir K, Kraitchman DL, Osman NF, Bluemke DA, and Lima JAC. Late systolic onset of regional LV relaxation demonstrated in three-dimensional space by MRI tissue tagging. *Am J Physiol Heart Circ Physiol* 287: H1740-1746, 2004.
28. Senzaki H, Fetters B, Chen CH, and Kass DA. Comparison of ventricular pressure relaxation assessments in human heart failure: quantitative influence on load and drug sensitivity analysis. *Journal of the American College of Cardiology* 34: 1529-1536, 1999.
29. Shmuylovich L and Kovács SJ. Load-independent index of diastolic filling: model-based derivation with in vivo validation in control and diastolic dysfunction subjects. *J Appl Physiol* 101: 92-101, 2006.
30. Solomon SB, Nikolic SD, Frater RW, and Yellin EL. Contraction-relaxation coupling: determination of the onset of diastole. *Am J Physiol* 277: H23-27, 1999.
31. Weiss JL, Frederiksen JW, and Weisfeldt ML. Hemodynamic determinants of the time-course of fall in canine left ventricular pressure. *J Clin Invest* 58: 751-760, 1976.
32. Yellin EL, Hori M, Yoran C, Sonnenblick EH, Gabbay S, and Frater RW. Left ventricular relaxation in the filling and nonfilling intact canine heart. *Am J Physiol* 250: H620-629, 1986.
33. Zile MR and Gaasch WH. Load-dependent left ventricular relaxation in conscious dogs. *Am J Physiol* 261: H691-699, 1991.

CHAPTER 12.

A CLINICALLY IMPLEMENTED GEOMETRIC APPROACH TO PDF

MODEL ANALYSIS OF TRANSMITRAL CONTOURS

12.1 INTRODUCTION

12.1.1 Kinematic Analysis in the Clinic: Opportunities and Challenges

The preceding chapters have provided numerous examples of novel applications of kinematic modeling to clinically relevant questions pertaining to diastolic function. These chapters represent a portion of a larger body of work based on kinematic modeling, published over the past 2 decades, that have demonstrated the power and applicability of quantitative mechanistic modeling in general, and the Parameterized Diastolic Filling (PDF) formalism in particular. These results should be applicable to any clinical practice, because the algorithms and mathematical methods have been extensively described and validated. Incorporation of these algorithms into the internal software of echocardiographic imagers by equipment manufacturers is in principle a simple task, and therefore the possibility exists for clinicians to routinely apply PDF modeling techniques through pre-packaged semi-automated techniques. However, there are a variety of challenges to automation of PDF analysis, and the root cause of these challenges relates to the method by which data is selected and fit, and the conceptual difficulties associated with clinical interpretation of the PDF based results. Indeed the PDF methodology is fairly technical, and is most easily understood using the language of mathematics, engineering, and physics. Re-expressing the PDF model in terms of conventional clinical parameters would therefore be advantageous.

12.1.2 Current Kinematic and Conventional Analysis

The current established techniques for extracting kinematic PDF model parameters from acquired transmitral flow contours (E- and A- waves) requires multiple steps, as shown in Chapter 2. First, the transmitral image must be cropped, the scale must be entered, and the

maximum velocity envelope must be chosen. In addition, the start and end of the waves to be fit must be chosen. Once these parameters are set, a computer algorithm minimizes the error between the model predicted velocity and the maximum velocity envelope pixels defined by user specified criteria. If the resulting fit does not visually appear to be in line with the image, then the user may adjust the parameters of the model. While manual adjustment is rare with clean data, noisier data, where errant pixels (i.e. noise) are picked up by the fitting algorithm, often requires operator guided feedback.

Thus the current methodology, though based on minimizing error between model prediction and experimental measurement, has several drawbacks. First, it requires teaching new steps for clinicians and sonographers to follow in order to generate the input to the fitting algorithm. In addition, it may be sensitive to what the user picks as the start and end of the data. Finally it does not provide an intuitive approach to adjusting the fit data manually. Thus even if the algorithms and methods were widespread, there is a nontrivial learning curve associated with PDF model analysis that should not be underestimated and that stands in the way of widespread application of the PDF model kinematic approach to quantitative diastolic function assessment.

In contrast, the current established methodology for conventional clinical analysis of E-wave attributes requires clinicians/sonographers to only determine the peak of the E-wave, the start of the E-wave, and the end of the E-wave (Chapter 2). This approach defines the familiar acceleration time (AT), deceleration time (DT), and E-wave peak (E_{peak}) parameters. Such an approach is advantageous because it is simple to teach, trivial to implement, and fairly repeatable across multiple investigators. In addition, it is a widespread established method, and therefore there is a great deal of experience in the cardiology community with this approach. Thus any novel analysis techniques would be more likely to be adopted across the general cardiology

community if they utilized components of the established conventional triangle-fitting algorithm. Specifically, a method for extraction of kinematic PDF parameters that mirrored conventional triangle fitting would represent a significant step forward toward widespread dissemination and clinical application of the PDF model.

12.2 METHODS

12.2.1 Determination of PDF Parameters from AT,DT and E_{peak} : Underdamped Kinematic Regime

E-wave Analysis

The triangle fit to the E-wave defines 3 points: the start, peak, and end of E-wave. Because there are only 3 parameters in the E-wave velocity expression, these 3 points should in principle be enough to uniquely determine the associated E-wave contour. To determine the exact mapping from geometrically determined AT, DT, and E_{peak} values to PDF model c , k , and x_0 values, we begin with the underdamped PDF model expression for velocity from Chapter 2:

$$v(t) = \frac{kx_0}{\omega} e^{-\frac{c}{2}t} \sin(\omega t) \quad \text{Equation 12.1}$$

where c , k , and x_0 are the damping, stiffness, and initial displacement of the equivalent harmonic oscillator whose velocity matches the E-wave velocity, and ω is the frequency of the oscillator, given by $\omega = \sqrt{k^2 - (c/2)^2}$. As shown in detail in Chapter 2, solving for the acceleration and

deceleration time of this wave, and introducing the parameter $y = \frac{c}{2\sqrt{k}}$, one finds:

$$AT = \frac{1}{\sqrt{k}} \frac{\cos^{-1}(y)}{\sqrt{1-y^2}} \quad \text{Equation 12.2}$$

$$DT = \frac{1}{\sqrt{k}} \frac{\pi - \cos^{-1}(y)}{\sqrt{1-y^2}} \quad \text{Equation 12.3}$$

Rearranging these equations one can cancel out the \sqrt{k} :

$$AT = \cos^{-1}(y) \frac{(AT + DT)}{\pi} \quad \text{Equation 12.4}$$

and solving for y yields:

$$y = \cos\left(\pi \frac{AT}{AT + DT}\right) \quad \text{Equation 12.5}$$

This demonstrates that y is determined uniquely by AT and DT , and, more specifically, by the relative asymmetry of the wave. As expected, when $AT=DT$ and the E-wave is symmetric, $y=0$ and we have an undamped wave. As relative damping to stiffness increases and y approaches 1, the E-wave asymmetry grows.

Expanding the E-wave frequency in terms of k and y , we find:

$$\omega = \sqrt{k} \sqrt{1-y^2} = \frac{\pi}{AT + DT} \quad \text{Equation 12.6}$$

This may be rearranged, with the help of Equation 12.5 to solve for k in terms of AT and DT :

$$k = \frac{1}{(AT + DT)^2} \frac{\pi^2}{1-y^2} = \frac{\pi^2}{(AT + DT)^2} \csc^2\left(\pi \frac{AT}{AT + DT}\right) \quad \text{Equation 12.7}$$

Finally the definition of y may be used to express c in terms of y and k , and therefore we may determine an expression for c in terms of AT and DT :

$$c = 2y\sqrt{k} = \frac{2\pi}{(AT + DT)} \cot\left(\pi \frac{AT}{AT + DT}\right) \quad \text{Equation 12.8}$$

Thus the c and k parameters of the kinematic PDF model can be extracted purely from the triangle AT and DT parameters, independent of the peak height of the E-wave. It is intriguing to consider that E-wave asymmetry alone defines PDF c and k parameters.

We may determine the remaining PDF parameter, x_o , by applying the final triangle-fit parameter, E_{peak} . In Chapter 2 we showed that according to the PDF model, the peak velocity is:

$$v(AT) = E_{peak} = \sqrt{k}x_o e^{\frac{y \cos^{-1}(y)}{\sqrt{1-y^2}}} \quad \text{Equation 12.9}$$

Thus x_o can be determined in terms of E_{peak} , y , and k :

$$x_o = \frac{E_{peak}}{\sqrt{k}} e^{\frac{y \cos^{-1}(y)}{\sqrt{1-y^2}}} \quad \text{Equation 12.10}$$

Finally with Equation 12.7 and 12.5, x_o may be expressed as:

$$x_o = E_{peak} \frac{(AT + DT)}{\pi} \sin\left(\pi \frac{AT}{AT + DT}\right) e^{\left(\pi \frac{AT}{AT + DT}\right) \cot\left(\pi \frac{AT}{AT + DT}\right)} \quad \text{Equation 12.11}$$

Taken together, Equation 12.7, 12.8, and 12.11 define a one to one mapping from conventionally determined triangle parameters and underdamped PDF parameters. Thus we have successfully re-expressed the more mathematically complex PDF parameters in terms of well-established clinical parameters. It is self evident that the accuracy of x_o , c and k determined from AT, DT and E_{peak} depends on the accuracy with which the triangle based parameters are determined. Nuances of the PDF model can be mapped onto nuances of E-wave AT vs DT asymmetry, and thus a new more clinically minded language may be applied to all PDF modeling based results.

These equations indicate that PDF parameters c and k are purely functions of AT and DT, whereas x_o is a function of E_{peak} , AT, and DT. However, x_o/E_{peak} is a function of AT and DT alone, and therefore the dependence of c , k , and x_o/E_{peak} on AT and DT may be visualized graphically if one holds AT+DT constant (Figure 12.1). Figure 12.1 also demonstrates the dependence of PDF parameters on AT/(AT+DT), thus explicitly showing the interdependence

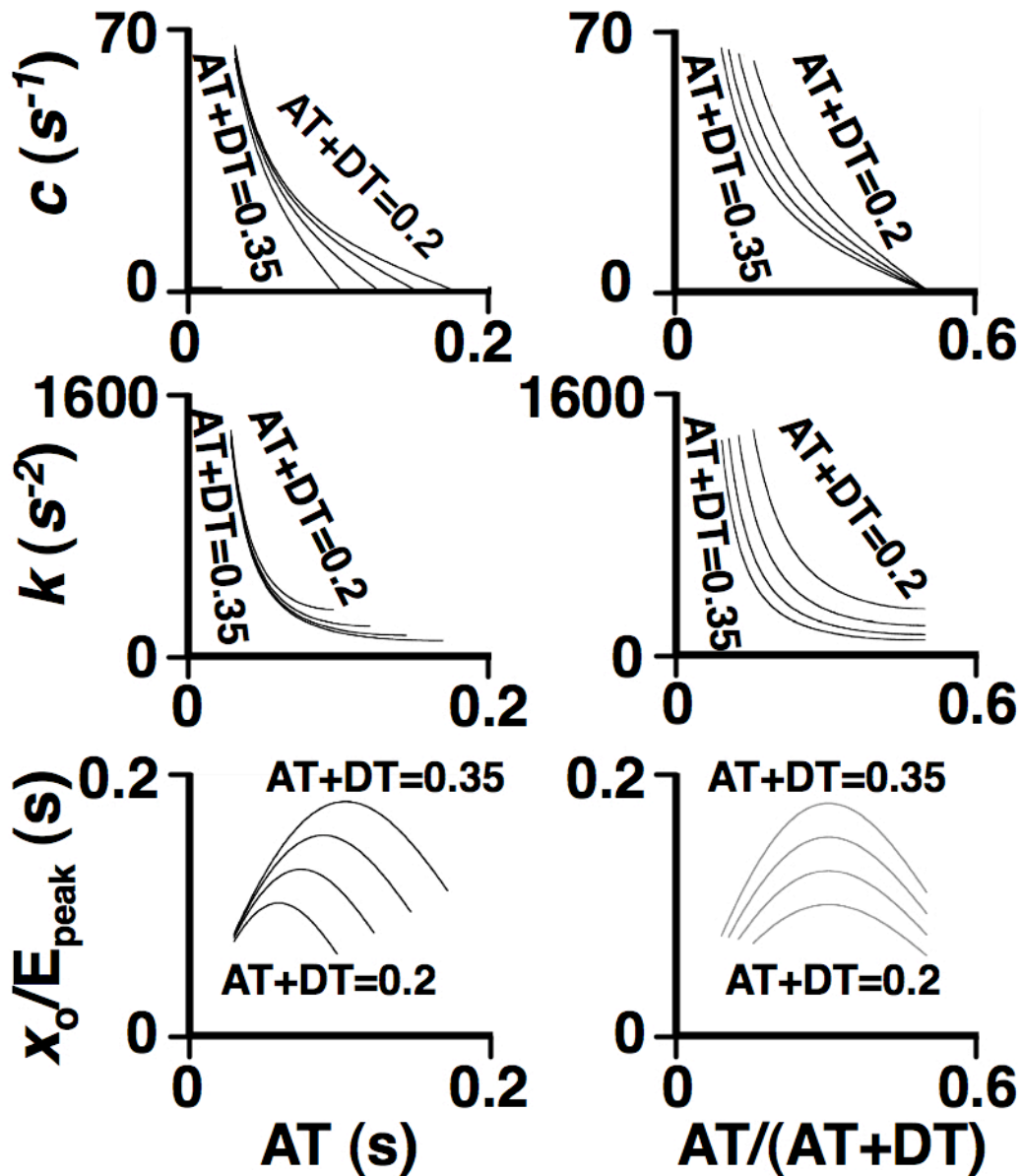


Figure 12.1. Plots of c , k and x_o vs AT and $AT/(AT+DT)$ for fixed $(AT+DT)$ values of 0.20s, 0.25s, 0.30s, and 0.35s. The maximum value for AT is $\frac{1}{2}(AT+DT)$, because values beyond that imply a negative damping constant.

between PDF parameters and E-wave asymmetry. As expected the symmetric E-wave, given by $AT/(AT+DT) = \frac{1}{2}$ is consistent with undamped kinematics ($c=0$).

A-wave Analysis

This analysis is not limited to the E-wave, and indeed the A-wave geometric connection to PDF parameters is even simpler than the preceding E-wave analysis. From Chapter 2, the A-wave velocity contour may be expressed by the following equation:

$$v(t) = \frac{F_o}{2} \left(\frac{\sin(\omega_A t)}{\omega_A} - t e^{-\omega_A t} \right) \quad \text{Equation 2.12}$$

As we show in Chapter 2, the duration of the wave is a function of the frequency, and therefore we may determine the frequency from the duration of the wave:

$$\omega_A = \frac{2.9907}{A_{dur}} \quad \text{Equation 2.13}$$

Alternatively the frequency may be determined if A-wave AT or DT are measured:

$$\omega_A = \frac{1.69897}{A_{AT}} = \frac{1.29177}{A_{DT}} \quad \text{Equation 2.14}$$

The only other A-wave parameter that needs to be determined is F_o , and applying the expression in Chapter 2 for the peak amplitude of the A-wave, we obtain:

$$F_o = 4.9888 \frac{A_{peak}}{A_{AT}} \quad \text{Equation 2.15}$$

Thus measurement of A_{peak} and A_{dur} or A-wave acceleration or deceleration time exactly defines the A-wave PDF parameters.

12.2.2 Determination of PDF Parameters from AT,DT and E_{peak} : Overdamped Kinematic

Regime

E-wave Analysis

Following the approach above, we begin with the overdamped version of E-wave velocity, described in Chapter 2:

$$v(t) = \frac{kx_o}{\beta} e^{-\alpha t} \sinh(\beta t) \quad \text{Equation 12.16}$$

where $\beta = \sqrt{\alpha^2 - k^2}$ and $\alpha = \frac{c}{2}$. As discussed in Chapter 2, the E-wave acceleration time and peak height may be found exactly for the overdamped E-wave:

$$AT_{over} = -\frac{1}{y\sqrt{k}} \Upsilon \quad \text{Equation 2.17}$$

$$E_{peak} = \sqrt{k}x_o e^{\Upsilon} \quad \text{Equation 2.18}$$

$$\text{where } \Upsilon = \ln \left(\frac{\alpha + \beta}{\alpha - \beta} \right)^{-\frac{\alpha}{2\beta}} = \ln \left(\frac{1 + \sqrt{1 - y^{-2}}}{1 - \sqrt{1 - y^{-2}}} \right)^{-\frac{1}{2\sqrt{1 - y^{-2}}}}$$

Because the deceleration time is not finite for the overdamped E-wave, an approximation to deceleration time must be made. As discussed in Chapter 2, the natural approximation is to define a line between the E-wave peak and inflection point in the deceleration portion, and extend that line to the velocity baseline. The horizontal distance between E-wave peak and point where the constructed line intersects the baseline defines an effective E-wave deceleration time, and this can be mathematically expressed as:

$$DT_{over} = \left(\frac{1}{\sqrt{k}} \right) \frac{\Upsilon}{2y^2 e^{\Upsilon} - y} \quad \text{Equation 12.19}$$

Thus the ratio of overdamped acceleration time to deceleration time is:

$$\frac{AT_{over}}{DT_{over}} = 1 - 2ye^{\Upsilon} \quad \text{Equation 12.20}$$

Plotting Equation 12.20 against y for $y > 1$ reveals that, as expected, the function is monotonically decreasing with increasing y (Figure 12.2). While Equation 12.20 does not have a simple analytic inverse, one can numerically invert the function and determine a unique value of

y from a measured AT/DT ratio.

Once y is determined, individual c and k parameters may be determined from Equations 12.17 above. Solving equation 12.17 for k yields:

$$k = \left(\frac{1}{AT_{over}} \frac{\Upsilon}{y} \right)^2 \quad \text{Equation 12.21}$$

Once k is determined c is found from the basic definition of y :

$$c = y \cdot 2\sqrt{k} = \frac{2}{AT_{over}} \Upsilon \quad \text{Equation 12.22}$$

Isolating x_0 in equation 12.18 above yields an expression for x_0 in terms of E_{peak} and Υ :

$$x_0 = \frac{1}{\sqrt{k}} e^{-\Upsilon} E_{peak} = E_{peak} \cdot AT_{over} \frac{y}{\Upsilon e^{\Upsilon}} \quad \text{Equation 12.23}$$

With Equations 12.21-23, PDF parameters c , k , and x_0 can be uniquely determined from measured AT, DT and E_{peak} values. As in the case of underdamped waves, AT and DT alone determine c , k , and x_0/E_{peak} . Thus we have determined expressions for PDF parameters in terms of measured triangle parameters. In the underdamped regime the expressions are exact, whereas in the overdamped regime the expressions are approximations because of the

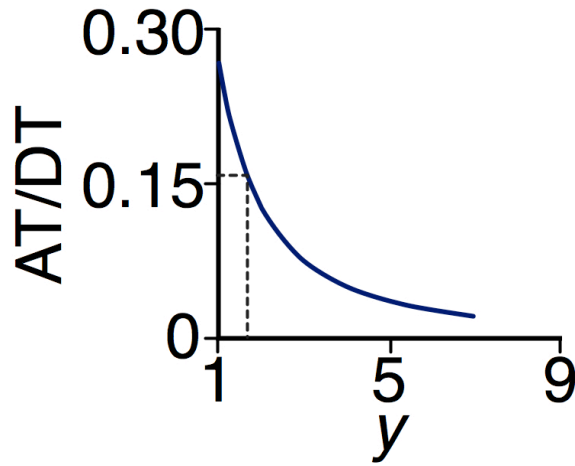


Figure 12.2. Plot of the ratio of acceleration time (AT) to deceleration time (DT) vs the damping to stiffness ratio y . Inversion of this plot allows for determination of y from AT/DT ratio. See text for details.

approximations that must be made in relation to overdamped deceleration time. What is not clear from initial inspection, however, is how one determines which regime of filling applies. Thus

further analysis is required to understand the transition between the underdamped and overdamped kinematic filling regimes.

12.2.3 Underdamped to Overdamped Transition

In the overdamped analysis above, we plotted the ratio of AT to DT against y and found that the ratio decreased monotonically with increasing y (Figure 12.2). The plot was limited, however, to the overdamped regime, and it is interesting to consider extending the plot into the underdamped kinematic regime ($0 \leq y < 1$). In Figure 12.3 we extend the plot using both the exact AT/DT ratio, found from Equation 12.3 and 12.2, as well as the ratio of exact AT to inflection point defined DT' , determined

from Equation 12.2 and Eq 2.31.

Recall that in Chapter 2 we

showed that the inflection point defined DT' was a close approximation to the exact DT for underdamped waves, with equality occurring at the undamped $c=0$ limit.

Figure 12.3 reveals a serious limitation of the exact DT equation in the underdamped case as y approaches 1. Just as in the case of overdamped waves, the

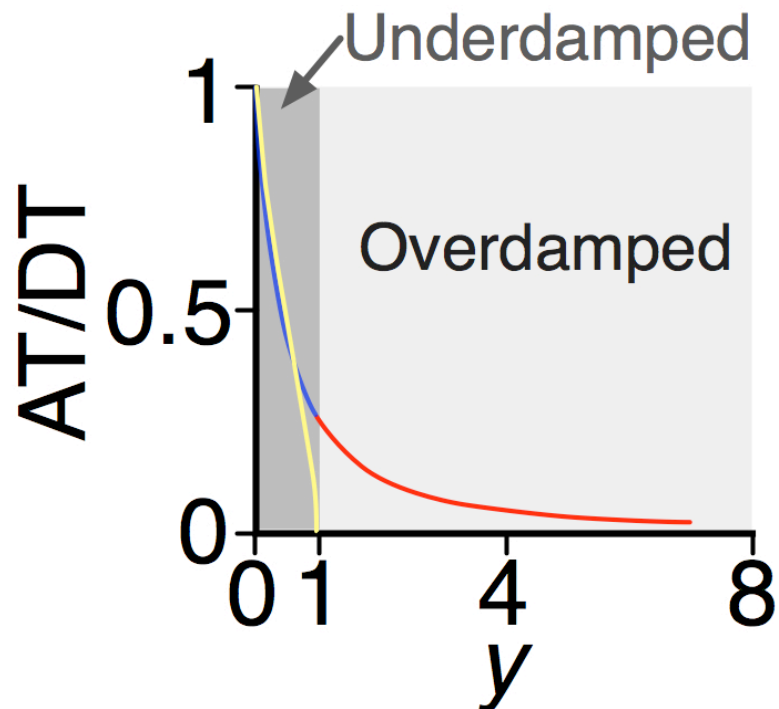


Figure 12.3 A plot of AT/DT vs y extended to both the underdamped (dark gray) and overdamped (light gray) regimes. The yellow curve applies the exact DT expression (Eq 12.3), while the blue and red curves use the inflection based DT' expression (12.28). The intersection between the yellow and blue curve suggests a transition point for the underdamped to overdamped fitting algorithm. See text for details.

$y=1$ wave is critically damped and attains 0 velocity at infinite time. Thus the predicted exact deceleration time approaches infinity as underdamped waves approach the critical damping regime, and therefore application of the exact deceleration time expression in nearly critically damped cases will lead to overestimation of deceleration time compared to the best fit linear deceleration times determined in the clinic (Figure 12.4). Thus for waves near the critical damping regime a more appropriate deceleration time is the one that is also defined in the overdamped case, as the base of the triangle whose hypotenuse is collinear with the E-wave peak and inflection point.

Indeed we see in Figure 12.3 that the exact AT/DT expression in the underdamped case drops precipitously as y approaches 1, while the AT/DT' , defined using the inflection point based DT , continuously transitions to the overdamped case as y approaches and exceeds 1.

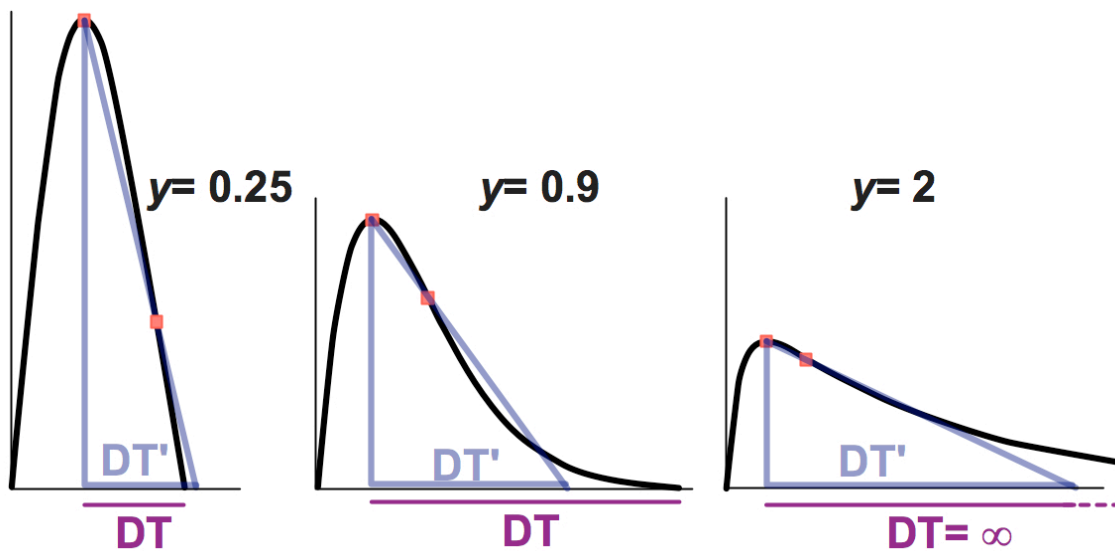


Figure 12.4. Theoretical E-waves with increasing y , showing both exact deceleration time (DT) and inflection point defined deceleration time (DT'). When $y > 1$ the wave is overdamped and exact DT is not defined. When y is low, as in the $y=0.25$ example, the inflection point derived DT and exact DT are similar in value. As y approaches 1, as in the $y=0.9$ example in the middle, the exact DT grows significantly. In the clinical setting, however, the best first deceleration line is used to define deceleration time, and therefore as y approaches 1, the exact deceleration time is likely to overestimate the visual best fit triangle based DT . The inflection point DT , however, provides a reasonable estimate of the visual best fit triangle. See text for details.

Figure 12.3 provides valuable insights into the transition between underdamped and overdamped kinematic regimes. It is natural to conclude that an important transition occurs at the point in the underdamped regime where the two AT/DT expressions are equal and cross over. This crossover can be numerically determined and occurs approximately at $y=0.65042$. Below this y value both the exact and inflection-point based DT are close in value, and significantly beyond this y -value the two DT expressions diverge. Plugging in this value to the expressions for AT/DT, we find that it corresponds to $DT/AT=2.64$. Thus, when the deceleration time of an E-wave exceed the 2.64 times the acceleration time, then the exact expression for deceleration time will be expected to inappropriately reflect the visually determined clinical deceleration time. However, the wave is still expected to be in the underdamped regime.

To determine the point where the wave is in the overdamped regime, we must consider value of AT/DT at $y=1$. This provides a natural transition from underdamped to overdamped physiology from E-wave asymmetry alone, and may be determined easily by plugged $y=1$ into Eq 12.20 above:

$$\frac{AT_{over}}{DT_{over}} = 1 - 2e^{\Upsilon(1)} \quad \text{Equation 12.24}$$

To make progress, we must evaluate at 1:

$$\Upsilon(1) = -\frac{1}{2} \lim_{z \rightarrow 0} \left(\ln \left(\frac{1+z}{1-z} \right)^{\frac{1}{z}} \right), \quad z = \sqrt{1-y^{-2}} \quad \text{Equation 12.25}$$

expanding around $z=0$:

$$\Upsilon(1) = -\frac{1}{2} \lim_{z \rightarrow 0} \left(\frac{1}{z} (z - z^2 \dots) - \frac{1}{z} (-z - z^2 \dots) \right) = -1 \quad \text{Equation 12.26}$$

Thus at the critical damping limit ($y=1$), we have:

$$\frac{AT_{over}}{DT_{over}} = \frac{e-2}{e} = 0.264 \quad \text{Equation 12.27}$$

Thus, when deceleration time exceeds 3.78 times the acceleration time, we expect the E-wave to follow overdamped rather than underdamped kinematics. This analysis suggests that we must extend our equations in the underdamped regime to include both the exact DT case (consistent with the underdamped equation for c , k , and x_0 in terms of AT, DT, and E_{peak} above), as well as the inflection point based DT. As we show in Chapter 2, the inflection point based expression for DT in the underdamped regime is:

$$DT = \frac{AT}{1 - \frac{v(2AT)}{v(AT)}} = \frac{1}{\sqrt{k}} \frac{\frac{\cos^{-1}(y)}{\sqrt{1-y^2}}}{1 - 2ye \frac{-y \cos^{-1}(y)}{\sqrt{1-y^2}}} \quad \text{Equation 12.28}$$

Thus, applying Eq 12.2 from above, the ratio of AT to DT' in the underdamped regime is

$$\frac{AT}{DT} = 1 - 2ye \frac{-y \cos^{-1}(y)}{\sqrt{1-y^2}} \quad \text{Equation 12.29}$$

Just as in the overdamped case above, this equation may be numerically inverted to yield a value for y given AT and DT values. Once y is determined, it may be plugged back into the exact expression for AT to find k , and then y and k yield c . Finally plugging those values into the expression for x_0 provides an expression for x_0 in terms of AT, DT, and E_{peak} . This analysis only applies in the regime where $2.64 < DT/AT < 3.78$, where the kinematics are underdamped but approaching critical damping.

12.2.2 Implementation of Triangle Based Fitting

Taken together the equations and insight above suggest a novel and simplified approach to model based image analysis for PDF parameter extraction from transmitral velocity contours. A summary of the novel methodology is provided in Figure 12.5 below.

Figure 12.5 demonstrates the approach for both E-wave and A-wave fitting using conventional clinically determined triangles. The methodology is far simpler than current inverse solution methods for PDF parameter extraction. With this conventional based analysis, given an acquired E-wave, a user needs to first determine the velocity and time scale for the E-wave image. Next the peak point must be chosen, thereby defining E_{peak} . Once the peak is chosen the cursor may be positioned along the deceleration portion of the wave to set the deceleration time

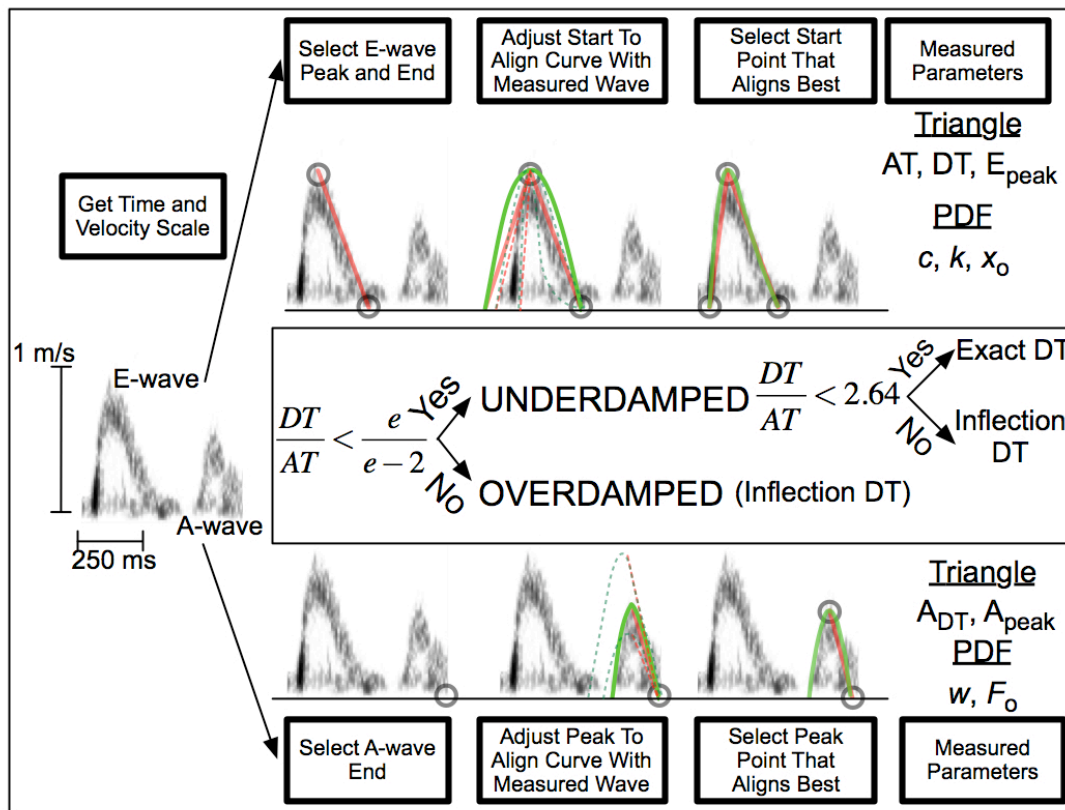


Figure 12.5. Summary of the methodology for extracting PDF parameters from triangle based analysis alone. Top panel summarizes E-wave fitting approach, which requires determination of 3 triangle points. Bottom pane summarizes A-wave fitting approach, which requires only the end and peak points of the triangle. See text for details.

(DT). Lastly the acceleration time must be set, and to aid in the fitting process the PDF model-predicted curvilinear fit to the E-wave may be superimposed in real-time as the investigator adjusts the start cursor position before setting the AT. The superimposed fit is dynamically generated using the set E_{peak} and DT values and the changing AT value. If $DT/AT > 3.78$ then the overdamped equations are used to extract k , c , and x_0 . (Equations 12.21-23) If $DT/AT < 2.64$ then the exact underdamped equation are applied (Equations 12.7-8, 12.10). If $2.64 < DT/AT < 3.78$ then the underdamped equations are applied but the DT is expressed in terms of the inflection point velocity, rather than in terms of the exact DT expression (Equations 12.2.9). Once the user is satisfied with the alignment of the superimposed fit and the E-wave image, they can set the start point and in so doing save the triangle AT, DT, and E_{peak} parameters, as well as the derived PDF c , k , and x_0 parameters.

The method for fitting the A-wave is similar and slightly simpler, because it only requires two points instead of 3. The user must define the end of the A-wave first, and then adjust the cursor to set the A-wave peak. As the cursor moves it defines specific A-wave peak velocities and A-wave deceleration times. These values may be plugged into Equations 12.14 and 12.15 to yield A-wave PDF parameters F_0 and ω . These values may be plugged into the A-wave velocity equation to yield a superimposed A-wave velocity contour, and the user simply must find the peak cursor position that results in the best alignment between superimposed A-wave contour and measured A-wave.

12.2.2 Initial Methodological Validation

The theoretical derivations presented above are promising in that they bridge the gap between correlative conventional clinical analysis and more mathematically complex but causal

kinematic modeling. However, the robustness of the novel simplified fitting approach must be checked against the more complex gold-standard inverse solution method for PDF parameter extraction presented in Chapter 2.

To achieve this, we perform two preliminary validation studies focused on fitting the E-wave contour by the geometric method. First, we re-evaluate already analyzed underdamped transmitral contours from the existing Cardiovascular Simultaneous Catheterization Echocardiography database for which PDF parameters have already been determined using the more complex methods described in Chapter 2, and for which triangle parameters have already been determined as well by conventional analysis. We use the determined triangle parameters (AT , DT , E_{peak}) to derive the PDF parameters according to the equations above, and compare these values to the already determined PDF parameters. Only underdamped waves were chosen for this analysis because of the small number of historical overdamped waves, and because of inconsistencies in the historical fitting of overdamped waves by triangles.

Second, 46 sample transmitral flow contours, picked from the existing Cardiovascular Simultaneous Catheterization Echocardiography, were reanalyzed using the novel methodology described above. This methodology was implemented using a custom written MATLAB graphical user interface. Two varieties of the geometric approach described above were implemented: one version requires the user to set the acceleration time first (AT-first method), while the other requires the user to set the deceleration time first (DT-first method).

In both methods the user begins by clicking on the peak of the E-wave velocity contour. In the AT-first method the user then selects the start of the wave, thereby defining the acceleration time. The cursor is then positioned along the deceleration portion of the wave, and because the cursor position defines the end of the wave and therefore the deceleration time of the

wave, the PDF parameters may be calculated in real time (from AT, E_{peak} , and DT as described above), and the model predicted velocity contour may be superimposed as the cursor position is changed. Once the user is satisfied with the agreement between the E-wave contour and the superimposed PDF velocity contour, they may click and lock in the value of deceleration time. The DT-first method is similar, with the exception that the second click defines the end of the wave, and motion of the cursor occurs along the acceleration portion of the wave. Thus in the AT-first method one is adjusting the end of the wave until a superimposed model fit agrees closely with the E-wave contour, whereas in the DT-first method one is adjusting the start of the wave until a superimposed model fit agrees with the input contour. Investigators with extensive experience in PDF analysis and conventional triangle analysis were chosen to fit the sample E-waves using the AT-first method, DT first method, and traditional model-based image processing approach described in Chapter 2, which will be referred to as the inverse solution method.

For each investigator agreement between the different methods of PDF analysis was determined by comparing c , k , and x_0 values for the same E-waves across multiple fitting approaches. Conventional triangle parameters (AT, DT, E_{peak}) and lumped PDF indexes, such as kx_0 , cE_{peak} , $1/2kx_0^2$, and KFEI were compared in a similar manner. Conventional triangle parameters were measured directly by the geometric approaches but had to be mathematically derived (using the methods described in Chapter 2) from the inverse solution derived PDF parameters.

The mean square error between the image extracted velocity contour and the inverse solution method as well as the geometric method predicted contour was also calculated and compared for each investigator. The mean square error for the PDF model is calculated from the portion of the E-wave that is selected by the user, and therefore a portion of the start and end of

the wave may not be included in the mean square error calculation. To mitigate for the variability in user determined E-wave start and end points, standardized E-wave start and end points (35% of peak velocity for start and 25% of peak velocity for end) were found. Using the standardized E-wave start and end points, standardized mean square error was determined between all E-wave contour model-based estimates and image extracted velocity contour.

In addition agreement across investigators was assessed by comparison of PDF parameters and lumped PDF indexes for a given wave and given fitting approach across different subjects. All statistical analysis was carried out using MS-Excel (Microsoft, Redmond, WA).

12.3 RESULTS

2.3.1 Historical Data

AT, DT, and E_{peak} values from 1412 underdamped E-wave were plugged into Equations 12.7-8, 12.10 to yield c , k , and x_o values which were compared to c , k , and x_o values extracted from the same waves using the inverse solution method. In addition the triangle parameters calculated from the inverse solution method fit contour were compared to the triangle parameters for the same waves measured by conventional analysis (See Figure 12.6). While peak velocity showed strong agreement across all waves, deceleration time and acceleration time showed only modest correlation. The PDF parameters c and k , which are functions of only AT and DT, similarly showed only modest correlation between geometrically predicted values and inverse solution determined values.

To test the sensitivity of the geometric approach on acceleration time, the 500 waves with closest agreement between PDF contour predicted acceleration time and geometric method measured acceleration time were chosen for a sub-analysis (Figure 12.7). Though the agreement between inverse solution PDF contour predicted deceleration time and geometric method

measured deceleration time remained weak, the correlation between inverse solution determined c and k and geometric method calculated c and k parameters improved significantly.

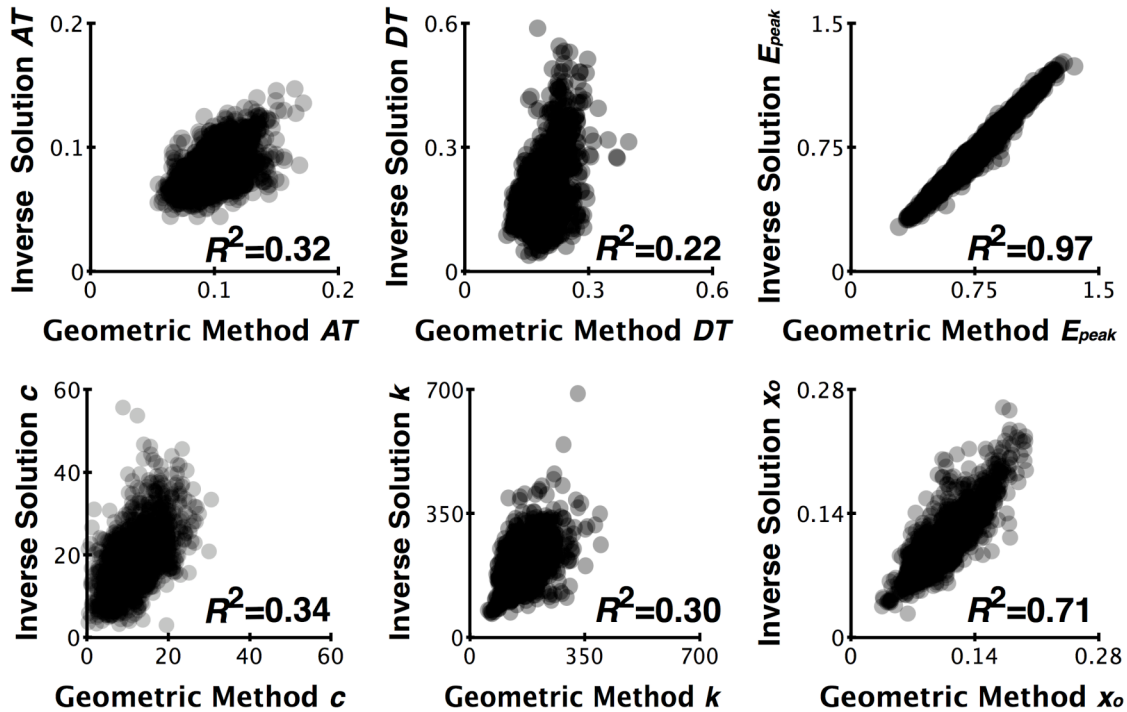


Figure 12.6. Comparison of inverse solution determined parameters to geometric method determined parameters from previously analyzed E-wave data. The units for AT and DT are seconds. The units for E_{peak} are m/s. The units for c are (1/s), for k are (1/s²), and for x_0 are (m). Note the weak correlation between inverse solution based acceleration time and triangle measured acceleration time.

12.3.2 Comparison of PDF and Triangle Parameters

Each investigator independently fit each of the 46 waves using the more complex inverse solution method, as well as the simplified AT-first and DT-first methods. Figure 12.8 shows representative data for one of the E-wave velocity contours analyzed by multiple investigators.

Results For Individual Investigators

Figure 12.9 shows the agreement between the inverse solution derived PDF parameters and the geometric approach derived PDF parameters for one of the investigators. In each panel

the y -coordinate shows the inverse solution method derived parameter, while the x -coordinate shows the geometric method derived parameter.

Blue dots indicate values derived from the AT-first method and red squares indicate values derived from the DT-first method. The average values from the two methods are shown as green triangles. The figure shows strong agreement between the inverse solution method and the geometric method, with the strongest correlation found from the average of the AT-first and DT-first methods. Table 12.1 provides r^2 values between inverse solution derived PDF parameters and geometric approach derived parameters for each investigator.

Along the bottom row, Figure 12.9 demonstrates the correlation between triangle

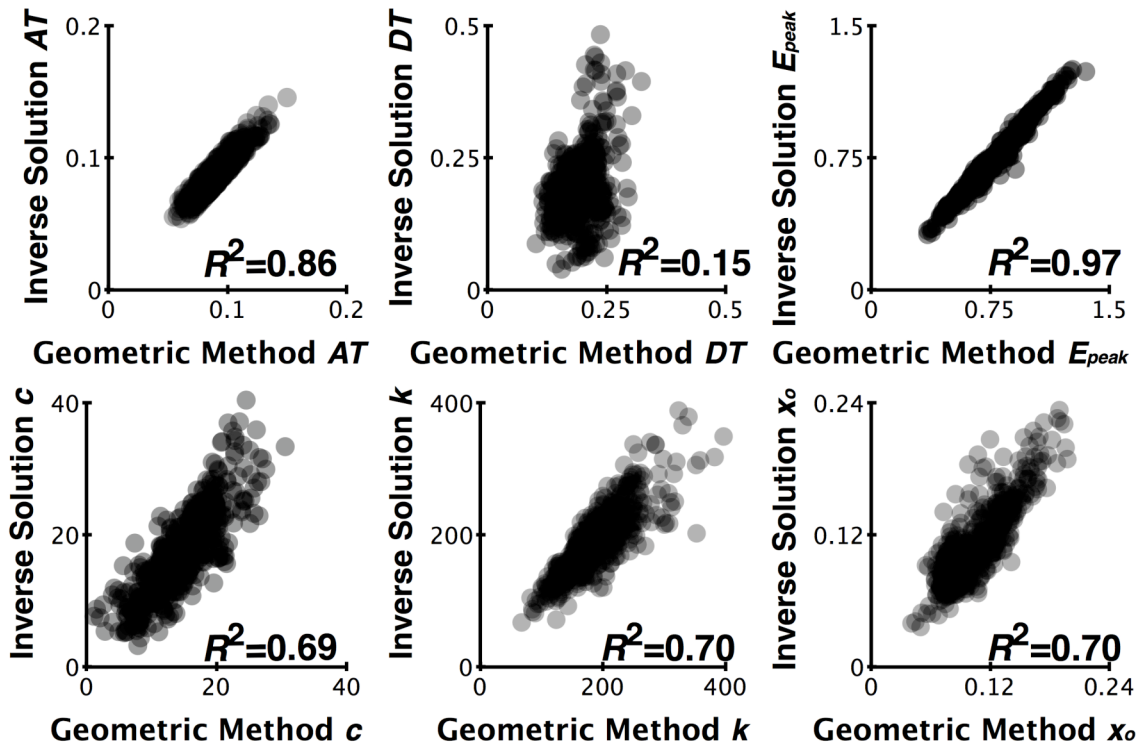


Figure 12.7. Comparison of inverse solution determined parameters to geometric method determined parameters from previously analyzed E-wave data, filtered for close agreement between triangle determined and PDF-model determined acceleration time (AT). The units for AT and DT are seconds. The units for E_{peak} are m/s. The units for c are $(1/s)$, for k are $(1/s^2)$, and for x_0 are (m). Note the more accurate agreement between geometric method and gold-standard inverse solution determined c and k values compared to Figure 12.6. See text for details.

parameters defined by the inverse solution derived PDF parameters (y -axis), and the directly measured triangle parameters by the AT-first and DT-first geometric methods. While strong agreement is seen for E_{peak} and AT, DT values show weak agreement between methods. Table 12.1 provides the r^2 values between inverse solution derived triangle parameters and directly measured triangle parameters for each investigator.

For each investigator the mean square error between model-predicted fit and input velocity data was lowest when the inverse solution method was applied. The mean square error based on standardized E-wave start and end was consistently higher than mean square error based on user defined

wave start and end. Mean square errors were similar across different fitting methods for investigator 1 but showed more variation for investigators 2 and 3. See Table 12.2 for details.

Interobserver Variability

Figure 12.10 provides a summary of the interobserver variability for PDF parameters extracted for E-wave contours by multiple methods. Data shaded in blue shows a comparison of inverse solution extracted parameters between investigators, and data shaded in red shows a

Table 12.1 Correlation coefficient (r^2) between inverse solution determined and geometric method determined PDF and triangle parameters.

	r^2		
c	1	2	3
AT-first	0.83	0.62	0.77
DT-first	0.85	0.68	0.62
AT-DT average	0.89	0.71	0.74
k			
AT-first	0.7	0.6	0.7
DT-first	0.8	0.7	0.5
AT-DT average	0.87	0.71	0.69
x_0			
AT-first	0.95	0.87	0.94
DT-first	0.96	0.9	0.9
AT			
AT-first	0.7	0.55	0.74
DT-first	0.78	0.53	0.72
AT-DT average	0.82	0.59	0.76
DT			
AT-first	0.15	0.28	0.25
DT-first	0.15	0.19	0.16
AT-DT average	0.16	0.27	0.23
E_{peak}			
AT-first	0.99	0.98	0.97
DT-first	0.99	0.98	0.97
AT-DT average	0.99	0.98	0.97
AT-DT average	0.96	0.92	0.94

c - PDF model damping parameter; k - PDF model stiffness parameter; x_0 - PDF model initial displacement; AT- Triangle E-wave acceleration time; DT- Triangle E-wave deceleration time; E_{peak} - E-wave peak velocity. Correlations are shown for investigators 1, 2, and 3.

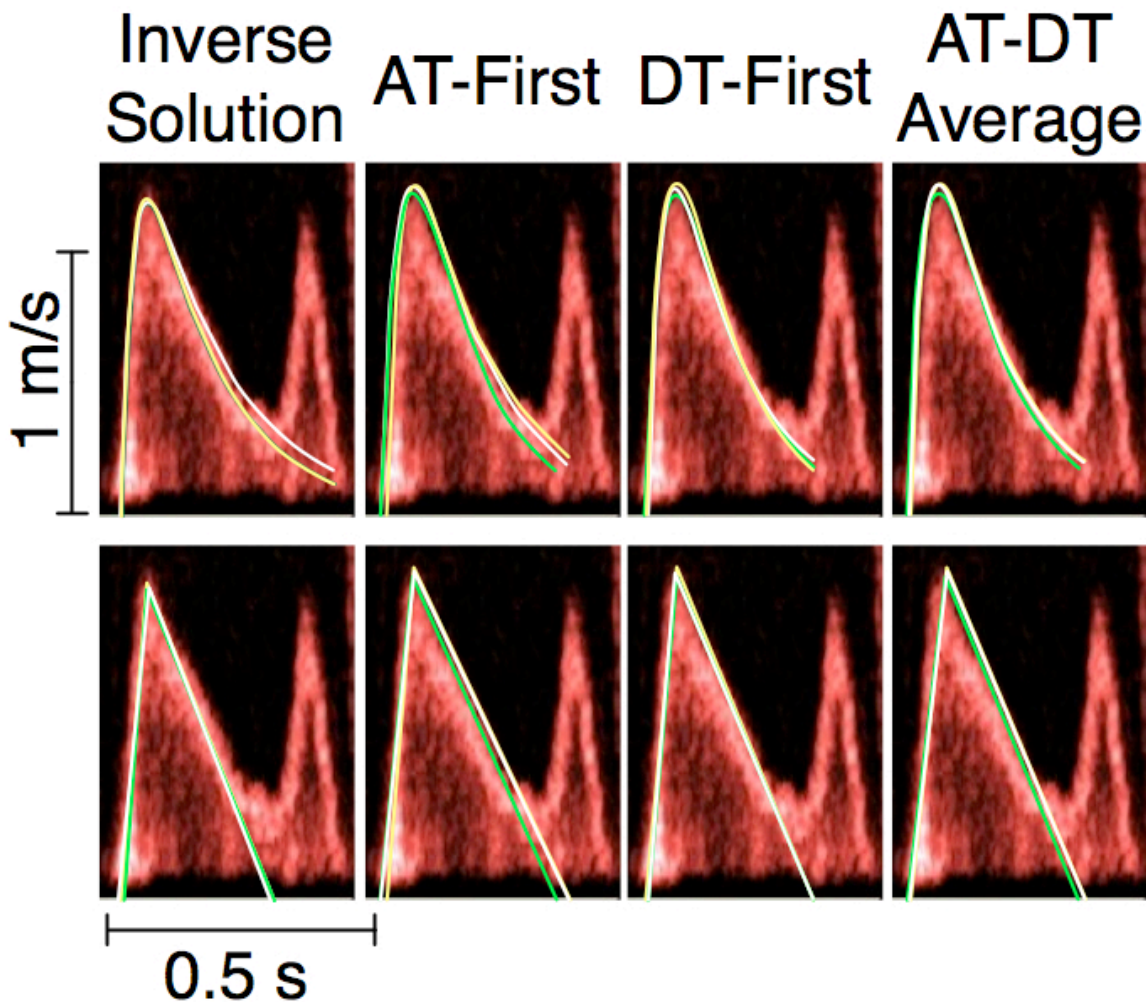


Figure 12.8. Multiple fitting approaches applied to the same E-wave. In each panel the fits from independent investigators are superimposed (white, green, and yellow curves), the top panels show the PDF model contour while the lower panels show the equivalent triangle fit to the wave. For the inverse solution approach the triangle is calculated from the model fit, while for the AT-first, DT-first, and AT-DT average approach the triangle parameters are measured directly. Note closer agreement between investigators in the DT-first and AT-DT first panels, compared to the AT-first panel. See text for details.

comparison of averaged geometric method parameters between investigators. Interobserver variability, defined as the difference between investigator determined parameters normalized to the average of the same parameters, is shown in Table 12.3 for both PDF and triangle parameters. The interobserver variability was highest, when AT-first derived parameters were compared between investigators. Interobserver variability was similar when determined from

inverse solution derived parameters or from the average of the AT first and DT-first geometric methods.

12.3.3 Comparison of PDF

Lumped Indexes

Figure 12.11 shows the agreement between inverse

solution derived PDF lumped indexes and equivalent geometric approach derived lumped PDF

indexes for one of the investigators, and Table 12.4 provides the r^2 values for all investigators. In

Table 12.2 Mean Square Error To Input Velocity Contour For Each Investigator

	1	2	3
<i>User Set Wave Start and End</i>			
Inverse Solution MSE	0.001 ± 0.001	0.004 ± 0.008	0.004 ± 0.007
AT-first MSE	0.006 ± 0.007	0.012 ± 0.012	0.024 ± 0.050
DT-first MSE	0.008 ± 0.016	0.008 ± 0.010	0.031 ± 0.082
AT-DT average MSE	0.004 ± 0.003	0.008 ± 0.010	0.025 ± 0.065
<i>Standardized Wave Start and End</i>			
Inverse Solution MSE	0.002 ± 0.004	0.008 ± 0.018	0.004 ± 0.006
AT-first MSE	0.007 ± 0.009	0.021 ± 0.035	0.008 ± 0.009
DT-first MSE	0.009 ± 0.009	0.035 ± 0.023	0.009 ± 0.011
AT-DT average MSE	0.009 ± 0.009	0.023 ± 0.027	0.011 ± 0.009

MSE- Mean square error; AT- acceleration time; DT-deceleration time. MSE determined from both user defined E-wave limits and standardized E-wave limits. MSE values are shown for investigators 1, 2, and 3.

Table 12.3 Interobserver variability for PDF model parameters and conventional triangle parameters measured by multiple approaches

	<i>PDF Parameters</i>			<i>Conventional Triangle Parameters</i>		
	1 to 2	1 to 3	2 to 3	1 to 2	1 to 3	2 to 3
<i>c</i>				<i>AT</i>		
Inverse Solution	21%	21%	33%	Inverse Solution	11%	9%
AT-First	51%	39%	77%	AT-First	13%	24%
DT-First	20%	32%	24%	DT-First	12%	16%
AT-DT Average	24%	22%	29%	AT-DT Average	10%	13%
<i>k</i>				<i>DT</i>		
Inverse Solution	17%	11%	19%	Inverse Solution	14%	11%
AT-First	14%	35%	30%	AT-First	23%	11%
DT-First	16%	21%	17%	DT-First	7%	13%
AT-DT Average	10%	19%	18%	AT-DT Average	12%	9%
<i>x_o</i>				<i>E_{peak}</i>		
Inverse Solution	12%	11%	11%	Inverse Solution	4%	3%
AT-First	26%	12%	23%	AT-First	3%	2%
DT-First	9%	11%	10%	DT-First	3%	3%
AT-DT Average	15%	8%	11%	AT-DT Average	2%	2%

c- PDF model damping parameter; *k*- PDF model stiffness parameter; *x_o*- PDF model initial displacement; AT- Triangle E-wave acceleration time; DT- Triangle E-wave deceleration time; *E_{peak}*- E-wave peak velocity. Interobserver variability is calculated in pairs between all 3 investigators.

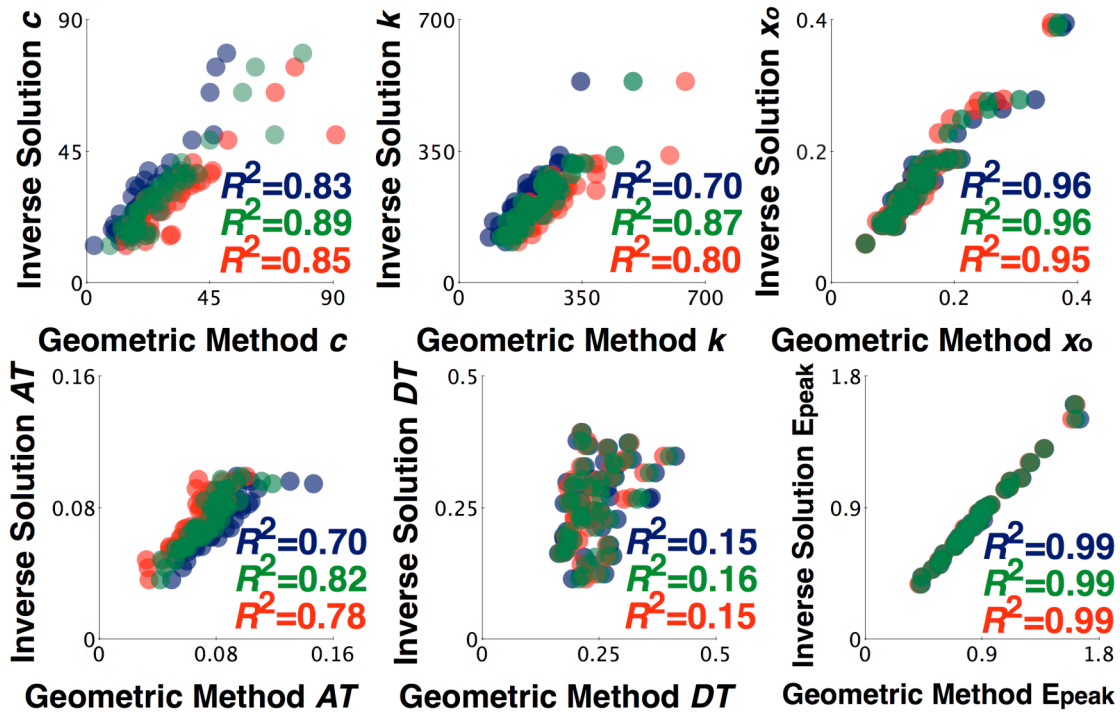


Figure 12.9. Top row demonstrates the correlation between the inverse solution derived PDF parameters and the simplified geometric approach derived parameters. The bottom row demonstrates the correlation between the E-wave triangles defined by each method. E-wave triangle parameters are directly measured by the geometric approaches (x-coordinate) and mathematically calculated in the inverse solution approach (y-coordinate) Data in blue is determined by the AT-first method, data in red is determined by the DT-first method, and data in green is the average of the AT-first and DT-first methods See text for details.

each panel the y-coordinate shows the inverse solution method derived parameter, while the x-coordinate shows the geometric method derived parameter. Stronger agreement is seen in each subject for lumped PDF indexes, compared to the correlations presented for individual PDF parameters.

Interobserver Variability

Interobserver variability for PDF lumped indexes, defined as above, is shown in Table 12.5. Similar to findings for individual PDF parameters, the interobserver variability was highest when AT-first derived parameters were compared between investigators.

12.4 DISCUSSION

Nearly all PDF model-based studies rely on extraction of PDF kinematic model parameters from clinically measured transmitral flow contours. The currently accepted methodology for PDF parameter extraction requires familiarity with the model and mathematical methods and differs significantly from conventional analysis techniques. However, a deep mathematical connection exists between conventional analysis techniques, which fit E-wave contours with triangles, and the more mathematically complex methods for PDF parameter extraction. We capitalize on this mathematical connection in the current work and define a novel method by which PDF parameters may be extracted from triangle approximations alone. We test the mathematical validity of the method using 1412 preexisting E-waves. We implement the novel methodology programmatically and validate the robustness of the method by analysis of 46 representative E-waves. Each E-wave is analyzed by 3 independent investigators using both the novel methodology and gold standard inverse solution based methodology,

Table 12.4 Correlation coefficient (r^2) between inverse solution determined and geometric method determined PDF lumped indexes.

y	r^2		
	1	2	3
AT-first	0.85	0.61	0.81
DT-first	0.87	0.66	0.68
AT-DT average	0.9	0.69	0.79
<i>kx_o</i>			
AT-first	0.93	0.84	0.9
DT-first	0.93	0.88	0.83
AT-DT average	0.91	0.89	0.88
<i>cE_{peak}</i>			
AT-first	0.92	0.8	0.89
DT-first	0.9	0.87	0.81
AT-DT average	0.92	0.87	0.87

y - damping to stiffness ratio; kx_o - peak force driving E-wave filling; cE_{peak} - peak force opposing E-wave filling. Correlations are shown for investigators 1, 2, and 3.

Table 12.5 Interobserver variability for PDF model lumped indexes.

	1 to 2	1 to 3	2 to 3
	<i>kx_o</i>		
Inverse Solution	15%	15%	23%
AT-First	25%	32%	50%
DT-First	16%	23%	17%
AT-DT Average	16%	18%	24%
<i>cE_{peak}</i>			
Inverse Solution	20%	22%	33%
AT-First	53%	41%	80%
DT-First	21%	32%	23%
AT-DT Average	25%	24%	33%
y			
Inverse Solution	16%	18%	26%
AT-First	50%	25%	65%
DT-First	15%	24%	19%
AT-DT Average	22%	15%	23%

y - damping to stiffness ratio; kx_o - peak force driving E-wave filling; cE_{peak} - peak force opposing E-wave filling. AT- Triangle E-wave acceleration time; DT- Triangle E-wave deceleration time; E_{peak} - E-wave peak velocity. Interobserver variability is calculated in pairs between all 3 investigators.

and parameters and indexes derived by different methods are compared. The novel methodology demonstrates close agreement to the gold standard approach and is reproducible across multiple investigators.

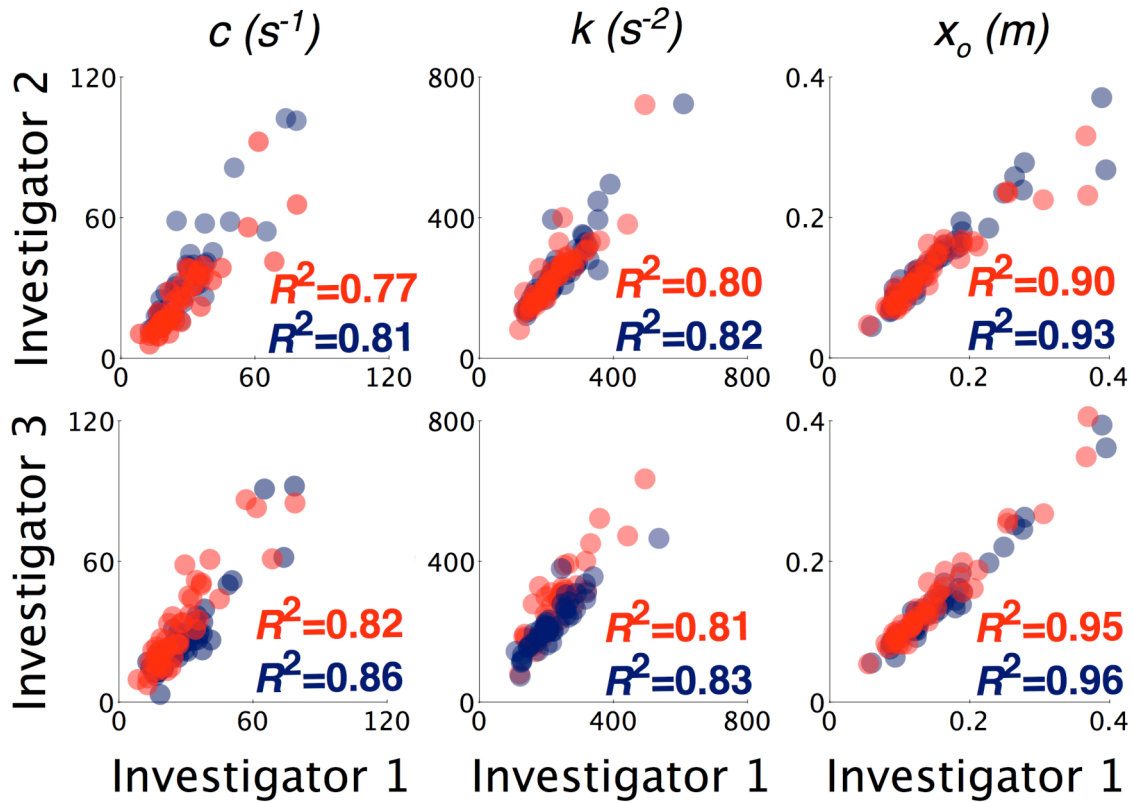


Figure 12.10. Comparison between individual investigators of PDF parameters values, measured by inverse solution and geometric methods. See text for details.

12.4.1 Sensitivity of Novel Methodology to Choice of AT and DT

The mathematical analysis presented in Figure 12.1 suggests that the PDF parameters are more sensitive to changes in acceleration time than deceleration time, and the results in Figure 12.7 further support that view. Importantly, Figure 12.7 demonstrates that errors in deceleration time do not significantly impact the ability of the geometric method to determine PDF parameters accurately.

The sensitivity of the method to acceleration time is likely related to a fundamental

limitation of the PDF model at the start of the E-wave. As described in greater detail in Chapter 2, the PDF model assumes that the atrioventricular pressure gradient driving flow begins at a maximum value and decays as filling progresses. This implies that the E-wave begins with a non-zero slope and has no inflection point during the acceleration portion. Clinical data shows, however, that the atrioventricular pressure gradient is zero at MVO and grows within a few ms to its maximum before decaying. Furthermore, in the absence of valve noise, one may routinely observe an inflection point in the E-wave acceleration portion. The inflection point in the E-wave has the effect of extending the visual start of the E-wave to a time earlier than the time predicted by the PDF model. Indeed the correlation between PDF model calculated acceleration time and geometrically measured acceleration time in Figure 12.6 is below the line of identity, suggesting that the PDF model systematically underestimates the geometrically determined E-wave acceleration time.

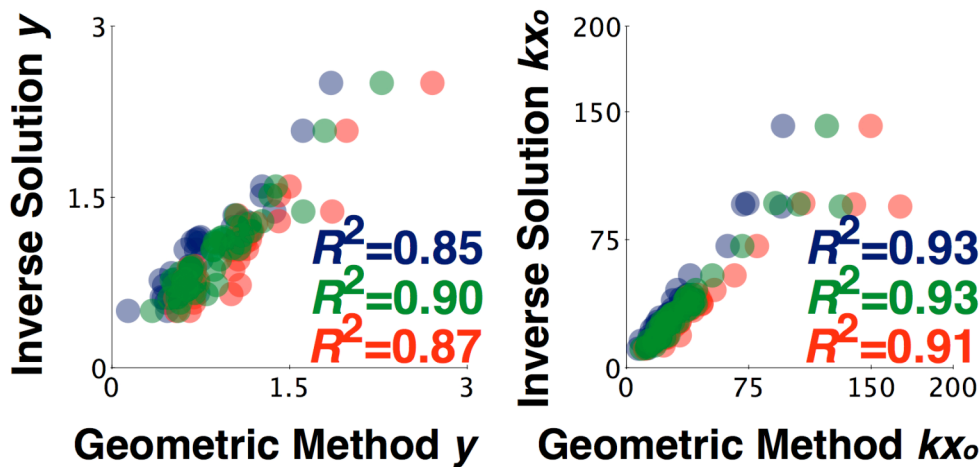


Figure 12.11. Top row demonstrates the correlation between the inverse solution derived PDF lumped indexes and the simplified geometric approach derived lumped indexes measured by investigator 1. Data in blue is determined by the AT-first method, data in red is determined by the DT-first method, and data in green is the average of the AT-first and DT-first methods. See text for details.

The sensitivity of the geometric method to acceleration time provides insight into the strengths and weaknesses of the AT-first and DT-first methods described above. Both methods

correctly begin with the user selecting the E-wave peak velocity, which, as the results demonstrate, investigators choose with high accuracy.

Next the user must set either the start of the wave (AT-first method) or the end of the wave (DT-first method), and understanding which choice is best requires a deeper understanding of the last step in the geometric fitting process. In the last step, the user must finish the fit by moving a cursor in order to set the remaining unknown parameter. However, the dynamic position of the cursor at any time defines the last unknown parameters, and with all parameters set, the PDF parameters are known and the resulting E-wave velocity contour is determined exactly. Thus, during the last step a superimposed velocity contour can be displayed in real time, consistent with the user defined cursor position. Therefore the user has a guide, like a French curve, that appears over the raw E-wave as they set the final point. This makes setting the final point much easier and more reproducible. Because the choice of acceleration is the most critical to the accuracy and reproducibility of the method, determining the acceleration time last with the aid of the superimposed velocity contour (as is the case in the DT-first method) represents the optimal method for geometrically estimating the PDF parameters. Indeed the interobserver variability was significantly lower when the DT-first method was applied than when the AT-first method was applied (Table 12.3 and 12.5).

Interestingly an average of the AT-first and DT-first method also provided an advantage to the AT-first method, and in some cases provided the best strongest agreement with the inverse solution method determined parameters. This approach would require measuring each E-wave twice, and therefore is not ideal, but warrants further consideration.

12.4.2 Mathematical Recasting of Previous Results

Recasting the PDF parameters in terms of triangle parameters allows one to determine novel geometric expressions for lumped PDF parameters that have in the past shown clinical and physiological utility. In the analysis below we focus on the underdamped case which can be solved exactly.

One of these lumped parameters, y , was already discussed in the derivation above. The index y is defined by the ratio of c and $2\sqrt{k}$, and therefore represents a dimensionless, relative damping to stiffness ratio that defines the kinematic filling regime. The geometric expansion for y in the underdamped limit is:

$$y = \frac{c}{2\sqrt{k}} = \cos\left(\pi \frac{AT}{AT + DT}\right) \quad \text{Equation 2.30}$$

which once again demonstrates the deep connection between E-wave asymmetry and balance between damping and stiffness effects.

Geometrically Recasting kx_o and cE_{peak}

kx_o has been shown in previous work to be a noninvasive surrogate for the peak atrioventricular pressure gradient. Furthermore, in conjunction with the peak force opposing diastolic filling, cE_{peak} , kx_o was used in Chapters 8-10 to define a load independent index of diastolic function. Applying Equations 12.7 and 12.10 above, kx_o may be written in terms of E_{peak} , AT , and DT :

$$kx_o = E_{peak} \frac{\pi}{(AT + DT)} \csc\left(\pi \frac{AT}{AT + DT}\right) e^{\left(\pi \frac{AT}{AT + DT}\right)} \cot\left(\pi \frac{AT}{AT + DT}\right) \quad \text{Equation 2.31}$$

cE_{peak} may be similarly written as:

$$cE_{peak} = E_{peak} \frac{2\pi}{(AT + DT)} \cot\left(\pi \frac{AT}{AT + DT}\right) \quad \text{Equation 2.32}$$

and the ratio of kx_o and cE_{peak} , which defines the slope of the line defined by the cE_{peak} , kx_o coordinate of any E-wave and the origin, is then a function of AT and DT alone:

$$\frac{kx_o}{cE_{peak}} = \frac{1}{2} \sec\left(\pi \frac{AT}{AT+DT}\right) e^{\left(\pi \frac{AT}{AT+DT}\right) \cot\left(\pi \frac{AT}{AT+DT}\right)} \quad \text{Equation 2.33}$$

Thus the load independent index of diastolic function may be derived from AT, DT, and E_{peak} values alone, and the location of any E-wave in the kx_o vs cE_{peak} plane may be understood in terms of E-wave asymmetry.

Geometrically Recasting $\frac{1}{2}kx_o^2$

The potential energy of the oscillator is defined by $\frac{1}{2}kx_o^2$, and as discussed in the Appendix, $\frac{1}{2}kx_o^2$ is the noninvasive analogue of the PV loop diastolic recoil energy. The geometric expression for $\frac{1}{2}kx_o^2$ is particularly simple:

$$\frac{1}{2}kx_o^2 = (E_{peak})^2 \left(\frac{1}{2} e^{2\left(\pi \frac{AT}{AT+DT}\right) \cot\left(\pi \frac{AT}{AT+DT}\right)} \right) \quad \text{Equation 2.34}$$

Thus one can easily appreciate that when the E-wave is symmetric, the initial potential energy and maximum kinetic energy are equal, as expected. As the wave becomes asymmetric, the initial potential energy becomes greater than the maximum kinetic energy, indicating energy loss.

Geometrically Recasting VTI and KFEI

A particularly interesting application is determination of E-wave contour area. The area is routinely approximated as the triangular area defined by a base of (AT+DT) and height of E_{peak} , but applying the equations above and from Chapter 2, one can express the E-wave velocity time

integral (VTI) as:

$$VTI = E_{peak} \frac{(AT + DT)}{\pi} \sin\left(\pi \frac{AT}{AT + DT}\right) \left(e^{\left(\pi \frac{AT}{AT + DT}\right) \cot\left(\pi \frac{AT}{AT + DT}\right)} + e^{-\left(\pi \frac{DT}{AT + DT}\right) \cot\left(\pi \frac{AT}{AT + DT}\right)} \right)$$

(Equation 2.35)

This is a fairly complex expression, though it can be greatly simplified by normalizing it to the VTI defined by the symmetric E-wave. This provides a simple expression for the kinematic filling efficiency index described in Chapter 2 and Chapter 8:

$$KFEI = \frac{1 + e^{-\pi \cot\left(\pi \frac{AT}{AT + DT}\right)}}{2} \quad \text{Equation 2.36}$$

In previous work KFEI has successfully differentiated between normal LVEF diabetics and matched non-diabetic controls, even when traditional E-wave parameters failed to do so. However, in that work the more complex inverse solution method was employed in order to calculate KFEI, and therefore application of KFEI in the clinical setting would have posed a challenge. The simpler expression above is in terms of conventional E-wave parameters, and therefore it is intriguing to consider if application of this simplified expression for KFEI to the previous diabetic and non-diabetic E-waves would yield the same results.

We tested this by reanalyzing the data from the previous study, where 5-10 E-waves were analyzed in 34 patients with normal systolic function (16 diabetic and 18 well matched non-diabetic controls). Conventional E-wave parameters, as well as the model based filling efficiency, and filling efficiency defined by AT and DT values, were calculated for each measured beat and compared between groups.

In agreement with the previously published results, end-diastolic volumes and pressures, E/A ratio, and E-wave DTs were indistinguishable between groups. While conventional E-wave

parameters failed to differentiate between diabetic and nondiabetic groups ($p>0.1$), the simplified filling efficiency in Equation 12.36, defined by E-wave AT and DT values alone, was significantly different between groups ($p<0.003$). Thus while DT alone failed to differentiate subjects, proper mathematical incorporation of AT and DT into a causally based kinematic index successfully differentiated between groups.

12.5 LIMITATIONS

The primary advantage of the inverse solution method for PDF parameter extraction is that it minimizes the error between model predicted fit and input data, thereby producing a unique, best fit set of parameters. In addition, the standard deviation of the parameters may in principle be determined, as long as the error in the input data is known. The geometric approach described in the current chapter is not based on a minimization procedure however, and relies on the user finding a close fit ‘by eye’ between model-predicted contour and input. This approach therefore may not yield best-fit parameters or error estimates for the parameters.

While this seems like a significant limitation from a theoretical perspective, the results of the current study demonstrate that the ‘by eye’ approach results in parameters that agree strongly with parameters determined through mathematical error minimization. Furthermore the minimization approach is limited by image quality, user selection of appropriate grayscale cutoff for maximum velocity envelope, and user selection of start and end points of the wave. While the minimization algorithm provides a best fit to the input data, a great deal of user input goes into choosing the input data, and therefore user bias can never be completely eliminated.

Furthermore, alternative methods of analysis must provide consistent measures of the same event, and therefore the PDF model contour must be consistent with the geometrically defined E-

wave. While the PDF model captures curvature of the wave, something that the triangle approximates with straight lines, the width and relative asymmetry of the wave must be consistent between methods. Historically conventional analysis and inverse solution based PDF analysis have not provided identical estimates of E-wave width and asymmetry (Figure 12.6 lower panel). The geometric approach, on the other hand, by design ensures consistency between conventional triangle shape and PDF contour derived triangle shape. Thus while the geometric approach does not provide best-fit parameters, it provides the advantage of being simple to implement and consistent with established clinical parameters and methods.

Furthermore if one has access to the raw E-wave velocity data, one could perform a minimization algorithm where error between predicted wave and input data is minimized while varying AT, DT or both AT and DT after E_{peak} is set either manually or in an automated fashion.

12.6 CONCLUSIONS

The results of this Chapter demonstrate the validity of a novel approach to PDF model parameter determination that makes use of the conventional triangle approximation to E-wave shape and uses AT, DT and E_{peak} as inputs. Furthermore, maximum robustness is achieved when the process is implemented by using the DT and E_{peak} components first. Although the method is inherently achieved ‘by-eye’, results compare favorably with inverse mathematical approaches where measurements of goodness of fit are available. Implementation of this approach in a graphical user interface on an echocardiographic platform will allow any clinician to quickly apply the PDF method, and to easily determine the indexes described throughout the thesis, including the load independent index of diastolic function, from their own data sets, using methods nearly identical to the methods that they routinely apply in the clinic or laboratory. Initial results

indicate that this methodology will be widely applicable and easily reproducible by any investigator independent of their mathematical sophistication. Further work applying and validating these novel methods using data from previously published PDF studies, thereby mapping decades of PDF model related research onto the established vocabulary of clinical echocardiography, is warranted.

In this thesis as a whole we have demonstrated the power of kinematic modeling. We have added novel insights and discovered new clinical indexes related to the fundamental determinants of diastolic function. We have shown definitively that the ventricle is a suction pump, and as such attains equilibrium at diastasis. We extended this result beyond the theoretical insight to a practical application in the case of atrial fibrillation and the determination of stiffness. We have provided extensive novel insights into viscoelasticity, the other intrinsic determinant of diastolic function, and we have resolved a long-standing issues in the field related to the confounding effect of load. All of these results may be more easily shared with the cardiology community given the work of the current chapter, and future effort will be focused toward that end.

APPENDIX

ABSTRACTS SHOWING ADDITIONAL CONTRIBUTIONS

1. Derivation of the fluid mechanics to left ventricular early, rapid filling relation, with in-vivo validation

Erina Ghosh, Leonid Shmuylovich, Sándor J. Kovács

During early rapid filling, (Doppler E-wave) blood aspirated by the left ventricle (LV) generates an asymmetric toroidal vortex whose development has been quantified using vortex formation time (VFT), a dimensionless index defined by the length to diameter ratio of the aspirated (equivalent cylindrical) fluid column. Since LV wall-motion (kinematics) generates the atrioventricular (AV) pressure gradient resulting in the E-wave and its associated vortex formation, we hypothesized that the causal relation between VFT and diastolic function (DF), parametrized by stiffness, relaxation, and load, can be elucidated via kinematic modeling.

Gharib et al approximated Doppler E-wave shape as a triangle and calculated VFT_{Gharib} as triangle (E-wave) area (cm) divided by peak mitral orifice diameter (cm). We used a validated, kinematic model of filling for the E-wave to calculate $VFT_{kinematic}$ as curvilinear E-wave area divided by peak effective (M-mode derived) orifice diameter. The derived fluid mechanics to left ventricular early, rapid filling relation predicts VFT to be a function of the peak E-wave to peak mitral annular tissue velocity (E') ratio as $(E/E')^{3/2}$.

Validation utilized 262 cardiac cycles of simultaneous echocardiographic-high fidelity hemodynamic data from 12 subjects. VFT_{Gharib} and $VFT_{kinematic}$ were calculated for each subject and were strongly correlated ($R^2=0.66$). In accordance with prediction the $VFT_{kinematic}$ to $(E/E')^{3/2}$ relationship was validated ($R^2 = 0.63$).

We conclude that $VFT_{kinematic}$ is a DF index computable from E-and E'-waves in terms of lumped stiffness, relaxation and load parameters. Validation of the fluid mechanics to chamber kinematics relation unites previously unassociated DF assessment methods and elucidates the mechanistic basis of the strong correlation between VFT and $(E/E')^{3/2}$.

2. The Thermodynamics of Diastole: Kinematic Modeling based Derivation of the P-V Loop to Transmitral Flow Energy Relation, with In-Vivo Validation

Sina Mossahebi, Leonid Shmuylovich, Sándor Kovács

Pressure-volume (P-V) loop based analysis facilitates thermodynamic assessment of LV function in terms of work, and energy. Typically these quantities are calculated for a cardiac cycle using the entire P-V loop, though thermodynamic analysis may be applied to selected phases of the cardiac cycle, specifically, diastole. Diastolic function is routinely quantified non-invasively by analysis of Doppler echocardiographic E-wave contours. The first law of thermodynamics requires that energy E computed from the Doppler E-wave ($E_{E\text{-wave}}$) and the same portion of the P-V loop ($E_{PV\text{-E-wave}}$) should be correlated. No previous studies have calculated these energies or experimentally tested their predicted relationship for validation. To test the hypothesis that $E_{PV\text{-E-wave}}$ and $E_{E\text{-wave}}$ are equivalent we employed a validated kinematic model of filling to derive the expression for $\mathcal{E}_{E\text{-wave}}$ in terms of chamber stiffness (k), relaxation/viscoelasticity (c) and load (x_0). For validation, simultaneous invasive (Millar) P-V data and non-invasive echocardiographic data from 11 subjects (185 total cardiac cycles) with normal diastolic function were analyzed. Kinematic modeling based $\mathcal{E}_{E\text{-wave}}$ for each E-wave was computed and compared to $\mathcal{E}_{PV\text{-E-wave}}$ calculated from simultaneous P-V data. Linear regression yielded: $\mathcal{E}_{PV\text{-E-wave}} = \alpha \mathcal{E}_{E\text{-wave}} + b$ ($R^2 = 0.68$), where $\alpha = 0.96$, and $b = 6E - 05$.

We conclude that kinematic modeling based analysis of the energy for suction initiated early rapid filling is an accurate measure of the energetics of filling provided by simultaneous P-V data.

3. Diastolic function to cyclic variation of myocardial backscatter relation: influence of parametrized diastolic filling formalism determined chamber properties

Christopher W. Lloyd, Leonid Shmuylovich, Mark R. Holland, James G. Miller, and Sándor J. Kovács

Myocardial tissue characterization represents an extension of currently available echocardiographic imaging. The systematic variation of backscattered energy during the cardiac cycle (the “cyclic variation” of backscatter) has been employed to characterize cardiac function in a wide range of investigations. However, the mechanisms responsible for observed cyclic variation remain incompletely understood. As a step toward determining the features of cardiac structure and function that are responsible for the observed cyclic variation, the present study makes use of a kinematic approach of diastolic function quantitation to identify diastolic function determinants that influence the magnitude and timing of cyclic variation. Echocardiographic measurements of 32 subjects provided data for determination of the cyclic variation of backscatter to diastolic function relation characterized in terms of E-wave determined, kinematic model-based parameters of chamber stiffness, viscosity/relaxation, and load. The normalized time delay of cyclic variation was found to be related to the relative viscoelasticity of the chamber and predictive of the kinematic filling dynamics as determined using the parametrized diastolic filling formalism.

Leonid Shmuylovich

Washington University in St. Louis

MSTP Student

Email: leoshmu@gmail.com;

Github: <https://github.com/leoshmu>

EDUCATION

Washington University School of Medicine, St. Louis, MO 2003-15
MD/PhD, with a PhD in Physics through School of Arts and Sciences
Granted leave of absence (2010 – 2013) to pursue ed-tech startup that I co-founded

Cornell University, College of Engineering, Ithaca, NY 2000-03
BS in Chemical Engineering, Magna Cum Laude (3.98 GPA)

TEACHING

Department of Physics, Washington University in St. Louis, MO 2006
Teaching Assistant for Physics 351, Introduction to Biomedical Physics
Guest Lecturer for Physics 314, Physics of the Heart

HONORS/ AWARDS

Selected as “30 under 30” award winner by St. Louis Business Journal 2010

First Place, Washington University Olin Cup Business Plan Competition 2009

Cardiovascular Systems Dynamics Society Nico Westerhof Award for “Striking New Concepts” by Beginning Investigators. 2008

Judith Ross Academic Scholarship in Mathematics and Physics 2007,08

Cornell Merrill Presidential Scholar 2003

RESEARCH EXPERIENCE

Washington University in St. Louis, St. Louis, MO 2005-10
Cardiovascular Biophysics Lab of Dr. Sándor Kovács
Graduate Research Assistant

I completed a Physics PhD thesis titled: “Kinematic Modeling of the Determinants of Diastolic Function”. An overarching theme of my work was the application of physics and mathematical techniques to extract clinically significant parameters from previously ignored data. In total I produced 16 publications, obtained 2 patents, presented numerous abstracts and papers at national meetings, and began collaborations with industry. I successfully competed for an American Heart Association Predoctoral Fellowship to support this work.

Cornell University, Ithaca, NY 2002-03
Chemical Engineering Department, Lab of Professor Michael Shuler
Undergraduate Research Assistant

I contributed to the development of a model of the blood brain barrier consisting of astrocytes and neurons cultured on opposite sides of a customized silicon wafer.

Harvard University, Cambridge, MA 2001
 Materials Research Center, Lab of Professor Howard Stone
 Research Experience for Undergraduates Summer Student
 I studied the fluid mechanics driving the patterns that form when coffee drops, and other suspensions, dry. This work led to a paper in *Langmuir* that was featured in *Science* magazine, and has subsequently been cited in multiple industry patents.

RESEARCH SUPPORT

Completed Support

American Heart Association, Heartland Affiliate Predoctoral Fellowship 2009-10
 3rd year extension for previous award

American Heart Association, Heartland Affiliate Predoctoral Fellowship 2007-09
 Prospective Validation of a Load-Independent Index of Diastolic Function with Clinical Correlation

WORK EXPERIENCE

ClinDesk, Inc, St. Louis, MO 2013-15
 Chief Technology Officer
 ClinDesk is a non-profit corporation dedicated to open medical education and clinical resources. I focus on building fast, intuitive web applications that teach medical concepts and provide useful toolsets for clinicians.

Pearson Education, Chicaco, IL 2013
 Independent Contractor
 I worked as an independent contractor for Pearson following the acquisition of Virtual Nerd. I focused on building a fully functional HTML5 version of Virtual Nerd's Dynamic Whiteboard instructional platform, as well as the Virtual Nerd Mobile Math iOS app.

Virtual Nerd, St. Louis, MO 2008-13
 Co-Founder and Vice President of Instruction and Technology
 I co-founded Virtual Nerd near the end of my PhD training, with the goal of providing math students and teachers with the best resources and tools for instruction and remediation. I served as vice president, head of instruction, and all-purpose engineer. We grew the team to 9 full-time staff, integrated our technology with several high profile partners, and served many satisfied paying customers, including both private individuals and public institutions. In May 2013, Virtual Nerd was acquired by Pearson Education, the world's leading education company.

Kleitz Education Group, St. Louis, MO 2006-09
 Private Tutor, MCAT Instructor and Trainer
 I provided private tutoring to dozens of St. Louis area middle and high school students studying math, chemistry, and physics. I also helped design the Washington University in St. Louis MCAT course, trained several of the MCAT instructors, and taught several of the Physics sections.

I taught physics and chemistry content and testing strategies to hundreds of pre-med students in the St. Louis area.

PUBLICATIONS

PATENTS

- 1) **Shmuylovich L**, Salcman J. Whiteboard Presentation of Interactive And Expandable Content. US Patent Application WO/2010/057106, 2010.
- 2) Kovács SJ, **Shmuylovich L**, Zhang W, Chung CS. Pressure Recovery Index to Assess Cardiac Function. US Patent Application 20090209869, 2009.
- 3) Kovács SJ, **Shmuylovich L**, Chung CS. Load Independent Index of Diastolic Function. US Patent Application 20090043213, 2009.

MANUSCRIPTS

- 1) Mossahebi S, **Shmuylovich L**, Kovács SJ. The Challenge of Chamber Stiffness Determination in Chronic Atrial Fibrillation vs. Normal Sinus Rhythm: Echocardiographic Prediction with Simultaneous Hemodynamic Validation. *J Afib*. 6(3): 46-51, 2013.
- 2) Lloyd CW, **Shmuylovich L**, Holland MR, Miller JG, Kovács SJ. The diastolic function to cyclic variation of myocardial ultrasonic backscatter relation: the influence of parametrized diastolic filling (PDF) formalism determined chamber properties. *Ultrasound Med Biol*. 37(8): 1185-95, 2011.
- 3) Mossahebi S, **Shmuylovich L**, Kovács SJ. The thermodynamics of diastole: kinematic modeling-based derivation of the P-V loop to transmitral flow energy relation, with in-vivo validation. *Am J Physiol Heart Circ Physiol*. 300: H514-H521, 2011.
- 4) Ghosh E, **Shmuylovich L**, Kovács SJ. Vortex formation time-to-left ventricular early, rapid filling relation: model based prediction with echocardiographic validation. *J Appl Physiol*. 109(6): 1812-1819, 2010.
- 5) Zhang W, **Shmuylovich L**, Kovács SJ. The E-wave delayed relaxation pattern to LV pressure contour relation: model-based prediction with in vivo validation. *Ultrasound Med Biol*. 36:497-511, 2010.
- 6) **Shmuylovich L**, Chung CS, Kovács SJ. Last word on point: Counterpoint: Left ventricular volume during diastasis is the physiological in vivo equilibrium volume and is related to diastolic suction. *J Appl Physiol*. 109(2): 615, 2010.
- 7) **Shmuylovich L**, Chung CS, Kovács SJ. Point: Left ventricular volume during diastasis is the physiological in vivo equilibrium volume and is related to diastolic suction. *J Appl Physiol*. 109(2): 606-608, 2010.

8) **Shmuylovich L**, Kovács SJ. Stiffness and relaxation components of the exponential and logistic time constants may be used to derive a load-independent index of isovolumic pressure decay. *Am J Physiol Heart Circ Physiol*. 295:H2551-9, 2008.

7) Boskovski MT, **Shmuylovich L**, Kovács SJ. Transmitral Flow Velocity-Contour Variation After Premature Ventricular Contractions: A Novel Test of the Load-Independent Index of Diastolic Filling. *Ultrasound Med Biol*. 34:1901-8, 2008.

8) Zhang W, Chung CS, **Shmuylovich L**, Kovács SJ. Last Word on Viewpoint: Is Left Ventricular Volume during Diastasis the Real Equilibrium Volume and What Is Its Relationship to Diastolic Suction? *J Appl Physiol*. 105: 1019, 2008.

9) Zhang W, Chung CS, **Shmuylovich L**, Kovács SJ. Viewpoint: Is Left Ventricular Volume During Diastasis the Real Equilibrium Volume and, What is its Relationship to Diastolic Suction? *J Appl Physiol*. 105:1012-4, 2008.

10) Zhang W, Chung CS, Riordan MM, Wu Y, **Shmuylovich L**, Kovács SJ. The kinematic filling efficiency index of the left ventricle: contrasting normal vs. diabetic physiology. *Ultrasound Med Biol*. 33:842-850, 2007.

11) **Shmuylovich L**, Kovács SJ. E-wave deceleration time may not provide an accurate determination of LV chamber stiffness if LV relaxation/viscoelasticity is unknown. *Am J Physiol Heart Circ Physiol*. 292:H2712-20, 2007.

12) **Shmuylovich L**, Kovács SJ. A load-independent index of diastolic filling: model-based derivation with in-vivo validation in control and diastolic dysfunction subjects. *J Appl Physiol*. 101: 92-101, 2006.

13) **Shmuylovich L**, Shen AQ, Stone H. Surface morphology of drying latex films: multiple ring formation. *Langmuir*. 18: 3441-3445, 2002. (Also in Science, Vol 296, Issue 5568, 619, April 2002.)

CHAPTERS/OTHER

1) Mossahebi, S., Zhu, S., Chen, H., Shmuylovich, L., Ghosh, E., Kovács, S. J. Quantification of Global Diastolic Function by Kinematic Modeling-based Analysis of Transmitral Flow via the Parametrized Diastolic Filling Formalism. *J. Vis. Exp*. 91:e51471, 2014.

2) Kovács SJ, **Shmuylovich L**, Zhang W. Imaging the motion of the heart and blood with echocardiography: advanced technology provides deeper insights into physiology and diastolic function. *Philips Medica Mundi*. 52:31-6, 2008.

CONFERENCE PUBLICATIONS

Conference Proceedings Papers

- 1) **Shmuylovich L**, Kovács SJ. Automated method for calculation of a load-independent index of isovolumic pressure decay from left ventricular pressure data. *Conf Proc IEEE Eng Med Biol Soc.* 2009:3031-4, 2009.
- 2) Ghosh E, **Shmuylovich L**, Kovács SJ. Determination of early diastolic LV vortex formation time (T^*) via the PDF formalism: a kinematic model of filling. *Conf Proc IEEE Eng Med Biol Soc.* 2009:2883-6, 2009.
- 3) Zhang W, **Shmuylovich L**, Kovács SJ. The pressure recovery ratio: The invasive index of LV relaxation during filling. Model-based prediction with in-vivo validation. *Conf Proc IEEE Eng Med Biol Soc.* 2009:3940-3, 2009.

Abstracts

- 1) Mossahebi S, **Shmuylovich L**, Kovács SJ. Echocardiographic Assessment of Chamber Stiffness - Contrasting Normal Sinus Rhythm and Chronic Atrial Fibrillation. AHA Scientific Session; Los Angeles, CA 2012.
- 2) Mossahebi S, **Shmuylovich L**, Kovács SJ. The thermodynamics of diastole: kinematic modeling-based derivation of the P-V loop to transmitral flow energy relation with in vivo validation. ACC Scientific Session; New Orleans, LA 2011.
- 3) **Shmuylovich L**, Kovács SJ. Derivation and validation of a load independent index of isovolumic relaxation. *American College of Cardiology Annual Meeting*, FL 2009.
- 4) Zhang W, **Shmuylovich L**, Kovács SJ. Left ventricular pressure recovery ratio: a catheterization derived global chamber relaxation index. *BMES Society Annual Fall Meeting*. MO 2008.
- 5) **Shmuylovich L**, Kovács SJ. Analysis of the "forces of filling plane" facilitates determination of ventricular diastolic reserve. *BMES Society Annual Fall Meeting*. MO 2008.
- 6) **Shmuylovich L**, Kovács SJ. Premature ventricular contraction provide a novel test for a load independent index of filling. *BMES Society Annual Fall Meeting*. MO 2008.
- 7) **Shmuylovich L**, Kovács SJ. Load independent index of isovolumic relaxation (LIIR): mathematical derivation and clinical validation. *BMES Society Annual Fall Meeting*. MO 2008.
- 8) **Shmuylovich L**, Kovács SJ. Analysis of Isovolumic Pressure Decay in the Relaxation (τ_c) vs Stiffness Plane (E_k) Provides Novel Physiologic Insight. *XVIII*

Congress of the Cardiovascular Systems Dynamics Society Fall Meeting, St Louis, MO 2008.

9) **Shmuylovich L**, Kovács SJ. Solution of the load independent index of diastolic function problem. *BMES Society Annual Fall Meeting, CA 2007.*

10) **Shmuylovich L**, Kovács SJ. Noninvasive LV end diastolic pressure estimation: model-based derivation with in-vivo validation. *BMES Society Annual Fall Meeting, CA 2007.*

11) **Shmuylovich L**, Kovács SJ. Load independent index of diastolic filling: model-based prediction with in-vivo validation. *XVII Congress of the Cardiovascular Systems Dynamics Society Fall Meeting, Netherlands 2006.*

12) **Shmuylovich L**, Kovács SJ. Load independent index of diastolic function: derivation with in-vivo validation. *BMES Society Annual Spring Meeting, MD 2005.*

13) Shen AQ, Stone H, **Shmuylovich L**. Surface morphology of drying latex films. *Society of Rheology Annual Meeting, MN 2002.*